

COAL-LIKE SUBSTANCES FROM LOW-TEMPERATURE PYROLYSIS
AT VERY LONG REACTION TIMES

R. A. Friedel, J. A. Queiser, and H. L. Retcofsky

U.S. Department of the Interior, Bureau of Mines,
Pittsburgh Coal Research Center, Pittsburgh, Pa. 15213

ABSTRACT

The importance of long reaction times in the coalification process has been demonstrated in the laboratory. Samples of cellulose and pine sawdust in evacuated, sealed glass vials have been heated at 200° C for two years. Black coal-like chars were produced; heating at 200° C for hours produced very little chemical change. The chars were characterized by infrared and electron spin resonance spectra. The infrared spectra of the pine sawdust char and of a subbituminous coal are nearly identical, except for differing carbonyl absorption. The spectrum of the cellulose char is also similar to that of the subbituminous coal. The electron spin resonance results show that g values and line widths are nearly identical for the chars and are very close to similar values for subbituminous coal.

200° C is considered a reasonable coalification temperature; depth of burial can provide such temperatures. The experimental coalification obtained in only two years appears to substantiate the hypothesis that geologic time could produce all ranks of coals at temperatures below 200° C.

INTRODUCTION

In the study of the structure and properties of coal, attempts have been made to prepare synthetic coals, principally by pyrolysis methods. Chars having properties identical to those of coals have not been produced. Initial attempts at studying the infrared spectra of coal-like chars prepared by pyrolysis of pure materials were carried out several years ago.^{1,2/} The pyrolysis method used was that of Smith and Howard, who had prepared from cellulose, chars that had some of the properties of coals.^{3/} We studied the infrared spectra of chars prepared from cellulose over a range of temperatures; the spectrum of a 400° C cotton char somewhat resembled that of high-volatile bituminous coal.^{1,2/} The spectrum of this char showed a definite carbonyl absorption band which is not present, except as a weak shoulder, in infrared spectra of coals. Carbohydrate chars prepared at 300°, 400°, and 500° C produced absorption bands in the aromatic region that were identical to the aromatic bands produced respectively by lignite, high-volatile bituminous, and anthracite coals; less similarity was observed in other parts of the spectra.^{4/} Similarities of reaction of coal and the carbohydrate, sucrose, were nicely illustrated by the identical spectra of products obtained in hydrogenation studies.^{5/}

Friedman and coworkers studied many coal-like chars prepared by pyrolysis of pure oxygenated compounds, mostly at 400° C and reaction times of one hour; several properties of these chars, including infrared spectra, have some resemblance to the corresponding properties of coals.^{6/} Pure hydrocarbons have been charred in the presence and absence of molecular oxygen; only when oxygen was present did the infrared spectra of the chars resemble those of coals, particularly in the 1600 cm⁻¹ region.^{4,7/} Unless oxygen is involved the 1600 cm⁻¹ band is weak or non-existent; thus it is believed that the strong 1600 cm⁻¹ band involves carbonyl groups.^{4,7/}

In another study, chars were prepared from O^{18} -labelled compounds in an attempt to ascertain whether an isotopic shift would occur at 1600 cm^{-1} and would thus indicate that carbonyl groups are involved. No isotopic shift was obtained; the infrared spectrum of an O^{18} -labelled chelate, dibenzoylmethane, demonstrated that if a C=O group is very strongly chelated the C=O vibration becomes completely delocalized and no isotopic shift occurs.^{8,9/}

In attempting to simulate coal the following principal variables are available: Starting material, temperature, rate of heating, reaction time, and pressure. The effect of pressure is considered minor compared to the effect of temperature.^{10,11/} The effect of pressure during many eons may be important; temperature during many eons is certainly important. Though presumptuous, it was assumed that some slight indication of the effect of geologic time might be observable in the laboratory. Pyrolysis experiments involving reaction times of years, rather than hours or days, were decided on. Temperatures at or below 200° C were chosen. The spectral methods selected for investigation of the coal-like properties of the chars were infrared and electron spin resonance spectrometry.

EXPERIMENTAL PROCEDURE

Pyrolyses. Pyrolytic oxidation of cotton and pine-wood sawdust was carried out at low temperatures. Two sets of samples were heated in air at 150° C and at 200° C for 10 months; the chars produced were investigated by infrared spectrometry.

For the pyrolysis experiments without air, samples of cotton, 0.43 g, and pine-wood sawdust, 0.20 g, were placed in heavy-walled Pyrex tubes which were evacuated and sealed. The sample-tube volumes were 3.1 cc. The samples were heated at 200° C for two years. Gases and other volatile products were analyzed by mass spectrometer.

Instrumental investigation. The principal methods of characterizing the pyrolysis products were infrared (Perkin-Elmer Model 521)^{a/} and electron paramagnetic resonance spectrometry (Varian Associates Model V-4500). Preliminary examinations of the chars were also made on a high-resolution mass spectrometer (Consolidated 21-110B). Ultimate microanalyses of the chars will be performed by the Huffman Laboratories; analyses will destroy the small samples remaining so none will be carried out until all possible experimental investigations are concluded.

RESULTS AND DISCUSSION OF RESULTS

Low pyrolysis temperatures and reaction times of several months were decided on in an attempt to simulate mild coalification conditions. Temperatures in the 200° C range are considered realistic; many coals have been subjected to such temperatures due to depth of burial. Initially pyrolytic oxidation runs were made on cellulose and on pine sawdust at 150° C in the presence of air. Pyrolysis of these materials for 10 months gave black insoluble solids having infrared spectra which indicated extensive oxidation. The second set of investigations was carried out at 200° C in the presence of air; as expected greater pyrolytic oxidation was produced. Then pyrolysis runs in the absence of air were initiated with samples of cotton and of pine sawdust sealed in evacuated, heavy-wall glass tubes. The samples were heated at 200° C for two years. Tarry products were observed during the early stages of pyrolysis; these became solid char long before two years elapsed. The gas produced in the pyrolysis of the cotton sample was lost by an explosion; most of the char was salvaged. The vial containing the pine sawdust

^{a/} Reference to trade names is made for identification only and does not imply endorsement by the Bureau of Mines.

char was then opened, with release of considerable pressure of gas (6.3 atm). A thin film of colorless liquid, mostly water, vaporized completely into the evacuated gas-handling system. The gas analysis in table 1 shows mainly H₂O and CO₂. Both chars were completely black; the yield of char from pine sawdust was about 85 percent. The infrared spectra of both samples are shown in figure 1, along with a spectrum of a subbituminous coal (Dietz bed, Wyoming, 70.8 percent C, m.a.f. Ultimate analysis is given in table 2). The spectra of the coal and the sawdust char are remarkably similar. In addition to the more obvious spectral similarities at 3400, 2950, 2920, 2860, 1600, 1440, 1370, 1280, and 1180 cm⁻¹, there is a considerable similarity at the aromatic band positions, 860, 810, and 750 cm⁻¹. The aromatic bands are weak in the spectra of subbituminous coals, but the similarity of the coal and char absorption patterns in this region is impressive. It is apparent from these spectra that it is possible over a long period of time to approach a coal-like spectrum, even at a low temperature.

Table 1.- Mass spectrometric analysis of gases from 200° pyrolysis of pine sawdust.
Volume of vial, 3.1 cc; pressure in vial 6.3 atm.

	<u>Mole percent</u>	<u>Milligrams</u>
Carbon dioxide	25.8	9.7
Water	57.9	8.9
Methanol	3.9	1.1
Dimethyl ether	<u>12.4</u>	4.9
	100.	
Total carbonyl compounds (estimate)		<u>5.</u>
		29.6

Table 2.- Ultimate analysis of Dietz bed subbituminous coal,
Big Horn Mine, Wyoming

	<u>Weight percent, m.a.f.^{a/}</u>
C	70.83
H	5.06
N	1.02
S	0.59
O (by difference)	22.50

a/ Ash content 3.23 percent (moisture-free)

Heating from room temperature to 190° C in one hour, the cellulose of Smith and Howard had produced a brown char (yield, 89 percent) but the infrared spectrum, as well as the elemental analysis, resembled those of cellulose with only minor differences.^{4/} No coal-like spectral features were observed. In the spectrum of the sawdust char there is a 1700 band as we have seen before in char spectra. But, for the first time in spectra of chars prepared at low temperature the 1600 band is more intense than the 1700 and thus is approaching the situation in coal spectra. Thus the very long heating time has produced a definite decrease in carbonyl-containing structures. In the coalification process it is feasible that simple

carbonyl groups are first formed in the early stages of pyrolysis and then are slowly converted to some other structure(s) during geologic time. Possibly the carbonyl groups are converted to modified carbonyl structures which can produce the intense 1600 cm^{-1} absorption band observed in infrared spectra of coals and chars. Substantiation of this hypothesis may exist in the behavior of carbonyl groups in chars that were prepared from cellulose at 300° , 400° , and 500° C .^{4,7/} In the spectrum of the 300° char the carbonyl absorption is stronger than the unknown absorption at 1600 cm^{-1} . Relative intensities are given in table 3. For the 400° C char the intensities become more similar; the spectrum of the 500° C char shows reversal of intensities with complete disappearance of the simple carbonyl absorption band.^{4,7/} These changes may be explainable by the postulation of conversion into a modified carbonyl-containing structure. This structure could be the conjugated chelated structure, such as the enol form of acetylacetone, that has been proposed previously as the source of the 1600 cm^{-1} absorption band.^{2,14/} It is interesting that the same kind of change, though more subtle, occurs in coals; infrared spectra of lignites and low rank coals have weak absorption shoulders at 1700 cm^{-1} which gradually disappear from spectra of higher rank coals.^{15,16/} For the coals the conversion of carbonyl compounds to the presumed conjugated chelated carbonyls is farther advanced than it is in these chars which were prepared at reaction times of only one hour.^{4,7/}

Table 3.- Relative absorption intensities in the infrared spectra of 300° , 400° , and 500° C cellulose chars at 1700 cm^{-1} (carbonyl compounds) and 1600 cm^{-1} (presumably chelated conjugated carbonyl groups)

<u>Cellulose char, preparation temperature</u>	<u>Relative intensities, percent</u>	
	<u>1700 cm^{-1}</u>	<u>1600 cm^{-1}</u>
300° C	78	22
400° C	59	41
500° C	0	100

Electron spin resonance spectrometry has been applied to the study of chars of cotton and pine sawdust. Values for the parameters are given in table 4 along with comparative values for subbituminous coal.^{17/} As with the infrared, the results for the chars are closely similar to those for the coal vitrain. The fact that a signal is detected is of interest for it demonstrates that stable free radicals can be formed in natural materials on exposure to very mild heating conditions. There are not many examples of free radical signals obtained from chars produced at temperatures as low as 200° C . It is probable that even lower temperatures will produce free radicals in carbonaceous materials over long periods of time.

Table 4.- Electron spin resonance data for chars and subbituminous coal vitrain

	<u>Cotton char</u>	<u>Pine sawdust char</u>	<u>Subbituminous vitrain, Wyoming</u>
g-Value	2.00321 ± 0.0001	2.00314 ± 0.0001	2.00381 ± 0.0001
Line width, gauss	5.6 ± 0.5	6.3 ± 0.5	8.0 ± 0.5

Preliminary work on mass spectra of these chars has shown mononuclear and polynuclear aromatics similar to those found in mass spectra obtained on coal; this investigation is continuing.

The striking importance of time in pyrolysis reactions has been demonstrated. If chars as coal-like as these can be produced in two years, at temperatures that have little effect during short times, then it appears that in geologic times coal could be produced at temperatures much lower than 200° as proposed by various people.^{10,12,13/} Our next experiments will run for greater lengths of time, with the expectation of producing chars that will resemble higher ranks of coal. Under the same experimental conditions that produced chars similar to subbituminous coal, chars having the characteristics of bituminous coals possibly could result from heating at 200° C for three or four years. It is expected that the distinctive aromatic absorption bands in the infrared spectra and the electron spin resonance parameters, of bituminous coals will be duplicated in such chars.

On the question of whether cellulose or lignin is the more important precursor of coal the results herein described indicate that at low temperatures and long reaction times the coal-like chars obtained from cellulose and from lignin plus cellulose are very similar. It may be significant that greater similarity between coal and char infrared spectra is observed for the char from lignin plus cellulose (pine sawdust).

REFERENCES

1. Friedel, R. A., and Pelipetz, M. G., *J. Opt. Soc. Am.*, 1953, 43, 1051.
2. Friedel, R. A., and Queiser, J. A., *Anal. Chem.*, 1956, 28, 22.
3. Smith, R. C., and Howard, H. C., *J. Am. Chem. Soc.*, 1937, 59, 234.
4. Friedel, R. A., *Proc. Fourth Carbon Conf.*, Univ. Buffalo, Pergamon Press, New York, 1960, 321.
5. Pelipetz, M. G., and Friedel, R. A., *Fuel*, 1959, 38, 8.
6. Friedman, S., Raymond, R., Reggel, L., Wender, I., and Friedel, R. A., *Abstracts of Papers*, April 1956 meeting, *Am. Chem. Soc.*, 6J.
7. Friedel, R. A., *Applied Optics*, 1963, 2, 1109.
8. Friedel, R. A., Durie, R. A., and Shewchyk, Y., *Carbon*, 1967, 5, 559.
9. Durie, R. A., Shewchyk, Y., and Friedel, R. A., *Spectrochim. Acta*, 1968, 24A, 1543.
10. Teichmuller, M., and Teichmuller, R., Ch. in *Coal Science*, ed. R. F. Gould, *Advances in Chem. Series No. 55*, 1966, Washington, 133.
11. Hryckowian, E., Dutcher, R. R., and Dachille, F., *Econ. Geology*, 1967, 62, 517.
12. Karweil, J., *Deutsch Z. Geol. Ges.*, 1956, 107, 132.
13. Francis, W., *Coal*, E. Arnold Ltd., London, 1961, 573.

14. Brown, J. K., J. Chem. Soc., London, 1955, 744.
15. Friedel, R. A., Ch. in Applied Infrared Spectroscopy, ed. D. N. Kendall, Reinhold Pub. Co., 1966, 312.
16. Friedel, R. A., Retcofsky, H. L., and Queiser, J. A., Bureau of Mines Bull. 640, 1967, 48 pp.
17. Retcofsky, H. L., Stark, J. M., and Friedel, R. A., Anal. Chem., 1968, 40, 1699.

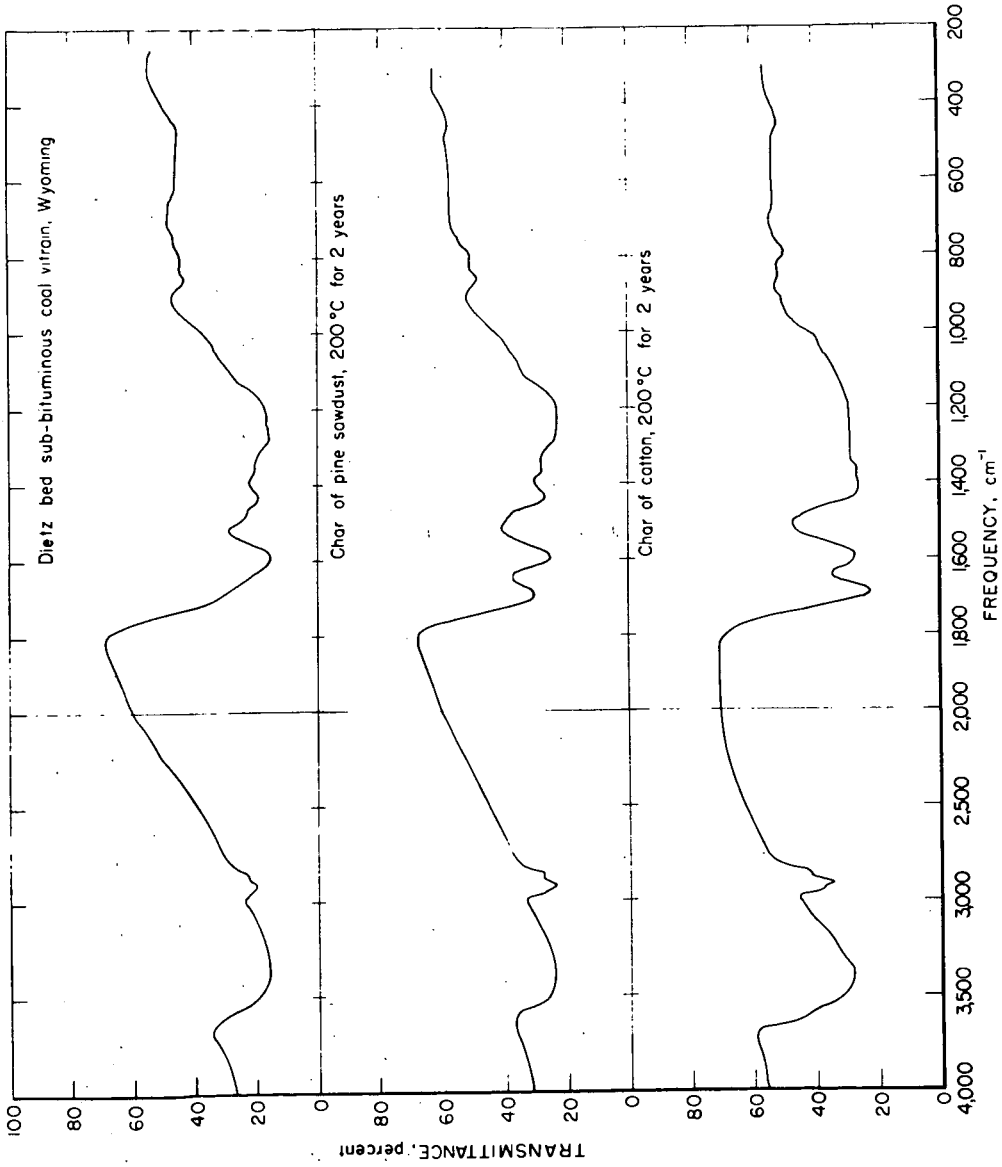


Figure 1.- Infrared spectra of Dietz bed subbituminous coal vitrain, 200° char of pine sawdust, and 200° char of cotton.

CHARACTERIZATION OF COAL LIQUEFACTION PRODUCTS BY
HIGH RESOLUTION-LOW VOLTAGE MASS SPECTROMETRY

By

Thomas Aczel, J. Q. Foster, J. H. Karchmer
Esso Research and Engineering Company, Baytown, Texas

INTRODUCTION

High resolution mass spectroscopy is one of the most promising tools for the characterization of very complex materials. Since commercial instruments became available in the early nineteen sixties, the technique has been applied with considerable success to the analysis of materials derived both from petroleum and coal (1, 2, 3, 4).

This paper deals with the application of a particular approach, high resolution-low voltage mass spectrometry, coupled with computerized data acquisition and reduction, to the analysis of liquid and solid materials derived from coal liquefaction processes. These processes are of considerable industrial interest at the present; and the particular analytical approach used permits one to obtain routine quantitative or at least semiquantitative data on the hundreds of components present in each sample. Pilot plant or bench scale experiments can be thus supported with detailed analytical data.

EXPERIMENTAL

The high resolution-low voltage technique used, as well as the computerized data acquisition and reduction system, has been described elsewhere (5, 6, 7). In brief, mass spectra are obtained on an AEI model MS 9 instrument at a resolving power of approximately 1/10,000, and at low ionizing voltages, approximately 12 volts. This resolving power is sufficient to separate all significant mass multiplets up to about m/e 400, with exception of the $^{13}\text{CH-N}$ doublet, the separation of which requires additional calculations. At the same time, the use of low ionizing voltages reduces the spectra to essentially parent peaks and their ^{13}C isotopes, so that interferences between sample components are practically eliminated, and data can be obtained both on the compound type and carbon number distribution. Quantitative information is obtained by using pure compound or extrapolated calibration coefficients. The data acquisition system consists of an IBM Model 1802 computer, which converts the analog signals from the mass spectrometer to digital data and records these on magnetic tape. Subsequent calculations, including the recognition of peaks, calculation of peak areas, precise masses, formulas and, finally, the complete quantitative analysis, are carried out on an IBM Model 360/50 computer. At present, the quantitative analysis provides data routinely for up to 58 compound types and up to 2900 components, in less than three hours, including instrument time and interpretation. These types include hydrocarbons with formulas C_nH_{2n} to $\text{C}_n\text{H}_{2n-44}$, oxygenated compounds from $\text{C}_n\text{H}_{2n-20}$ to $\text{C}_n\text{H}_{2n-360}$, and sulfur compounds from $\text{C}_n\text{H}_{2n-2}\text{S}$ to $\text{C}_n\text{H}_{2n-34}\text{S}$. Semiquantitative information on additional compound types, such as those containing N, or containing more than one heteroatom per molecule, or possessing a higher condensation than outlined above, can be obtained in a short additional time. The analysis is normalized to the volatile portion of each sample, determined by weighing the sample and any observed residue.

DISCUSSION

Application of the high resolution-low voltage method to coal liquefaction products yields a very detailed characterization. Isomeric hydrocarbon types, possessing the same general formula, but different aromatic nuclei, can be separated and determined at least semiquantitatively. The behavior of the components during processing can be closely followed. The analysis includes data on aromatic and heteroaromatic components ranging from ppm to several percent in concentration and from 78 to 500+ in molecular weight. A large number of components and compound types can be determined rapidly in each sample. The degree of sophistication attained is best illustrated with practical examples.

The ability of distinguishing isomeric hydrocarbon types is based on the observed fact that the concentrations of the aromatic nuclei are higher than those of the alkyl-substituted members in any homologous series. Thus maxima in the carbon number distribution in any series correspond in most cases to the appearance of an individual nucleus. A number of these nuclei are naphthenoaromatic compounds. Examination of samples hydrogenated to different extents can thus corroborate the presence of naphthenoaromatic nuclei, as the concentration of these increases with the extent of the hydrogenation. The data reported below will serve to illustrate the procedure.

Carbon Number Distribution in the C_nH_{2n-10} Series, Weight Percent

<u>Formula</u>	<u>Mildly Hydrogenated Material</u>	<u>Severely Hydrogenated Material</u>
C_9H_8	0.062	0.056
$C_{10}H_{10}$	0.220	0.408
$C_{11}H_{12}$	0.168	0.162
$C_{12}H_{14}$	0.444	0.926
$C_{13}H_{16}$	0.552	1.175
$C_{14}H_{18}$	0.702	1.493
$C_{15}H_{20}$	0.278	0.624
$C_{16}H_{22}$	0.314	0.443
$C_{17}H_{24}$	0.122	0.252
$C_{18}H_{26}$	0.006	0.088

The only reasonable structure for a C_9H_8 hydrocarbon is indene. $C_{10}H_{10}$ could be methyl-indene or dihydronaphthalene. As the total C_{10} concentration is higher than the C_9 concentration, dihydronaphthalene is believed to be the major component. This assumption is corroborated by the fact that this difference in concentration is enhanced in the more severely hydrogenated material, and dihydronaphthalene is an obvious hydrogenation product from naphthalene. Analogously, increases in concentration at C_{12} , C_{13} , C_{14} , and C_{16} , all enhanced in the severely hydrogenated material, indicate the presence of additional nuclei, respectively identified as tetrahydroacenaphthene, benzohydrindane, octahydroanthracene and dodecahydropyrene. Data from other series of the same general formula are treated similarly. Only maxima or increases in concentration which appear at the same carbon number and series in a large number of samples are accepted as a genuine indication of more than one compound type in a given series.

As mentioned above, the concentration of alkyl-substituted components is considerably lower than that of the respective nuclei. This can be observed best in series and carbon number intervals where only one compound type is present, as shown below.

Carbon Number Distribution in the C_nH_{2n-8} Series, Weight Percent

<u>Formula</u>	<u>Mildly Hydrogenated Material</u>	<u>Severely Hydrogenated Material</u>
$C_{10}H_{12}$	5.804	9.180
$C_{11}H_{14}$	2.977	5.291
$C_{12}H_{16}$	1.805	2.671
$C_{13}H_{18}$	1.043	1.291

The decrease in concentration with increasing carbon number is approximately twofold. This rate of decrease has also been observed for other series, and in a large number of samples. We were able thus to develop a method to estimate the concentration of each isomeric compound type in a given series. The procedure, illustrated below, starts with extrapolating the concentrations of the homologs of the compound type with the lowest molecular weight nucleus. The concentration of the nucleus of the next compound type is obtained by subtracting the extrapolated concentration of the homolog of the first compound type at the carbon number involved from the concentration observed for the series. Concentrations of the homologs of the second compound type are then extrapolated; and the procedure continues similarly for all other compound types. The extrapolation is used, of course, only in carbon number intervals where more than one type is conceivably present. In addition, the method is applicable only to samples with boiling range wide enough to contain all isomers involved in the separation.

Separation of Isomeric Compound Types in the C_nH_{2n-14} Series, Weight Percent

<u>Formula</u>	<u>Total C_nH_{2n-14} Series</u>	<u>Acenaphthenes</u>	<u>Tetrahydro-anthracenes</u>	<u>Octahydro-pyrenes</u>
$C_{12}H_{10}$	2.954 ^(1,2)	2.954 ⁽²⁾	-	-
$C_{13}H_{12}$	1.894 ⁽²⁾	1.894 ⁽²⁾	-	-
$C_{14}H_{14}$	2.536 ^(1,2)	0.947 ⁽³⁾	1.589 ⁽⁴⁾	-
$C_{14}H_{16}$	1.105 ⁽²⁾	0.474 ⁽³⁾	0.631 ⁽⁴⁾	-
$C_{16}H_{18}$	1.146 ⁽¹⁾	0.237 ⁽³⁾	0.316 ⁽³⁾	0.593 ⁽⁴⁾
$C_{17}H_{20}$	0.631 ⁽²⁾	0.118 ⁽³⁾	0.158 ⁽³⁾	0.355 ⁽⁴⁾
$C_{18}H_{22}$	0.316 ⁽²⁾	0.059 ⁽³⁾	0.079 ⁽³⁾	0.178 ⁽⁴⁾

- (1) Maxima in carbon number distribution, indicating the appearance of respectively, acenaphthene, tetrahydroanthracene and octahydro-pyrene.
- (2) Raw concentrations.
- (3) Concentrations obtained by extrapolation.
- (4) Concentrations obtained by subtraction.

The information thus obtained on the concentration of the individual compound types can be used to follow their behavior upon hydrogenation. Typical data obtained are shown below.

Ring Systems	Weight Percent	
	Mildly Hydrogenated Material	Severely Hydrogenated Material
<u>Naphthalene System</u>		
Naphthalenes, $C_n H_{2n-12}$	14.2	7.9
Dihydronaphthalenes, $C_n H_{2n-10}$	0.5	0.7
Tetralins, $C_n H_{2n-8}$	11.5	18.4
Octahydronaphthalenes, $C_n H_{2n-4}$	0.3	0.4
Decalins, $C_n H_{2n-2}$	<u>2.0</u>	<u>2.6</u>
Total	28.5	30.0
<u>Anthracene System</u>		
Anthracenes, $C_n H_{2n-18}$	7.2	5.4
Tetrahydroanthracenes, $C_n H_{2n-14}$	3.0	3.8
Hexahydroanthracenes, $C_n H_{2n-12}$	1.3	1.5
Octahydroanthracenes, $C_n H_{2n-10}$	0.7	1.5
Decahydroanthracenes, $C_n H_{2n-8}$	<u>0.6</u>	<u>1.2</u>
Total	12.8	13.4
<u>Acenaphthene System</u>		
Acenaphthylenes, $C_n H_{2n-16}$	0.1	0.0
Acenaphthenes, $C_n H_{2n-14}$	6.6	5.3
Tetrahydroacenaphthenes, $C_n H_{2n-10}$	<u>0.7</u>	<u>1.7</u>
Total	7.4	7.0
<u>Fluorene System</u>		
Fluorenes	<u>5.0</u>	<u>5.0</u>
Total	5.0	5.0

Another aspect of the characterization of coal liquefaction products is the determination of components containing heteroatoms. Most of these can be directly identified from the computer output of the high resolution-low voltage spectra as illustrated below for typical mass multiplets.

Computer Identification of FormulasMultiplets at m/e 310 and 330

<u>Intensity, % I</u>	<u>Measured Mass</u>	<u>Error, mmu</u>	<u>Formula</u>
0.0016	310.0857	+0.7	C ₁₉ H ₁₈ S ₂
0.0332	310.1346	-1.2	C ₂₃ H ₁₈ ⁰
0.5825	310.1736	+1.5	C ₂₄ H ₂₂
0.0075	310.2276	-2.0	C ₂₂ H ₃₀ ⁰
0.0435	310.2675	+1.5	C ₂₃ H ₃₄
0.0017	330.1360	-4.8	C ₂₆ H ₁₈
0.0064	330.1605	-1.5	C ₂₃ H ₂₂ O ₂
0.0131	330.1963	-2.1	C ₂₄ H ₂₆ ⁰
0.1219	330.2360	+1.3	C ₂₅ H ₃₀
0.0051	330.3291	+0.5	C ₂₄ H ₄₂

The resolving power of our instrument, however, is insufficient to separate the ¹³CH-N doublet above m/e 120-130. Components containing one N atom are therefore detected using isotope correction techniques. The presence of N compounds of odd molecular weights is indicated by residual peakheights after isotope correction and shift in the measured mass from the value of the ¹³C isotope to that of the N compound, as shown in the example reported below.

<u>Measured Mass</u>	<u>Formula</u>	<u>Error, mmu</u>	<u>Intensity, % I</u>
180.093	C ₁₄ H ₁₂	-0.6	1.903
181.090	-	-	0.845

<u>Formula</u>	<u>Theoretical Mass</u>	<u>Theoretical Intensity, % I</u>
¹³ CC ₁₃ H ₁₂	181.096	0.290
C ₁₃ H ₁₁ N	181.089	0.555*

• Residual after isotope correction.

Theoretical mass for unresolved doublet:

$$\frac{(181.096 \times 0.290) + (181.089 \times 0.555)}{0.845} = 181.091$$

Error of mass calculation for unresolved doublet: -1.0 mmu (-0.4 with respect to 180.093).

The techniques discussed above result in a thorough characterization of coal liquefaction products. The wealth of data obtained is illustrated by the list of compound types detected in one individual sample, reported below.

Series	Model Structure	Series	Model Structure
$C_n H_{2n}$	Cyclohexanes	$C_n H_{2n-20}$	Naphthenoanthracenes
$C_n H_{2n-2}$	Decalins	$C_n H_{2n-20}$	Tetrahydrochrysenes
$C_n H_{2n-2}$	Hydrindans	$C_n H_{2n-22}$	Pyrenes
$C_n H_{2n-4}$	Hydrindenes	$C_n H_{2n-22}$	Hexahydrobenzopyrenes
$C_n H_{2n-4}$	Octahydronaphthalenes	$C_n H_{2n-24}$	Chrysenes
$C_n H_{2n-4}$	Perhydroanthracenes	$C_n H_{2n-24}$	Tetrahydrobenzopyrenes
$C_n H_{2n-6}$	Benzenes	$C_n H_{2n-26}$	Cholanthrenes
$C_n H_{2n-8}$	Indanes	$C_n H_{2n-28}$	Benzopyrenes
$C_n H_{2n-8}$	Tetralins	$C_n H_{2n-30}$	Picenes
$C_n H_{2n-10}$	Indenes	$C_n H_{2n-32}$	Anthanthrenes
$C_n H_{2n-10}$	Dihydronaphthalenes	$C_n H_{2n-34}$	Dibenzopyrenes
$C_n H_{2n-10}$	Tetrahydroacenaphthenes	$C_n H_{2n-36}$	Coronenes
$C_n H_{2n-10}$	Benzhydrindanes	$C_n H_{2n-38}$	Benzanthanthrenes
$C_n H_{2n-10}$	Octahydroanthracenes	$C_n H_{2n-4}^S$	Thiophenes
$C_n H_{2n-10}$	Dodecahydropyrenes	$C_n H_{2n-10}^S$	Benzothiophenes
$C_n H_{2n-12}$	Naphthalenes	$C_n H_{2n-12}^S$	Naphthenobenzothiophenes
$C_n H_{2n-14}$	Acenaphthenes	$C_n H_{2n-14}^S$	Indenothiophenes
$C_n H_{2n-14}$	Tetrahydroanthracenes	$C_n H_{2n-16}^S$	Dibenzothiophenes
$C_n H_{2n-16}$	Acenaphthylenes	$C_n H_{2n-18}^S$	Acenaphthenothiophenes
$C_n H_{2n-16}$	Fluorenes	$C_n H_{2n-20}^S$	Fluorenothiophenes
$C_n H_{2n-16}$	Dihydroanthracenes	$C_n H_{2n-2}^O$	Dihydrofurans
$C_n H_{2n-16}$	Hexahydropyrenes	$C_n H_{2n-4}^O$	Furans
$C_n H_{2n-18}$	Anthracenes	$C_n H_{2n-6}^O$	Phenols
$C_n H_{2n-18}$	Tetrahydropyrenes	$C_n H_{2n-8}^O$	Naphthenophenols
$C_n H_{2n-18}$	Hexahydrochrysenes	$C_n H_{2n-10}^O$	Benzofurans
$C_n H_{2n-18}$	Decahydrobenzopyrenes	$C_n H_{2n-12}^O$	Naphthols
		$C_n H_{2n-14}^O$	Naphthenonaphthols
		$C_n H_{2n-16}^O$	Dibenzofurans
		$C_n H_{2n-18}^O$	Hydroxyanthracenes
		$C_n H_{2n-20}^O$	Hydroxynaphthenoanthracenes
		$C_n H_{2n-22}^O$	Hydroxypyrenes

$C_n H_{2n-24} O$	Hydroxychrysenes	$C_n H_{2n-6} O_2$	Dihydroxybenzenes
$C_n H_{2n-26} O$	Hydroxycholanthrenes	$C_n H_{2n-8} O_2$	Dihydroxyindanes
$C_n H_{2n-28} O$	Hydroxybenzopyrenes	$C_n H_{2n-10} O_2$	Hydroxybenzofurans
$C_n H_{2n-30} O$	Hydroxypicenes	$C_n H_{2n-12} O_2$	Dihydroxytetralins
$C_n H_{2n-32} O$	Hydroxyanthanthrenes	$C_n H_{2n-14} O_2$	Hydroxyindenofurans
$C_n H_{2n-38} O$	Hydroxybenzanthanthrenes	$C_n H_{2n-16} O_2$	Hydroxydibenzofurans
$C_n H_{2n-5} N$	Pyridines	$C_n H_{2n-18} O_2$	Dihydroxyanthracenes
$C_n H_{2n-7} N$	Naphthenopyridines	$C_n H_{2n-20} O_2$	Dihydroxynaphthoanthracenes
$C_n H_{2n-9} N$	Indoles	$C_n H_{2n-22} O_2$	Dihydroxypyrenes
$C_n H_{2n-11} N$	Quinolines	$C_n H_{2n-24} O_2$	Dihydroxychrysenes
$C_n H_{2n-13} N$	Naphthoquinolines	$C_n H_{2n-26} O_2$	Dihydroxycholanthrenes
$C_n H_{2n-15} N$	Carbazoles	$C_n H_{2n-8} SO$	Hydroxycyclopentenothiophenes
$C_n H_{2n-17} N$	Acridines	$C_n H_{2n-10} SO$	Hydroxybenzothiophenes
$C_n H_{2n-19} N$	Naphthenobenzoquinolines	$C_n H_{2n-12} SO$	Hydroxynaphthenobenzothiophenes
$C_n H_{2n-21} N$	Benzocarbazoles	$C_n H_{2n-16} SO$	Hydroxydibenzothiophenes
$C_n H_{2n-23} N$	Benzacridines	$C_n H_{2n-18} SO$	Hydroxynaphthenonaphthothiophenes
$C_n H_{2n-25} N$	Naphthenobenzacridines	$C_n H_{2n-20} SO$	Hydroxyfluorenoothiophenes
$C_n H_{2n-27} N$	-	$C_n H_{2n-16} O_3$	Dihydroxydibenzofurans
$C_n H_{2n-29} N$	-	$C_n H_{2n-10} SO_2$	Dihydroxybenzothiophenes
$C_n H_{2n-31} N$	-	$C_n H_{2n-16} SO_2$	Dihydroxydibenzothiophenes
		$C_n H_{2n-18} SO_2$	Dihydroxynaphthenonaphthothiophenes
		$C_n H_{2n-20} SO_2$	Dihydroxyfluorenoothiophenes

The model structures listed above were deduced by observing the molecular weight of the first member for each compound type in a large number of samples. This observed molecular weight was in most cases identical to that of the model structures proposed. As isomeric compound types of the same nuclear molecular weight, such as anthracenes and phenanthrenes, cannot be separated by mass spectrometric means, these structures should be considered only indicative.

Additional compound types have been of course detected in other samples. The most interesting among these were compounds as condensed as $C_n H_{2n-48}$, $C_n H_{2n-42} O$, $C_n H_{2n-34} O_2$, $C_n H_{2n-32} SO$, and several compound types containing NO, and S_2 groups.

The presence of O, O_2 groups, most probably in the hydroxyl form, is considered quite revealing, particularly in view of the fact that these hydroxyl groups are located on hydrocarbons containing up to 8 aromatic rings. The detection of these very condensed heterocompounds in coal liquefaction products corroborates the views on coal structure, reported by Hill (8). According to this and other authors, coal is viewed as a polymer composed of polyaromatic nuclei linked by -O- and -S- bridges.

It is reasonable to expect that these linkages break upon hydrogenation, thus giving rise to the polyaromatic phenols detected in our analyses.

Another interesting insight in the structure of coal is provided by the analysis of the heavier fractions (700°F.+) of hydrogenated material. As shown by the example reported below, these materials contain considerable amounts of polynuclear aromatics, associated with as many as a total of fifteen to twenty C atoms in side chains. It is conceivable, of course, that naphthenoaromatic nuclei are also present. It is believed that these side chains are short, with one or two C atoms per side chain, although due to the insolubility of this type of material in any solvent, this assumption could not be confirmed by NMR techniques. These short side chains could be derived from hydrocracking of naphthenoaromatic compounds or from hydrogenation of methylene linkages in the original coal structure.

Analysis of a Heavy Hydrogenated Fraction

<u>Compound Type</u>	<u>Weight Percent</u>	<u>Avg. MW</u>	<u>Compound Type</u>	<u>Weight Percent</u>	<u>Avg. MW</u>
$C_n H_{2n-0}$	0.033	308	$C_n H_{2n-36}$	0.147	379
$C_n H_{2n-2}$	0.077	129	$C_n H_{2n-38}$	0.072	386
$C_n H_{2n-4}$	0.254	185	$C_n H_{2n-40}$	0.013	410
$C_n H_{2n-6}$	0.298	102	$C_n H_{2n-42}$	0.015	415
$C_n H_{2n-8}$	0.792	153	$C_n H_{2n-44}$	0.002	400
$C_n H_{2n-10}$	1.675	195	$C_n H_{2n-4}^S$	0.004	126
$C_n H_{2n-12}$	1.425	228	$C_n H_{2n-16}^S$	0.003	226
$C_n H_{2n-14}$	2.196	236	$C_n H_{2n-18}^S$	0.002	231
$C_n H_{2n-16}$	4.312	248	$C_n H_{2n-20}^S$	0.005	252
$C_n H_{2n-18}$	5.743	270	$C_n H_{2n-10}^O$	0.006	203
$C_n H_{2n-20}$	6.931	286	$C_n H_{2n-12}^O$	0.010	215
$C_n H_{2n-22}$	7.628	282	$C_n H_{2n-14}^O$	0.013	178
$C_n H_{2n-24}$	6.066	302	$C_n H_{2n-16}^O$	0.066	228
$C_n H_{2n-26}$	4.407	322	$C_n H_{2n-18}^O$	0.163	240
$C_n H_{2n-28}$	2.794	327	$C_n H_{2n-20}^O$	0.062	248
$C_n H_{2n-30}$	1.393	340	$C_n H_{2n-22}^O$	0.093	264
$C_n H_{2n-32}$	1.095	341	$C_n H_{2n-24}^O$	0.122	294
$C_n H_{2n-34}$	0.378	365			

$C_n H_{2n-26}^O$	0.125	302	$C_n H_{2n-32}^O$	0.012	356
$C_n H_{2n-28}^O$	0.056	317	$C_n H_{2n-34}^O$	0.004	357
$C_n H_{2n-30}^O$	0.015	328			
Nonvolatile residue 51.50					

Note: This is the routine format, which does not include O_2 or N compounds, and does not separate isomeric hydrocarbons.

Carbon Number Distribution in a Heavy Hydrogenated Fraction

<u>Carbon Number</u>	<u>$C_n H_{2n-22}$</u>	<u>$C_n H_{2n-28}$</u>	<u>$C_n H_{2n-32}$</u>	<u>$C_n H_{2n-38}$</u>
16	0.740	-	-	-
17	0.447	-	-	-
18	0.333	-	-	-
19	0.311	-	-	-
20	0.582	0.128	-	-
21	0.760	0.220	-	-
22	0.750	0.218	0.100	-
23	0.685	0.220	0.102	-
24	0.690	0.255	0.074	-
25	0.500	0.295	0.094	-
26	0.475	0.300	0.104	0.007
27	0.370	0.305	0.110	0.005
28	0.330	0.220	0.092	0.006
29	0.243	0.184	0.094	0.012
30	0.165	0.152	0.111	0.006
31	0.135	0.080	0.051	0.006
32	0.040	0.084	0.046	0.007
33	0.044	0.074	0.030	0.008
34	0.028	0.044	0.017	0.012
35	-	0.015	-	0.003
Total	7.628	2.794	1.025	0.072

CONCLUSION

High resolution-low voltage mass spectrometry is thus a very powerful tool for the characterization of coal liquefaction products and for yielding rapid and detailed data useful for process development studies. The method can also be applied to the volatile portions of powdered coal and coal extracts. The data obtained on a great many samples analyzed permitted us to gain some insight into the structure of coal.

ACKNOWLEDGEMENT

The authors wish to thank Mr. G. R. Taylor and Mr. J. L. Taylor who obtained the experimental mass spectral data.

LITERATURE CITED

1. Lumpkin, H. E., *Anal. Chem.* 36, 2399 (1964).
2. Sharkey, A. G., Jr., Shultz, J. L., Kessler, T., "Procedures of the 15th Annual Conference on Mass Spectrometry and Allied Topics, May 1967, pp. 443-446. ASTM E-14; Denver, Colorado.
3. Kessler, T., Raymond, R. I., Sharkey, A. G., Jr., "Procedures of the 16th Annual Conference on Mass Spectrometry and Allied Topics, May 1968, pp. 356-358. ASTM E-14, Pittsburgh, Pennsylvania.
4. Shultz, J. L., Kessler, T., Friedel, R. A., Sharkey, A. G., Jr., *Ibidem*, pp. 359-361. LJ
5. Johnson, B. H., Aczél, Thomas, *Anal. Chem.* 39, 682, 1967.
6. Aczél, Thomas, Johnson, B. H. Preprints of papers, Division of Petroleum Chemistry, 153rd National Meeting of the American Chemical Society, Miami Beach, Florida, April 1967.
7. Aczél, Thomas, Allan, D. E., Harding, J. H., Knipp, E. A., "Procedures of the 16th Annual conference on Mass Spectrometry and Allied Topics, May 1968, pp. 366, 367. ASTM E-14, Pittsburgh, Pennsylvania.
8. Hill, G. R., Lyon, Lloyd B., *Ind. & Eng. Chem.* 54, 37 (1962).

CHARACTERIZATION OF IRON MINERALS IN COAL BY LOW-FREQUENCY INFRARED SPECTROSCOPY

Patricia A. Estep, John J. Kovach, Clarence Karr, Jr.,
Edward E. Childers, and Arthur L. Hiser

Morgantown Coal Research Center, Bureau of Mines,
U. S. Department of the Interior, Morgantown, West Virginia 26505

The Bureau of Mines, U. S. Department of the Interior, is conducting basic research on minerals occurring in coal to assist in solving problems created by their presence. Of particular interest in these studies are the abundant iron-bearing minerals which are directly linked with air and water pollution, are important in coal combustion, carbonization and hydrogenation, and offer potential for profitable utilization. Iron is second only to aluminum as the most abundant metallic constituent of coal, reflecting its natural abundance in the crust of the earth. Iron is a major element of high-temperature coal ash and ranges from 5 to 35 weight-percent (reported as Fe_2O_3) for United States bituminous coals (1). Although some of the iron may be organically bound in the coal (2), a large portion is known to occur in a variety of mineral forms.

Previous studies have shown that one of the most effective methods for determining the structure and concentration of coal minerals is low-frequency infrared spectroscopy (3). The application of infrared analysis to a study of iron minerals in coal required a unique compilation of spectral data. Much of the required data was not available from the literature or was of such a poor quality as to be unreliable. In addition, most earlier work did not include the new and useful low-frequency data made available for most minerals by extension of high-resolution commercial infrared instrumentation to 200 cm^{-1} .

The purpose of this paper is to present the infrared data that we have collected for some iron-bearing minerals in bituminous coal, in both their original and altered forms, and to demonstrate the usefulness of this data for analysis of a variety of typical bituminous coal mineral samples. While iron minerals not included here may occur in coal, the iron minerals for this study were selected on the basis of their frequency of occurrence in samples examined at the Morgantown Coal Research Center and in coals described in the literature.

EXPERIMENTAL

To prepare the standard spectra required for this work, several specimens of each of the iron minerals were obtained from different localities. Milligram amounts of each of these samples were selected with a stereomicroscope under 10-60X magnification. As an aid in isolation of pure specimens, we made extensive use of microchemical and determinative mineralogy tests. The purities of specimens were verified from x-ray powder diffraction data and from infrared literature data, when available. These checks showed that many of the mineral samples had been incorrectly identified by the supplier. Several minerals were obtained as pure synthetic polycrystalline phases from Tem-Pres Research, Inc., State College, Pa., and infrared spectra of these synthetic minerals were used as further purity checks on natural mineral specimens.

Pellets for infrared analysis were prepared by hand blending one milligram of the preground mineral with 500 milligrams of powdered cesium iodide (Harshaw) for five minutes in a mullite mortar. This mixture was triple pressed in a die at 23,000 pounds total load, with a 15 minute total press time. Pellets were scanned immediately on a Perkin-Elmer 621 infrared grating spectrophotometer purged with dry air. Further considerations in solid state sampling of minerals for infrared analysis have been treated in an earlier publication (3). Coal minerals to be analyzed by infrared were enriched by a variety of techniques. Low-temperature ashing, under 150° C, in an oxygen plasma produced by an r. f. field of 13.56 MHz, for example, gave essentially unaltered mineral residues from coal. In addition, conventional gravity and magnetic separation methods and hand selection with a microscope were used.

RESULTS AND DISCUSSION

Sulfides. Iron disulfides, pyrite and marcasite (FeS_2), the most abundant iron-bearing minerals in coal, contain much reactive sulfur and thus are major contributors to air and water pollution. These dimorphs (cubic and orthorhombic, respectively) can be identified and differentiated by their infrared spectra in the low-frequency region only (3). Spectral differences, shown in Figure 1 and Table 1, were used to demonstrate that pyrite predominates in the bituminous coals investigated in this work. The detection and determination of pyrite by infrared spectroscopy has been helpful in research on methods for its removal from coal. Gravity separation methods are frequently employed and Figure 2 demonstrates the enrichment of pyrite in the 2.9 specific gravity sink fraction of a mine refuse sample from a West Virginia bituminous coal. The 1.7 specific gravity fraction, curve (a), is shown here to point out that absorption bands from other commonly occurring coal minerals, e. g., kaolinite, may overlap those of pyrite and thus decrease its detectability in mixtures not subjected to separation methods.

Pyrrhotite (Fe_{1-x}S) is an iron sulfide found in coal (4) and in coal ash slag, where it had been produced from the breakdown of pyrite (5). We did not detect infrared absorption bands out to 17 cm^{-1} for either the monoclinic or hexagonal crystalline forms of pyrrhotite, hence it is possible that this mineral cannot be determined in natural mixtures by infrared spectroscopy. We have not identified it in any of our bituminous coal samples examined to date by x-ray diffraction analysis.

The iron-bearing sulfide mineral, chalcopyrite (tetragonal, CuFeS_2), has been identified in coal (6, 7). It is known to be the most widely occurring copper mineral and is commonly associated with pyrite ores. Figure 3 and Table 1 show that its absorption bands are shifted to lower frequencies from the corresponding bands for pyrite. These data are in good agreement with those of Gillieson (8).

Carbonates. The carbonate mineral, siderite (FeCO_3), has been identified in coal and is believed to have been formed at the time of burial of plant remains (9). Weathering can convert it to limonite which can then lose water to produce hematite. Siderite has been identified in coals from wide geographic localities and varying ranks. Figure 4 demonstrates its detection in a Virginia bituminous coal. Here, siderite is seen to be the major constituent of a heavy sink fraction from fine coal washing. Adler (10) and Hunt (11) have presented the infrared

spectrum for siderite to 625 cm^{-1} and Angino (12) has published its infrared data only in the low-frequency region below 500 cm^{-1} . The distinction of siderite from other possible coal mineral carbonates was facilitated through use of the complete infrared spectrum, as shown in Figure 4, containing all relative intensity information.

Another common iron carbonate often found in coal is ankerite (6, 13, 14). Infrared data has been presented for ankerite by Huang (15) to 667 cm^{-1} and by Moenke (16) to 500 cm^{-1} . Both workers utilized very minor band shifts (3 to 5 cm^{-1}) for distinguishing ankerite from the isostructural members of its group, and attributed these shifts to cation substitution effects. In a recent study of the carbonate minerals in coal (17) we examined seven ankerite samples from different localities. We observed no detectable frequency shifts in the carbonate fundamentals from those of dolomite. In the low-frequency lattice vibration region, however, there was a general broadening of bands and other detectable changes. In going from dolomite to ankerite, the 252 cm^{-1} dolomite band was reduced in intensity, the 312 cm^{-1} band was reduced in intensity and shifted to higher frequency, and the 391 cm^{-1} shoulder was less resolved. This mineral was frequently misidentified by the supplier because five additional samples of ankerite that we examined were shown by infrared and x-ray analysis to be siderite.

Oxides and Hydrus Oxides. The iron oxides, hematite and magnetite, and the hydrous iron oxides goethite and lepidocrocite have all been identified in coal by petrographic or x-ray methods (18). These may occur in coal as original minerals or as products of weathering of iron-bearing minerals. Very little reliable infrared data is available in the literature for these oxides. Absorption bands for hematite, reported in the $1000\text{-}1110\text{ cm}^{-1}$ region by Hunt (11) and Omori (19), are in error, as none of the anhydrous oxides absorb above 600 cm^{-1} . The infrared spectrum of hematite presented by Liese (20) contains absorption bands due to an impurity, and our data indicate that his sample contained maghemite. Recently, infrared spectra for iron oxides, available as commercial chemicals, have been presented to 200 cm^{-1} by Afremow (21) and McDevitt (22). The spectra we obtained for naturally occurring mineral samples are only in partial agreement with the data in these two references. For example, the distinction between $\alpha\text{Fe}_2\text{O}_3$ (hematite, trigonal) and $\gamma\text{Fe}_2\text{O}_3$ (maghemite, cubic) is not readily apparent from the spectra presented in either paper. Our spectra for these dimorphs, Figure 5, show frequency differences for all three major absorption bands. These shifts were found to be consistent for several samples from different localities and are believed to be reliable. For magnetite (Fe_3O_4), Liese (20) reports (to 300 cm^{-1}) only one absorption band at 570 cm^{-1} for a number of naturally occurring magnetite specimens. Our magnetite spectrum, Figure 5, with two absorption bands, is in better agreement with that presented by Afremow (21) for the black iron oxide (Fe_3O_4). The conversion of magnetite through maghemite to hematite can be readily followed by use of their spectral differences, shown in Figure 5.

The iron oxide, wüstite (essentially FeO), is an alteration product of the iron minerals in coal, and has been found in coal ash slags and fly ash. The spectrum of a nonstoichiometric, single phase sample of synthetic wüstite exhibits only one broad absorption band at 375 cm^{-1} .

The titanium containing iron oxide, ilmenite (trigonal, FeTiO_3), which is frequently associated with hematite and magnetite, has been identified in coal (23). Titanium commonly occurs in United States bituminous coals (1), and shows a close correspondence to its natural abundance in the earth's crust. Hunt (11) and Omori (19) report infrared absorption bands for ilmenite in the region above 625 cm^{-1} which are undoubtedly in error. Liese (20) found three strong absorption bands, all in the low-frequency region, that differ as the Ti/Fe ratio varies. He shows these bands to shift systematically from 540, 461, and 325 cm^{-1} to 532, 440, and 295 cm^{-1} as Ti increases and Fe decreases. He points out that this frequency shift is not in the expected direction and suggests that the presence of intergrown hematite may be causing this effect. Data from our laboratory support his intergrowth interpretation. Our spectra for ten samples of ilmenite from various localities show consistent band positions at 525 (s), 438 (m), and 300 (s) cm^{-1} . Figure 6 shows the spectrum of a sample from Norway. This spectrum agrees better with Liese's set of lower frequency bands, while his set of higher frequency bands agrees better in frequency and shape with our hematite data.

Adler (24) and White (25) have shown that the hydrous oxide dimorphs goethite, $\alpha\text{FeO}(\text{OH})$, and lepidocrocite, $\gamma\text{FeO}(\text{OH})$, both orthorhombic, can be readily distinguished by differences in the $4000\text{-}600 \text{ cm}^{-1}$ region. Figure 7 shows their marked spectral differences and presents additional data for the low-frequency region to 200 cm^{-1} . A further useful distinction between these dimorphs is their behavior on heating. Goethite dehydrates to form paramagnetic hematite while lepidocrocite dehydrates on heating to form ferromagnetic maghemite. We used these conversions for further verification of the spectra for all four forms. The absence of vibrations due to OH groups considerably simplifies the infrared spectrum, as shown by a comparison of Figures 5 and 7.

We have frequently identified the oxides of iron and their hydrous forms in samples obtained by magnetic separations from coal. For example, Figure 8 demonstrates the detection of substantial amounts of goethite in the magnetic fraction from a mine refuse sample from a West Virginia bituminous coal. The highly characteristic goethite bands at 800 and 900 cm^{-1} , assigned by White (25) to an OH bending vibration and an Fe-O stretching mode, respectively, are particularly useful because this doublet occurs in a range not extensively overlapped by bands of other common mineral components. Similarly, the weaker bands at 215, 358, and 1018 cm^{-1} , seen in the spectrum of the magnetic fraction in Figure 8, can be assigned to minor amounts of lepidocrocite. The capability of infrared spectroscopy for distinguishing between goethite and lepidocrocite can be applied to the determination of the mineralogical composition of limonite, $\text{FeO}(\text{OH}) \cdot x\text{H}_2\text{O}$, an amorphous mixture of hydrous iron oxides with variable water content that is difficult to characterize by x-ray diffraction. We have observed goethite to be the predominant species in several limonite specimens from a variety of world localities. Limonite has frequently been reported to be present in coal as a product of weathering.

Other types of coal product samples typically containing iron oxides as alteration products of original iron minerals are combustion products such as fly ash, boiler deposits, conventional high-temperature ash residues from coal, and burned mine refuse. Figure 9, curve (c), for example, demonstrates the extensive oxidation of pyrite to hematite in a sample of burned mine refuse from a West Virginia bituminous coal. The sample, obtained from a burning coal refuse bank, was

pulverized and subjected to float sink separations. The infrared spectrum of the 2.9 specific gravity sink fraction shows hematite to be predominant, with only minor amounts of pyrite remaining. This particular analysis demonstrates the necessity for using the low-frequency region, 600-200 cm^{-1} , because there were no major absorptions above 600 cm^{-1} in the refuse sample. Comparison of curves (a) and (b) for pyrite and hematite shows that the specificity of their absorption bands affords an excellent opportunity for quantitative analysis and thus determination of degree of oxidation by burning or weathering.

$\text{Fe}(\text{OH})_3$, a hydrolysis product of ferric sulfates, known as "yellow boy," is frequently precipitated from alkaline streams containing drainage from coal mines. Although this compound exhibits a rather diffuse infrared spectrum, we have used its broad absorption bands centered at 450, 575, 675, and 3450 cm^{-1} for identification. We have been unable to find any infrared data to 200 cm^{-1} for this compound in the literature.

Sulfates. Iron sulfates occur in coals primarily as oxidation products of the iron sulfides, and various forms can be produced, depending on weathering conditions. Anhydrous FeSO_4 , or its various hydrates, can easily form and be converted by further oxidation into $\text{Fe}_2(\text{SO}_4)_3$ or any of its possible hydrates. Nufer (26), by x-ray diffraction, has determined that the species typically found in West Virginia bituminous coal are principally szomolnokite, $\text{FeSO}_4 \cdot \text{H}_2\text{O}$, and melanterite, $\text{FeSO}_4 \cdot 7\text{H}_2\text{O}$. Iron sulfates are associated with water pollution problems resulting from mine drainage, coal processing plants, and weathered refuse banks (27). The infrared spectra that we obtained for a number of samples from these sources showed different hydration states for the iron sulfates. For example, the surface film from a sample of coal mine refuse is seen from its infrared spectrum in Figure 10, curve (c), to be predominantly anhydrous iron sulfate, indicating oxidation in a very dry atmosphere. Minor amounts of the hydrated forms of ferrous sulfates and pyrite were also present in this sample. When considerable atmospheric moisture is present, the surface film on pyrite-rich mine refuse was usually identified as melanterite, as seen in Figure 11.

Hydrous iron sulfates are another class of minerals for which very little reliable infrared data is available in the literature. Adler (28) has presented the infrared spectrum of szomolnokite only to 800 cm^{-1} . Omori (29) has published poorly resolved infrared spectra for siderotil, $\text{FeSO}_4 \cdot 5\text{H}_2\text{O}$, melanterite, and coquimbite, $\text{Fe}_2(\text{SO}_4)_3 \cdot 9\text{H}_2\text{O}$, only to 600 cm^{-1} . Infrared data for the synthetically prepared forms of $\text{FeSO}_4 \cdot 7\text{H}_2\text{O}$ and $\text{Fe}_2(\text{SO}_4)_3 \cdot x\text{H}_2\text{O}$ have been presented by Miller (30, 31) to 300 cm^{-1} and Sadtler (32) to 400 cm^{-1} . However, no systematic study has been made of the various hydrated sulfates of Fe^{2+} or Fe^{3+} showing the dependency of the infrared spectrum on additions of water to the crystal lattice. In the present work, infrared spectra were obtained for samples of naturally occurring and microscopically identified iron sulfate minerals. These included iron in both ferrous and ferric states and in the commonly found hydrated forms. The hydration states of some of these iron sulfate minerals are known to be easily altered (33). However, variations of temperature and relative humidity in our pellet preparation produced no detectable spectral changes. The spectral data for these minerals are shown in Tables 2 and 3, with their tentative vibrational assignments. In the absence of data for several intermediate hydrates, and the possibility of mixed crystalline phases for some samples, it was not possible to make any rigorous spectral-structural correlations. However, several spectral

differences among these minerals were observed and used in identifications. For example, the marked spectral differences allowing a distinction between anhydrous ferrous sulfate and one of its hydrated forms, melanterite, are shown in Figure 10, curve (b), and in Figure 11, curve (a). The weak OH absorptions appearing in the spectrum of the anhydrous form agree with those in the monohydrate and may be due to small amounts of this form.

Some systematic spectral variations were noted for lattice water vibrations. For example, the ferrous sulfate hydrate system (Table 2) showed the expected systematic increase in intensity of the OH stretching and HOH deformation modes with an increasing number of lattice water molecules. Absorption for ferrous sulfate hydrates in the OH stretching region showed two to four components, while absorption for ferric sulfate hydrates in this region was asymmetrically broadened to one band and generally shifted to lower frequencies. The frequency for the HOH deformation mode remained essentially independent of the amount of water present. It appeared near 1620 cm^{-1} (usually split) for the ferrous sulfate hydrates, but shifted to a higher frequency position near 1640 cm^{-1} for the ferric sulfate hydrates.

The fundamental vibrations of the sulfate ion, ν_1 , ν_3 , and ν_4 , as tentatively assigned in Tables 2 and 3 for iron sulfates, all indicate lower symmetry than that of the free tetrahedral ion. Ross (34) has discussed the reasons for lower symmetry of the sulfate ion in the solid state. When this occurs, degeneracies are removed and new selection rules allow forbidden vibrations to appear. For example, the degenerate ν_3 sulfate group vibration appears as a triplet in all samples examined. The ν_1 appears in all spectra, although it shows a substantially reduced intensity when just one water molecule is added. The frequency variations for the sulfate fundamentals are not systematic with additions of lattice water and changes in the oxidation state of the iron. However, the observed spectral variations for these iron sulfates, in spite of their irregularities, can be of diagnostic value and can provide a basis for identification of an individual compound.

ACKNOWLEDGMENT

The authors are grateful to John S. White, Division of Mineralogy, Smithsonian Institution, Washington, D. C., and R. I. Gait, Royal Ontario Museum, Toronto, Canada, who supplied several samples of hydrated iron sulfates, and to John J. Renton, Geology Department, West Virginia University, Morgantown, who provided x-ray data on mineral samples.

LITERATURE CITED

1. Selvig, W. A., and F. H. Gibson, BuMiner Bull. 567 (1956), 33 pp.
2. Lefelhocz, J. F., R. A. Friedel, and T. P. Kohman, Geochim. Cosmochim. Acta 31, 2261 (1967).
3. Estep, P. A., J. J. Kovach, and C. Karr, Jr., Anal. Chem. 40, 358 (1968).

4. Sen, P., and A. N. Roy, *J. Mines, Metals, Fuels* 10, 7 (1962).
5. Watt, J. D., *Brit. Coal Util. Res. Assoc., Monthly Bull.* 26, No. 2, 49 (1959).
6. Kemezys, M., and G. H. Taylor, *J. Inst. Fuel* 37, 389 (1964).
7. Bethell, F. V., *Brit. Coal Util. Res. Assoc., Monthly Bull.* 26, No. 12, 401 (1962).
8. Gillieson, A. H., Dept. of Energy, Mines, and Resources, Ottawa, Ontario, Canada, private communication (1968).
9. Smyth, M., *Fuel* 45, 221 (1966).
10. Adler, H. H., and P. F. Kerr, *Am. Mineralogist* 48, 124 (1963).
11. Hunt, J. M., M. P. Wisherd, and L. C. Bonham, *Anal. Chem.* 22, 1478 (1950).
12. Angino, E. E., *Am. Mineralogist* 52, 137 (1967).
13. Dixon, K., E. Skipsey, and J. T. Watts, *J. Inst. Fuel* 37, 485 (1964).
14. Brown, H. R., R. A. Durie, and H. N. S. Schafer, *Fuel* 34, 59 (1960).
15. Huang, C. K., and P. F. Kerr, *Am. Mineralogist* 45, 311 (1960).
16. Moenke, H., *Infrared Phys.* 2, 111 (1962).
17. Estep, P. A., J. J. Kovach, A. L. Hiser, and C. Karr, Jr., Ch. in "Spectrometry of Fuels and Related Materials," ed. by R. A. Friedel, Plenum Press, New York, N. Y., 1969 (in press).
18. Rekus, A. F., and A. R. Haberkorn, III, *J. Inst. Fuel* 39, 474 (1966).
19. Omori, K., *Sci. Rept. Tohoku Univ., Third Ser.* 9, 65 (1964).
20. Liese, H. C., *Am. Mineralogist* 52, 1198 (1967).
21. Afremow, L. C., and J. T. Vandenberg, *J. Paint Tech.* 38, 169 (1966).
22. McDevitt, N. T., and W. L. Baun, *Spectrochim. Acta* 20, 799 (1964).
23. Alekseev, L. S., *Geomorjol, Paleogeogr., Geol., Polezn. Iskop. Priamur'ya, Dal'nevost. Filial Sibirsk. Otd. Akad. Nauk SSSR* 21, (1964).
24. Adler, H. H., *Econ. Geol.* 58, 558 (1963).
25. White, W. B., and R. Roy, *Am. Mineralogist* 49, 1670 (1964).
26. Nufer, E. B., Master's Thesis, West Virginia University (1967), 73 pp.

27. Lorenz, W. C., BuMiner. Inf. Circ. 8080 (1962), 40 pp.
28. Adler, H. H., and P. F. Kerr, Am. Mineralogist 50, 132 (1965).
29. Omori, K., and P. F. Kerr, Geol. Soc. Am. Bull. 74, 709 (1963).
30. Miller, F. A., and C. H. Wilkins, Anal. Chem. 24, 1253 (1952).
31. Miller, F. A., G. L. Carlson, F. F. Bentley, and W. H. Jones, Spectrochim. Acta 16, 135 (1960).
32. Sadtler Research Laboratories, Philadelphia, Pa. High Resolution Spectra of Inorganics and Related Compounds 1 (1965), Supplement, (1967).
33. Ehlers, Ernest G., and D. V. Stiles, Am. Mineralogist 50, 1457 (1965).
34. Ross, S. D., Spectrochim. Acta 18, 1575 (1962).

Table 1. - Infrared Absorption Bands for Common Iron Minerals

Mineral	Frequency, cm^{-1} ^a
Pyrite (Gilman, Eagle County, Colorado)	284 (w), 340 (m), 391 (vw), 411 (s)
Marcasite (Ottawa County, Oklahoma)	285 (w), 321 (m), 350 (m), 396 (s), 412 (s), 422 (vw)
Chalcopyrite (Messina, Transvaal, South Africa)	268 (w), 315 (m), 351 (s), 365 (sh)
Siderite (Washington, Connecticut)	~200 (w), 316 (s), 728 (m), 858 (m), 1410 (s)
Hematite (Ironton, Minnesota)	330 (s), 370 (sh), 470 (m), 550 (s)
Maghemite (LaCodocera, Badajoz, Spain)	320 (s), 451 (m), 530 (s)
Magnetite (Iron Mountain, Utah)	385 (s), 575 (s)
Wüstite (Synthetic, Tem-Pres Research, Inc.)	375 (s)
Ilmenite (Kraggerö, Norway)	300 (s), 325 (sh), 438 (m), 525 (s), 675 (sh)
Goethite (Cary Mine, Ironwood, Gogebic County, Michigan)	248 (w), 280 (s), 385 (w), 402 (s), 450 (sh), 568 (m), 662 (w), 800 (m), 900 (m), 3095 (m), 3430 (b)
Lepidocrocite (Fellinghausen, Hessen, Germany)	215 (w), 275 (m), 358 (s), 480 (s), 740 (m), 1018 (m), ~3000 (b), ~3350 (b)

^a s = strong; m = medium; w = weak; sh = shoulder; b = broad.

Table 2. - Infrared Absorption Bands for Ferrous Sulfate Minerals, cm^{-1}

Tentative assignments	Anhydrous ferrous sulfate FeSO_4 Orthorhombic Fisher Chem. Co.	Szomolnokite $\text{FeSO}_4 \cdot \text{H}_2\text{O}$ Monoclinic Dividend, Utah	Rozenite $\text{FeSO}_4 \cdot 4\text{H}_2\text{O}$ Monoclinic Ontario, Can.	Siderotil ^b $\text{FeSO}_4 \cdot \text{SH}_2\text{O}$ Crystal system undetermined	Melanterite $\text{FeSO}_4 \cdot 7\text{H}_2\text{O}$ Monoclinic Honshu, Japan
OH stretch, lattice water	3410 (w) 3250 (w)	3420 (m) 3240 (sh)	3430 (ms) 3250 (sh)	3448 (ms)	3530 (sh) 3455 (s) 3390 (sh) 3260 (sh)
HOH bend, lattice water	1490 (w)	1650 (w) 1620 (w) 1490 (w)	1620 (w) 1505 (w)	1622 (mw)	1650 (sh) 1618 (m)
γ_3 , sulfate	1150 (s) 1135 (s) 1076 (m)	1165 (m) 1125 (s) 1095 (m)	1175 (sh) 1140 (s) 1100 (m)	1143 (sh) 1099 (s)	1140 (m) 1105 (s) 1085 (sh)
γ_1 , sulfate	1010 (m)	1015 (m)	1020 (m)		988 (w)
γ_4 , sulfate	815 (m) 660 (m) 618 (m) 595 (m)	830 (mw) 660 (m) 620 (m) 599 (m)	860 (mw) 670 (m) 627 (m) 607 (m)	862 (w)	605 (m)
	525 (m) 290 (m) 270 (m) 210 (m)	522 (m) 290 (m) 270 (m) ~ 200 (m)	560 (m) 470 (w) 340 (w) 275 (m)		510 (w) 425 (w) 330 (w)

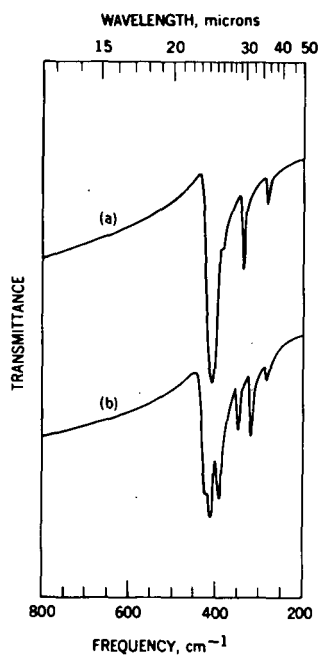
^a s = strong, m = medium, w = weak, sh = shoulder, b = broad.

^b Approximate values read from Omori and Kerr (see Ref. 29).

Table 3. - Infrared Absorption Bands for Ferric Sulfate Minerals, cm^{-1} ^a

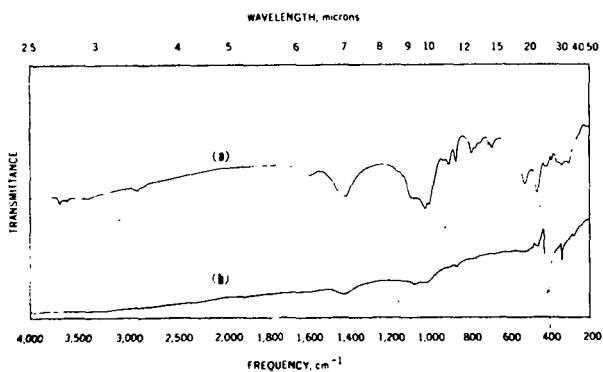
Tentative assignments	Kornelite $\text{Fe}_2(\text{SO}_4)_3 \cdot 7\text{H}_2\text{O}$ Monoclinic Inyo County, Cal.	Coquimbite $\text{Fe}_2(\text{SO}_4)_3 \cdot 9\text{H}_2\text{O}$ Hexagonal San Rafael Swell, Utah	Romerite $\text{Fe}_3(\text{SO}_4)_4 \cdot 14\text{H}_2\text{O}$ Triclinic Trinity County, Cal.	Ferric sulfate $\text{Fe}_2(\text{SO}_4)_3 \cdot x\text{H}_2\text{O}$ J. T. Baker Chemical Co.
OH stretch, lattice water	3410 (s, b)	3300 (s, b)	3300 (s, b)	3360 (s, b), 3200 (sh)
HOH bend, lattice water	1640 (w)	1640 (w)	1640 (w)	1645 (m) 1610 (sh)
γ_3 , sulfate	1185 (sh) 1115 (s) 1050 (sh)	1165 (s) 1105 (s) 1065 (sh)	1129 (s) 1105 (s) 1085 (sh)	1150 (m) 1105 (s) 1052 (m)
		1023 (w)		
γ_1 , sulfate	990 (w)	1010 (w)	982 (w)	
	810 (w) 685 (w) 650 (w)	940 (w) 820 (w) 685 (w)	750 (w, b)	800 (w)
γ_4 , sulfate	595 (m)	608 (sh) 590 (m) 575 (sh)	626 (m) 605 (sh)	630 (sh) 595 (m)
	270 (w)	480 (w) 440 (w) 330 (w) 270 (w)	480 (w) 450 (w) 335 (w) 270 (w) 225 (w)	550 (m) 335 (w) 300 (w) 272 (w)

a s = strong; m = medium; w = weak; sh = shoulder; b = broad.



(a) Pyrite (Colorado)
 (b) Marcasite (Oklahoma)

FIGURE 1. - Infrared Spectra for Iron Disulfide Dimorphs.



a. "Clay Fraction", 1.7 s.g. slm / kaolinite, quartz, calcite)
 b. "Iron Fraction", 2.8 s.g. slm / pyrite

FIGURE 2. - Gravity Separation of Slurry Pond Refuse from a W. Va. Bituminous Coal.

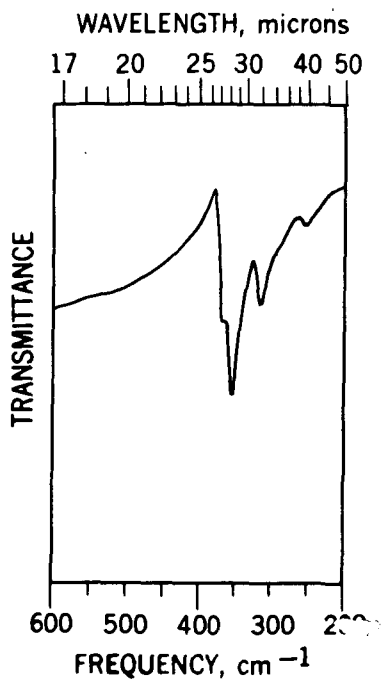
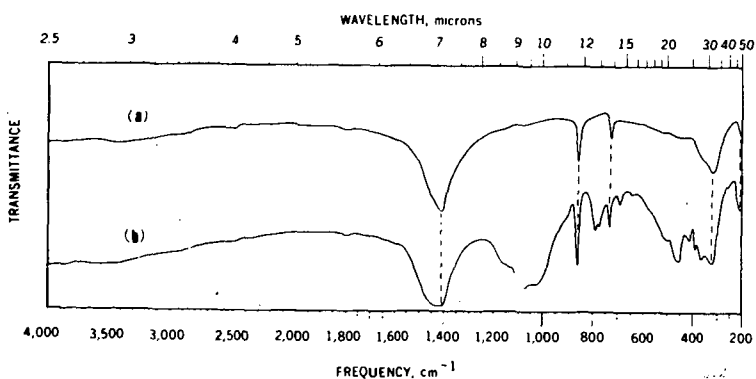


FIGURE 3. - Infrared Spectrum of Chalcopyrite from Messina, Transvaal, South Africa



- (a) Siderite (Connecticut)
- (b) Heavy sink fraction from the fine coal washing, 2.9 s.g. sink

FIGURE 4. - Identification of Siderite from a Virginia Bituminous Coal

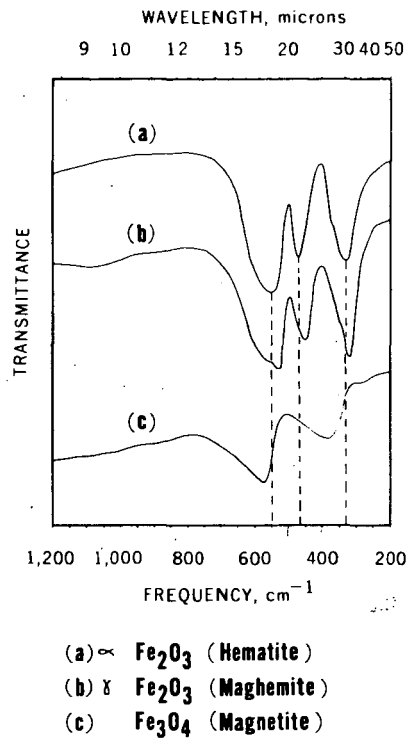


FIGURE 5. - Infrared Spectra of Iron Oxides

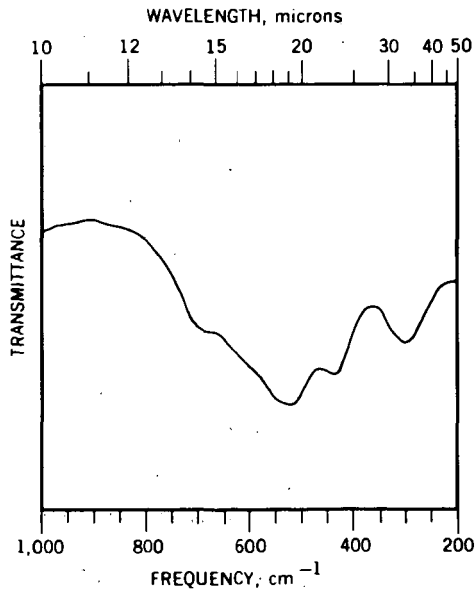


FIGURE 6. - Infrared Spectrum of Ilmenite (Norway)

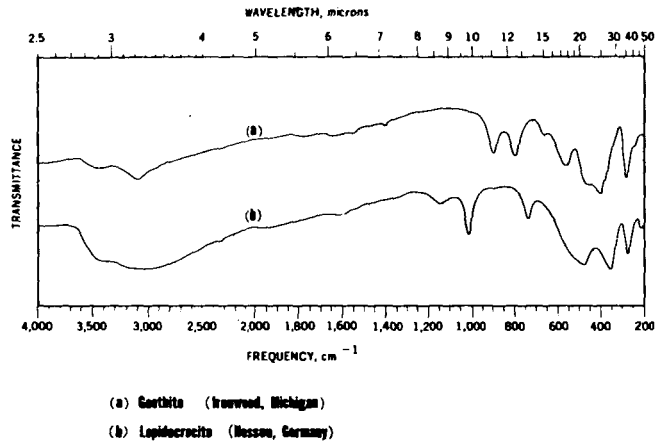


FIGURE 7. - Infrared Spectra of Hydrrous Iron Oxide Polymorphs

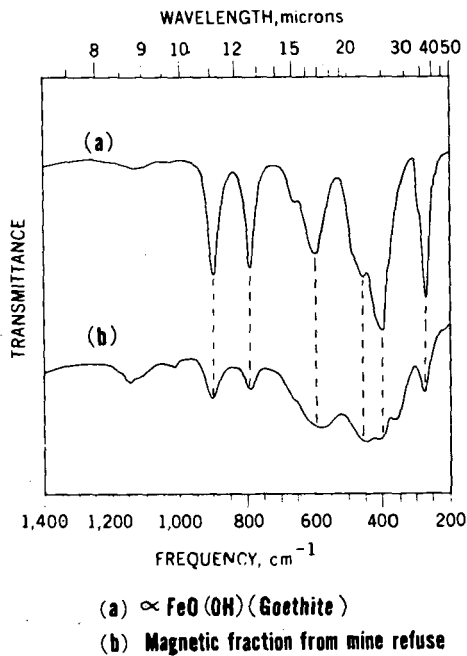
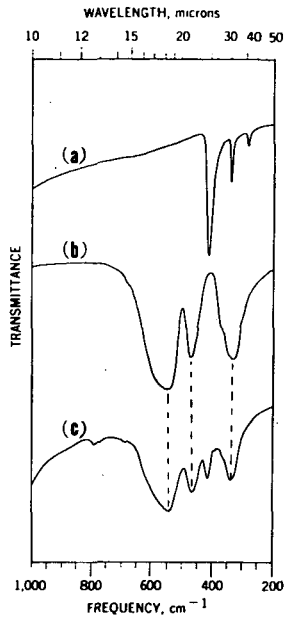


FIGURE 8. - Identification of Goethite in Mine Refuse from a W. Va. Bituminous Coal



- (a) Pyrite (Gilman, Colorado)
 (b) Hematite (Ironton, Minnesota)
 (c) Burned mine refuse

FIGURE 9. - Conversion of Pyrite to Hematite in Mine Refuse by Burning

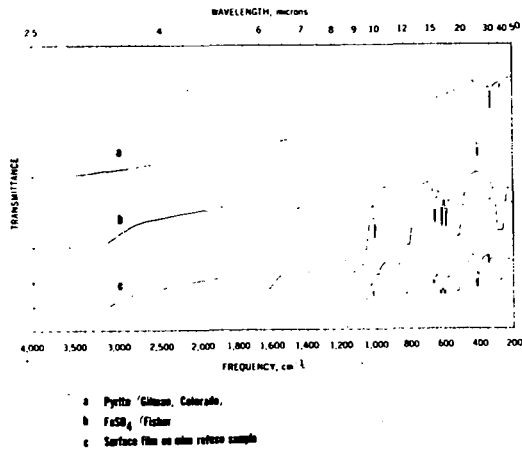


FIGURE 10. - Surface Oxidation of Pyrite from Coal Refuse in a Dry Atmosphere

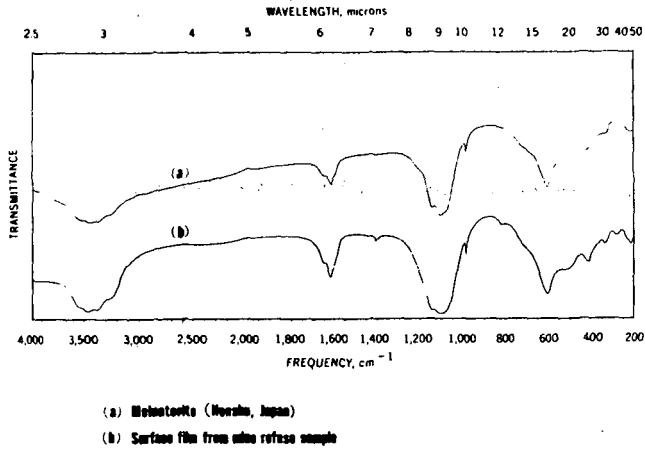


FIGURE 11. - Surface Oxidation of Mine Refuse in a Moist Atmosphere

DIRECT DETERMINATION OF OXYGEN IN COAL

B.S. Ignasiak*, B.N. Nandi**, D.S. Montgomery***

Fuels Research Centre, Mines Branch, Department of Energy, Mines and Resources,
Ottawa, Ontario, Canada

INTRODUCTION

There are two known methods for the direct determination of oxygen in organic matter:

- 1) Schütze method (1) and modifications (2,3,4,5,6,7,8)
- 2) Neutron activation method (9,10)

The principle of the Schütze method depends on thermal decomposition of the sample in a temperature range of 1000° - 1150°C, in an oxygen free atmosphere of inert gas. The gaseous products of pyrolysis are carried over a layer of carbon black or lampblack at a temperature 1120°C. At this temperature all oxygen containing products are transformed into CO which is quantitatively oxidized using I₂O₅ to CO₂. The oxygen content of the sample for analysis can be calculated from the gain in CO₂ measured gravimetrically or from the gain in I₂ measured volumetrically. Instead of oxidizing CO to CO₂ some authors suggest the determination of CO directly using chromatographic analysis. (5)

Using platinum on lampblack (7) or nickel on lampblack (5) as a catalyst, it is possible to decrease the temperature for the quantitative conversion to carbon monoxide of the products of pyrolysis of the sample.

All modifications of the Schütze method for the direct determination of oxygen are based on the thermal decomposition of the sample in an inert gas. This requires a very pure sweeping gas and therefore rather complicated methods for the purification of this gas. In effect this means that the analysis is much more prolonged.

The determination of oxygen using the neutron activation method has been described many times in detail. (10) This method allows the total concentration of oxygen to be determined in both the organic and inorganic constituents of the sample. The advantages of this method are: the short time of duration of the analysis and the fact that this is a non-destructive type of test. On the other hand the equipment for the determination of oxygen using neutron activation analysis is very expensive and the sample must be relatively large.

* Permanent address: Department of Coal Chemistry, Adam Mickiewicz University, Poznan, Poland.

** Research Scientist, Fuels Research Centre

*** Head, Fuels Research Centre

Also, if the principal quantity of interest is the oxygen content of the organic matter in the coal, the mineral matter must be removed. This is a rather laborious process.

The recognized methods of determining the oxygen content of coal, based on Schütze (1) Unterzaucher (2) and Burns (8) are slow and require considerable skill to achieve satisfactory levels of accuracy. The method described here is much more rapid and requires considerably less technique.

EXPERIMENTAL

Principle of the Method.

A fast and simple method is described for the determination of oxygen in coals. The principle of the method depends on the pyrolysis of a sample at 1050°C in a vacuum, conversion of all oxygen in the pyrolysis products into CO, the determination of the volume of evolved gas and the measurement of the concentration of carbon monoxide in this gas using gas chromatography.

Apparatus.

The basic part of the determination, which is the pyrolysis and the measurement of the volume of evolved gas is conducted in the apparatus indicated in Figure 1. The part of this apparatus indicated by 1 referred to as the pyrolyser and is used for the pyrolysis of the sample located at a and the evacuation of the catalyst situated at b. As it must withstand relatively high temperature it is made from Vycor glass. The pyrolyser is connected through the unit 2 to a gas burette, capacity 100 ml, by means of heavy rubber tubing. After completion of the pyrolysis, the mercury from the reservoir is introduced into the apparatus through the one-way stopcock c. The pyrolysis is conducted in a hinged tubular electric furnace into which the pyrolyser unit is placed as shown in Figure 2. The additional equipment required for the determination of oxygen includes a vacuum pump and gas chromatograph suitable for the measurement of carbon monoxide. In this investigation a Fisher Partitioner was used with a double column: - hexamethylphosphoramide on Chromosorb P followed by a Linde molecular sieve 13X. Using such a set of columns it was a simple matter to determine whether the conversion process was quantitative or not as the presence of any CO₂ shows that the conversion is incomplete.

The sample for analysis (60 mg - 100 mg) was weighed in the quartz tube 5 whose shape and dimension are presented in Figure 1. With high oxygen content coals such as lignite the sample weight is kept to 60 mg while for anthracite the sample weight is increased to 100 mg.

Preparation of the Catalyst.

Two hundred gram of lampblack dried at 105°C for 3 hours was mixed in a beaker with a concentrated solution of nickelous nitrate consisting of 991 g $\text{Ni NO}_3 \cdot 6 \text{H}_2\text{O}$ dissolved in 200 ml of distilled water. The suspension was mixed mechanically and heated to evaporate the water. The heating was stopped when the residue started to solidify. The contents of the beaker were dried for 24 hours at 105°C in an oven. Then, the catalyst was transferred to a Vycor tube swept with argon. The temperature was increased gradually to 1050°C and maintained under these conditions for 5 hours. The catalyst was then cooled and stored in an air-tight container. The particles of the catalyst, 16-60 mesh Tyler, were used for the oxygen determinations.

Method of Analysis.

Five g of catalyst was introduced into the tube b of the pyrolyser Figure 1. The part a was cleaned carefully to remove all vestiges of catalyst particles and the sample in the quartz tube 5 was introduced into part pyrolyser. The apparatus was assembled, set up on a stand, and evacuated initially for 5 minutes. Then part b of the pyrolyser was inserted into an oven for 30 minutes at 1050°C. Five minutes before the end of this period in which the catalyst was degassed, the apparatus was re-evacuated. At the conclusion of this 5 minute period the tubing b was withdrawn from the furnace and the tubing a was inserted for 10 minutes into a thermostat at a temperature of 70°C to remove traces of moisture from the coal sample. After the tubing b was cold the catalyst was transferred into a by rotating the pyrolyser and the apparatus was disconnected from the vacuum pump using stopcock c. After the pressure dropped to 0.3 mm of Hg, the hinged furnace was opened for some seconds and the tubing a of the apparatus was placed in the furnace as shown in Figure 2 to avoid heating the coal. After some minutes when the temperature stabilized again at 1050°C the furnace was moved very slowly in the direction of the sample. The rate of evolution of the pyrolysis gases from the sample could be observed by eye, and the rate of advance of the furnace was controlled to avoid sudden bursts of gas. The sample was finally advanced to the mid-point of the furnace and retained there for 10 minutes. After this time the pyrolyser was withdrawn from the furnace and 3 to 4 minutes later the mercury from the reservoir was introduced into the apparatus with vibration from 4. The converted pyrolysis gas was displaced into the gas burette. The volume of the gas was measured and the temperature and atmospheric pressure was noted. The concentration of carbon monoxide was determined by withdrawing a sample for gas chromatography.

The concentration of oxygen in analysed sample was calculated from the equation:

$$\%O = \frac{(0.07143)}{G} \left[\frac{\%CO \cdot P_1 \cdot V_1 \cdot 0.003592}{T_1} - K \right]$$

where: G - weight of sample g ; V₁ - volume of evolved gas (ml)
(at temperature T₁ pressure P₁)

P₁ - atmospheric pressure mm Hg.

T₁ - temperature °K; K - volume of CO ml at temperature 273°K,
pressure 760 mm of Hg obtained from
pyrolysis of pure chemical compound not
containing oxygen.

K is a function of the conditions of analysis such as: temperature,
time of pyrolysis, method of the preparation
of catalyst, time and temperature of the
degasification of catalyst. Consequently,
to obtain reproducible results it is
important to adhere strictly to the same
analytical procedure.

Results and Discussion.

The proposed method for the direct determination of oxygen in coal was tested on two standard pure compounds, namely, benzoic acid and acetanilide. Comparative analyses by the neutron activation method were performed on these standards. The results presented in Table 1 show that the proposed method can be considered as a basically suitable analytical procedure for the direct determination of oxygen in many organic compounds. Some caution will have to be used in those cases where the component is known to contain elements that will poison the nickel catalyst.

The establishment of this method for the determination of oxygen in coal required finding the temperature of pyrolysis at which essentially all oxygen from organic matter of coal was evolved from the coke. It was found from the determination of the concentration of oxygen by neutron activation in cokes resulting from the pyrolysis of some coals of different rank demineralized according to Radmacher (11), that the temperature of 1050°C is suitable. This is illustrated in Figure 3. Only in the case of anthracite was the concentration of oxygen in cokes pyrolysed at temperatures of 1050°C and 1100°C relatively high, that is to say approximately 0.9%. At the same time the concentration of ash in this particular anthracite after treatment with hydrochloric acid and hydrofluoric acid was surprisingly high as shown in Table 2, Column 7. So it is assumed that the high concentration of oxygen in cokes from pyrolysis of anthracite at 1050°C and 1100°C is related to the inorganic matter in these cokes. It is worth mentioning that the concentrations of oxygen in both these cokes though heated to different temperatures, i.e., 1050 and 1100°C were the same. Had the oxygen been contained in the organic matter some decrease in concentration should have been observed.

Coals of different rank were analysed before and after removal of the mineral matter using the direct method of determining oxygen. The results are shown in Table 2. Here it is evident that the oxygen content of the demineralized samples are in good agreement with those found by neutron activation analysis.

ACKNOWLEDGEMENTS

The authors wish to acknowledge the assistance of the Mineral Science Division and Mr. C. McMahon in particular for determining the oxygen content of the coal and coke samples by neutron activation analysis and Mr. M. Pleet for preparing the drawings.

REFERENCES

1. Schütze, M. Zeitschr. Anal. Chem. 1939, 118, 245.
2. Unterzaucher, J. Ber. Dtsch. Chem. Ges. 1940, 73B, 391; Analyst. 1952, 77, 584.
3. Kuck, J.A., Andreatch, A.J., Mohns, J.P. Anal. Chem. 1967, 39, 1249.
4. Korszun, M.D. Zaw. Lab. 1941, 10, 241.
5. Tierientiew, A.P., Turkieltaub, A.M., Bondariewska-ja, E.A., Domoczkina, L.A. Dokl. Akad. Nauk SSSR. 1963, 148, 1316.
6. Kuzniecowa, L.W., Stolarowa, E.N., Dobyczin, S.L. Ž. Anal. Chim. Russian, 1965, 20, 836.
7. Oita, I.J., Conway, H.S. Analyt. Chem. 1954, 26, 600.
8. Burns, M.S., Macara, R., Swaine, D.J. Fuel, London 1964, 43, 354.
9. Bate, L.C., Nucleonics. 1963, 21, 72.
10. Dibbs, H.P., Department of Mines and Technical Surveys, Mines Branch, Technical Bulletin TB 55, March, 1964.
11. Radmacher, W., Mohrhauer, O., Brennstoff Chem. 1956, 37, 353.

TABLE 1. Results from the determination of oxygen in standards

Standards	Oxygen (%)				
	Determined using				Theoretical
	Pyrolysis method	Mean	Neutron activation method	Mean	
1) Benzoic acid	26.3; 26.7; 26.3; 26.0; 26.5; 26.7; 26.2; 26.3; 26.3;	26.4	26.14; 27.16; 27.12; 25.82; 25.54; 25.71;	26.25	26.20
2) Acetanilide	12.2; 11.7; 12.1;	12.0	12.12; 12.24; 11.76;	12.04	11.84

TABLE 2. Oxygen in coal (the results expressed on the dry coal basis)

Sample	Oxygen (%)				Carbon d.a.f.	Ash
	by pyrolysis method	Mean	by neutron activation method	Mean		
1	2	3	4	5	6	7
<u>Bituminous coals</u>						
Moss 3	6.4; 6.9; 6.4; 7.1; 7.1; 6.9;	6.8	8.17; 8.58; 8.84; 8.60;	8.55	82.4	6.73
Moss 3-demineralized	6.6; 6.6; 6.9;	6.7	6.75; 6.73; 6.13;	6.54		0.29
Itmann	4.2; 4.5; 4.0; 4.0;	4.2	6.40; 6.47; 6.68; 6.58;	6.53	85.1	6.30
Itmann-demineralized	4.3; 4.5; 4.2;	4.3	4.26; 4.24; 4.44;	4.31		0.15
<u>Lignites</u>						
Turow-demineralized	24.9; 26.4; 26.4; 26.5;	26.0	26.13; 26.21; 27.77; 25.99; 25.81;	26.38	68.8	0.25
Smogory-demineralized	29.9; 31.0; 29.8;	30.2	33.75; 32.38; 36.33; 30.77;	31.62	66.3	0.26
<u>Subbituminous coal</u>						
fresh	-	-	24.30; 24.59;	24.43	75.0	6.24
demineralized	-	-	20.00; 20.29;	20.14		0.11
<u>Anthracite</u>						
fresh	1.8; 2.1	2.0	7.59;	7.59	92.5	11.05
demineralized	2.3; 2.0; 2.2;	2.2	2.66;	2.66		0.91

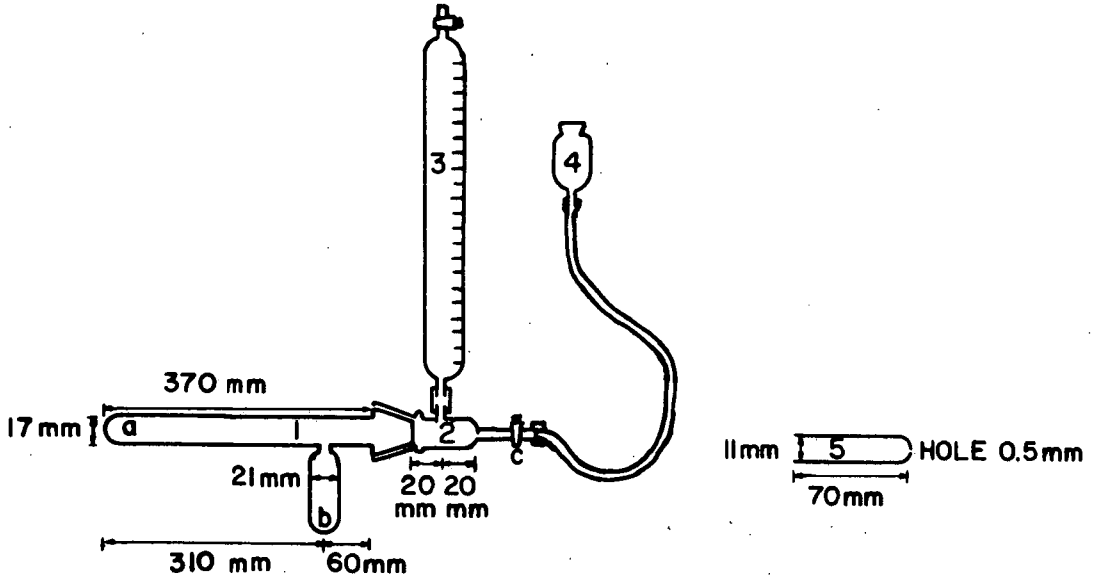


FIGURE 1 - APPARATUS FOR PYROLYSIS CONVERSION AND MEASUREMENT OF VOLUME OF EVOLVED GASES

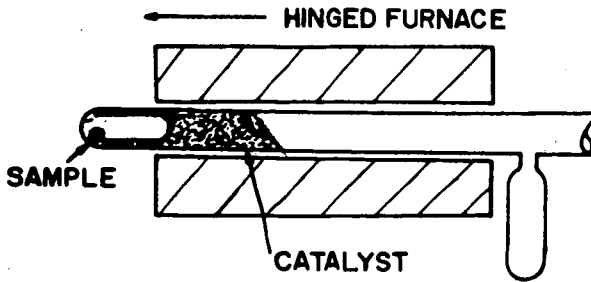


FIGURE 2 - LOCATION OF THE PYROLYSIS TUBING IN OVEN AT THE BEGINING OF EXPERIMENT

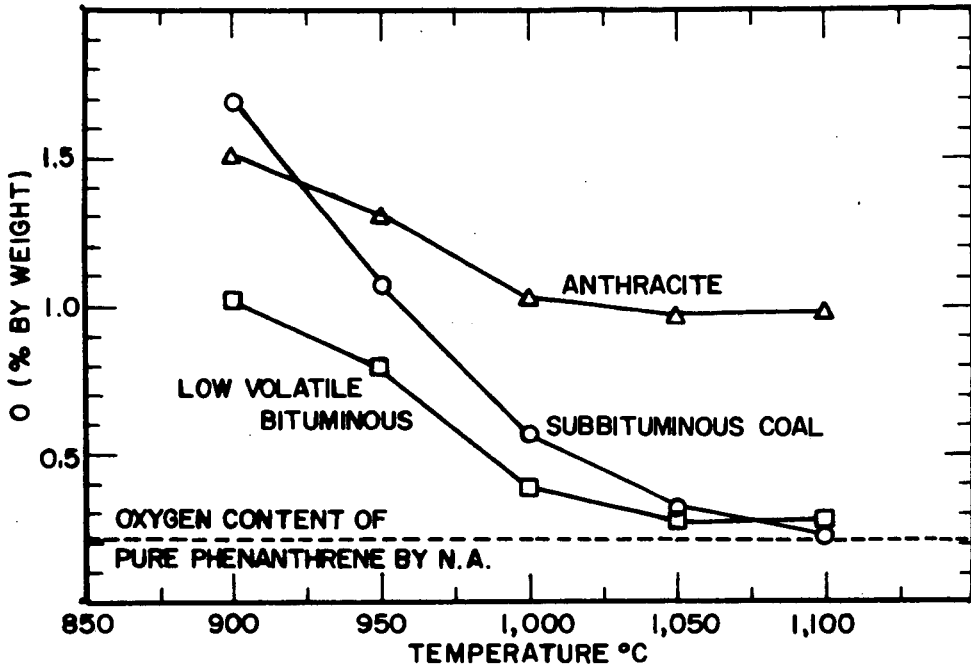


FIGURE 3 - OXYGEN CONTENT BY NEUTRON ACTIVATION OF COKE FROM DEMINERALIZED COAL, PYROLYSED FOR 10 MINUTES AT INDICATED TEMPERATURE

FRACTIONATION OF LOW TEMPERATURE COAL TAR
BY GEL PERMEATION CHROMATOGRAPHY

Benjamin C. B. Hsieh, R. E. Wood, and L. L. Anderson

Department of Mineral Engineering

University of Utah, Salt Lake City, Utah 84112

Abstract

The use of gel permeation chromatography as a separation tool makes it possible to fractionate coal tar or similar products into three groups of compounds. These are aliphatics, aromatics, and tar acids. The aliphatic hydrocarbons are fractionated as a function of molecular length or carbon number. The aromatic ring compounds are fractionated as a function of molecular size and shape. The effect of adsorption between the polar tar acids and the column support material delays their elution until the other two groups have passed through the column. The elution curves of selected coal tars show the distribution conditions and permit the calculation of percentage composition.

Gel permeation chromatographic data from coal tar distillates (150° to 350°C) were compared to the results of chemical extraction (USBM NaOH-H₂SO₄ procedure) and the results of FIA (ASTM D-1319 fluorescence indicator adsorption) on the same distillation fraction. A gas chromatograph was used for the qualitative identification of these products. The portion boiling above 350°C also can be analyzed with GPC where chemical extraction, FIA, GC, and mass spectrometric methods are not generally applicable. Because GPC is performed at room temperature, the problems of thermal cracking and polymerization that occur with distillation techniques are avoided.

Introduction

Gel permeation chromatography (GPC) was first mentioned in the literature by Moore in 1964 (1). A comprehensive historical review was published by Cazes (6) in 1966. This technique has since become an accepted method for the determination of molecular weight distribution of polymers and for the fractionation of medium and high molecular weight materials (6). This analytical tool is still somewhat limited to use in the area of polymer sciences and biochemistry. Very few articles have appeared which apply this technique to coal, coal tar, and petroleum products. Hendrickson and Moore (2) first described the elution behavior of aliphatic and aromatic hydrocarbons. Altgelt (3) has studied the molecular weight distribution of asphaltenes by GPC and infrared spectroscopy. Edstrom and Petro (4) reported that aromatic hydrocarbons were fractionated by GPC and also gave elution curves of coal tar pitch and thermal aromatic residues. These authors concluded that separations occur not as a function of a single parameter, but as a complex function of molecular size, shape, and polarity. Their elution curves were correlated with the softening point of the pitch samples with reference to standard aromatic materials. In our laboratory we have applied GPC to the elution

behavior of various kinds of coal tar, crude petroleum, and related materials based on molecular size, shape, and polarity. We have also measured separation characteristics of neutral oils, tar acids, and thermal distillation fractions from coal tar. These were compared to standard aliphatic and aromatic hydrocarbons by means of conventional gas chromatography.

Experimental Procedure

The general operation technique for gel permeation chromatography is to dissolve the sample containing materials of different molecular weight in a small volume of solvent. The sample and solvent are introduced at the top of the column. High molecular weight materials pass more rapidly through, while low molecular weight materials pass more slowly due to their diffusion into pores in the beads of the column support materials (5, 6, 7). Chemical affinity of polar materials may act to retard passage of a specific species more than would be expected on the basis of molecular size alone. ^{1/} Edstrom and Petro (4) first pointed out this effect and it has been verified in our work. The overall effect of the procedure is a separation based on molecular size and shape, but some chemical affinity effects must also be considered.

Tetrahydrofuran (THF) was chosen as the solvent for elution through a Sephadex organic solvent resistant column packed with Sephadex LH-20 beads. The column and support material were supplied by Pharmacia Fine Chemicals, Inc. ^{2/} The advantages of using THF were pointed out by Hendrickson and Moore (2). A reagent grade tetrahydrofuran from J. T. Baker Chemical Company was used. Its purity was checked by gas chromatography. A small amount of Butylated Hydroxytoluene as stabilizer was added by the manufacturer.

The separation range of Sephadex LH-20 is reported to be from molecular weight 100 to 2000 by the manufacturer (5). A column of approximately 86.5 cm length was operated at room temperature and the solvent was degassed at 55°C before introduction to the column. Samples were introduced by injection with a syringe through a Y-shaped junction with a rubber septum mounted at the head of the column.

The eluted fractions were collected automatically with a Gilson ^{3/} volumetric fractionator at approximately 10-minute intervals and a flow rate near 0.34 ml per minute. This resulted in 3.40 ml collected for each fraction. Qualitative identification of standard materials passing through the column was

^{1/} Moore and Hendrickson (7) considered the adsorption and partition effects "are not significant in GPC, since the gel is quite free from associative forces with the sample and is eluted with a solvent having a similar polarity, so that negligible partition of the solute occurs between the gel and solvent phases."

^{2/} Pharmacia Fine Chemicals, Inc., 800 Centennial Avenue, Piscataway, N. J. 08854.

^{3/} Gilson Medical Electronics, Middleton, Wisconsin.

attained by injection of fractions into an F&M Model 720 gas chromatograph. Apiezon L (4 ft.), silicone grease (2 ft.), and carbowax 20M (8 ft.) columns were used. This unit was programmed from 100° to 300°C at 10 degrees per minute. He carrier gas was used at a flow rate of 100 ml/min.

Quantitative measurement of the amount of sample material collected in each fraction by GPC was done by evaporating the tetrahydrofuran at about 70°C and weighing the residue. Duplicate weighings were reproducible within 0.10 mg on the same fraction residues

Samples of Spring Canyon, Big Horn, and River King coals were selected for study. These coals were carbonized at 550°C. The coal tars from this process were distilled to 150°C. The portions distilling below 150°C were discarded and the portions distilling about 150°C were used as samples. Spring Canyon coal tar was again distilled to give two fractions: 150° to 350°C (distillate) and above 350°C (pitch). The neutral oil and tar acids were chemically separated from the Spring Canyon coal tar distillates by the Bureau of Mines extraction method (8). One other pyrolysis coal tar was studied. This was furnished by Food Machinery Corporation and was examined without further treatment. A petroleum crude oil, a shale oil distillate, and a tar sand benzene extract were fractionated by GPC without prior treatment

Results and Discussion

Since chemical affinity or absorption between specific materials in the sample and column support beads may affect the physical separation of components, it is important that standard reference materials be measured on the column. Figure 1 is a plot of molecular weight of known reference materials, paraffinic, olefinic, and aromatic hydrocarbons, versus the fraction number where the greatest concentration of each material can be expected to occur. Although each reference material will occur in 4 or 5 adjacent fractions, its greatest concentration, as found by gas chromatography (GC), will occur in the fraction indicated in Figure 1. As shown by this comparison, there is a considerable overlap between aliphatic and aromatic-type compounds. A plot of the data from Hendrickson and Moore (2) where paraffinic and olefinic hydrocarbons and their isomers are all in one group and all aromatic hydrocarbons in another group is in agreement with Figure 1.

The fractions of the Spring Canyon coal tar distillate elution curve, shown in Figure 2, are clearly divided into three groups. The first two groups contain the aliphatic and aromatic hydrocarbons. The third group contains the polar tar acids. Evidence for these statements is found in Figure 3 where elution curves for neutral oil without tar acids and for tar acids alone are shown. The presence of material in the total coal tar distillate, Figure 2, in fractions numbered greater than 85 is attributed to acids and bases that could have an affinity for the Sephadex LH-20. These materials are not found in the sample of neutral oil, Figure 3.

Gas chromatography was used in an effort to more fully understand the GPC separation of coal tar. The fractions collected from GPC were combined into three groups by redissolving the fraction residues in THF. Group I was taken

from fraction number 50 to 66. Group II was taken from fraction number 67 to 85, and group III was taken from fraction number 86 to 125 as indicated in Figure 2. These three portions of the original sample were then analyzed with gas chromatography. A comparison of results from these three composited groups of fractions with standard paraffinic hydrocarbons, aromatic compounds, and tar acids are shown in Figures 4-6. Also, the aromatic compounds were extracted from the same coal tar distillate with pyridine by the method of Qader, et al. (9), for comparison with the composited groups.

The pyridine extraction removes both aromatic and tar acid compounds from the distillate. This is shown by a comparison of Figure 5a (Group II) and Figure 5b (pyridine extract). Removal of the tar acid peaks from Figure 5b shows good agreement between the two. The pattern of Group I shown in Figure 4a compares very well with that from selected standard straight chain paraffinic compounds shown in Figure 4b. The pattern of Group III, Figure 6a, agrees almost exactly with the pattern of tar acids chemically separated from the same distillate, Figure 6b.

In Figures 4-6 peak (1) was identified as the inhibitor from the THF solvent. Although in low concentration in the solvent, its concentration is increased by evaporation of the solvent.

The GC chart of the original coal tar distillate is shown in Figure 7. The total pattern of Figure 7 is the summation of the three separate patterns of Figures 4a, 5a, and 6a. These three group samples were analyzed with an Apiezon L column and also with Silicone Grease and Carbowax 20M columns. Different known standard paraffins, aromatics, and phenols were added to these three samples separately. Some peaks were matched and identified as paraffins, aromatics, and phenols in the three composited fraction portions of the original sample, respectively.

Using GPC, it is possible to separate coal tar products into aliphatic and aromatic fractions by molecular shape. Tar acids are separated into a third fraction by chemical affinity with the GPC column support material. This separation is as precise and accurate as the standard chemical methods which are used for coal tar analysis (8, 10, 11).

The fundamental separation of GPC is determined by molecular size. Figure 8 shows a comparison of two distillation fractions from a low temperature coal tar sample. The solid line represents the chromatogram obtained from the 150° to 350°C fraction, distillates, and the dotted line that from the 350° to 550°C fraction, pitch. These curves show that in the pitch or high boiling material, the paraffinic group and the aromatic group are both distributed toward the lower fraction numbers. In the low boiling distillates the two groups are distributed toward the higher fraction numbers. This indicates that the pitch portion contains compounds of greater molecular size than does the distillates portion, as would be expected. The summation of these two curves gives the total coal tar distribution curve almost identical to that of the original material shown in Figure 9c.

The pattern of the distillate portion, Figure 2, begins with fraction number 50. From this we infer (Figure 1) that the highest molecular weight paraffinic

compound in the distillate is C₃₁. This is in agreement with the GC data. Although we can find C₃₂ and C₃₃ peaks on the GC pattern, they are very small compared to the C₃₀ and C₃₁ peaks. At the low temperature boundary of the distillate range (150°C), the smallest paraffinic number possible is C₉ (boiling point 150.8°C). This is also in agreement with the GC pattern, Figure 7, where C₉ is the first peak indicated. Termination of Group I at fraction number 66 would suggest, from Figure 1, that C₁₁ paraffins could be included. However, the paraffins C₉ to C₁₁ are easily vaporized and may be lost in the solvent evaporation step. As a result, C₁₂ is the lowest boiling compound found in Group I by GC, Figure 4a.

It is important that the coal tar components that boil below 150°C be removed prior to GPC. The aliphatic materials that boil in this range, primarily components of the conventional "gasoline cut," may overlap into the aromatic portion of the GPC curve. The lower boiling aromatic components, such as benzene, xylene, and toluene which are also removed by this process, do not overlap into the tar acid portion of the GPC curve. The GC patterns of Groups II and III show no evidence of overlapping materials (Figures 5a and 6a).

GC peaks of Group I, Figure 4a, are produced by paraffinic hydrocarbons. Although olefinic compounds may be present, they are low in concentration (2-3%) as shown by FIA tests and are not registered in Figure 4a. The absence of aromatics in group I is evidence that aromatic compounds of high ring number (over 4) are not present in coal tar. If present, these high-boiling materials would elute with the C₉-C₁₂ aliphatic hydrocarbons. The lack of high ring number aromatics is to be expected since low temperature carbonization (550°C) should produce only those coal tar components with boiling point below this temperature. The most significant aromatic materials (Figure 5) are those boiling in the naphthalene to anthracene range (218° to 354°C).

Again, reference to Figure 1 shows a different slope or separation factor for homologous aromatic compounds of different size or configuration. The slope of the curve propyl benzene, ethyl benzene, and toluene was plotted from the data of Hendrickson and Moore (2). The slopes of the two curves (a) 2 methyl anthracene, 2 methyl naphthalene, and toluene, and (b) biphenyl, terphenyl, quaterphenyl, etc., are plotted from the data of Edstrom and Petro (4). All the data were transposed to our reference scales based on the slope of the benzene, naphthalene, anthracene, and naphthacene curve. From these four curves we infer that a simple curvilinear function does not describe the GPC separation characteristic for aromatic compounds. Therefore, in Group II, we do not find an orderly distribution of components by number of rings or any other single parameter.

The distribution curves of coal tars from some representative coal types are shown in Figure 9. The chemical characteristics of these coals are listed in Table 1. All these coals were carbonized at 550°C and the fraction boiling below 150°C removed prior to separation by GPC. Figure 10 shows the GPC curves for a crude petroleum, a shale oil, and a tar sand extract.

Table 2 contains the percentages of aliphatics, aromatics, and tar acids found in the samples of Figures 9 and 10. Coal tars from the low temperature

carbonization of three coals (Big Horn, River King, and Spring Canyon), a petroleum crude (Red Wash), a shale oil distillate from Rifle, Colorado, a tar sand extract from the Utah Geological Survey, and a pyrolysis low temperature tar (FMC) were included. Also included in Table 2 are GPC data for products from Spring Canyon coal tar. Pitch (B.P. 350° to 550°C), duplicate measurements on distillates (B.P. 150° to 350°C), and neutral oil from the distillate fraction are shown. A chemical measurement of the tar acids in the distillate sample and an FIA (10) measurement of the aliphatics and aromatics in the neutral oil sample are also shown. The weights of residues in fractions 1-66 (aliphatics), 67-85 (aromatics), and 86 to 125 (tar acids) were used in the calculation of percentage composition. The figures in parentheses represent the calculated percentages of aliphatics and aromatics in the neutral oil; that is, the product following removal of tar acids and bases from each sample.

Spring Canyon coal, which is a high volatile bituminous coal, was used for most of our determinations. The percentages of aliphatics and aromatics in the total coal tar from this coal are about the same. The tar acids percentage in the total coal tar is less than that reported from the distillates. This means that the tar acids are distributed toward the lower boiling point (or low molecular weight) compounds. In pitch, the opposite is true. The tar acids percentage is lower than in the total coal tar and aliphatic compounds are predominant. Another high volatile bituminous coal used in this study was River King, which contains 3.30 percent sulfur. The GPC elution curve indicates that this coal tar contains a high percentage of aromatic and tar acid compounds and a relatively low percentage of aliphatic hydrocarbons. Coal tar from a subbituminous coal, Big Horn, is little different from coal tar from Spring Canyon coal. However, this low rank coal (17.2% O₂), when carbonized, did produce more water and somewhat more acids than did the Spring Canyon coal.

The three low temperature coal tars studied show very little weight percent in fractions numbered less than 50. This is an indication that aliphatic hydrocarbons of length C₄₀ and higher are not produced in the low temperature carbonization process at 550°C. However, the GPC curve from a pyrolysis coal tar (FMC), also shown in Figure 9, does show a significant weight percent in fractions numbered less than 50. This curve indicates a predominantly aliphatic content rather than aromatic or tar acid composition. This is due to the fact that this material was pyrolyzed at a temperature of 870°C.

Shale oil distillates, petroleum crude oil, and benzene extractants from a tar sand sample, Figure 10, show high percentages of aliphatic hydrocarbons. The increased proportion of high carbon number paraffins can be seen in the higher weight percent in fractions numbered less than 50

Conclusions

The results of this investigation show that GPC is a useful tool for the study of distribution of coal-derived liquids. These liquids may come from carbonization coal tars, hydrogenation or hydrocracking products, or solvent extracted products, etc. Similar composition materials such as petroleum

crude and its products, shale oil, gilsonite, and tar sand extractants, etc., can also be fractionated. GPC readily fractionates these samples into three groups, aliphatics, aromatics, and tar acids, based on the factors of molecular size, shape, and polarity. This procedure is specifically interesting because it is capable of making separations of these high boiling, high molecular weight materials at room temperature. The problems of thermal cracking and polymerization when distillation is used for fractionation are minimized. High boiling pitches and tars that cannot be analyzed with gas chromatography, mass spectrometry, the ASTM FIA or the USBM chemical extraction method can be fractionated with this procedure.

Acknowledgement

The research work reported in this paper is sponsored by the U. S. Office of Coal Research and the University of Utah.

Table I. Proximate and ultimate analysis of selected coals

	Spring Canyon		Big Horn		River King	
	H.V. bituminous		subbituminous		H.V. bituminous	
V.M.	47.60	(53.10)	38.80	(46.49)	38.64	(48.26)
Moisture	1.90	Free	14.30	Free	8.26	Free
Ash	8.46	Free	2.22	Free	11.68	Free
F.C.	42.04	(46.90)	44.68	(53.51)	41.42	(51.74)
S	0.46		0.60		3.30	
O	9.67		17.21		9.61	
C	71.10		62.40		62.40	
N	1.40		0.70		1.40	
H	5.10		4.10		4.20	

Table II. Percentage results from GPC fractionation method.

Sample	I	II	III
	aliphatics 0-66	aromatics 67-85	tar acids 86-125
Red Wash (Crude oil)	82.21% (87.89%)*	11.33% (12.11%)*	6.46%
Tar sand (Benzene extractants)	69.10% (79.30%)	18.04% (20.70%)	12.86%
Shale oil (Distillate from Rifle, Colorado)	68.24% (83.21%)	17.77% (16.79%)	13.99%
F.M.C. (Pyrolysis coal tar)	57.71% (67.89%)	27.30% (32.11%)	14.99%
Spring Canyon (High volatile bituminous coal)	37.22% (47.98%)	40.36% (52.02%)	22.42%
Big Horn (Subbituminous coal, 17.2% O ₂)	31.21% (44.80%)	38.45% (55.20%)	30.34%
River King (High volatile bituminous coal, 3.30% S)	18.37% (29.71%)	43.47% (70.29%)	38.16%
Pitch (From Spring Canyon coal tar)	47.07% (58.87%)	32.88% (41.13%)	20.05%
Neutral oil (From Spring Canyon coal tar distillate)	42.60% (41.77%)	57.40% (58.23%)	
Tar acids from Spring Canyon coal tar by chemical method			34-36%
Neutral oil from Spring Canyon coal tar by FIA method	(38-42%)	(58-62%)	
Distillates (1) from Spring Canyon coal tar (150°-350°C)	24.09% (38.28%)	38.03% (60.43%)	37.88%
Distillates (2) from Spring Canyon coal tar (150°-350°C)	22.62% (36.72%)	38.98% (63.27%)	38.40%

* The percentages of aliphatics and aromatics in the neutral oil where tar acids and tar bases have been removed are indicated by the use of parentheses.

Literature Cited

1. Moore, J. C., J. Polymer Sci., Part A, 2, 835-843 (1964), "Gel Permeation Chromatography, I. A New Method for Molecular Weight Distribution of High Polymers"
2. Hendrickson, J. G., and Moore, J. C., J. Polymer Sci., Part A-1, 4, 167-188 (1966), "Gel Permeation Chromatography, III. Molecular Shape versus Elution"
3. Altgelt, K. H., J. of Applied Polymer Sci., 9, 3389-3393 (1965), "Fractionation of Asphaltenes by Gel Permeation Chromatography"
4. Edstrom, T., and Petro, B. A., ACS Chicago meeting, Sept. 1967, "Gel Permeation Chromatographic Studies of Polynuclear Aromatic Hydrocarbon Materials"
5. Sephadex gel filtration in theory and practice, Pharmacia Fine Chemicals, Inc., 1967
6. Cazes, J., J. of Chemical Education, 43, A 567-582 (1966), "Gel Permeation Chromatography, Part One," 43, A625-642 (1966), "G.P.C., Part Two"
7. Moore, J. C., and Hendrickson, J. G., J. of Polymer Sci., Part C, 8, 233-241 (1965), "Gel Permeation Chromatography II. The Nature of the Separation"
8. Fisher, C. H., and Eisner, A., Industrial and Eng. Chem. Analytical Edition, 9, 213-218 (1937), "Determination of Tar Acids and Bases by Extraction Methods"
9. Qader, S. A., et al., India Patent No. 94932, Oct 29, 1966
10. ASTM, D1319, Hydrocarbon Types in Liquid Petroleum Products (FIA Method)
11. Standard Methods for Testing Tar and its Products, Fifth Edition (1962), published by the Standardization of Tar Products Tests Committee, printed in Great Britain, W. Heffer & Sons Ltd., Cambridge, England

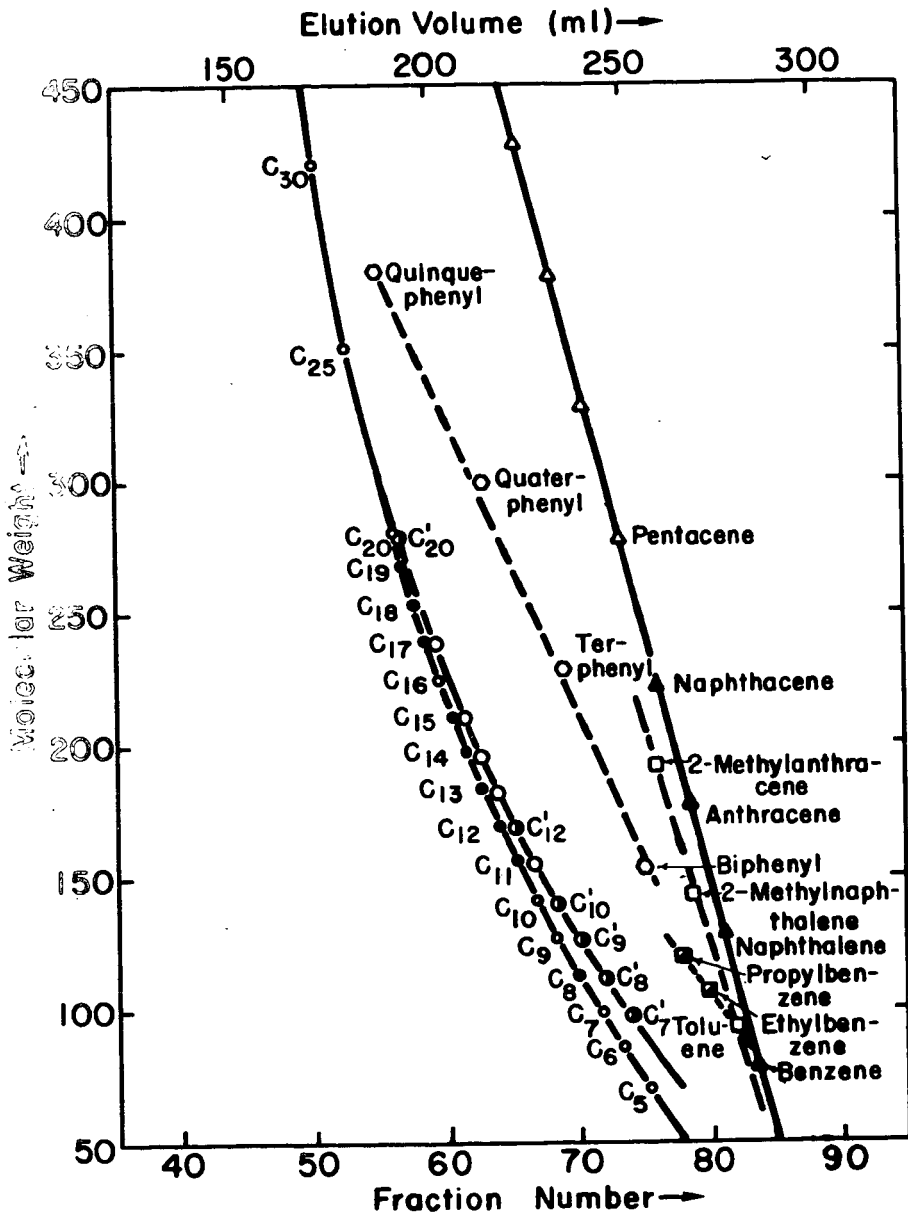


Figure I. GP Chromatography of known hydrocarbons: paraffins, olefins, and aromatics.

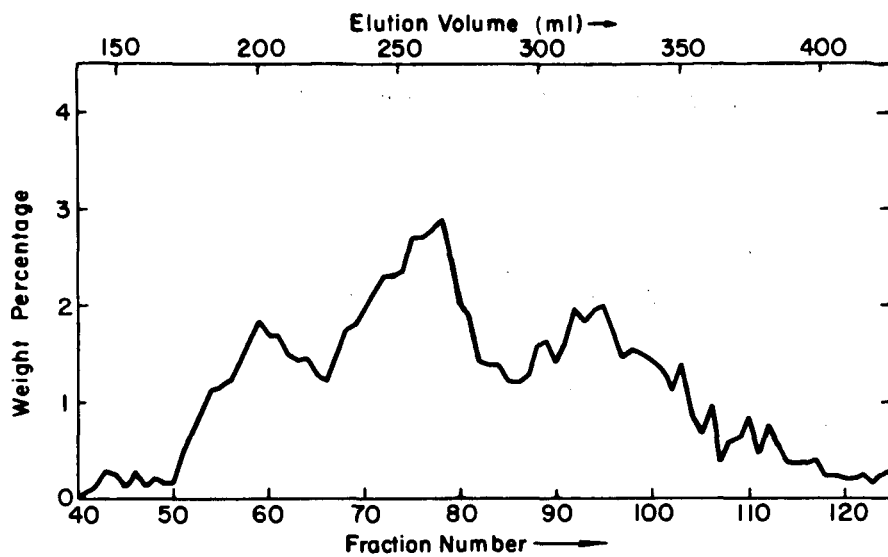


Figure 2. Elution curves (GPC) of low temperature coal tar distillates (150°–350°C) from Spring Canyon coal.

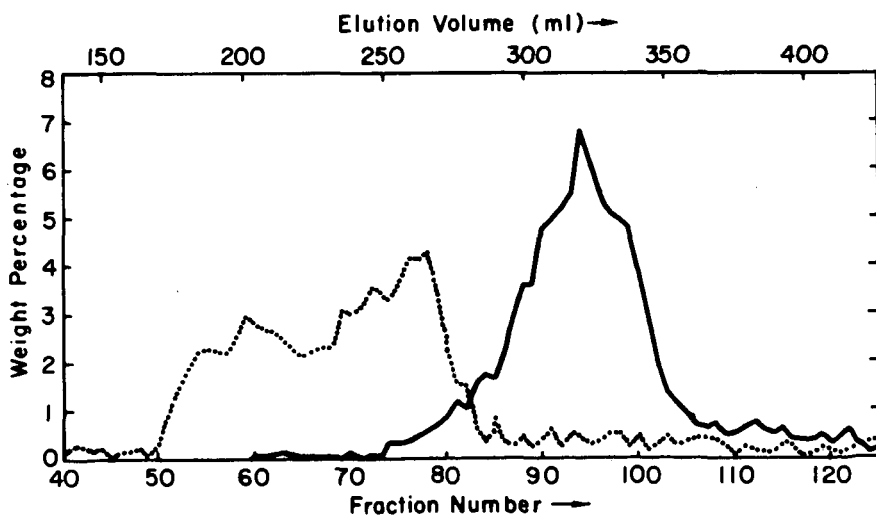


Figure 3. Elution curves (GPC) of neutral oil and tar acids from Spring Canyon coal tar distillates (150°–350°C).

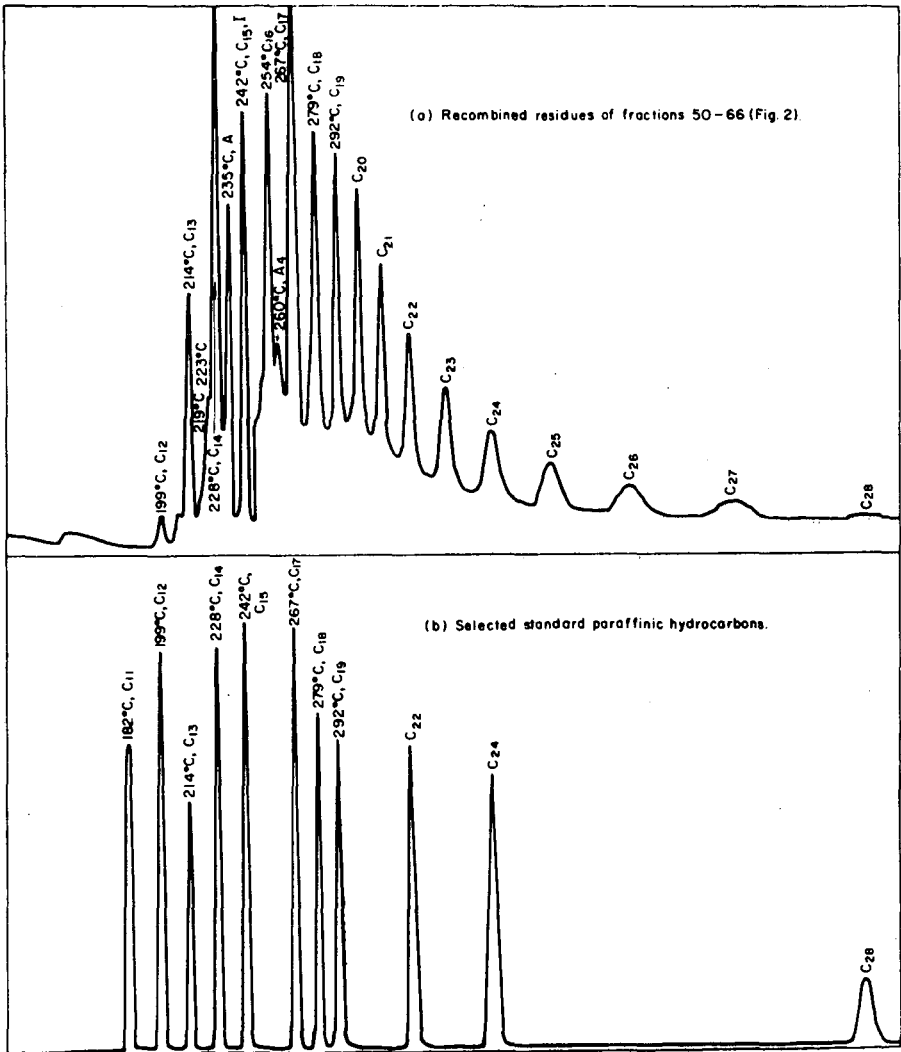


Figure 4. GC Chromatograms.

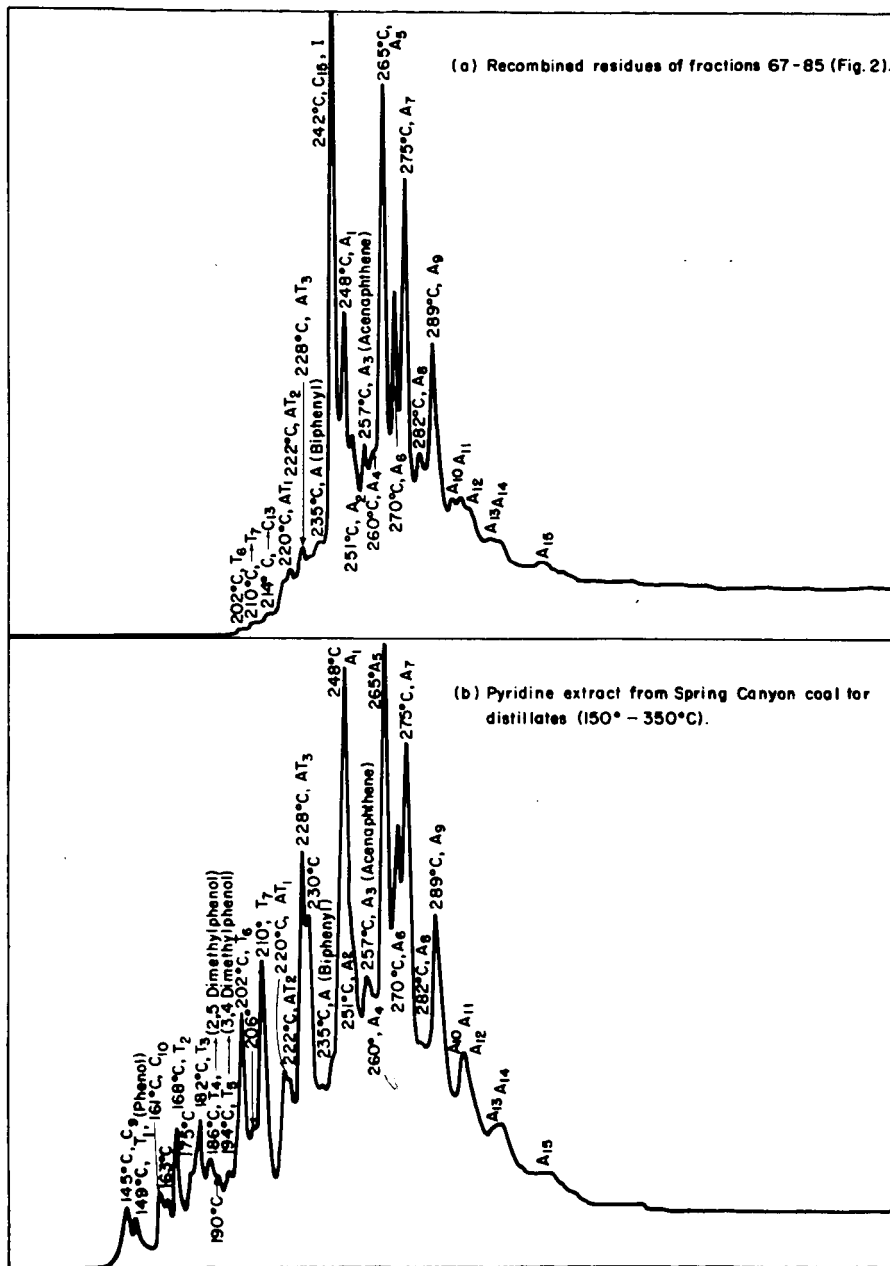
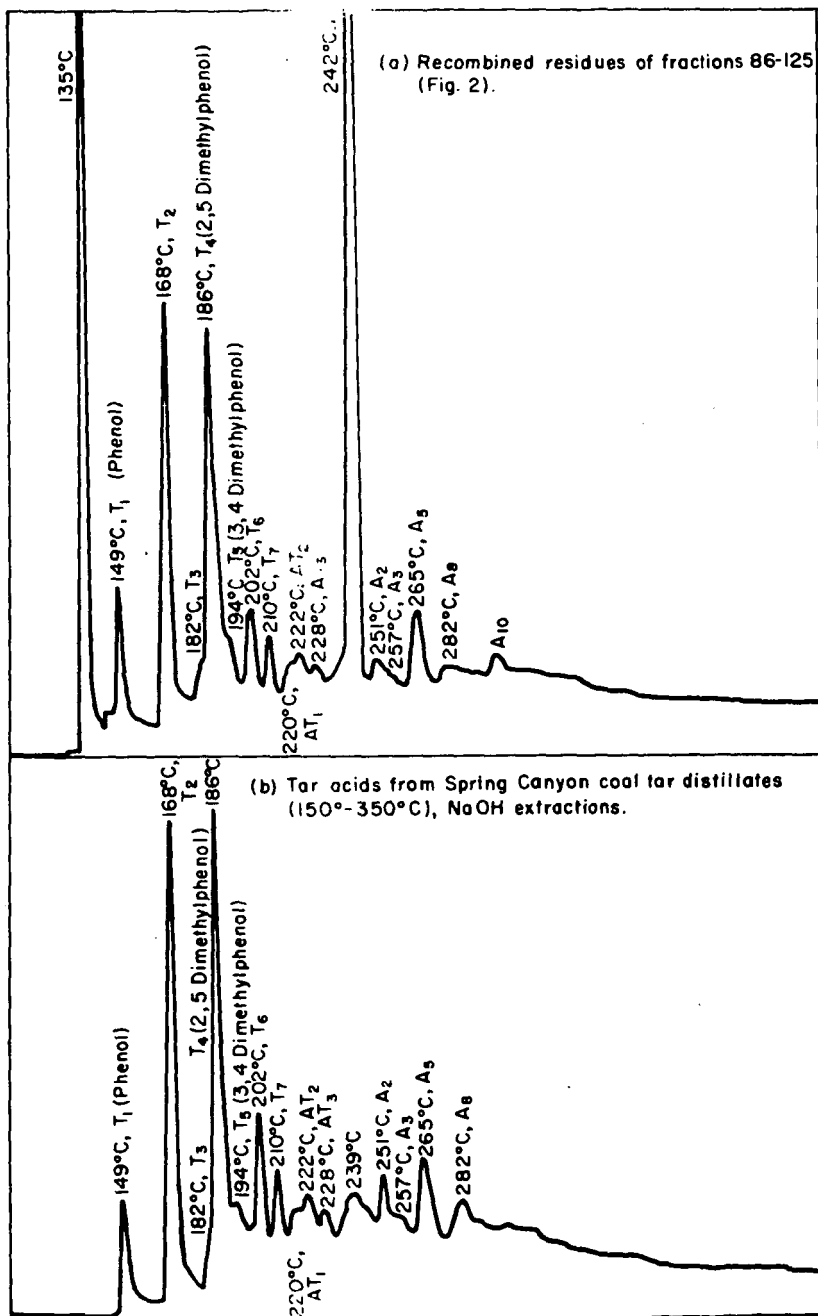
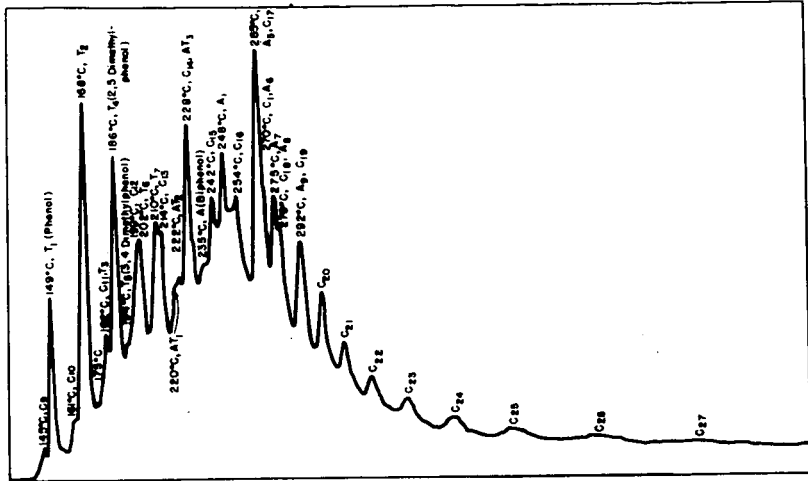


Figure 5. GC Chromatograms



DSC thermograms.



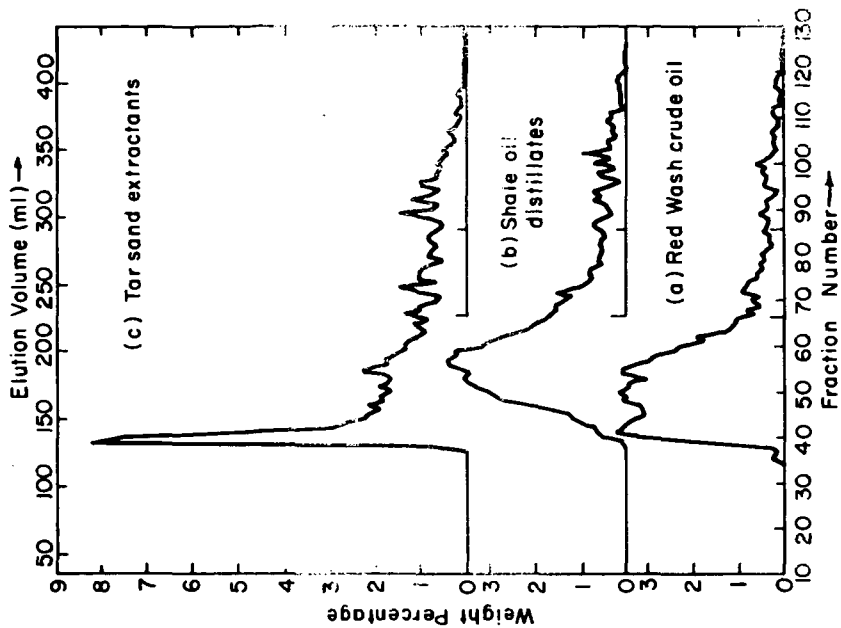


Figure 10. GPC elution curves.

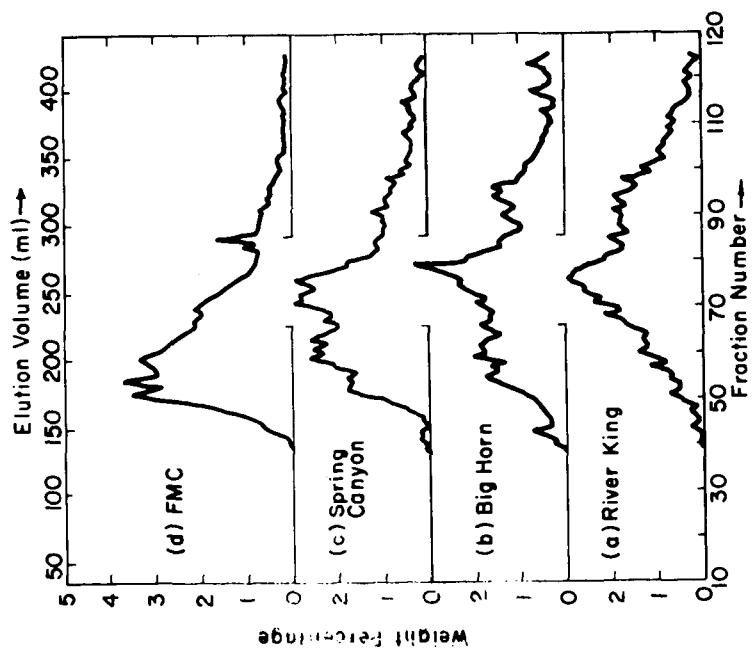


Figure 9. GPC elution curves.

(a) River King coal tar (150°-550°C)

(b) Big Horn coal tar (150°-550°C).

(c) Spring Canyon coal tar (150°-550°C.)

(d) Food Machinery Corporation pyrolysis coal tar.

SILYLATION OF ASPHALTS WITHIN GLC COLUMNS. EFFECTS ON INVERSE GLC DATA AND INFRARED SPECTRA

S. M. Dorrence and J. C. Petersen

Laramie Petroleum Research Center, Bureau of Mines
U. S. Department of the Interior, Laramie, Wyoming

INTRODUCTION

Inverse gas-liquid chromatography (IGLC) has indicated differences in the chemical composition of whole asphalts (1-4) as well as fractions from asphalts (1, 5). IGLC measures interactions between the functional groups of volatile test compounds and functional groups in the liquid phase, which in our studies is asphalt. The asphalt may be analyzed either as-received or after an in-column oxidation procedure.

Asphalt contains many types of functional groups that may exhibit selective affinity for specific test compounds. The identification of selective interactions between functional groups of asphalts and test compounds would provide interpretive information about IGLC data and its relation to the chemical composition of asphalts. Such information is important because previous work has established empirical correlations between IGLC data for specific test compounds and in-use performance (4) or accelerated weathering durability (2, 3).

One approach to the identification of IGLC interactions is selective blocking of functional groups in the asphalt. Work with other materials has shown that silylating reagents are reactive toward certain functional groups containing active hydrogens. Such groups are known to be present in asphalts. These active hydrogen groups are believed to interact strongly with certain test compounds used in IGLC. In the present study N,O-bis(trimethylsilyl)acetamide (BSA) was used to silylate these groups in asphalts. Using a novel approach, silylation is conveniently carried out *in situ* by injecting BSA directly into the IGLC column. Independent work published after completion of this study made use of in-column silylation of volatile solutes (6).

In the present study, IGLC data were obtained on a number of oxidized and unoxidized asphalts that had been silylated. These data are compared with data from samples before silylation.

Infrared spectra were obtained on asphalts recovered from the columns. These spectra are correlated with IGLC data to provide information about functional group interactions between test compounds and asphalts.

EXPERIMENTAL

Apparatus and Procedure

IGLC data were obtained on a Beckman GC-2A gas chromatograph.* Columns were prepared using $\frac{1}{8}$ -inch by 12 $\frac{1}{2}$ -foot aluminum tubing packed with 1 part asphalt on 10 parts by weight of 20-40 mesh Fluoropak 80. Columns were conditioned at 130°C for at least 6 hours, using a helium inlet gauge pressure of 15 psi. Following conditioning, test compounds (0.1 μ l) were then

*Mention of specific products or brand names is made for information only and does not imply endorsement by the Bureau of Mines.

introduced separately and retention times determined. In this study, two columns were prepared from each asphalt. One column was used to obtain test compound retention data on the original asphalt followed by in-column silylation after which retention data were again obtained. The second column was oxidized by the introduction of air under conditions previously reported (2, 3), and retention data were obtained. This was followed by in-column silylation, and retention data were again obtained.

Silylation. - The in-column silylation of asphalt samples was performed in a manner similar to that used to treat column packing supports to prevent "tailing of peaks" from polar materials (7-10). The column to be treated was heated to 160° C while blanketing with helium carrier gas. Four portions of BSA were then injected at 30-minute intervals, the first portion being 200 μ l and the remainder being 100- μ l quantities. One hour after injection of the final portion, the temperature was lowered to 130° C and held overnight (at least 15 hours) to elute excess BSA and reaction by-products. Inverse GLC data were then obtained.

Infrared Spectra. - Infrared spectra were obtained with a Perkin-Elmer Model 521 double-beam spectrophotometer using solvent compensation. Asphalt samples were recovered from the IGLC packing for infrared study with CCl_4 using a modified Soxhlet extraction. The solution obtained was adjusted so that the asphalt concentration was 20g/l. The spectra were obtained on these solutions using 1 cm sodium chloride cells.

Materials. - N,O-Bis(trimethylsilyl)acetamide (BSA) and hexamethyldisilazane (HMDS) were used as received from Pierce Chemical Company. Wilmington (Calif.) asphalt (11) and two asphalts, D and J, from the Zaca-Wigmore Experimental Road Test (12) were used in this study. The former was prepared in this laboratory, and the latter two were furnished by the Materials Division of the Bureau of Public Roads.

Calculation of the Specific Interaction Coefficient (I_g)

Specific interaction coefficients for the test compounds were calculated according to the following equation:

$$I_g = 100 [\log V_g (\text{test compound}) - \log V_g (\text{hypothetical n-paraffin})].$$

I_g is different from the interaction coefficient (I_p) used in earlier work (1) in that specific retention volume (V_g) rather than corrected retention volume (V_R^0) is used in the calculations. The specific interaction coefficient thus obtained is a measure of interactions between the chemical functionalities of the asphalt and the test compound.

RESULTS AND DISCUSSION

Effect of Silylation on Inverse GLC Retention Data

Treatment of an inverse GLC column at 160° C with either HMDS or BSA resulted in a rapid reaction. By observing changes in the IR spectra of recovered asphalts following silylation, BSA was found to be more reactive than HMDS and, therefore, was chosen for further studies. Attempts to silylate asphalt samples in solution, using either BSA or HMDS, were unsuccessful because of slow reaction due to low boiling points of the solvents.

Data in Table I show that the specific interaction coefficients for phenol and propionic acid decrease on silylation. The interaction coefficients for acidic test compounds, particularly phenol, have been shown to correlate with service performance in both accelerated weathering and road test studies (2-4). Values of the I_g on all asphalts (oxidized or not) fall into narrow ranges for both test compounds after silylation. The range for phenol on silylated, as-received asphalts is 112 to 117; that for silylated-oxidized asphalts is 113 to 117. Ranges for propionic acid were 65 to 67 and 69 to 71, respectively. As a net result, all of the silylated asphalts are indistinguishable by these two test compounds. These data indicate that certain functional groups

TABLE I. - Comparison of specific interaction coefficients for asphalts, oxidized asphalts, and trimethylsilyl derivatives of both

Test compound	Asphalt sample ^a	Specific interaction coefficients (I _g)											
		W	WS	WO	WOS	D	DS	DO	DOS	J	JS	JO	JOS
Phenol		129	112	161	113	136 134	116 113	154 155	117 115	120	117	160	115
Propionic acid		94	67	108	71	97 ----- b	65 65	154 157	71 69	72	65	99	71
Formamide		150	142	172	165	155 157	----- 150	b 188 187	183 185	126	128	155	153

^a W, D, and J refer to Wilmington (Calif.) asphalt, asphalt D and asphalt J, respectively. S designates a sample silylated with BSA, and O designates a column-oxidized sample. Separate determinations on different samples of asphalt D are shown.

^b This value was not obtained.

that form on oxidation and interact strongly with phenol and propionic acid are blocked by silylation. Silylation also appears to block a portion of the strongly interacting groups present in as-received asphalts.

Phenols and carboxylic acids are compound types present in asphalts. These compound types contain active hydrogens and are believed to interact strongly with the test compounds phenol and propionic acid in IGLC columns via hydrogen bonding. Silylating reagents such as BSA form ethers and esters with phenols and carboxylic acids, respectively, thus reducing their ability to hydrogen bond. Therefore, it is concluded that the phenolic and carboxylic acid OH groups in asphalts are silylated by the technique used in this study, thus strongly suggesting that decreases in the I_g values for the test compounds phenol and propionic acid result from silylation of these groups.

Data in Table I show that even though the I_g values for phenol and propionic acid after silylation have narrow ranges the values are still high. These high, relatively constant values indicate that the silylated asphalt samples contain approximately the same concentration of other types of functional groups that interact with phenol or propionic acid.

The formamide I_g values (Table I) for oxidized or silylated-oxidized asphalts are in the same range (155 to 188, compared to 153 to 185). Ranges for as-received and silylated asphalts are also comparable, these being 127 to 157 and 128 to 150, respectively. Because the specific interaction coefficients for formamide decrease only slightly on silylation, it appears that formamide does not interact appreciably with groups that can be silylated. The carbonyl group is a major type of functional group formed on oxidation (13) that is not silylated with BSA by the current technique. Carbonyl groups have been shown (14) to interact strongly with formamide in GLC determinations. Because oxidized asphalts (whether silylated or not) have higher I_g values than corresponding unoxidized samples, and because carbonyl groups are polar functions formed on oxidation which are not silylated, it is concluded that carbonyl groups contribute appreciably to I_g values for formamide.

Effect of Silylation on Infrared Spectra

Infrared spectra of dilute solutions of trimethylsilylacetamide, a silylated asphalt, and an asphalt are shown in Figure 1. The infrared band at 3610 cm^{-1} has been assigned to the free phenolic OH stretching band (15). Based on work in this laboratory, the band at 3540 cm^{-1} has been assigned to the free carboxylic acid OH stretching band. The band at 3420 cm^{-1} is attributed to the free amide NH stretching band of trimethylsilylacetamide. The latter assignment was made on the basis of trapping the effluent from silylation reactions and comparing its infrared spectrum with that of trimethylsilylacetamide obtained by hydrolysis of BSA. These spectra were essentially identical. The band at 3420 cm^{-1} appeared within the known range for NH stretching of amides. The infrared spectrum for BSA has no such band.

The infrared spectra of silylated asphalts show that silylation significantly decreases the absorbance in the 3610 and 3540 cm^{-1} regions. Little, if any, trimethylsilylacetamide remains in the asphalt sample after silylation. This is demonstrated by the absence of a sharp band in the silylated asphalt spectrum in the 3420 cm^{-1} region. The infrared data are summarized in Table II. In all cases, decreases in absorbances for free phenolic and carboxylic acid OH groups are evident after silylation, indicating that most of these groups react with BSA. Previous discussion of IGLC data concluded that silylation blocks phenolic and carboxylic acid OH groups in asphalt and that these groups probably interact strongly with phenol and propionic acid in IGLC columns. The infrared spectra show that free phenolic and carboxylic acid OH groups are essentially eliminated by silylation.

When free carboxylic acid and phenolic OH absorbance values for as-received asphalts are compared with values for oxidized asphalts, decreases in absorbance values for Wilmington

TABLE II. Comparison of infrared spectra of asphalt samples

Sample ^b	Absorbance ^a	
	Free phenolic OH, 3610 cm ⁻¹	Free carboxylic OH, 3540 cm ⁻¹
W	0.130	0.045
WS	<0.005 ^c	<0.005
D	0.097	0.028
DS	0.019	<0.005
J	0.035	0.020
JS	0.009	0.006

WO	0.070	0.028
WOS	<0.005	<0.005
DO	0.111	0.034
DOS	0.017	<0.005
JO	0.015	0.009
JOS	0.006	<0.005

^aThe values given are for 20g/l solutions of the sample in CCl₄ using 1 cm cells without solvent compensation. They were determined by the base-line technique.

^bSee footnote from Table I for sample designation

^cThe lower limit of detectability was about 0.005 absorbance units.

asphalt and asphalt J are observed. These results seem contradictory to the conclusion that increased concentrations of phenolic and carboxylic acid OH groups relate to the increase in I_g values for phenol and propionic acid. However, it has been shown previously (15) that column oxidation of asphalts results in a decrease of free OH absorbance while hydrogen-bonded OH absorbance increases significantly. Much of this hydrogen bonding remains intact even in dilute solutions so that the net result is a loss of free OH absorbance even though the total OH in the sample has increased. Upon silylation a general decrease is noted in the hydrogen-bonded absorbance; however, no quantitative determination could be made of the hydrogen-bonded region (about $3500\text{--}2500\text{ cm}^{-1}$) because it is overlapped by the C-H stretching region.

Repeatability of the Silylation Technique

Two separate packings were prepared, using asphalt D as the substrate. Two columns of each packing were processed in the manner described in the Experimental section. The data, included in Table I, show a maximum variation in specific interaction coefficients for a given test compound on duplicate asphalt samples of three I_g units. This is within the normal variation on duplicate runs of the same sample. The preliminary indication is that the technique gives reproducible results.

SUMMARY AND CONCLUSIONS

Silylation of an asphalt within an IGLC column offers a convenient means to study asphalt functionality. More specifically, the reagent, BSA, reacts with most of the phenolic and carboxylic acid hydroxyl groups present in either as-received or column-oxidized asphalts. Comparison of infrared spectra before and after silylation substantiates this conclusion.

Silylation reduces the phenol and propionic acid I_g values on both oxidized and unoxidized asphalts to a common value characteristic for each individual test compound. This results from the blocking of the carboxylic acid and phenolic OH groups in the asphalts. These groups are believed to be the ones by which phenol and propionic acid differentiate among asphalts. The functional groups which interact strongly with formamide remain after silylation. These groups appear to be carbonyl functions.

The silylation technique should be applicable to investigations of the chemical structure of macromolecules and nonvolatile materials.

ACKNOWLEDGMENTS

Technical discussions with Dr. George Bohner of the Denver Research Institute are gratefully acknowledged.

Work presented in this paper was done under a cooperative agreement between the Bureau of Mines, U.S. Department of the Interior and the University of Wyoming.

LITERATURE CITED

1. T. C. Davis, J. C. Petersen, and W. E. Haines, *Anal. Chem.*, **38**, 241 (1966).
2. T. C. Davis and J. C. Petersen, Highway Res. Rec. No. 134, Highway Research Board, National Research Council, 1 (1966).
3. T. C. Davis and J. C. Petersen, *Anal. Chem.*, **38**, 1938 (1966).
4. T. C. Davis and J. C. Petersen, *Proc. Assoc. Asphalt Paving Technologists*, **36**, 1 (1967).
5. T. C. Davis and J. C. Petersen, *Anal. Chem.*, **39**, 1852 (1967).
6. G. G. Esposito, *Ibid.*, **40**, 1902 (1968).

7. J. Bohemen, S. H. Langer, R. H. Perrett, and J. H. Purnell, *J. Chem. Soc.*, 1960, 2444.
8. D. T. Sawyer and J. K. Barr, *Anal. Chem.*, 34, 1518 (1962).
9. R. H. Perrett and J. H. Purnell, *J. Chromatog.*, 7, 455 (1962).
10. R. A. Dewar and V. E. Maier, *Ibid.*, 11, 295 (1963).
11. W. E. Haines, *Proc. Amer. Petrol. Inst., Sect. VIII*, 42 (8) 51 (1962).
12. F. N. Hveem, E. Zube, and J. Skog, *ASTM Special Technical Publication No. 277*, 3 (1959)
13. P. G. Campbell and J. R. Wright, *J. Res. Nat. Bur. Stand.*, 68C, 115 (1964).
14. J. Novák and J. Janák, *Anal. Chem.*, 38, 265 (1966).
15. J. C. Petersen, *Fuel*, 46, 295 (1967).

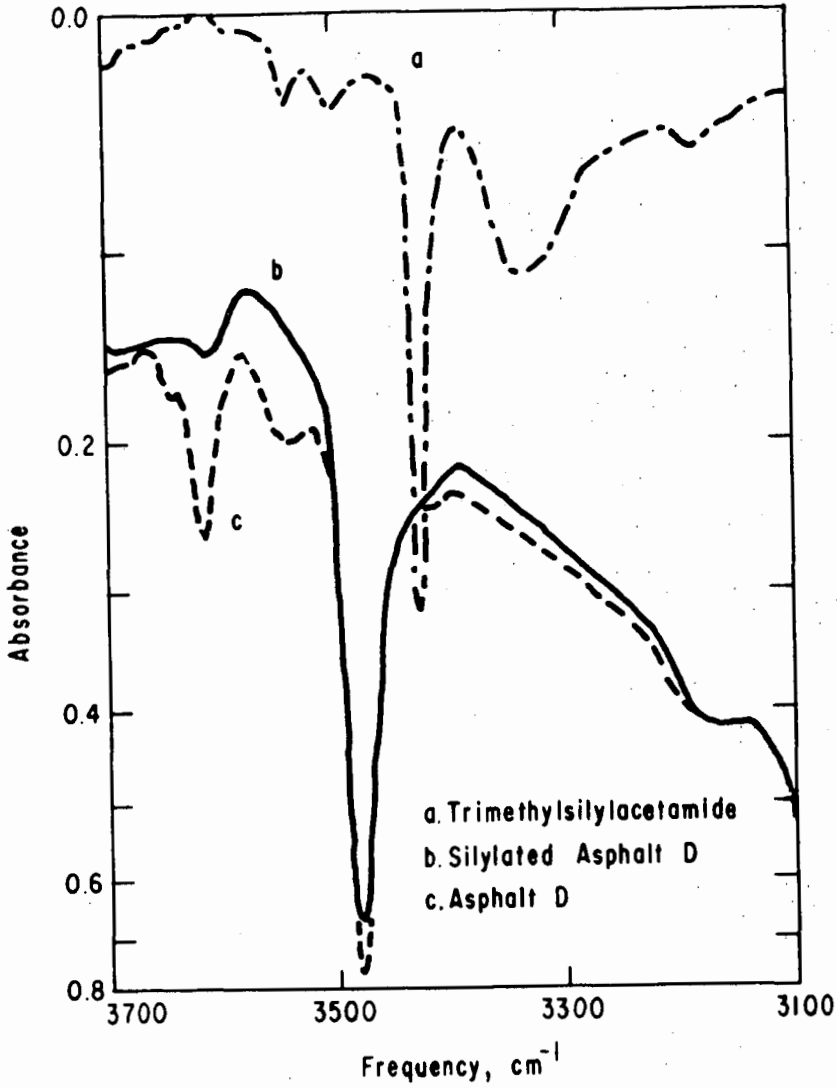


Figure 1. Infrared Spectra of Trimethylsilylacetamide, Silylated Asphalt D, and Asphalt D

KINETICS OF HYDRAZINIUM DIPERCHLORATE THERMAL DECOMPOSITION BY FLASH MASS THERMAL ANALYSIS*

J. A. Hammond, Yuji A. Tajima, W. Glenn Stapleton, W. E. Baumgartner

Lockheed Propulsion Company, Redlands, California

1. INTRODUCTION

The kinetic mechanisms of decomposition of propellant ingredients are of vital interest to the propellant chemist when it becomes necessary to forecast propellant thermal stability and shelflife, to determine the ignition and combustion kinetics of the propellant, and to predict the sensitivity of the propellant to impact (shock) or frictional forces. In each case, the energetics and mechanism of the initiation step, and the products formed thereby are important. These parameters are not easily obtained by most experimental techniques for measuring reaction kinetics.

2. BACKGROUND

Unique techniques for determining the energetics and kinetics of the initiating reaction which occur during pyrolysis of solid propellant ingredients have been developed. These techniques involve the use of very small samples coated on a platinum ribbon heater/thermometer mounted in close proximity to the electron beam of a Bendix Time-of-Flight (TOF) mass spectrometer. Heating of the sample by capacitor or battery discharge was synchronized with the TOF analysis cycles. These techniques afford several distinct advantages in the study of thermal decompositions:

- o The vacuum essential to operation of the TOF assures identification of the primary decomposition species.

- o A very small amount (5-10 micrograms) of sample is applied as a thin coating on a comparatively large mass of supporting ribbon, assuring close compliance of the sample temperature to the ribbon temperature at all times.

- o The inclusion of the platinum ribbon in a resistance bridge circuit so that it acts as its own thermometer to eliminate errors in temperature measurement associated with external measuring systems, i.e., emittance values for optical pyrometry, large heat sink and thermal lag of attached thermocouples or other heat-sensing devices.

- o Method sensitivity, resolution, wide response range, allows continuous separation and analysis of decomposition species at widely different reaction rates.

* This work was supported by Air Force Contract AF04(611)11385, from Air Force Rocket Propulsion Laboratory, Research and Technology Division, Edwards, California, Air Force Systems Command, United States Air Force.

o The very rapid (3×10^7 °C/sec.) heating rate attainable with the capacitor discharge permits stepwise isothermal analysis of the sample decomposition at the desired pyrolysis temperature. This is essential for determining induction times to explosion, similar to Wenograd's method (Ref. 1). This method is called Isothermal Flash Mass Thermal Analysis (or Isothermal FMTA).

o The less rapid heating rates (10-1000 °C/sec.) attainable over longer times (linear up to 2 sec. at 100 °C/sec.) permit study of reactions which control the stability/shelflife of the material or propellants, as well as of the reactions which occur in the thermal wave zone at the surface of a burning propellant. All quantities measured by this system are mathematically differentials so that many factors may be derived without extensive, tedious, and possibly inapplicable calibration procedures. This method is called Dynamic FMTA.

o Reaction mechanisms can be inferred from the order of appearance and temperature of appearance of the various pyrolysis species.

These techniques were originated in 1962 for the study of the phenomena which occur in the fizz zone of a burning propellant when the temperature rises from that of the bulk of propellant (~ 300 °K) to that of the flame (up to 3000°K), within a distance of approximately 1 millimeter, creating high temperature and concentration gradients. Subsequently, and with some modification, this technique has provided an equally powerful tool for elucidating the decomposition mechanisms and energetics of high energy binders and oxidizer pyrolyses at heating rates in the range of 100 to 200 °C/sec. Data acquisition, as well as data reduction techniques, have been developed which are necessary to elucidate the detailed decomposition reactions for the primary products under a broad range of experimental conditions (e.g., heating rates). Mathematical models have been developed which have been used in conjunction with a computer to establish the temperature across the sample area on the platinum ribbon heater. A mathematical technique has been developed which takes advantage of the unique differential data acquisition mode during dynamic FMTA to derive reaction activation energies, and eventually, the absolute reaction rates.

3. EXPERIMENTAL TECHNIQUES

Thermal decomposition rates of propellants/propellant ingredients can be very high. The instruments and techniques used to study the pyrolysis of these compounds should, therefore, be capable of acquiring data at rates characteristic of the processes. The mass thermal analytical technique developed for such investigations utilizes the fast scan speed of the Bendix TOF mass spectrometer. The sample, weighing 5 to 20 micrograms, is coated on a resistive platinum ribbon which is located 2 millimeters from the ionizing electron beam of the mass spectrometer. The ribbon and sample is heated by means of a battery discharge for slow heating rates or a capacitor discharge for fast heating rates. The ribbon forms one arm of a Wheatstone bridge, by means of which the temperature-time profile of the ribbon and sample is determined. For heating rates in the range of 10 to 1000 °C/sec., the mass spectra displayed on an oscilloscope are monitored continuously by fast cinematography. The experimental arrangement is shown schematically in Figure 1.

a. The Bendix Time-of-Flight Mass Spectrometer (TOF)

The TOF instrument consists basically of three sections: the ionization chamber, the flight tube, and the detector multiplier. In the normal mode of operation, ions are produced by a beam of electrons of controlled energy every 50 to 100 microseconds. (A 100 microsecond cycle can be easily achieved). Immediately after the electron pulse, voltage pulses are applied which accelerate the positive ions with identical kinetic energies per unit charge into the flight tube. Because the flight tube is field-free, the ions travel at velocities proportional to $\sqrt{e/m}$ (e and m are charge and mass, respectively) and thus arrive at the detector at different times. The detector multiplies the signal resulting from each group of ions with given arrival times, yielding an intensity--arrival time (m/e) spectrum of the ions produced in the ionization chamber. When the voltage and electron pulses are applied every 100 microseconds, a complete spectrum (in the m/e range of interest here) is obtained every 100 microseconds.

Mass resolution of the Bendix is such that no more than a 1 percent peak height contribution exists between adjacent peaks (one mass unit apart) in the Hg spectrum at m/e of 200.

b. The Sample Holder

To achieve high heating rates, it is essential that the sample holder be of low mass (low heat content). Since it is desirable to electrically heat the sample, the geometry must be such as to ensure a reasonable electrical resistance for ohmic heating. The sample holder must also be constructed of a relatively non-reactive metal. All these constraints dictated the use of a platinum ribbon sample holder. The wide, flat ribbon (15 by 1.02 by 0.025 mm) permits distribution of the small sample over a large area, resulting in a very thin film which ensures good thermal contact and close compliance of sample temperature to the ribbon temperature.

A Bendix Direct Inlet Probe, Model 843A, which permits access to the mass spectrometer ionization chamber by means of a pumped vacuum lock, was adapted to support the platinum ribbon which bears the sample. The arrangement is shown in Figure 2. When the probe is positioned in the mass spectrometer, the sample is approximately 2 millimeters from the ionizing electron beam. This arrangement results in a higher intensity spectrum than would be possible for a system in which the sample was located at greater distances from the electron beam. Also, products which are shortlived may be detected before they decay to secondary species.

The ionization chamber is cryogenically pumped with two specially designed liquid nitrogen cold traps. Their function is two-fold; (a) the residual H₂O background is reduced to practically zero and (b) pyrolysis products which escape from the ionization region are trapped before they can rebound from the walls and reenter the ionization region. This insures that most of the products which are being analyzed are detected while in a high energy state and have not collided with sampling system walls.

c. Sample Heating System

In these experiments, the sample may be heated in two different modes: (a) flash heating (3×10^7 °C/sec.) to an isothermal condition and (b) a slower temperature rate of increase which has been varied from 100-200 °C/sec. In either case, the platinum filament constitutes one arm of a Wheatstone bridge. Just prior to each sample run, the bridge is nulled. As the ribbon is heated, its resistance changes and the bridge becomes unbalanced. The output signal of the bridge is fed to an oscilloscope and recorded photographically. The circuit diagram is presented in Figure 3.

The heating of the ribbon during Dynamic FMTA is produced by a 24-volt battery connected in series with the bridge. The rate of heating may be varied with a rheostat also in series with the bridge. This is the only method which was used for the work reported herein.

Flash heating of the sample to an isothermal condition for Isothermal FMTA is accomplished by discharging a high voltage from a capacitor through the platinum ribbon. The capacitor is charged by the hydrogen thyratron. A constant low voltage from a 24-volt battery serves as the bridge power supply which enables the temperature to be measured after the current surge from the capacitor has subsided. The duration of the capacitor discharge is less than 10 microseconds. As in the dynamic FMTA, the bridge output is fed to an oscilloscope and is recorded photographically.

In both modes, the resistance of the platinum ribbon is calculated from the well-known Wheatstone bridge relationships, using the bridge imbalance potential at selected time intervals. The temperature at each time is then derived from the known resistance-temperature behavior of the platinum ribbon.

d. Data Recording Techniques

Time-of-flight mass spectrometry lends itself well to fast pyrolysis studies because of its rapid sampling rate (10 KHz) over the spectrum of 12 to 250 mass units. This rapid rate permits the use of very small samples and small heat sources which characteristically possess low heat capacities and therefore require less energy for a given temperature increase.

Rapid analysis coupled with extremely short periods in which the pyrolysis products are available for detection present some stringent requirements for recording data. In these experiments, the time range of interest may be as short as a hundred microseconds or, at most, two seconds. Obviously, the data must be recorded photographically from an oscilloscope trace.

For the dynamic FMTA, a Milliken DBM-5C high speed framing camera was employed to photograph the spectrum oscilloscope trace at a speed of 200 frames/second or 1 frame each five milliseconds. In general, the nominal heating rate was 100 °C/sec. With the small sample, the pyrolysis event was usually completed within two seconds. To synchronize the temperature trace oscilloscope with the spectrum displayed on the oscilloscope, a flashlamp was triggered simultaneously with the beginning of current input to the ribbon. The flash overexposes the first few frames

of the spectrum, thereby marking the beginning of the heating. The same trigger pulse that fires the flashlamp is also used to trigger the sweep of the temperature trace oscilloscope. Since the mass spectrograph operates continuously at 100 microsecond intervals, the experiment may be begun at any time without an error in time of greater than 100 microseconds. This presents no serious error in time or temperature for experiments lasting one second; covering 10,000 complete spectra. The mass spectra, from $m/e = 12$ to $m/e = 250$ are continuously displayed on another oscilloscope. This trace is photographed by a camera operating at 200 frames per second, so that data is recorded at five millisecond intervals. This is sufficiently fast to permit accurately following the species formed in reactions induced by heating at rates from 100 to 200°C/sec. In this heating rate range, the rate of temperature rise is 0.1 to 0.2°C/millisecond, which corresponds to 0.01 to 0.02°C/complete mass spectrum trace or to 0.5 to 1.0°C/frame of film. Therefore, errors in temperature correlation, induced by one or several frame uncertainty for the start of the experiment would introduce an error no greater than that involved in the initial (zero time) sample temperature measurement.

e. Sample Preparation

A critical step in this analysis technique is insuring that the sample is uniformly distributed over the surface of the pyrolyzing heat source. From the standpoint of heat transfer to the sample source heat capacity and low pressure requirement of the mass spectrometer vacuum the sample must be on the order of 5-20 micrograms to achieve the best results. Samples of solid oxidizers or fuels have been dissolved in suitable solvents and deposited on the center 0.5 centimeter of the platinum ribbon in a dry box. For example, HP_2 is applied to the surface as a uniform film of a known concentration in dry methyl alcohol by means of a micro syringe, and the solvent allowed to evaporate. The sample is then transferred, in a dry bag, to either the mass spectrometer or to a bell jar and subjected to vacuum for 2 to 20 hours to remove the last traces of solvent. The sample, on the ribbon and holder, is then affixed to a probe, inserted into position inside the mass spectrometer through the vacuum lock. The sample is then heated by the battery discharge for dynamic FMTA.

4. DATA REDUCTION AND ANALYSIS

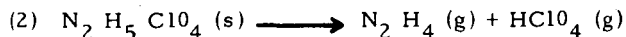
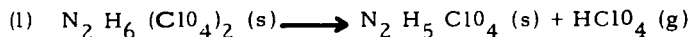
a. Hydrazinium Diperchlorate (HP_2) Decomposition

The technique has been termed Dynamic Flash Mass Thermal Analysis (or Dynamic FMTA, for short). This terminology arises by analogy to thermal methods of analysis already in use, especially thermogravimetric analysis (TGA) techniques which it most closely resembles. There are two basic modes of operation. The first mode utilizes linearly programmed heating combined with continuous analysis by the mass spectrometer, and thus is analogous to dynamic TGA. The second mode uses an extremely fast heating to an isothermal condition, and thus resembles isothermal TGA. Since the heating rates in either mode are extremely rapid compared to those in common use, the heating mode is analogous to "flash" heating by other means. Therefore, the first and second modes are aptly described as Dynamic FMTA, and Isothermal FMTA, respectively. The dynamic FMTA method has been used to study the decomposition mechanisms and energetics of HP_2 and NC, and to establish the validity of the technique.

This method also closely resembles the Differential Thermal Analysis (DTA) or Differential Scanning Calorimetry (DSC) techniques as regards linearly programmed sample heating rates and data evaluation, except that the data represent analytical time resolved mass spectra data instead of integrated caloric/thermal data, and a considerably faster instrument response time is provided by using high speed cinematography of the scope display rather than recorders (as in DTA).

The films taken of the mass spectral traces are analyzed frame-by-frame for the order of appearance of species, and the parent species deduced from structural considerations and comparison with standard mass spectra (when available). Figure 4 shows a typical sequence for HP_2 .

It is expected that the key species in the initiation reaction(s) for thermal decomposition can be those which are attached to the molecule with the weakest bonds, and hence appear first (at low temperatures) in the films of the mass spectra. Several of the key species are selected, and their spectral intensities are plotted as a function of time (and/or temperature), as in Figure 5, to facilitate deduction of the pyrolysis mechanism. The data are consistent with the mechanisms postulated by Grelecki and Cruice (Ref. 2) and by Levy, Von Elbe, Friedman, Wallin and Adams (Ref. 3):



The first peak in the time/intensity plot is definitely due only to HClO_4 , corresponding to equation (1), whereas the second peak has definite contributions from both N_2H_4 and HClO_4 .

To be able to extrapolate the data obtained at one temperature and reaction rate to another temperature, e. g., shelflife prediction, combustion rates, etc., it is necessary to derive the activation energies and preexponential factors for the reactions. Fortunately, for the determination of the activation energy (E), absolute reaction rate data are not required, but only the shape of the curve and the slope which can be derived therefrom. In the uncalibrated mass spectrometer, the line intensity, I, of a given species is related to its partial pressure, P, in the ion chamber in an unknown but constant proportion during any particular experiment. P, in turn, is proportional to the difference between the rate of generation of a species and the rate at which it is removed by pumping and by injection into the flight tube as ions. The difference is also an unknown but constant factor during any given experiment.

Method I

If the rate of generation of a species can be represented by the Arrhenius rate expression as a first order reaction, then:

$$I \propto P \propto (1/x) (dx/dt) = k = A \exp. (-E/RT)$$

or

$$I = B \exp. (-E/RT)$$

Wherein B contains the Arrhenius frequency factor, A, the mass spectrometer system constants, and the fraction, x, of a given species which remains unreactive at any given time. Consideration of x as constant over a small time or temperature interval introduces only a small error in calculating E, since it is the fraction reacted which is important in this case, and not the absolute quantity. Taking the logarithm of the function yields:

$$2.303 \log I = -E/RT + 2.303 \log B$$

A plot of $\log I$ versus $1/T$ should yield a straight line with a slope of $-E/(2.303R)$. The intercept at $\log I = 0$ will yield a value of $\log B$ which may be of value later to evaluate A, specific reaction rates, and mass spectrometer system constants.

Method II

For complete definition of the reaction kinetics, the value of the reaction rate, reaction rate constant, or pre-exponential factor must be determined as well as the activation energy. The rate of disappearance of reactant, hence rate of appearance of products, during a first order reaction is given by:

$$dx/dt = kx$$

or:

$$(1/x)(dx/dt) = k$$

which is mathematically identical to:

$$d(\ln x)/dt = k \text{ (where } \ln \text{ refers to natural logarithms)}$$

on integration between limits:

$$\ln x_2 - \ln x_1 = \ln (x_2/x_1) = k (t_2 - t_1)$$

Since the ratio x_2/x_1 is the same whether x is an absolute value or a fraction of the absolute value, the above rate expressions are likewise indifferent to the way in which x is expressed. This fact, together with the differential nature of the analytical technique provides the key whereby the absolute reaction rates and pre-exponential factors may be derived from the data taken by the uncalibrated system. The total area enclosed by the intensity/time curve for a given mass species represents the total quantity of that species which was formed as the result of the reaction. Any portion of the total area, taken at a definite time, then represents a definite fraction of the quantity of that species which has been formed. The total area, and suitable fractions thereof, taken at short time intervals during the initial stages of the reaction, can be replotted as $\ln x$ versus time. Since each time corresponds to a definite temperature, the slopes of the plot, taken at several times, correspond to values of the absolute reaction rate constant, k , taken at several temperatures. The $\ln k$ can then be plotted against reciprocal absolute temperature in the conventional manner, and both the activation energy and the pre-exponential factor, A , determined routinely.

It is expected that the activation energy for the thermal decomposition reaction of a compound will reflect the activation energy of the primary decomposition species. Therefore, the Arrhenius plots of the first detected species in the HP_2 decomposition calculated by Method I are presented in Figure 6. There are two distinct regimes - the first, "low temperature" regime (labeled "A" on the graphs) is driven solely by the energy input from the platinum ribbon, while the second, "high temperature" regime (labeled "B" on the graphs) is one in which autoacceleration of the reaction occurs.

Work on HP_2 was performed at Thiokol's Reaction Motors Division (RMD) (Ref. 2), using time-to-acceleration techniques with a closed vessel. This technique yields the activation energy for a reaction which occurs before autoacceleration - which corresponds to the "A" regime. The data as presented in Figure 6 for the "A" regime yields a value of 23 Kcal/mole, which compares remarkably well with the value of 23.5 Kcal/mole obtained at RMD. Thus, the validity of the experimental and data reduction techniques is established. The activation energy and frequency factor determined from the more detailed data treatment of Method II are given in Table I. It should be noted that the activation energy is determined from the first $\frac{1}{2}\%$ decomposition, and very small errors in the determination of the fractional areas will yield large errors in the value of the activation energy. Other large errors can be introduced when small errors are made in selecting the slopes from the curves of fraction reacted versus time (from which the reaction rate constant, k , is obtained). The slopes are very sensitive to the way in which the curves are drawn, and to personal judgment in estimating the tangent line. Under these circumstances, the agreement of the two sets of data is encouraging. Future determinations will be made with much more care over the first one to two percent of the decomposition in order to improve the accuracy of the results.

When the activation energy of 23 Kcal/mole is used with the absolute rate constants obtained in the detailed treatment, the Arrhenius factor is found to be $(5 \pm 2) \times 10^{13} \text{ sec.}^{-1}$, which is a reasonable value for these types of reactions.

It is of interest to note that the vacuum conditions prevailing in these experiments precludes the acceleration of the reaction by reaction products, so that another explanation for the observed acceleration must be sought. The experimental results show that the activation energy for the initial step changes from 23 Kcal per mole during the pre-acceleratory period to 86 Kcal per mole during acceleration. This means that the acceleration of the reaction (rate of change in reaction rate due to one degree centigrade temperature rise) is more than 12 times as great for the portion with the 86 Kcal/mole activation energy as for the portion with the 23 Kcal/mole activation energy.

b. Hydrazinium Monoperchlorate (HP) Sublimation

The postulated decomposition mechanism, chemical equations (1) and (2) suggests the possibility of also obtaining the heat of sublimation of HP from the FMTA data. Since N_2H_4 is characteristic of HP only, then the heat of sublimation should be found by applying the Clausius-Clapeyron equation to the $m/e = 23$ ion species ($N_2H_3^+$). The previous arguments regarding mass spectrometer system constants apply to this determination as well. The integrated form of the Clausius-Clapeyron equation is:

$$-\ln I \propto -\ln P = \left(\frac{\Delta H_{\text{sub.}}}{R} \right) \left(\frac{1}{T} \right) + \text{constant}$$

As before, the pressure ratios are equivalent to the intensity ratios, so that a plot of $\ln I$ versus $1/T$ will yield a straight line with slope equal to $-\Delta H_{\text{sub.}}/R$. From this plot, shown in Figure 7, the heat of sublimation, $\Delta H_{\text{sub.}}$, is calculated to be 32 Kcal/mole. This compares very well with the value of 29.2 Kcal/mole determined by Levy et alii (Ref. 3), using an equilibrium vacuum sublimation technique.

5. CONCLUSIONS

The FMTA technique has been shown to be a powerful tool for the investigation of thermal decomposition of solid materials since the reaction mechanisms and kinetic rate data can be obtained from a single experiment. In some cases, kinetic data (e.g., Arrhenius frequency factors) and primary decomposition species can be obtained by no other current technique. The results of the FMTA technique do not depend upon tedious, unreliable, and repeated mass spectrometric calibration procedures, therefore many more useful experiments can be performed with equipment previously considered unsuitable for quantitative measurements.

BIBLIOGRAPHY

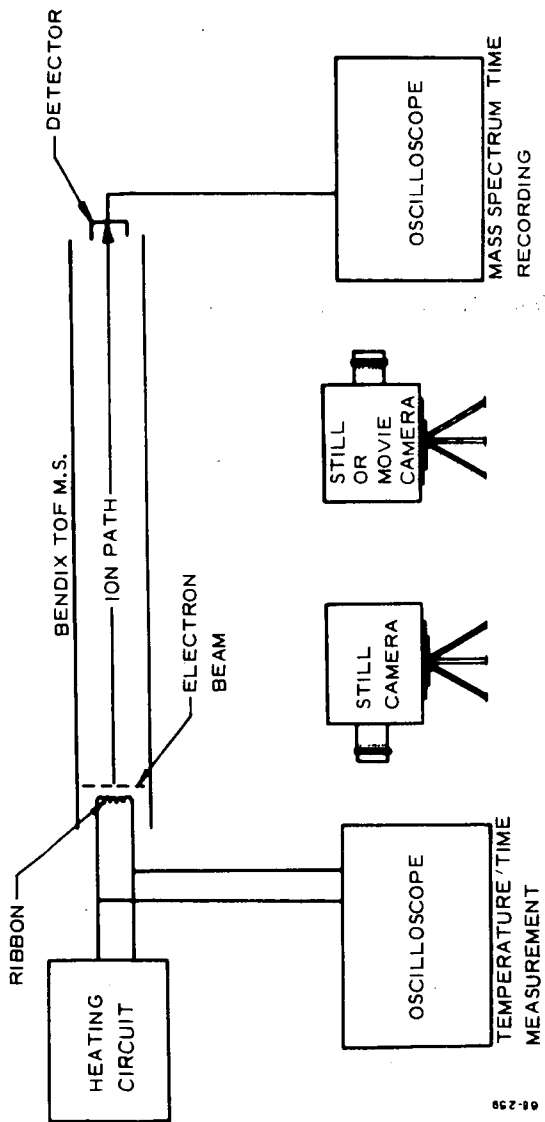
1. J. Wenograd, "The Behavior of Explosives at Very High Temperatures", U.S. NOL, NAVWEPS Report 7328, Oct. 1960
2. C. J. Grelecki, W. Cruice, "Thermal Decomposition of Hydrazinium Monoperchlorate and Hydrazinium Diperchlorate", pp 73-81, in Advanced Propellant Chemistry, Advances in Chemistry Series 54, American Chemistry Society, Washington, D. C. (1966)
3. J. B. Levy, G. Von Elbe, R. Friedman, T. Wallin, S. J. Adams, "The Deflagration of Hydrazine Perchlorate", pp 55-72, *ibid.*

TABLE I
ENERGIES FOR HP₂ THERMAL EVENTS

<u>Species</u>	<u>m/e</u>	Decomposition Activation Energies (Kcal/mole)		
		<u>This Work</u>		<u>(Ref. 2)</u>
		<u>A</u>	<u>B</u>	
HClO ₄ ⁺ (parent)	100	23	86	23.5

HP HEAT OF SUBLIMATION (Kcal/mole)

<u>Species</u>	<u>This Work</u>	<u>(Ref. 3)</u>
N ₂ H ₃ ⁺ (from N ₂ H ₄)	32	29.2



9-23

Figure 1 MTA Experiment Schematic

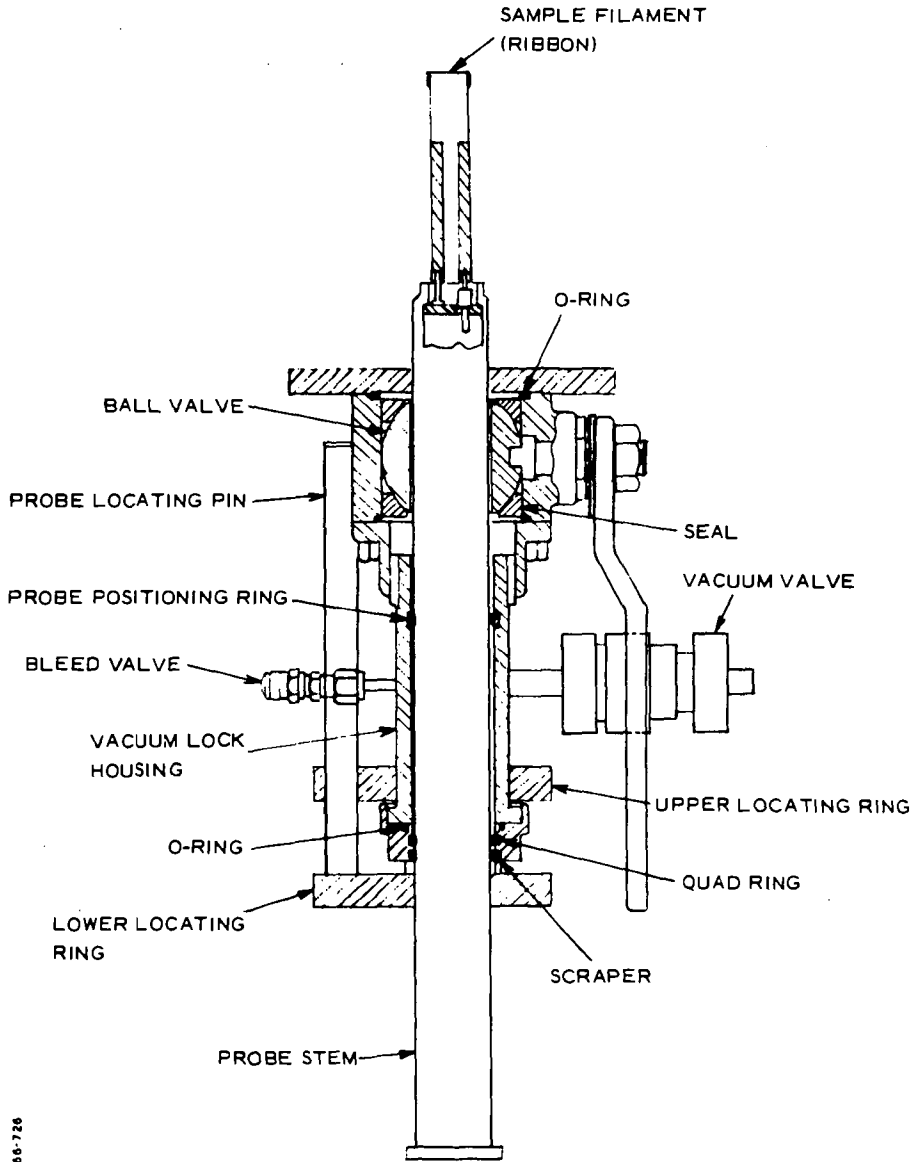


Figure 2 Bendix Direct Inlet Sample Probe

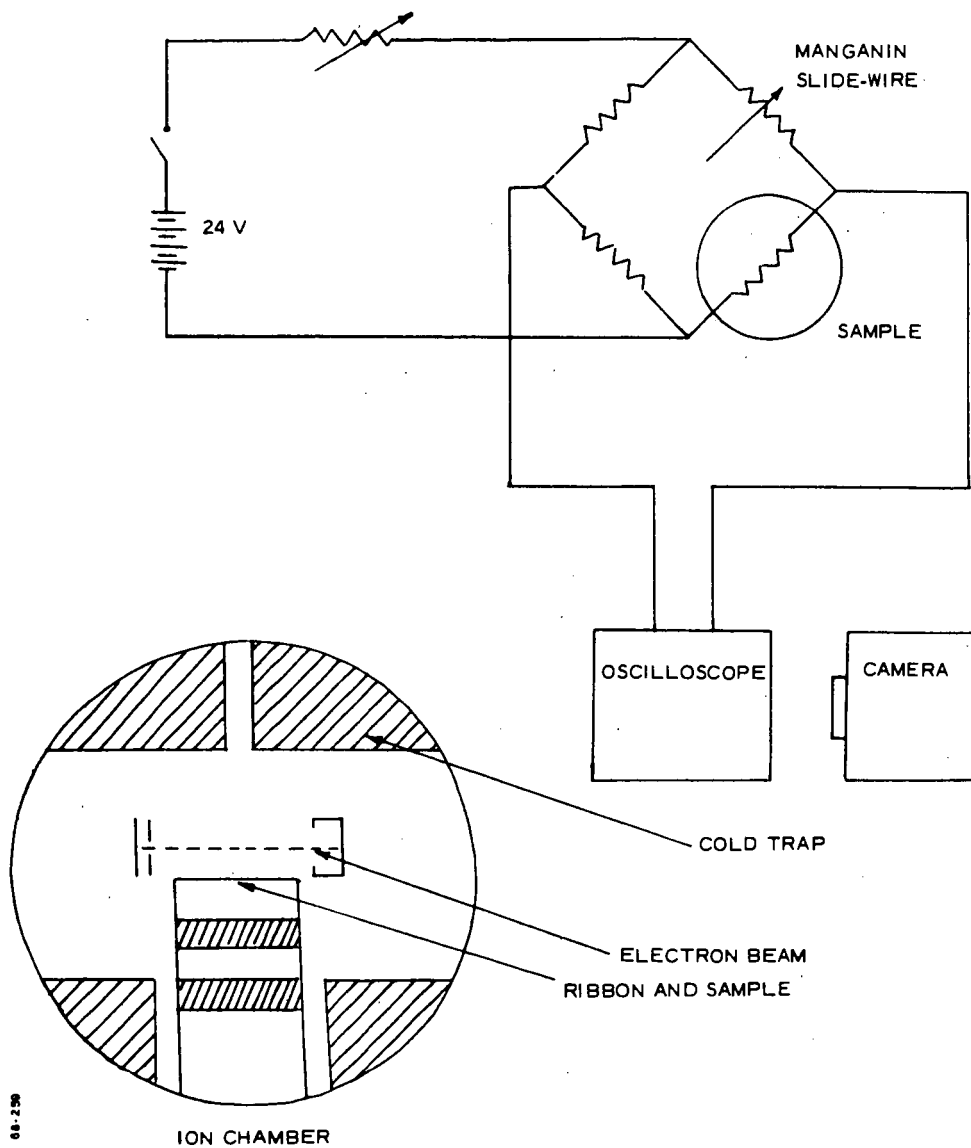


Figure 3 Dynamic FMTA Schematic

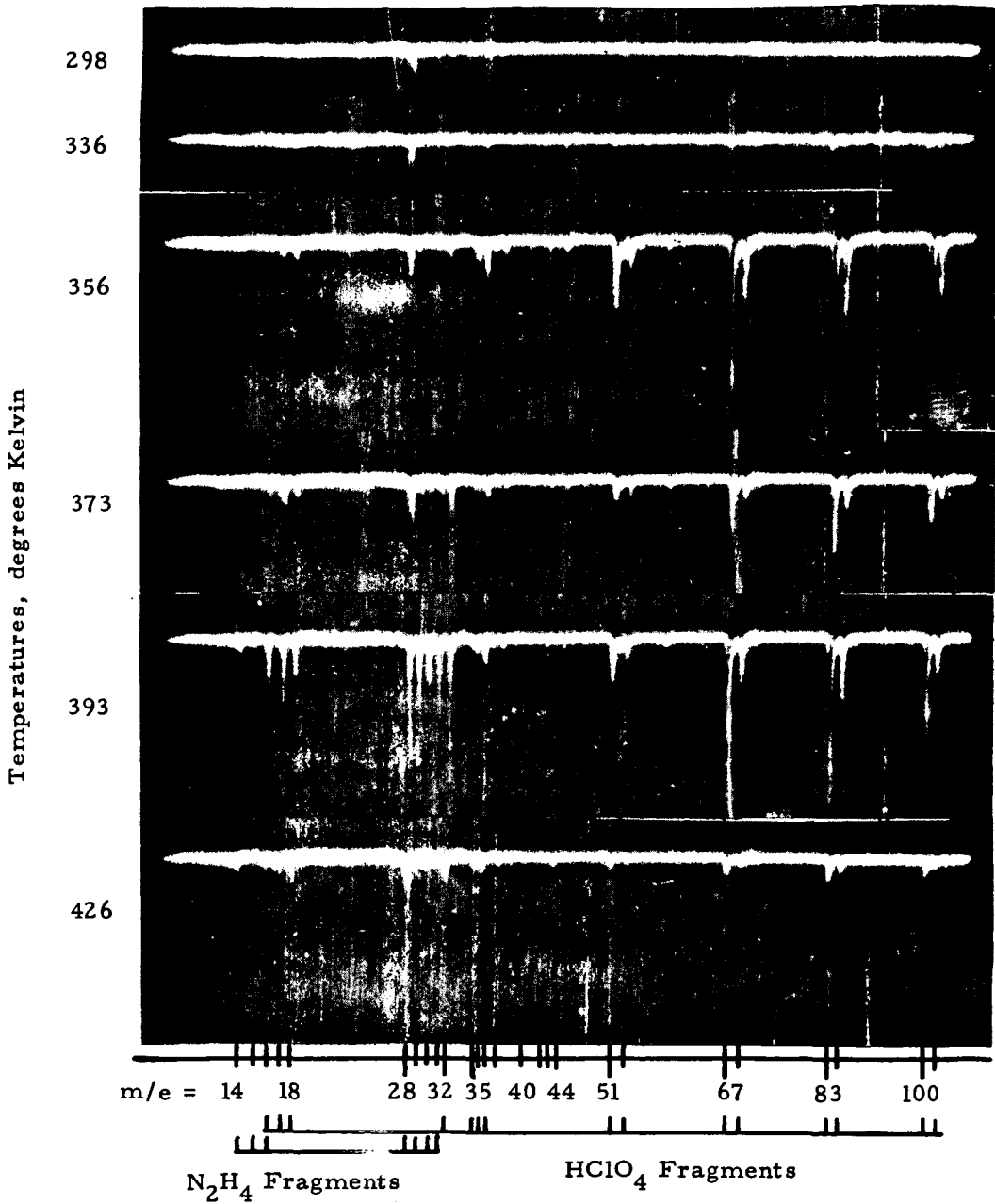


Figure 4 Mass Spectra from FMTA of HP_2

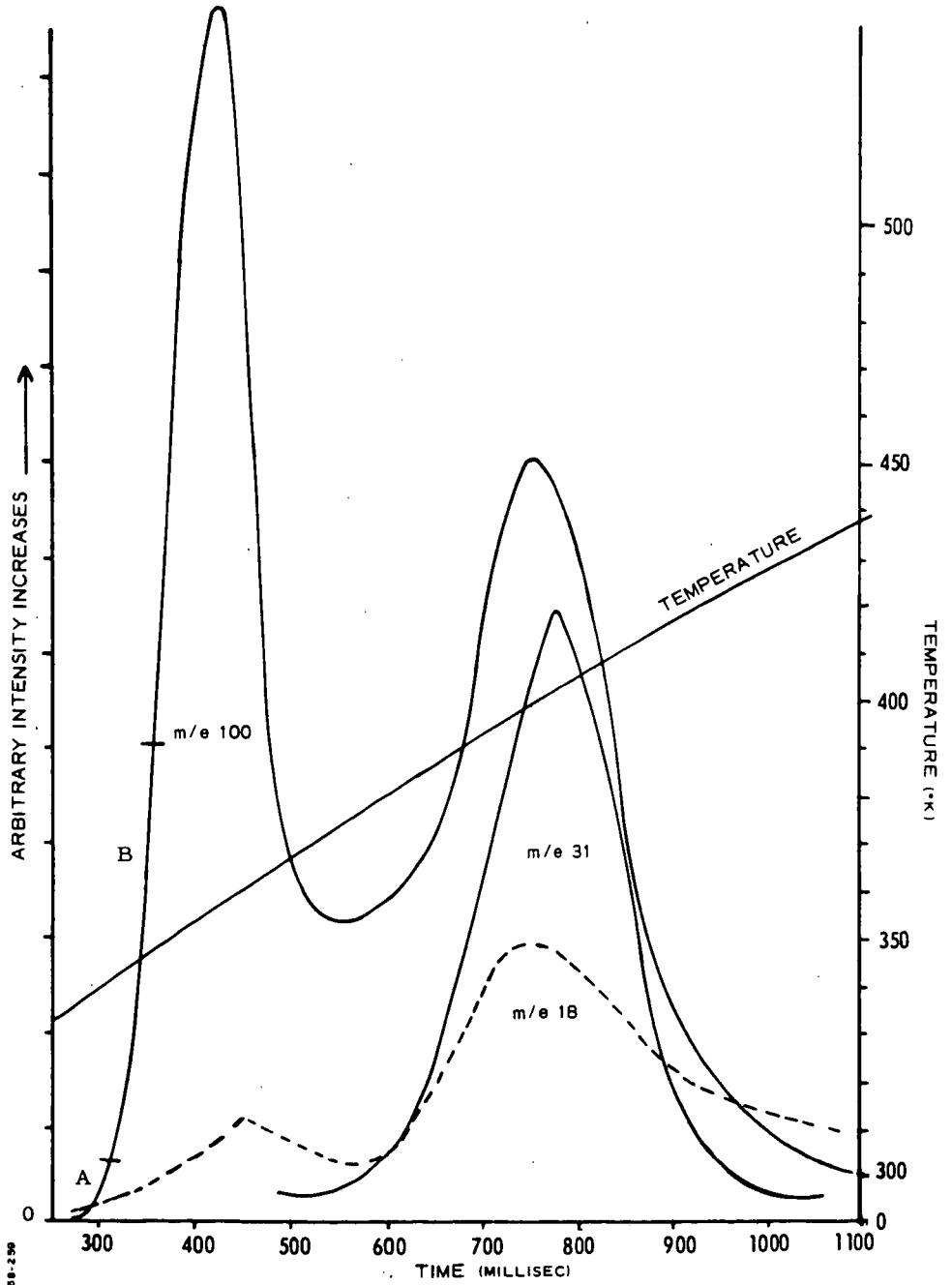


Figure 5 HP_2 Pyrolysis Fragment Histories

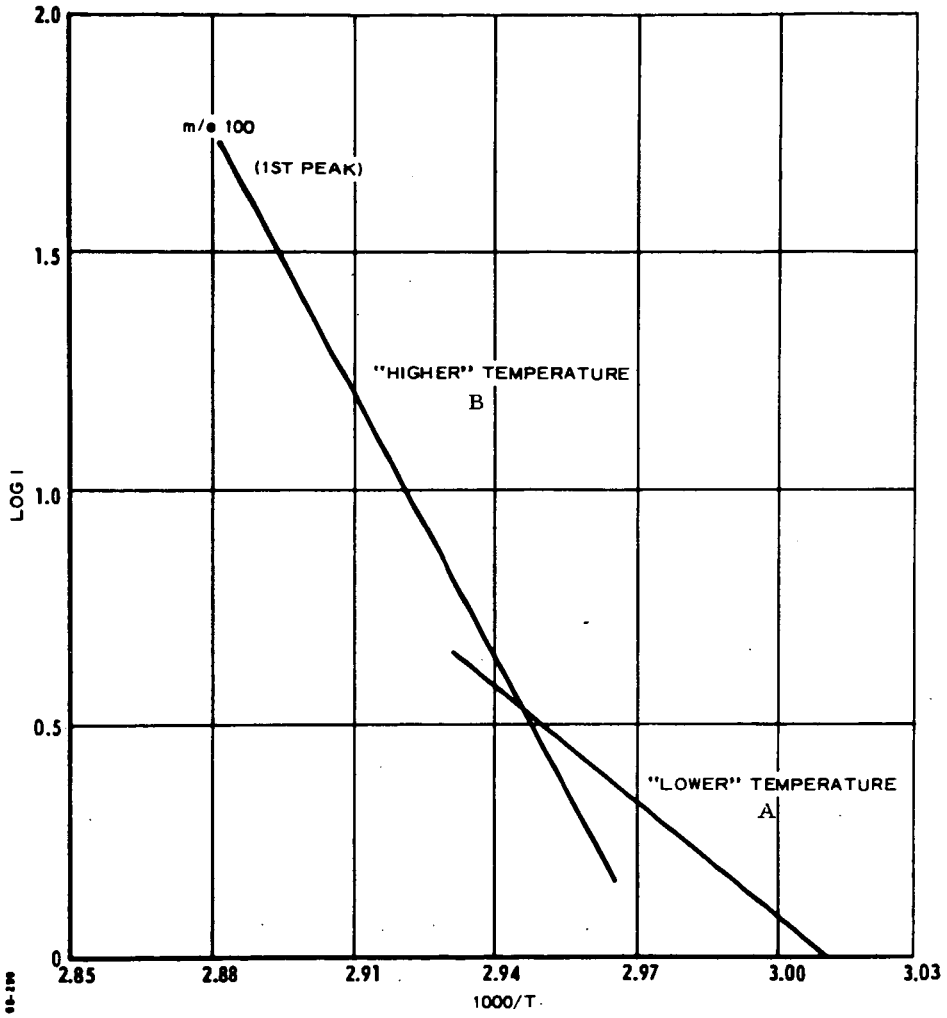


Figure 6 Arrhenius Plot of HClO_4^+ from Flash MTA of HP_2

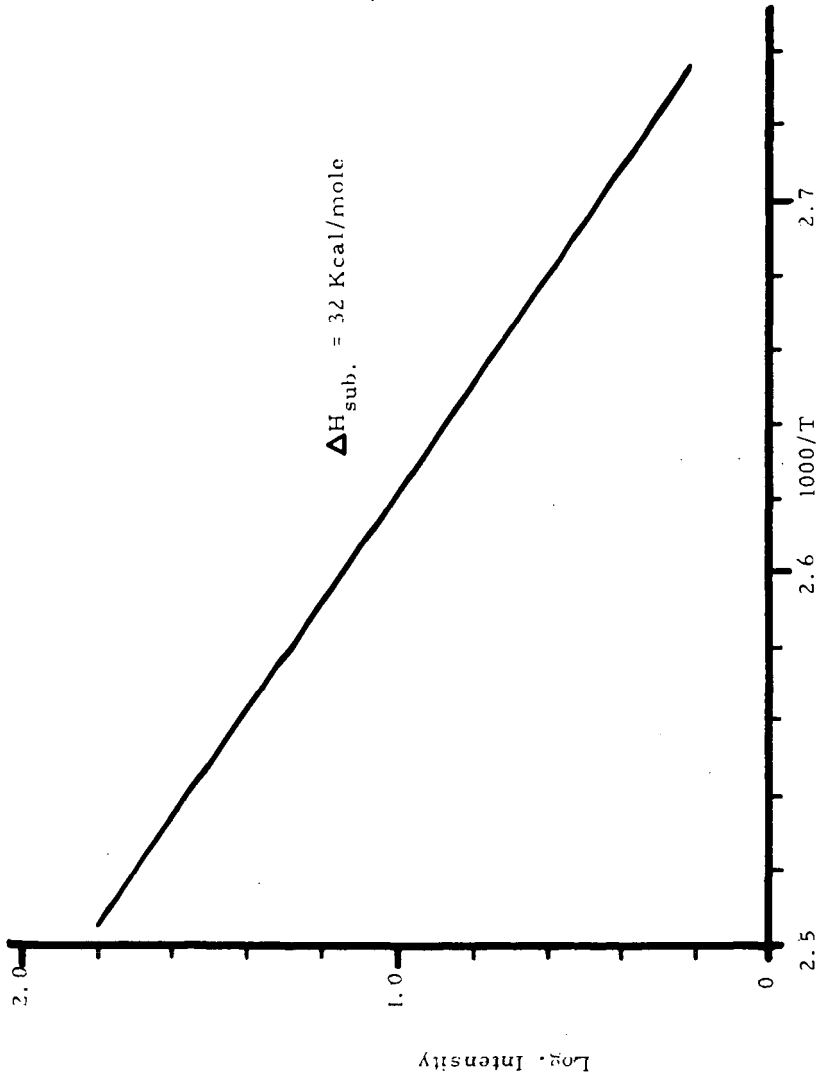


Figure 7 Clausius-Clapeyron Plot for HP Sublimation

HYDROCRACKING OF COAL AND PETROLEUM OILS

S. A. Qader and G. R. Hill

Department of Mineral Engineering

University of Utah, Salt Lake City, Utah 84112.

Abstract

Hydrocracking of coal-based oils needs higher hydrogen pressure when compared to petroleum oils and both types of oils affect almost similar naphtha yields of 77 to 80% at a pressure of 2000 p.s.i. and 500°C. Coal-based oils produce naphtha of superior quality but with higher hydrogen consumption. At about 80% yield, naphtha from coal oil had a clear research octane number of 88 with a hydrogen consumption of about 1550 cu. ft. per barrel of feed, whereas the product from gas oil has an octane number of 78 with a hydrogen consumption of only about 1125 cu. ft. Both types of oils exhibited similar kinetic behavior with activation energies ranging from 14,000 to 16,000 cal./mole. The hydrocracking of coal-based and petroleum oils must be preceded by the hydrorefining of the feed stocks to ensure low coke yield and longer catalyst life. The disadvantages associated with the processing of coal-based oils can be offset by the superior quality of their products, thereby affecting the overall processing almost similar to petroleum oils.

Introduction

Hydrocracking is employed in the petroleum industry, in recent years, for the processing of different types of feed stocks (Craig and Forster, 1966; Duir, 1967). It was also applied as a potential method for the refining of coal-derived liquids (Alpert, et al., 1966, Katsobashvili and Elbert,

1966). The hydrocracking of coal-based oils differs to some extent from petroleum oils since the former contain larger quantities of oxygenated compounds and aromatic hydrocarbons. In view of the anticipated shortage of crude petroleum, the petroleum refineries may have to augment their feed stocks with synthetic oils and process them in the existing equipment. The additional oil requirements may be met in the near future from coal liquifaction processes and, hence, it is necessary and useful to understand the fundamental differences that may exist between the refining of petroleum and coal-based oils. Hydrocracking is a versatile processing method and it may be valuable to study and compare the behavior of petroleum and coal-based oils under hydrocracking conditions. The fundamental aspects of hydrocracking of petroleum and coal-based oils are not well understood at the present time though some work was earlier reported mainly on the study of product distributions or catalyst performance (Carpenter, et al., 1963; Archibald, et al., 1960). Some data, however, were reported on the mechanism of hydrocracking of some pure hydrocarbons (Archibald, et al., 1960; Flinn, et al., 1960). In the present communication, the results of hydrocracking of three petroleum fractions and two coal-based oil fractions are reported. A comparison was made between the petroleum and coal-based oils with respect to their behavior under hydrocracking conditions.

Experimental

Materials.

The petroleum fractions were obtained from a mixed base crude oil by atmospheric distillation. The coal oil was obtained from a high volatile bituminous coal by hydrogenation in an entrained bed reactor unit at 2000 p.s.i. pressure and 510°C with stannous chloride as the catalyst. Low

temperature tar was prepared from the same coal in a laboratory oven at 580°C. The coal oil and tar fractions were obtained by distillation of the whole oils, respectively. The hydrorefining catalyst contained 3% cobalt oxide and 12% molybdenum trioxide supported on alumina in the form of pellets of 0.083-inch diameter and 0.125-inch height with a surface area of 210 sq. meters per gram. The hydrocracking catalyst contained 6% nickel sulfide and 19% tungsten disulfide supported on silica-alumina in the form of pellets of 0.083-inch diameter and 0.125-inch height with a surface area of 198 sq. meters per gram.

Equipment.

The hydrocracking unit (Figure 1) contained a vertical tubular stainless steel reactor of 0.75-inch inside diameter and 40-inch length with precision equipment for controlling temperature, pressure, and gas and liquid flow rates. The reactor was heated uniformly by a tubular ceramic furnace of 1.5-inch inside diameter and 38-inch length. The first 20-inch length of the reactor from the top was packed with ceramic beads of 0.17-inch diameter, the next 6.5 inches with the catalyst (60 c-c), and the following 12 inches again with ceramic beads. The temperature of the catalyst bed was maintained constant and the reaction temperature was measured by a thermocouple placed at the center of the catalyst bed. The hydrogen supply was taken from hydrogen tanks. The hydrorefining was also done in the same unit but with the refining catalyst.

Hydrocracking procedure.

The whole system was first flushed with hydrogen to remove air, pressurized, and heated to the reactor temperature. The pressure was then adjusted to the experimental pressure and the oil was fed at the desired rate. The

initial one hour was taken as an offstream period for bringing the reactor and the product recovery system to equilibrium. The hydrogen to oil feed ratio was maintained at about 500. The values of space velocities varied in the range of $\pm 10\%$ and were rounded off. The product was cooled in the condenser and the liquid product was collected in the separator. The gaseous product containing some uncondensed oil was passed through an active carbon tower to adsorb the oil and a gas meter to measure the rate and total volume passed. Several gas samples were withdrawn during each experiment for analysis. The difference in the weight of active carbon before and after the experiment was taken as the amount of uncondensed naphtha. The yield of the liquid product varied between 95 and 100% with an initial boiling point between 50° and 65°C . The yield of gas and each hydrocarbon component of the gas were calculated from the total gas and its composition. The liquid product was distilled and the fraction boiling up to 200°C was designated as naphtha. The fraction boiling up to 100°C was designated as light naphtha and the fraction boiling from 100° to 200°C as heavy naphtha. The hydrorefining was also done in a similar manner at 1500 p.s.i. pressure, 425°C , and 1-space velocity. All the products reported are double-pass products and the product distribution data were obtained at a space velocity of about 0.5. Cumene was hydrocracked over the fresh catalyst and also intermittently during the experimental work to test the activity of the catalyst. The catalyst was either regenerated or replaced by fresh catalyst when the activity with respect to cumene cracking fell by about 5 percentage points.

Coke determination.

The used catalyst was taken out from the reactor and dried at 110°C for two hours to remove moisture and volatile hydrocarbons. Twenty-five grams of

the dried catalyst was packed in a glass tube of 0.5-inch internal diameter and 12-inch length heated to 600°C by a tubular furnace. A stream of air was passed through the tube at the rate of about 15 c.c per minute and the effluent was passed through a furnace containing cupric oxide at 700°C to oxidize carbon monoxide to carbon dioxide, a tower containing Drierite to adsorb any moisture and a tower of Ascarite to adsorb carbon dioxide. The carbon on the catalyst was calculated from the weight of carbon dioxide and reported as coke. The catalyst deposit was not strictly carbon but coke containing both carbon and hydrogen. The coke values reported actually refer to the carbon content of the coke, the latter amounting to about 95% of the former, the remaining being hydrogen.

Product analysis.

All the analyses of the liquid products were done by ASTM and other standard methods and gaseous products by gas chromatographic and mass spectrometric methods (Qader and Hill, 1969).

Results and Discussion

The yield of naphtha from petroleum fractions increased linearly with the reaction temperature. The stove, diesel, and gas oils yielded a maximum of 79, 78, and 77% naphtha at 1500 p.s.i. pressure and 79, 80, and 79% at 2000 p.s.i. pressure and 500°C, respectively. Increasing the reaction pressure from 1500 to 2000 p.s.i. did not change the naphtha yield to any appreciable extent (Figure 2). On the other hand, the naphtha yield from coal-based oils was increased significantly with an increase in the hydrogen pressure. The coal oil and low temperature tar yielded a maximum of 63 and 60% naphtha at 1500 p.s.i. pressure and 79 and 77% at 2000 p.s.i. pressure and 500°C, respectively. The yield of naphtha did not vary linearly with temperature at 1500 p.s.i. pressure while it was linear at a pressure of 2000 p.s.i. The effect was more pronounced at temperatures above 450°C (Figure 3). The results

indicate that the hydrocracking of coal-based oils needs higher hydrogen pressures when compared to the petroleum oils and both types of oils affect almost similar naphtha yields at a pressure of 2000 p.s.i. In case of coal oils, the higher hydrogen pressure is needed for the hydrogenation of aromatic hydrocarbons and the heterocyclic compounds. At pressures of 2000 p.s.i. and above, the petroleum and coal oils exhibit similar behavior under hydrocracking conditions.

The API gravity and the characterization factor of a liquid fuel mainly depend upon its boiling range and the aromatic hydrocarbon content. In case of petroleum oils investigated, the characterization factor increased with a decrease in gravity (Figure 4) which appears to be mainly due to the differences in the boiling ranges of the feed stocks since they have similar composition (Table 1). Though a similar relationship was exhibited by coal-based oils (Figure 4), the factors contributing to such a behavior seem to be different. While the lower gravity of the coal oil when compared to coal tar may be due to the differences in the boiling ranges and aromatic contents of the oils, the high characterization factor of the coal oil does not seem to commensurate with a slight difference in the boiling range and the aromatic hydrocarbons. The characterization factor might have been influenced by the presence of higher concentrations of hydroaromatics in the coal oil. This is further evidenced by the higher naphtha yield from coal oil at 1500 p.s.i. pressure (Figures 5 and 6) where the hydrogenation of aromatics to the corresponding hydroaromatics which undergo subsequent cracking does not occur to any appreciable extent (Qader, et al., 1968). However, hydrogenation of aromatics to the corresponding hydroaromatics does take place at a pressure of 2000 p.s.i., thereby narrowing down the gap between naphtha yields from coal oil

and coal tar fractions as shown in Figures 5 and 6. The increase in the yield of naphtha with gravity and the decrease with characterization factor of petroleum fractions (Figures 5 and 6) are mainly due to the differences in their boiling ranges.

The product distribution data indicated that the hydrocracking of petroleum fractions produces higher quantities of gaseous product when compared to coal-based oils at all levels of naphtha formation (Figure 7). Coal-based oils produced more C₁-C₃ hydrocarbons than petroleum oils at different levels of butane production (Figure 8). The production of +200°C oil fraction was higher in the hydrocracking of coal-based oils. However, the differences are not large enough to alter the product distribution significantly. Isomerization is an important aspect of hydrocracking and the results shown in Figure 9 indicated the occurrence of more isomerization in the hydrocracking of petroleum oils when compared to the coal-based oils at all levels of naphtha formation. The iso-normal ratios in butanes varied between 1 and 4 in the case of petroleum oils, while the ratios varied between 1 and 2.75 in the case of coal-based oils. Occurrence of isomerization during hydrocracking produces better quality naphtha and this is an advantage associated with the petroleum oils under hydrocracking conditions. However, there may be several other factors which influence the quality of naphtha. The relative proportions of light and heavy fractions of naphtha will also contribute to the overall quality of the naphtha. Normally light naphthas produced from petroleum fractions have higher octane ratings than heavy naphthas, necessitating the subsequent reforming of heavy naphtha. The results in Figures 10 and 11 indicated that petroleum oils produce more light naphtha relative to heavy naphtha when compared to coal-based oils. The ratios of heavy-light naphthas varied

between 2 and 4 in the case of petroleum oils, while the ratios varied between 3.5 and 4.5 in the case of coal-based oils. This is again an added advantage associated with petroleum oils, though this is not the final deciding factor.

The hydrocarbon composition of naphthas obtained from petroleum and coal-based oils was shown in Figure 12. Coal-based naphthas contained higher proportions of aromatic hydrocarbons than petroleum naphthas. At about 80% formation, petroleum naphthas contained about 35 to 40%, while coal-based naphthas contained about 55% aromatic hydrocarbons. This may make a great difference in the octane rating of the naphthas and coal-based naphthas are expected to have high octane values. Petroleum naphthas contained slightly higher concentrations of naphthenes and isoparaffins than coal-based naphthas, while the contents of normal paraffins and olefins were almost the same in both cases. The quality of coal-based naphthas was found to be much superior to the petroleum naphthas, as shown in Figure 13. The clear research octane numbers of coal-based naphthas varied between about 80 to 90, while the octane numbers of the petroleum naphthas varied only in between about 65 to 80. At the maximum yield of about 80%, coal-based naphthas had clear research octane numbers of about 90, while the octane ratings were below 80 numbers in the case of petroleum naphthas. The coal-based naphthas can be used as regular grade gasoline without further treatment and as premium grade product simply by the use of additives. Petroleum naphthas need to be reformed before they can be used either as regular or premium grade materials. Coal-based naphthas have slightly higher concentrations of sulfur and nitrogen which, however, are much below the specified limits.

Hydrogen requirement is an important factor which contributes significantly to the overall refining cost of fuel oils. The results shown in Figure 14

illustrated that hydrogen consumption was high in the hydrocracking of coal-based oils when compared to petroleum oils. At the maximum yield of about 80% naphtha, hydrogen consumption varied between 800 to 1100 and 1500 to 1600 cu. ft. per barrel of feed stock in the hydrocracking of petroleum and coal-based oils, respectively. The high hydrogen consumption in the case of coal-based oils was due to the hydrogenation of aromatic hydrocarbons and heterocyclic compounds, especially the oxygenated compounds. This is one of the disadvantages associated with the refining of coal-based oils.

Kinetics

For the kinetic study the gas oil and coal oil fractions were used and the hydrocracking experiments were conducted at a constant hydrogen pressure of 2000 p.s.i. The overall rates of hydrocracking were studied by the application of Equation 1 assuming first-order kinetics (Qader and Hill, 1969).

$$\ln \frac{X_i}{X_f} = k \frac{1}{\text{LHSV}} \quad (1)$$

where

X_i = initial concentration of the reactant, wt. %

X_f = final concentration of the reactant, wt. %

LHSV = liquid hourly space velocity, volume of liquid feed per hour per volume of catalyst

k = specific reaction rate constant

The plots of reciprocal space velocity versus $\log \frac{X_i}{X_f}$ are shown in Figures 15 and 16. The plots were linear and, thus, the first-order rate constants can be represented by Equations 2 and 3.

$$-\frac{d(\text{gas oil})}{dt} = k_g (\text{gas oil}) \quad (2)$$

$$-\frac{d(\text{coal oil})}{dt} = k_c (\text{coal oil}) \quad (3)$$

where k_g and k_c are rate constants for gas oil and coal oil hydrocracking, respectively. The Arrhenius plots (Figure 17) were linear and the rate constants were found to be represented by Equations 4 and 5.

$$k_g = 0.3651 \times 10^4 e^{-14,300/RT} \text{ hr.}^{-1} \quad (4)$$

$$k_c = 0.8395 \times 10^4 e^{-15,500/RT} \text{ hr.}^{-1} \quad (5)$$

The following values of enthalpies and entropies of activation were calculated from plots of $\log \frac{k}{T}$ versus $\frac{1}{T}$ by applying Eyring equation (Figure 18).

$$\Delta H_g^\ddagger = 12,800 \text{ cal./mole,} \quad \Delta S_g^\ddagger = -52 \text{ e.u.}$$

$$\Delta H_c^\ddagger = 1,400 \text{ cal./mole,} \quad \Delta S_c^\ddagger = -50 \text{ e.u.}$$

The kinetic data indicates that both the gas oil and coal oil exhibit similar kinetic behavior under hydrocracking conditions except the coal oil needs a slightly higher activation energy. The mechanisms of hydrocracking of gas oil and the coal oil appear to be similar as proposed earlier and the energetics suggest that chemical reactions involving the cracking of C-C, C-O, C-S, and C-N bonds will control the reaction rate (Qader, et al., 1968 and 1969). The catalyst used in this investigation is a dual-functional one, containing both a cracking component and a hydrogenation component. Since cracking is the rate controlling step in hydrocracking, the reaction rates and the product yields are mainly influenced by the activity of the cracking component of the catalyst. Therefore, it is essential to carry out the hydrocracking process under conditions wherein the cracking component maintains high activity. The cracking activity of the catalyst is due to the acidic surface sites of silica which may get poisoned due to the accumulation of coke and the basic nitrogen compounds. The coke formation may also reduce the activity of the hydrogenation component of the catalyst. Therefore, it is important to study the coke deposition on the catalyst during hydrocracking. Figure 19 shows the coke

deposition on the catalyst by the hydrocracking of gas oil and coal oil at a temperature of 480°C, 2000 p.s.i. pressure, and 1-space velocity. The coke formation by the coal oil was almost double the amount by the gas oil, which suggests that the catalyst life will be shortened to a great degree during the hydrocracking of coal oil. This may make the hydrocracking of coal oil more expensive when compared to the gas oil. However, if the feed stocks are hydrorefined in a preceding step to remove the nitrogen compounds which otherwise will poison the acidic sites of the cracking component of the catalyst during hydrocracking, the coke formation on the catalyst can be reduced to a great extent as shown in Figure 20. Further, the gas oil and the coal oil affect almost the same amount of coke deposition on the catalyst during the hydrocracking of the hydrorefined feed stocks. The results suggest that the hydrocracking of either petroleum or coal-based oils on the dual-functional catalyst must be preceded by the hydrorefining of the feed stocks and the hydrocracking of the preredefined feed stocks will exhibit similar characteristics with respect to catalyst requirements. This investigation indicates that though the hydrocracking of petroleum oils has certain advantages over the coal-based oils, the disadvantages associated with the latter may be offset by the superior quality of their products, thereby affecting the overall processing of both types of oils almost similarly.

Table 1. Properties of feed materials.

	Stove oil	Diesel oil	Gas oil	Coal oil fraction	Low tem- perature tar fraction
Gravity, °API	38.2	36.5	32.4	21.5	23.4
Characterization factor	11.2	11.6	11.9	9.9	9.5
Sulfur, wt. %	0.24	0.22	0.38	0.62	0.84
Nitrogen, wt. %	0.18	0.16	0.14	0.42	0.58
Oxygen, wt. %	Nil	Nil	Nil	3.6	4.8
Distillation					
I.B.P., °C	200	250	350	200	200
50%	250	302	430	238	260
F.B.P., °C	300	380	490	370	360
Hydrocarbon analysis, vol. %					
Saturates	80	80	81	38	28
Aromatics	20	20	19	57	54
Olefins	Nil	Nil	Nil	5	18

Literature Cited

1. Alpert, S. P., Johanson, E. S., Schuman, S. C., Chem Eng. Progress, 60, No. 6, 35 (1964).
2. Archibald, R. C., Greensfelder, B. S., Holzman, G., Rowf, D. H., Ind. Eng. Chem., 52, 745 (1960).
3. Carpenter, H. C., Cottingham, P. L., Frost, C. M., Fowkes, W. W., Bureau of Mines Report of Investigation, No. 6237 (1963).
4. Craig, R. G., Forster, H. A., Oil Gas J., 45, 159 (1966).
5. Duir, J. H., Hydrocarbon Processing and Petrol. Refiner, 46, 127 (1967).
6. Flinn, R. A., Larson, O. A., Beuther, H., Ind. Eng. Chem., 52, 153 (1960).
7. Katsobashvili, Ya. R., Elbert, E. A., Coke and Chemistry, U.S.S.R., 1, 41 (1966).
8. Qader, S. A., Wisner, W. H., Hill, G. R., Preprints, 155th National Meeting, ACS, Division of Fuel Chemistry, 12, No. 2, 28 (1968).
9. Qader, S. A., Wisner, W. H., Hill, G. R., Ind. Eng. Chem. Proc. Res. Develop., 7, 390 (1968).
10. Qader, S. A., Hill, G. R., Ind. Eng. Chem. Proc. Res. Develop., 1, (1969).
11. Zielke, C. W., Struck, R. T., Evans, J. M., Costanza, C. P., Gorn, E., Ind. Eng. Chem., 5, 151 and 158 (1966).

Acknowledgement

Research work supported by the Office of Coal Research and the University of Utah.

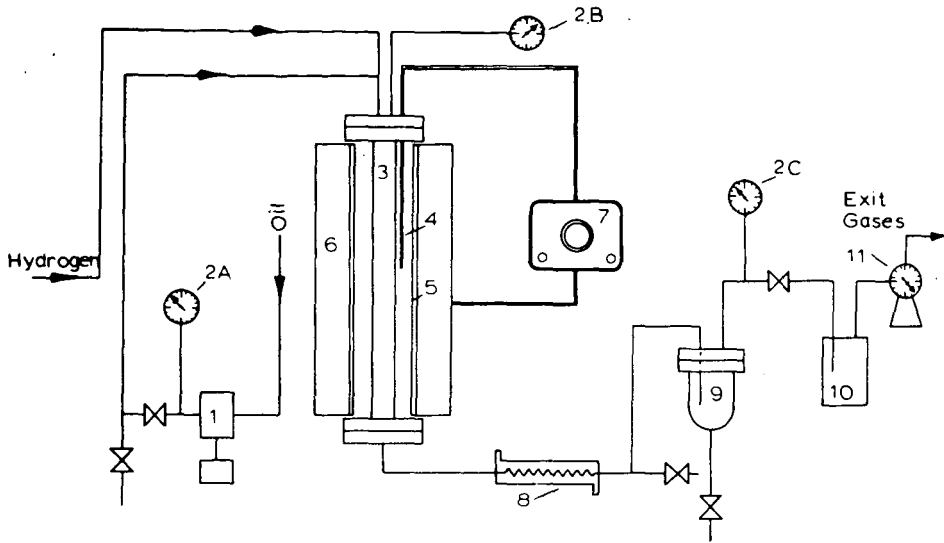


FIGURE 1. FLOW SHEET OF THE HYDROTREATING UNIT.
 1. HIGH PRESSURE PUMP, 2A, 2B, 2C. PRESSURE GAUGE, 3. REACTOR, 4. THERMOCOUPLE,
 5. CERAMIC FURNACE, 6. INSULATION, 7. TEMPERATURE CONTROLLER, 8. CONDENSER,
 9. SEPARATOR, 10. ACTIVE CARBON TOWER, 11. GAS METER.

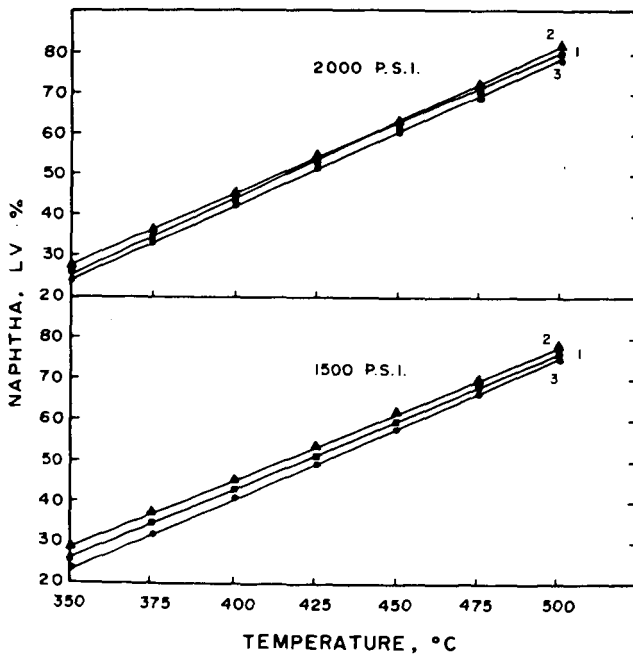


FIGURE 2. INFLUENCE OF TEMPERATURE AND PRESSURE ON NAPHTHA YIELD.
 1. STOVE OIL, 2. DIESEL OIL, 3. GAS OIL.

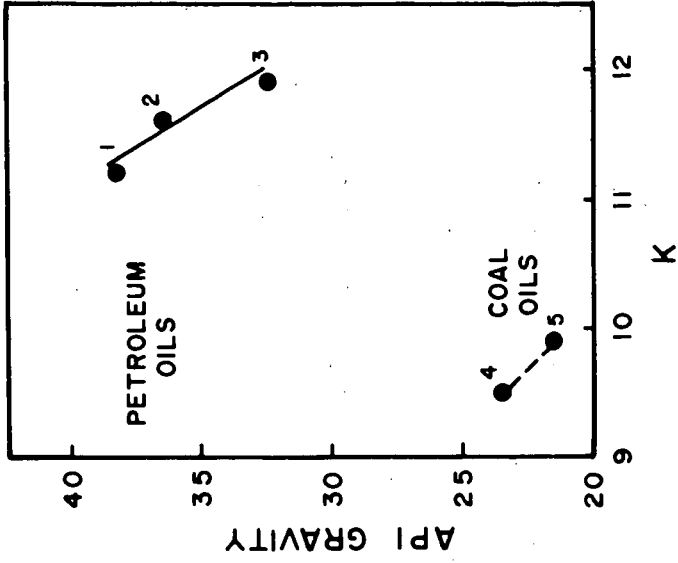


FIGURE 4. RELATIONSHIP BETWEEN GRAVITY AND CHARACTERIZATION FACTOR.
 1. STOVE OIL, 2. DIESEL OIL, 3. GAS OIL, 4. LOW TEMPERATURE TAR, 5. COAL OIL.

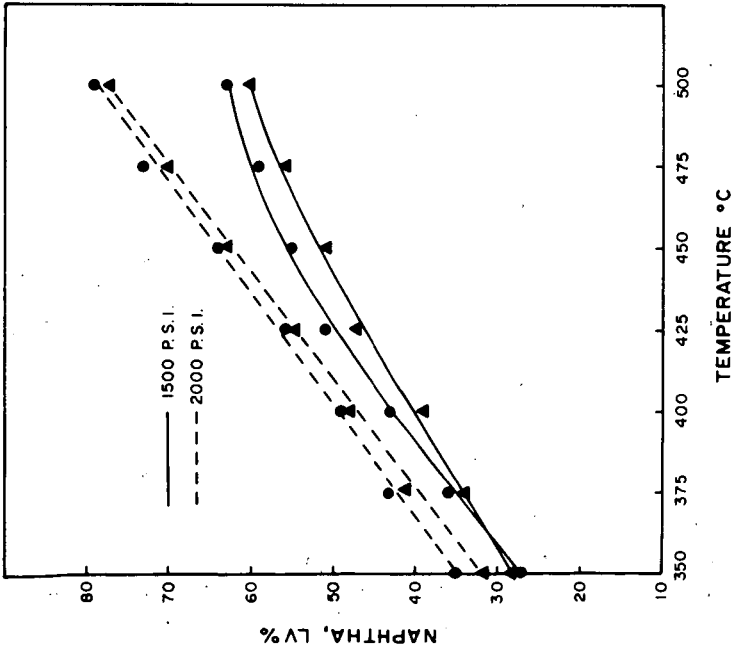


FIGURE 3. INFLUENCE OF TEMPERATURE AND PRESSURE ON NAPHTHA YIELD.
 1. COAL OIL, 2. LOW TEMPERATURE TAR.

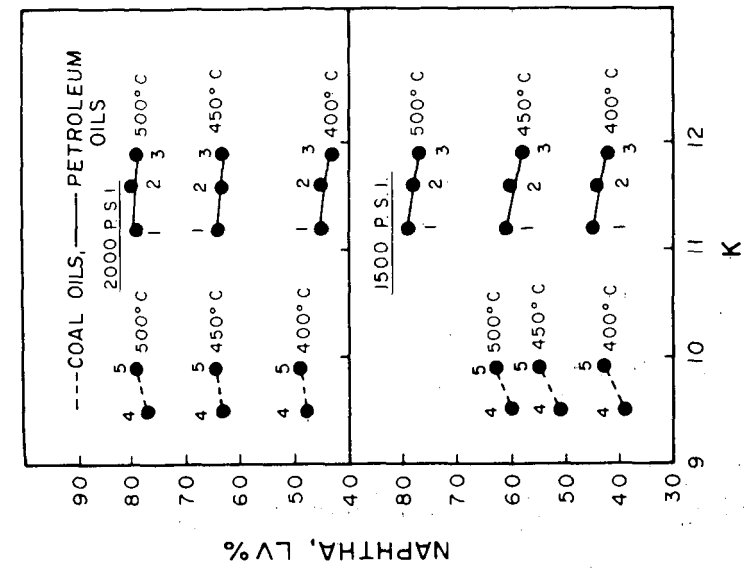


FIGURE 5. RELATIONSHIP BETWEEN NAPHTHA YIELD AND GRAVITY OF FEED STOCKS.
1. STOVE OIL, 2. DIESEL OIL, 3. GAS OIL, 4. LOW TEMPERATURE TAR, 5. COAL OIL.

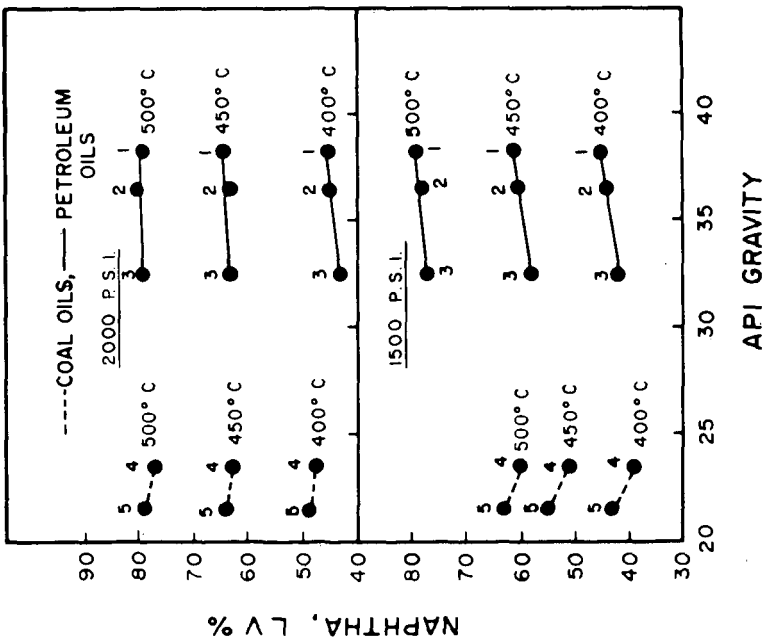


FIGURE 6. RELATIONSHIP BETWEEN NAPHTHA YIELD AND FEED TEMPERATURE FACTOR OF FEED STOCKS.
1. STOVE OIL, 2. DIESEL OIL, 3. GAS OIL, 4. LOW TEMPERATURE TAR, 5. COAL OIL.

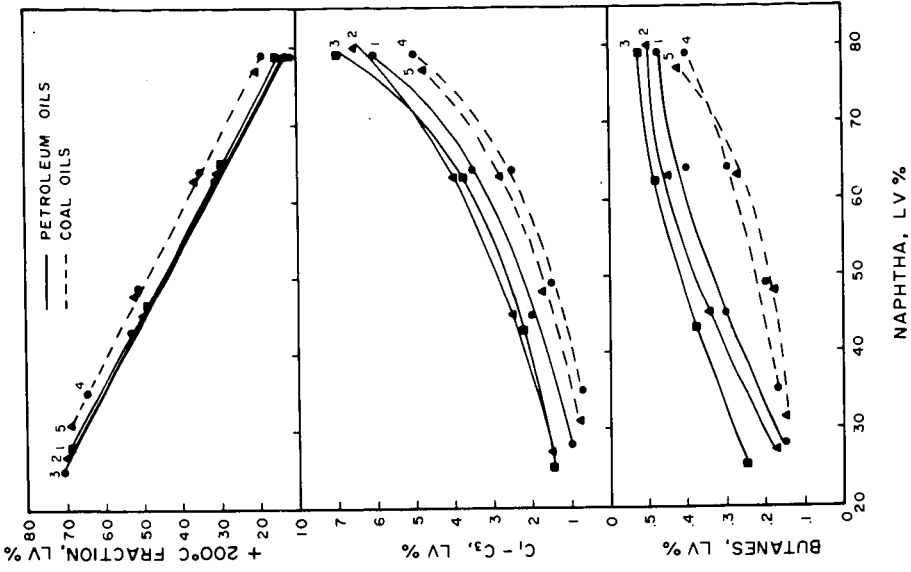


FIGURE 7. PRODUCT DISTRIBUTION AT DIFFERENT LEVELS OF NAPHTHIM YIELD.
 1. STOVE OIL, 2. DIESEL OIL, 3. GAS OIL, 4. LOW TEMPERATURE TAR, 5. COAL OIL.

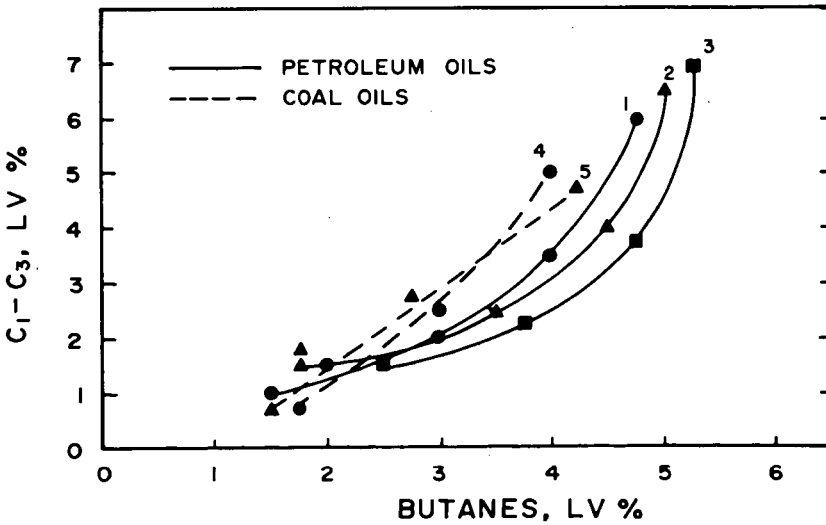


FIGURE 8. RATIO OF BUTANES AT DIFFERENT LEVELS OF NAPHTHIM YIELD.
 1. STOVE OIL, 2. DIESEL OIL, 3. GAS OIL, 4. LOW TEMPERATURE TAR, 5. COAL OIL.

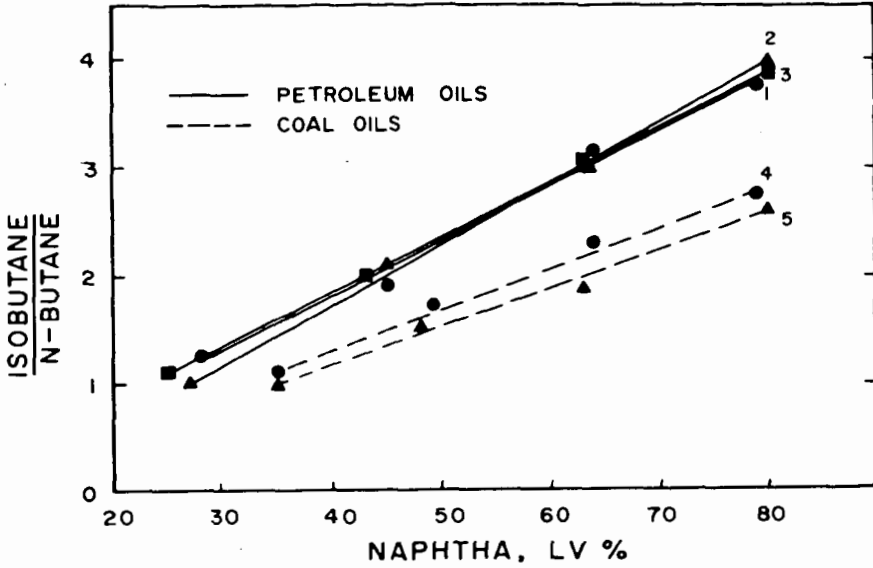


FIGURE 9. RELATIONSHIP BETWEEN THE FORMATION OF C_1-C_3 HYDROCARBONS AND BUTANES.
1. STOVE OIL, 2. DIESEL OIL, 3. GAS OIL, 4. LOW TEMPERATURE TAR, 5. COAL OIL.

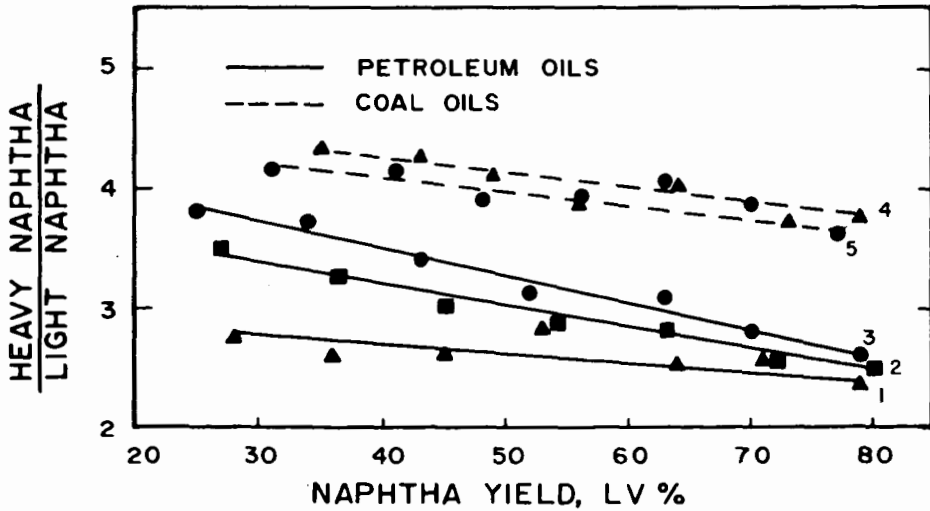


FIGURE 10. RATIO OF LIGHT AND HEAVY NAPHTHA AT DIFFERENT LEVELS OF CONVERSION.
1. STOVE OIL, 2. DIESEL OIL, 3. GAS OIL, 4. LOW TEMPERATURE TAR,
5. COAL OIL.

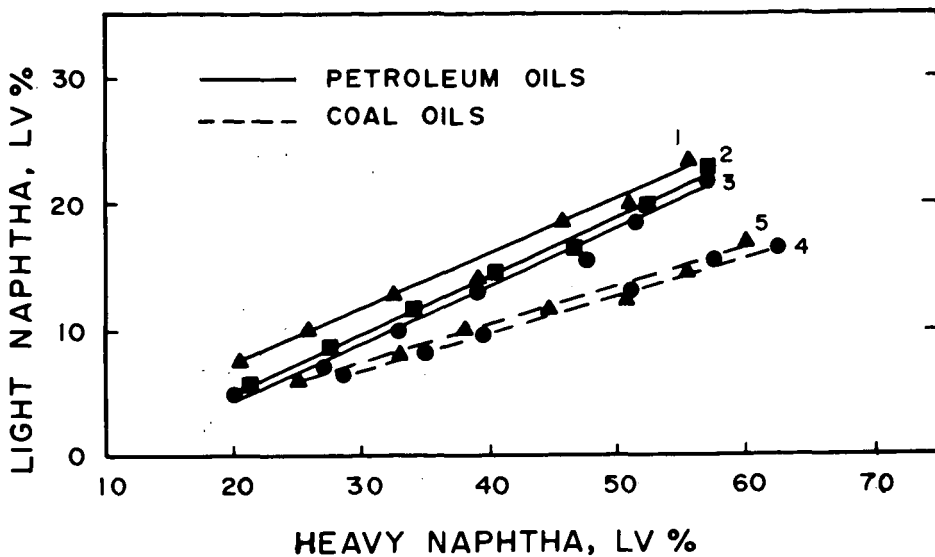


FIGURE 11. RELATIONSHIP BETWEEN THE FORMATION OF LIGHT AND HEAVY NAPHTHA.
 1. STOVE OIL, 2. DIESEL OIL, 3. GAS OIL, 4. LOW TEMPERATURE TAR,
 5. COAL OIL.

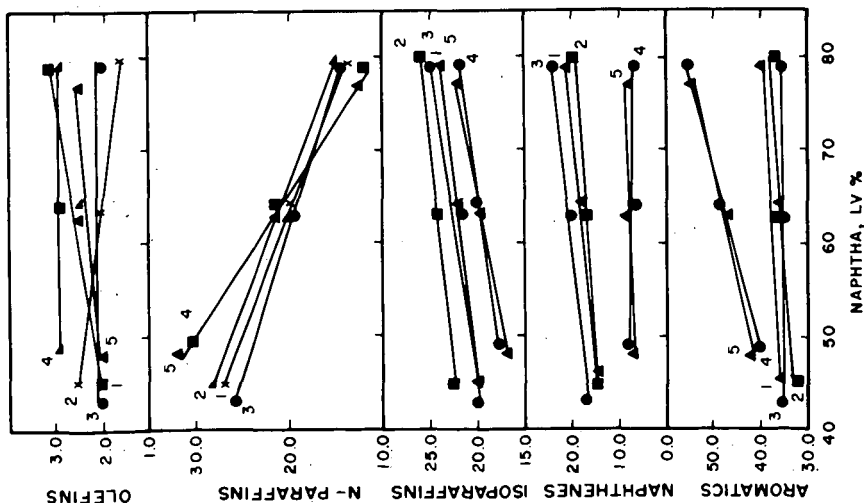


FIGURE 12. COMPOSITION OF NAPHTHA AT DIFFERENT LEVELS OF FORMATION.
 1. STOVE OIL, 2. DIESEL OIL, 3. GAS OIL, 4. LOW TEMPERATURE TAR, 5. COAL OIL.

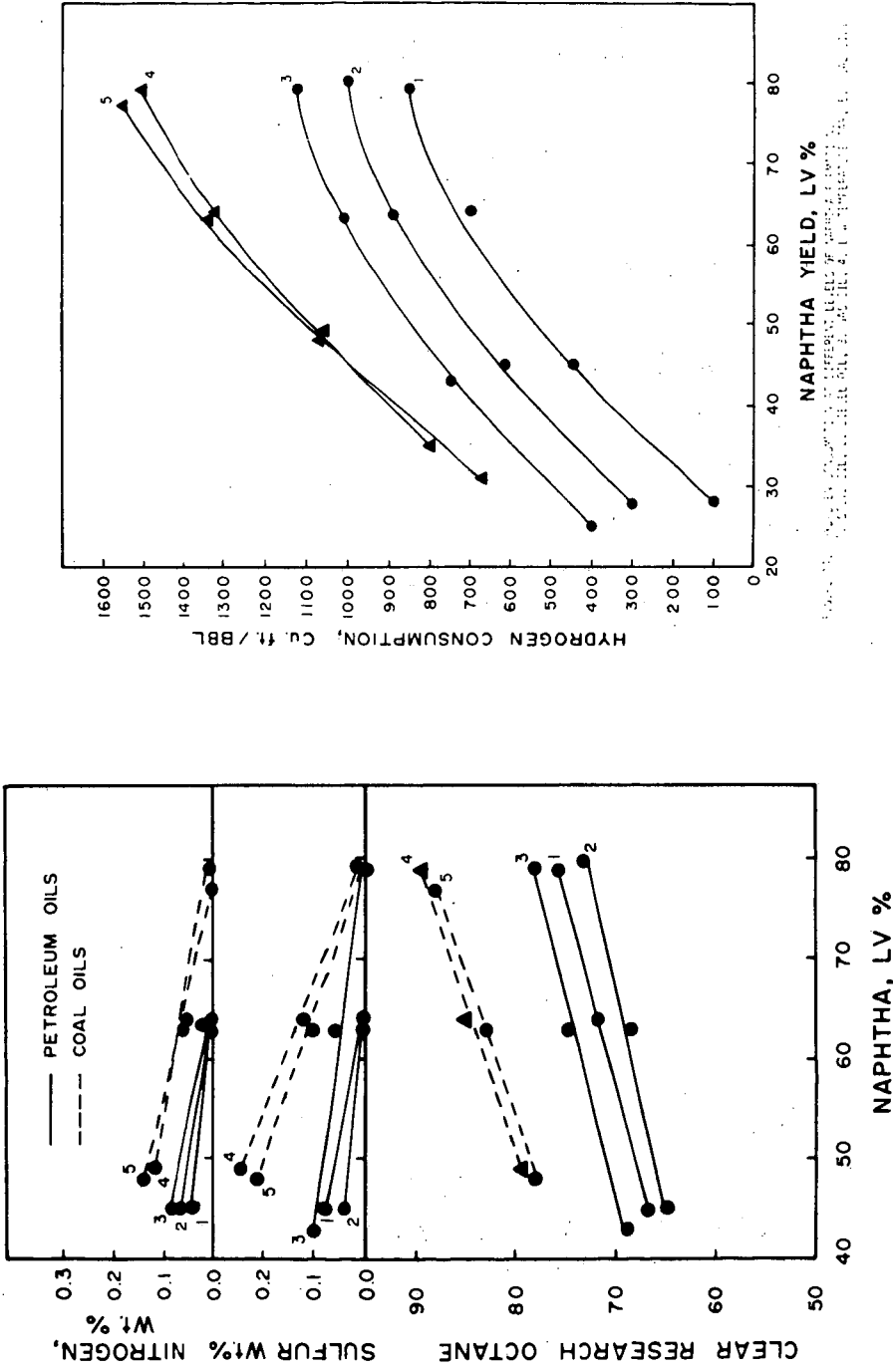


FIGURE 13. QUALITY OF NAPHTHA AT DIFFERENT LEVELS OF FORMATION.
 1. STOVE OIL, 2. DIESEL OIL, 3. GAS OIL, 4. LOW TEMPERATURE TAR, 5. COAL OIL.

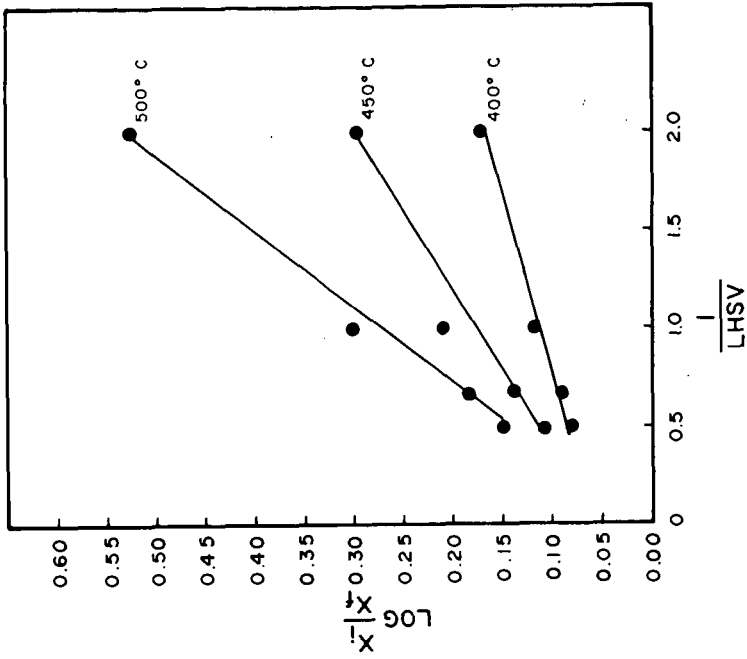


FIGURE 15. FIRST-ORDER PLOT FOR HYDROCRACKING OF BAS OIL.

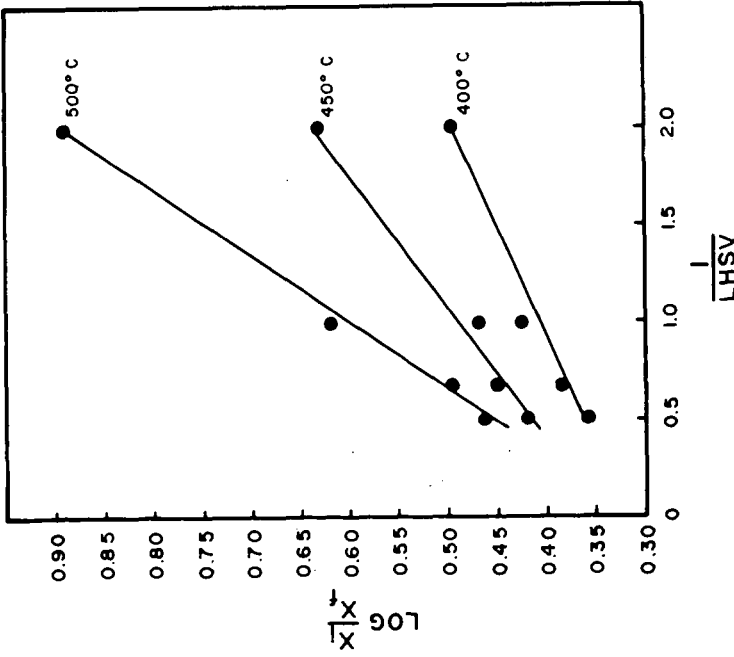


FIGURE 16. FIRST-ORDER PLOT FOR HYDROCRACKING OF COAL OIL.

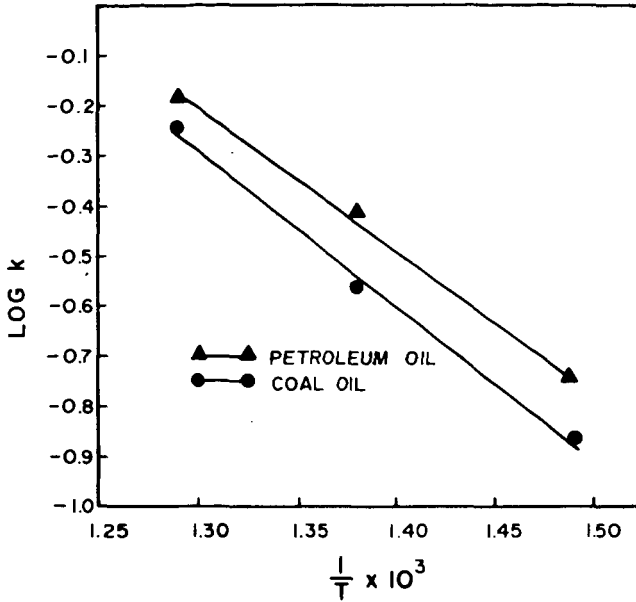


FIGURE 17. ARRHENIUS PLOT FOR HYDROCRACKING OF GAS OIL AND COAL OIL.

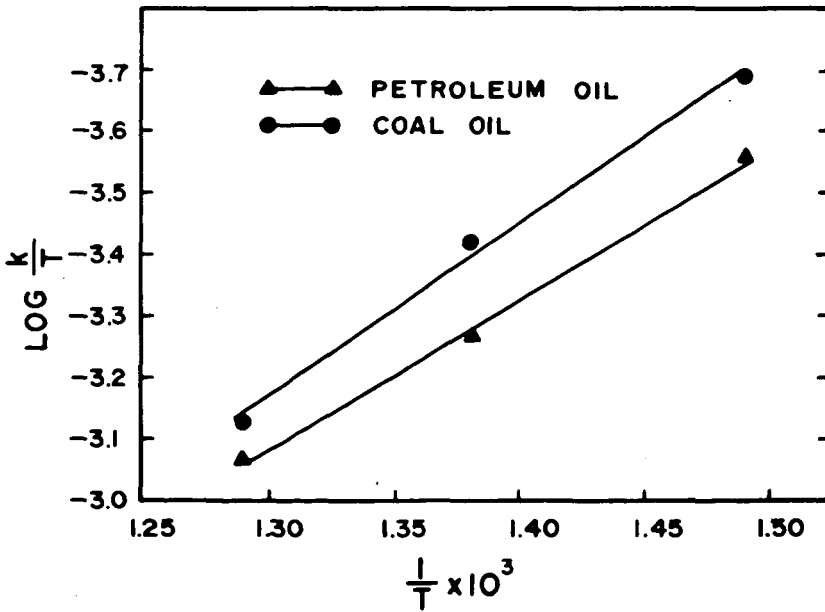


FIGURE 18. EYRING PLOT FOR HYDROCRACKING OF GAS OIL AND COAL OIL.

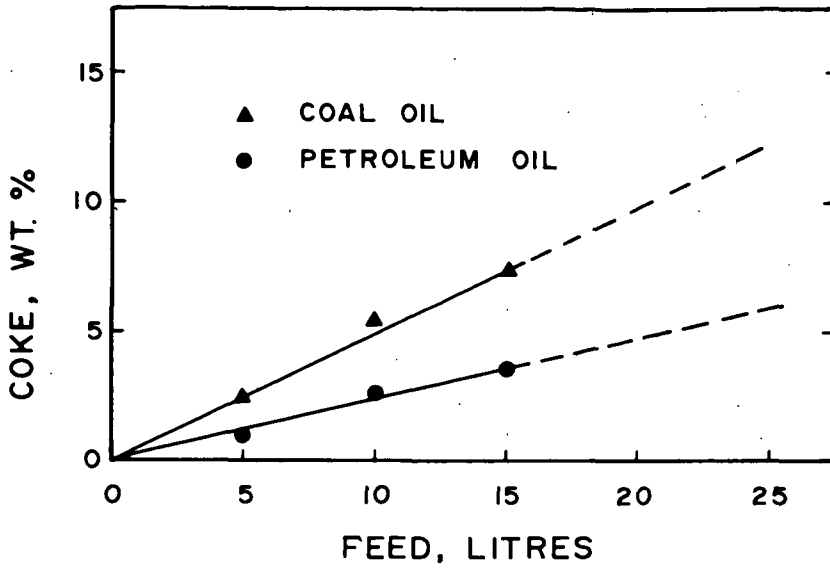


FIGURE 19. COKE FORMATION DURING HYDROCRACKING OF GAS OIL AND COAL OIL.

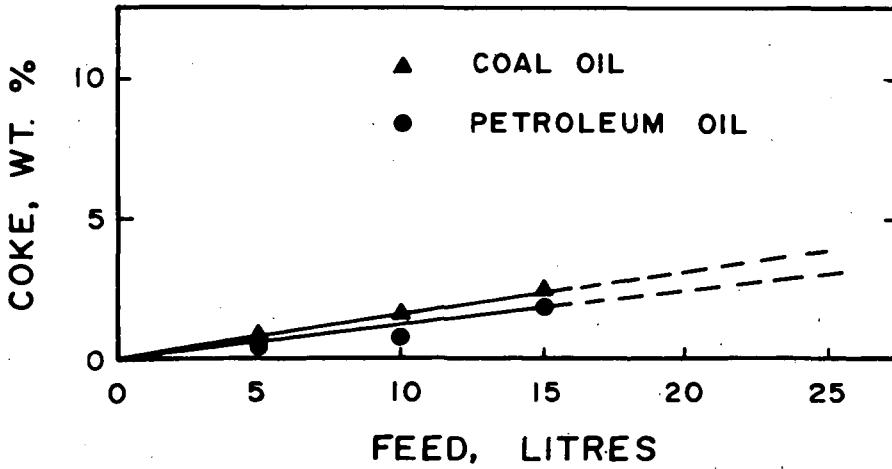


FIGURE 20. COKE FORMATION DURING HYDROCRACKING OF REFINED GAS OIL AND COAL OIL.

CONTINUOUS RAPID CARBONIZATION OF POWDERED COAL BY ENTRAINMENT:
RESPONSE SURFACE ANALYSIS OF DATA

by

John J. S. Sebastian, Robert J. Belt, and John S. Wilson

Morgantown Coal Research Center, Bureau of Mines
U.S. Department of the Interior, Morgantown, W. Va.

INTRODUCTION

In recent years increased interest in processes for converting coal into high-Btu pipeline gas and smokeless low-sulfur char for powerplants prompted the Morgantown Coal Research Center to study the rapid or flash carbonization of bituminous coal. The coal selected for carbonization was a strongly caking, high-volatile A bituminous from the Pittsburgh bed (34.4% V.M., 7.0% ash).

Of primary interest has been the development of a low-cost process for carbonizing high-volatile bituminous coals at high throughput rates in entrainment. Previously proposed low-temperature entrainment processes (1)¹, as well as our prior low temperature-entrainment carbonization work² in an externally heated 9-foot-long 4-inch-diameter isothermal reactor, yielded a high-Btu gas and a highly reactive char, along with a high yield of tar plus light oil. However, coal throughput rates were prohibitively low owing to dilute phase operation--0.35 g of coal per cu ft gas volume. Projection of such data to a commercial-scale process would result in excessively large equipment and high operating costs, although the throughput per unit cross sectional area would increase to some extent with larger carbonizers operated at higher pressures.

Dense phase entrainment, on the other hand, offered the prospect of a significant increase in coal throughput. Hence, experiments were conducted with a 4-inch-diameter by 1-foot-long carbonizer at higher temperatures with 20 times the coal concentration. The objective of this work was 3-fold: (1) to determine the effects and interactions of process variables as a guide to process feasibility; (2) to evaluate external and internal methods of applying the heat required for carbonization; and (3) to obtain data for the design of a pilot-scale carbonizer.

This paper describes these experiments, including the main steps in applying a 3-factor 5-level response surface analysis of the factorially designed test-runs, a technique that evaluates all of the significant process variables with a minimum of experimental work. Two of the 13 responses, char yield and percent volatile matter in the char, are discussed in detail.

DESCRIPTION OF EQUIPMENT

The equipment for the two test series differed in the method of heating the carbonizer and in most of the product recovery system, as shown in figures 1 and 2. The coal-feeding system was identical in both series and consisted of a vibratory screw feeder receiving coal from a pressure-equalized hopper. The feeding

¹Underlined numbers in parentheses refer to items in the list of references at the end of the paper.

²The results of these preliminary investigations will be summarized in a forthcoming U.S. BuMines Report of Investigations.

in each case was facilitated by injection of the coal into nitrogen in different dilutions with methane, before entering the flash carbonizer.

The carbonizer consisted of a 12-inch length of 4-inch-diameter, schedule 40 pipe made of type 310 stainless steel. For the external heating series, three 4-inch-long circular thermoshell heating elements were installed around the carbonizer tube. The coal particles were carbonized while being carried downward by the entraining gas. For internal heating, natural gas was burned with a slight deficiency of air in a refractory-filled combustor, the hot combustion products being injected directly into the carbonizer. The 70 percent through 200-mesh coal was further entrained in the hot gases which provided the required heat for carbonization. Internal heating changed the heat transfer from radiation controlled to turbulent convective, although some external heating was also applied to balance the heat losses from the carbonizer.

Because of the different gas flow rates for the two test series, the product recovery trains were different. In each case, the objective was complete recovery from the gas stream of all solid and liquid products. In both cases, coarser char particles fell directly into a char receiver below the carbonizer. For the externally heated unit, where the gas flow rate was lower, a baffled knockout chamber was used to remove the fine char particles. Tar and pitch were removed by two electrostatic precipitators, followed by a dry-ice trap for removal of light-oil and water, and a silica gel trap for final recovery of light-oil and water before metering and venting the gas. For the internally heated unit, which received much larger gas volumes from the combustor, the recovery train consisted of two cyclones in series for the removal of char dust, and a water scrubber followed by a steam-water scrubber for final tar, pitch, and light-oil removal.

The carbonizer was designed to rapidly heat coal particles at atmospheric pressure as they passed through the 12-inch hot zone. The feed tube was constructed to inject the powdered coal at a high velocity into the carbonization zone. After less than one second residence time, during which the particles are rapidly pyrolyzed and devolatilized, the char particles carried by the gas enter the recovery train.

In a typical test-run the carbonizer is preheated to the desired wall temperature. When the carbonizer temperature becomes constant at the desired level, the coal feeding is begun to start the run. During the run, char is periodically removed from the bottom lock hopper and the gas is sampled. All other products are collected after the run and a period of cooling.

EXPERIMENTAL DESIGN

To evaluate the data, the "composite factorial design" method (2) was used to obtain, in the least time, the best reliable estimates of the effects and interactions of system variables. Several of these variables, called "factors", were systematically changed and the effects in each case determined by statistical analysis.

A 3-dimensional coordinate system was assumed with three factors--coal-feed rate, reactor wall temperature, and entraining gas composition³--changed simultaneously while all other variables were held constant. Within this 3-dimensional

³Methane is the chief component of carbonization gases and was used in order to simulate the entrainment of coal in recycle gases as would be done in pilot-scale and commercial carbonizers. Entraining gas composition is expressed in terms of methane-to-nitrogen ratios.

system, a range of values in each operating variable was chosen for examination, based on actual results. The effects and interactions of these three factors at various levels were determined on two types of responses, product-yield and quality.

The composite factorial design allowed detailed examination of the responses at 14 points plus five replications at the center of the cube, from which the entire response surface was derived. The computation of variances was based on these five replications. The three factors were varied in an established pattern as shown in table 1 and figure 3. In these illustrations, for convenience, the factors are identified as x_1 (reactor wall temperature), x_2 (coal-feed rate) and x_3 (gas composition). The levels in each factor were coded into five values: -2, -1, 0, 1, 2. The operating factors and corresponding experimental results obtained are summarized in table 2.

The main steps in response surface analysis follow:

1. Design the experiment to obtain a second degree regression equation,
2. Transform this equation into its standard or canonical form,
3. Illustrate it by means of a contour diagram or 3-dimensional model.

Assuming that a second degree equation with three factors represents the system adequately, it will have the following general form:

$$y = b_0x_0 + b_{11}x_1^2 + b_{12}x_1x_2 + b_{13}x_1x_3 + b_1x_1 + b_{22}x_2^2 + b_{23}x_2x_3 + b_2x_2 + b_{33}x_3^2 + b_3x_3 \quad (1)$$

where b_0x_0 represents the average value of all trials. This equation contains a linear term and a quadratic term for each factor and all possible 2-factor interactions. The coefficients are calculated from the data.

TABLE 1. - Composite factorial design

Factors	Level					Symbol
	-2	-1	0	1	2	
Temperature.....°F	1,500	1,600	1,700	1,800	1,900	x_1
Feed rate.....g/hr	250	500	750	1,000	1,250	x_2
Gas composition.....%	100 N ₂	75	50	25	0	x_3
	0 CH ₄	25	50	75	100	

Note: Constants: (1) Coal type--Pittsburgh-bed hvAb, 34.4% V.M., 7.0% ash (dry basis).
 (2) Coal size--70 percent through 200 mesh.
 (3) Entraining gas rate--10.0 scfh.

Responses:

- | | | |
|---------------------------------|------------------------------|------------------------|
| (1) Char yield. | (5) Sulfur per Btu. | (9) Gas heating value. |
| (2) Char heating value. | (6) Percent volatile matter. | (10) Gas fuel value. |
| (3) Char fuel value. | (7) Percent sulfur. | (11) Light-oil yield. |
| (4) Extent of devolatilization. | (8) Gas yield. | (12) Tar yield. |
| | | (13) Pitch yield. |

TABLE 2. - Summary of data

Coded coordinates	Operating variables			Experimental results			
	Temp., °F	Feed rate, g/hr	Gas comp., % CH ₄	External heating		Internal heating	
				% V.M.	Char yield, lb/ton	% V.M.	Char yield, lb/ton ¹
-1 -1 -1	1,600	500	25	23.83	1,521	15.46	1,029
-1 -1 1	1,600	500	75	25.73	1,556	15.02	1,048
-1 1 -1	1,600	1,000	25	30.11	1,732	24.81	1,253
-1 1 1	1,600	1,000	75	28.91	1,719	20.56	1,178
1 -1 -1	1,800	500	25	24.20	1,433	13.74	1,030
1 -1 1	1,800	500	75	23.20	1,454	16.01	1,074
1 1 -1	1,800	1,000	25	25.71	1,513	20.85	1,221
1 1 1	1,800	1,000	75	26.07	1,619	19.76	1,194
0 0 0	1,700	750	50	26.56	1,635	14.74	1,088
0 0 0	1,700	750	50	27.76	1,589	17.11	1,117
0 0 0	1,700	750	50	28.55	1,642	18.83	1,138
0 0 0	1,700	750	50	28.96	1,638	16.62	1,060
0 0 0	1,700	750	50	28.28	1,604	15.27	1,037
-2 0 0	1,500	750	50	31.18	1,721	23.35	1,246
2 0 0	1,900	750	50	24.65	1,468	12.05	983
0 -2 0	1,700	250	50	22.58	1,305	11.99	960
0 2 0	1,700	1,250	50	31.94	1,729	16.38	1,010
0 0 -2	1,700	750	0	29.61	1,661	16.96	1,115
0 0 2	1,700	750	100	28.90	1,593	16.32	1,000

¹The low char yields from internal heating are attributable to some carry-over of fine dust into tar and pitch.

Since the regression equation is difficult to interpret, it is transformed into its standard or canonical form. The transformation is orthogonal and consists of translation of the original center of the design to the stationary point (where the slope with respect to all factors is zero) and rotation of the axes. Translation eliminates the linear terms; rotation causes the interactions to vanish. The transformed equation has the following general form:

$$Y - Y_0 = B_{11}X_1^2 + B_{22}X_2^2 + B_{33}X_3^2 \quad (2)$$

where Y_0 is the response at the stationary point and the X_1 's are the coordinates with respect to the new axes after translation and rotation.

The magnitude and signs of the coefficients in the canonical equation show the nature of the response surface. If all signs are positive, the value of the response is increasing in any direction from Y_0 , and Y_0 has a minimum value; if all signs are negative, the value of the response is decreasing, and Y_0 has a maximum value; if both positive and negative signs are present, the surface is "saddle" shaped (i.e., a ridge connecting two elevations) and there is no single maximum or minimum.

The transformation is straightforward and is based on sound mathematical procedures. The two equations, empirical and canonical, do not differ except for the location of the reference point.

All of the regression equations as well as the canonical forms have been programmed in FORTRAN IV language for the determination of the coefficients by an IBM 7040 Computer, and for plotting of the responses by an accessory CALCOMP plotter.

RESULTS

Analysis of the data by composite factorial design yields empirical equations describing the response surfaces in terms of the factors and their interactions. The coefficients of the equations indicate by their relative magnitudes the significance of the factors and the extent of their interactions as well as the curvature of the surfaces. From the equation, both linear and quadratic effects can be assessed.

The response surfaces for char yield in the external heating series are described by the regression equation:

$$y/10^3 = 1.603 - .0044x_1^2 - .0161x_1x_2 + .0131x_1x_3 - .0634x_1 \quad (3)$$

$$- .0238x_2^2 + .0046x_2x_3 + .0917x_2$$

$$+ .0037x_3^2 + .008x_3$$

The coefficients of the linear terms, $0.0634x_1$ and $0.0917x_2$, are larger than any others, thus these linear effects have the greatest significance on the char yield. Statistical analysis of the data indicates that these two factors, temperature and feed-rate, are the only significant ones at the 95 percent confidence level. Based on a similar equation for the internal heating series, the char yield response is significantly dependent only upon the coal-feed rate. In absolute magnitude, these coefficients are small, indicating that the surfaces have only a slight curvature within the limits of the experiment.

The canonical equation for char yield in external heating is:

$$Y - 1,974 = -27.4X_1^2 - 4.7X_2^2 + 7.5X_3^2 \quad (4)$$

The form of this equation indicates that the surface is saddle-shaped since both positive and negative terms appear. The stationary point in this case is an inflection point in the surface, (i.e., neither a maximum or a minimum), and since it occurs outside the experimental limits, any description of the behavior of the surface near the point is meaningless. The saddle-shaped surface indicates only a trend in the data. Figures 4 and 5 present a comparison of the shapes of the surfaces for yields of char produced by external and internal heating, respectively.

Similarly derived from another regression equation, the 3-dimensional diagrams in figures 6 and 7 show the response surfaces for volatile matter in the char, resulting from external and internal heating, respectively. Both sets of surfaces are saddle-shaped as were those for char yield. The results of the computed data (table 3) show that the surfaces for percent volatile matter in the char depend only on coal-feed rate in the case of internal heating. With external heating, both temperature and coal-feed rate have significant effects. Table 3 also summarizes the results for the four responses discussed above.

Figure 8 shows the quantitative relationship between char yield and coal-feed rate for both the internal and external heating series. In this diagram, the wall temperature of the carbonizer and the percent volatile matter in the char are shown as parameters. The solid curves represent the char yield as a function of the coal-feed rate at the temperature levels shown. The broken lines represent similarly a functional relationship between char yield and coal-feed rate, but with percent volatile matter as a parameter at the levels shown. The diagram also shows the percent volatile matter in char as a function of the coal-feed rate at given

carbonization temperatures. This follows from the fact that the char yield is a function of coal-feed rate at any carbonization temperature, as stated above.

TABLE 3. - Results of factorial analysis:
yield and quality of the char produced

Response	Significant factors ^{1,5}	Best value of response ²	Conditions yielding best response value ³	Variance accounted for ^{4,5}	Heating Method
Char yield	Temperature, feed rate	Maximum at 15% V.M. in char	Low temperatures; high feed rates; CH ₄ in gas	98.5	External
Percent volatile matter in char	Temperature, feed rate	15%	Low temperatures; low feed rates; gas composition immaterial	84.8	External
Char yield	Feed rate	Maximum at 15% V.M. in char	Low temperatures; low feed rates (250-500 g/hr); low %CH ₄ in gas	92.4	Internal
Percent volatile matter in char	Feed rate	15%	Surface extending from low temp.-- low feed rate to high temp.--high feed rate	83.1	Internal

¹ Factors causing systematic variation in response.

² Desired value of response from process standpoint.

³ Values of variables (factors) required to give the desired response.

⁴ Percentage of random error accounted for in the experiment (below 80% validity of the result is poor.)

⁵ At 95% confidence level.

The factorial design indicates that both temperature and coal-feed rate are significant factors at the 95 percent confidence level in the external heating series, while only the coal-feed rate is significant at the 95 percent level in internal heating. The diagrams in figure 8 reflect these conclusions. The larger effect of temperature in the external series is seen from the greater spread between the curves compared with the set of curves for internal heating. The effect of temperature is clearly present in the internal heating series, but at a much lower statistical level of confidence.

The diagrams in figure 8 show that for a given coal-feed rate, the char yield decreases with increasing carbonization temperatures, as would be expected. However, the effect of the coal-feed rate on the char yield, at higher feed rates, is contrary to what one would expect: the char yield decreases as the feed rate increases. The observed deviation in curvature can be explained by the method used to measure temperature. When the temperature of the reactor wall is measured, as in this investigation, there is a direct correlation between the true temperature of the suspended solid particles and the measured wall temperature as long as the particles are in dilute phase in the moving gas stream. However, above a certain particle concentration the correlation between wall temperature and particle temperature ceases because the particles moving downward in dense phase near the center of the carbonizer tube will not "see" as much of the source of radiant heat as the particles moving near the tube wall. In the externally heated carbonizer, this shadowing effect becomes so large that the wall temperature is no longer a true

measure of the actual temperature. The same effect is confirmed by noting the percent volatile matter remaining in the char. Since the same coal is used throughout, the amount of volatile matter remaining in the char that is carbonized in dilute phase is directly related to the char yield. At high coal-feed rates in the external heating series, the curves representing the percent volatile matter in the char drop significantly with increasing coal-feed rate, also indicating that the linear relationship between wall temperature and carbonization temperature has ceased.

Differences in char yield and percent volatile matter remaining in the char for both series are evident from the diagram discussed. The upper plot shows that the minimum volatile matter left in the char from the external heating series was approximately 20 percent, or 5 percent above the 15 percent considered optimum for coal-burning powerplants. The optimum of 15% V.M. could not be attained by means of external heating over the entire range of factor levels investigated. On the other hand, the lower group of curves for the internal heating series indicate that 15 percent V.M. char can be made (with an entraining gas composition of 50 percent N_2 and 50 percent CH_4) at any temperature within the design limits of 1,500° to 1,900°F, and at coal-feed rates from 375 to 750 g/hr. The corresponding char yield was 1,075 lb per ton of coal carbonized.

A complete description of the yields and qualities of all of the products (including gas, light oil, tar and pitch) will be included in a forthcoming U.S. BuMines Report of Investigations.

CONCLUSIONS

The experimental results of the two test series show that even highly caking coals may be carbonized at a rapid rate in entrainment. The quantities and qualities of the products can be controlled within the limits of the experiment by appropriately combining the temperature, coal-feed rate and entraining gas composition.

Larger coal throughput rates, with the desired amount of volatile matter remaining in the char, were possible when the carbonizer was heated internally rather than externally because of more effective heat transfer, although at the expense of gas quality. Thus, by internal heating, optimum char quality (15% V.M.) was achieved with a throughput of 750 g/hr in a 4-inch-diameter carbonizer at 1,900°F. Comparable char quality could not be attained by external heating over the entire range of the variables investigated.

Diagrams obtained by response surface analysis of the two series of test-runs were found useful in predicting the conditions under which a product of given yield and quality can be produced. Optimization of product yields and qualities could be achieved by subsequent series of factorially designed test-runs guided by the trends indicated by the present results.

REFERENCES

1. Sebastian, J. J. S. Process for Carbonizing Coal in a Laminar Gas Stream. U.S. Patent 2,955,988, October 11, 1960.
2. Davies, O. L., Ed., The Design and Analysis of Industrial Experiments. Hafner Publishing Co., N. Y., 1963.

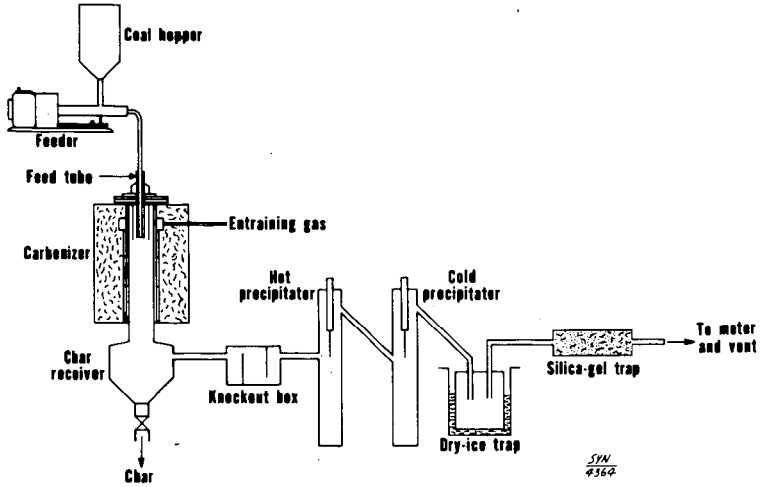


FIGURE 1. - Flash Carbonization of Powdered Coal with Externally Heated Reactor

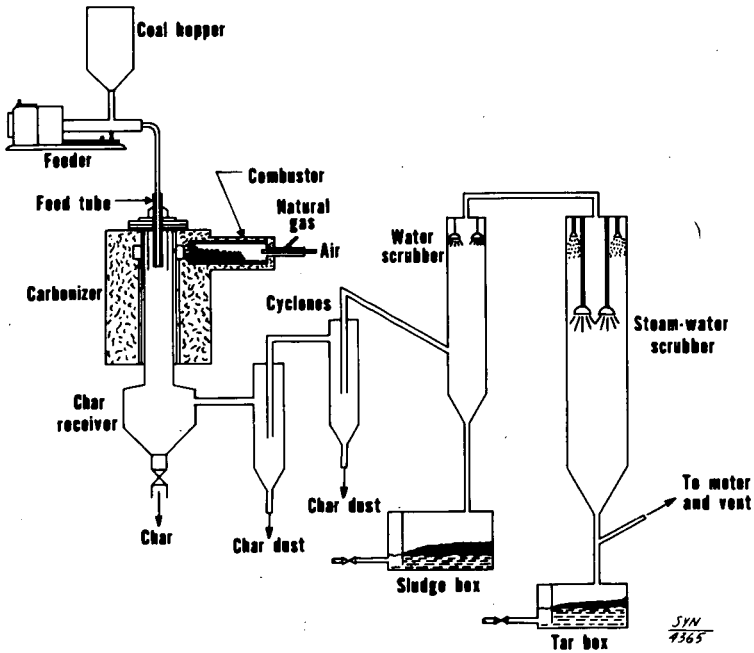
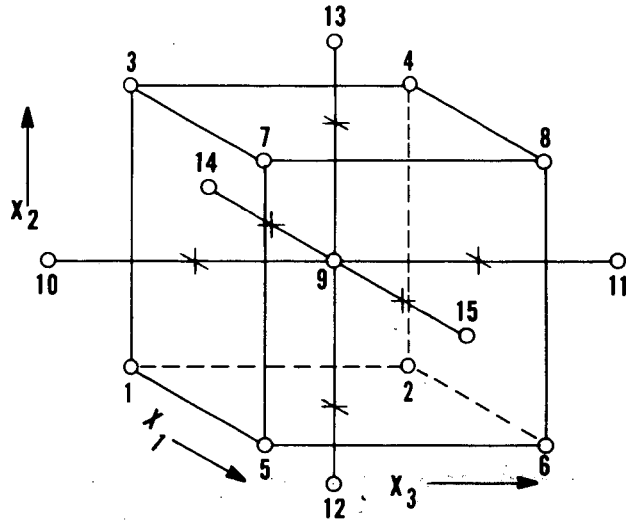


FIGURE 2. - Flash Carbonization of Powdered Coal with Internally Heated Reactor



EXPERIMENTAL
POINTS IN
CODED
COORDINANTS

POINT	X ₁	X ₂	X ₃
1	-1	-1	-1
2	-1	-1	1
3	-1	1	-1
4	-1	1	1
5	1	-1	-1
6	1	-1	1
7	1	1	-1
8	1	1	1
9	0	0	0
10	0	0	-2
11	0	0	2
12	0	-2	0
13	0	2	0
14	-2	0	0
15	2	0	0

FIGURE 3. - Three-Factor Composite Design

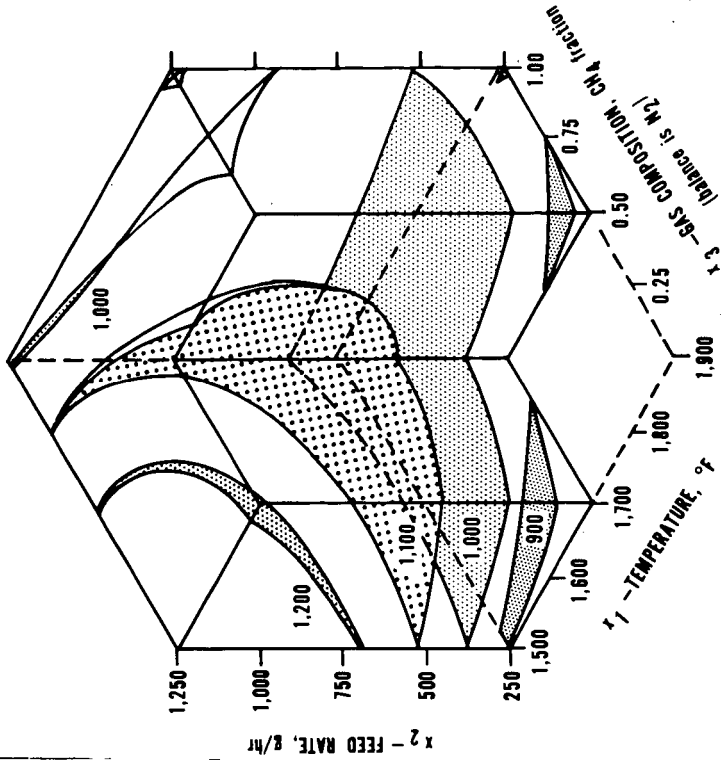


FIGURE 5. Three-Dimensional Response Surfaces, Char Yield in lbs/ton
—Internally Heated Carbonizer—

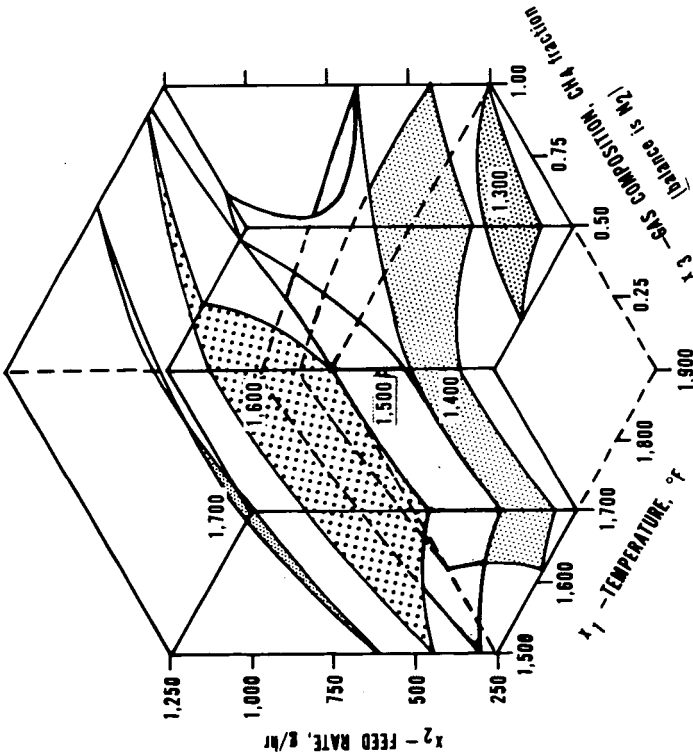


FIGURE 4. Three-Dimensional Response Surfaces, Char Yield in lbs/ton
—Externally Heated Carbonizer—

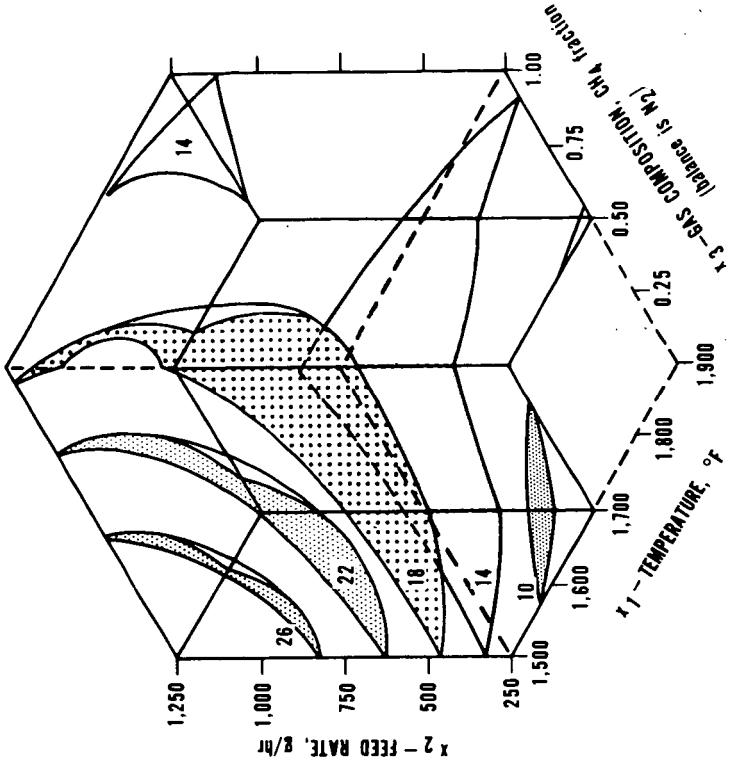


FIGURE 7. Three-Dimensional Response Surfaces, Percent Volatile Matter in Char
—Internally Heated Carbonizer—

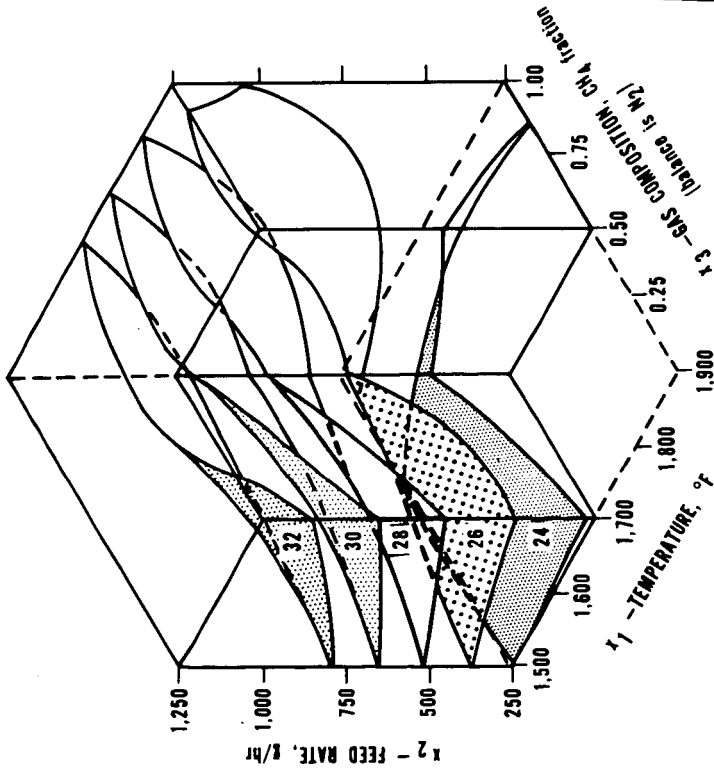


FIGURE 6. Three-Dimensional Response Surfaces, Percent Volatile Matter in Char
—Externally Heated Carbonizer—

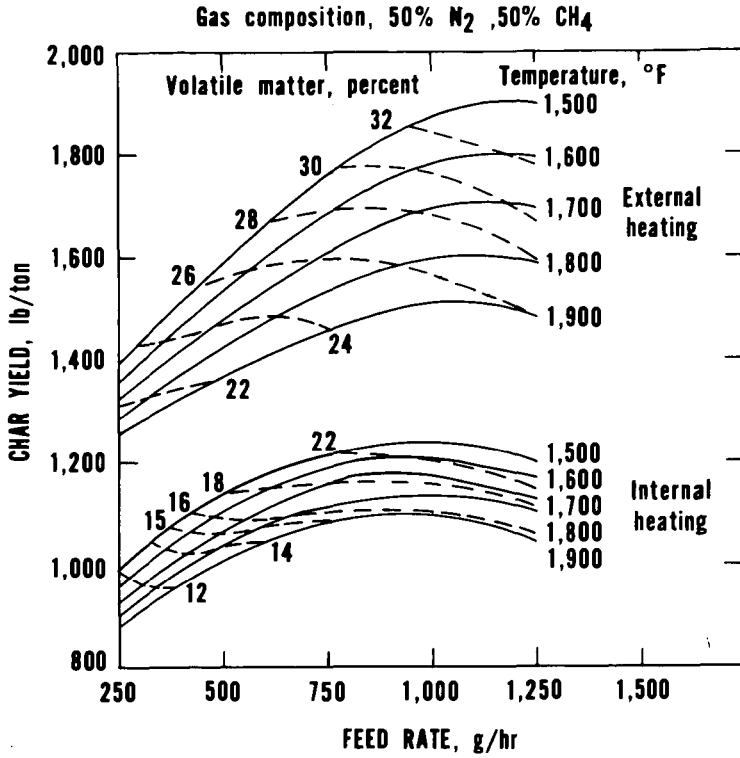


FIGURE 8. - Effect of Feed Rate and Temperature on Char Yield and Percent Volatile Matter in Char.

THERMAL CRACKING OF LOW-TEMPERATURE LIGNITE PITCH. PART II.

Richard L. Rice, Delmar R. Fortney, and John S. Berber

Morgantown Coal Research Center, Bureau of Mines,
U. S. Department of the Interior, Morgantown, W. Va. 26505

Thermal cracking of pitch from the carbonization of Texas lignite at low temperature has been under investigation as a means of producing aggregate and a binder that could be used to fabricate carbon metallurgical electrodes. A previous report on this subject covered preliminary tests on the thermal cracking of lignite pitch at 1,450° F in a 2-1/2 inch diameter reactor and showed that a variety of products could be obtained (1). In this work, a 4-inch diameter reactor was utilized to evaluate oil, coke, and gas quality and yields as a function of pitch feed rate temperature between 1,200° and 1,450° F.

EQUIPMENT AND MATERIALS

Figure 1 is a flowsheet of the system. The cracking unit consisted of a 93-inch length of 4-inch schedule 40, type 304, stainless-steel pipe, heated electrically. Total heating capacity of the cracker was 13.74 kw. A 1-inch pipe extended up through the center to within about 2-1/2 feet of the top and was perforated with 1/4-inch openings to allow withdrawal of gas and oil vapors from the reaction zone.

Pitch utilized as feed material was prepared by distilling crude low-temperature lignite tar under vacuum to an atmospheric boiling point of 660° F. The pitch yield was about 45% of the tar. Ultimate analysis and physical properties of the pitch are summarized in Table 1.

PROCEDURE

Pitch heated to 400° F was pumped from the feed tank by a gear pump through electrically heated lines into the top of the thermal cracker. Pitch utilized in all the runs came from the same source and was analyzed each time for C and H content. No significant difference was found. A flow of purge gas (11% CO₂, 88% N₂) swept products from the reaction zone. Cracked pitch was collected in the receiver and the oil was condensed and separated. Gas was passed through the scrubber and gas meter, then sampled and vented. After each run, which lasted 1-1/2 hours, the pitch flow was stopped and the pump was flushed with tar distillate fraction (from tank) to keep the pump from freezing during shutdown. It is not likely that true steady state was achieved owing to change in reactor geometry by build-up of coke. Also, heat transfer changed for the same reason. Steady state conditions are believed to have been approached, however.

After the cracking unit cooled, it was opened at the top and bottom and the coke was removed from the walls. Cracked pitch was removed from the receiver and oil was drained from the condenser and knockout. Each of the three products was weighed to the nearest one-tenth pound. The oil was distilled under vacuum to an atmospheric boiling point of 752° F, giving about 20 to 30% distillate and 70

to 80% residue. This residue was tested for carbon and hydrogen content and for softening point. If the test results were in the desired range, the residue was used as an electrode binder. The distillate was oxidized to phthalic and maleic anhydrides or separated into acids, bases, and neutral oils. The neutral oils were separated into n-olefins, paraffins, and aromatics.

Gas produced by the thermal cracking was analyzed by gas chromatography.

RESULTS AND DISCUSSION

Thermal cracking was carried out at temperatures from 1,200° to 1,450° F and pitch feed rates varying from 5.5 to 9.5 lb/hr.

A residence time (liquid basis) of nearly 0.70 second was found necessary to crack the pitch. In initial tests with a 5-foot-long cracker, the residence time was only slightly more than 0.55 second and cracking was not effected. Addition of a 2-1/2 foot length of pipe to the cracker increased the residence time to 0.68 second, an increase sufficient to crack the pitch.

Figure 2 shows the coke yield for three different feed rates at the temperatures investigated. Highest coke yields were obtained at the lowest feed rate, indicating that the lower space velocity (gas basis) led to a greater percentage of the pitch coming into contact with the hot wall of the cracker. The higher cracking temperatures also produced more coke. In the 2-1/2 inch diameter reactor that had been used before, coke yields were lower and cracked pitch yields were higher.

The oil yield, shown in Figure 3, was higher at the 5.5 lb/hr pitch rate, but a yield inversion occurred between 7.0 and 9.5 lb/hr. Thus, the oil yield decreased with increase in feed rate to a certain point, then increased. Possibly, the oil is derived by two means during the cracking process: (1) distillation of feed pitch, and (2) cracking, with the latter predominant at low rates and giving way to distillation at high rates. This seems to be verified by the decrease in carbon-hydrogen ratio of the oil residue with increase in feed rate, as shown in Figure 4. Figure 4 also shows that the carbon-hydrogen ratio of the oil residue increases with increasing temperature, this indicating the greater cracking effect of higher temperatures.

Gas yields, Figure 5, appear to have been less affected by feed rate until 1,300° F when the yields leveled out at different percentages, the leveling plateau being higher at lower feed rates. This indicates that higher cracking temperatures and longer residence time both tend to produce more gas due to the greater amount of cracking that occurs.

Typical material balances are given in Table 2. Product recovery was generally greater than 90 percent. Some losses were incurred in removing the coke from the reactor and the cracked pitch from the receiver. Material balances had been established for the system in previous experiments and were published (1). In these earlier tests, material balances ranged from 91.6 to 99.1 percent.

TABLE 2. - Material Balance for Thermal Cracking of
 Low-Temperature Lignite Pitch

Crude pitch rate, pph	Coke rate, pph	Oil rate, pph	Cracked			Total, pph	Loss, pph	Loss, pct
			pitch rate, pph	Gas rate, pph	Loss, pct			
9.0	2.5	2.5	0.8	2.6	8.4	0.6	6.7	
7.0	1.9	1.6	0.9	2.0	6.4	0.6	8.6	
9.2	2.5	2.6	0.9	2.6	8.6	0.6	6.5	
6.7	1.8	1.8	0.7	2.2	6.5	0.2	3.0	
9.5	2.7	2.7	0.9	2.7	9.0	0.5	5.2	
5.6	1.6	1.6	0.2	1.7	5.1	0.5	9.0	

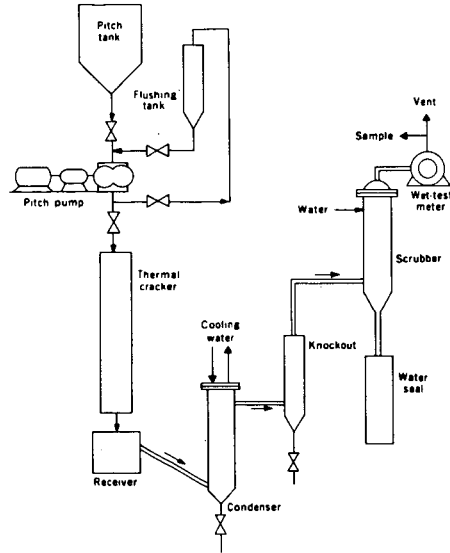


FIGURE 1. - Thermal Cracking System.

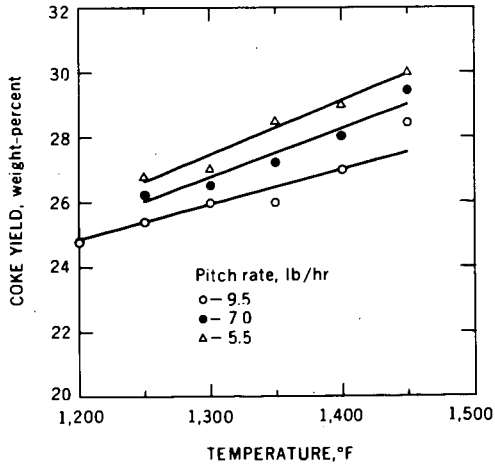


FIGURE 2. - Coke Yield as a Function of Pitch Rate and Temperature.

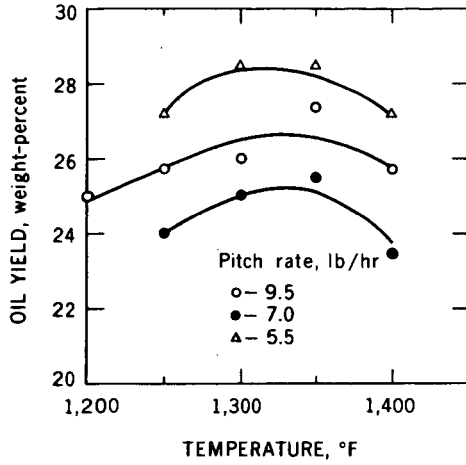


FIGURE 3. - Effect of Pitch Rate and Temperature on Oil Yield.

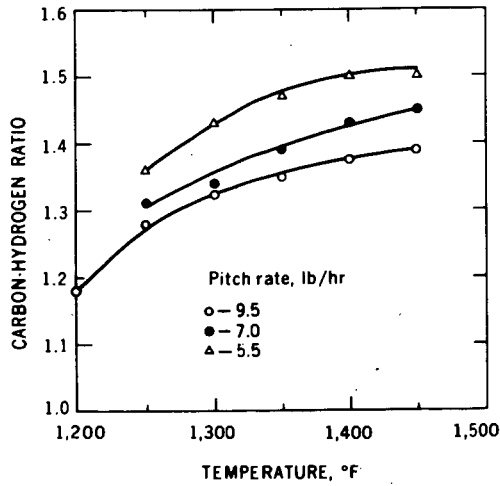


FIGURE 4. - Carbon-Hydrogen Ratio of Oil Residue.

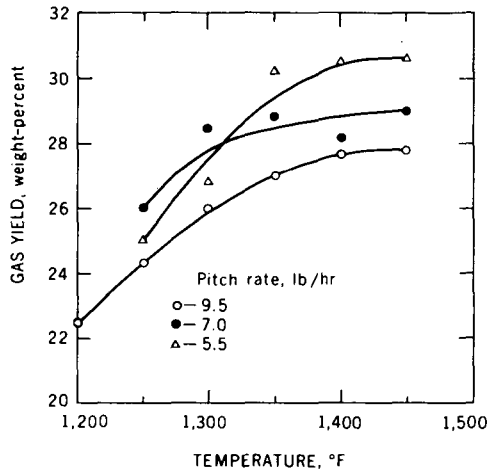


FIGURE 5. - Effect of Pitch Rate and Temperature on Gas Yield.

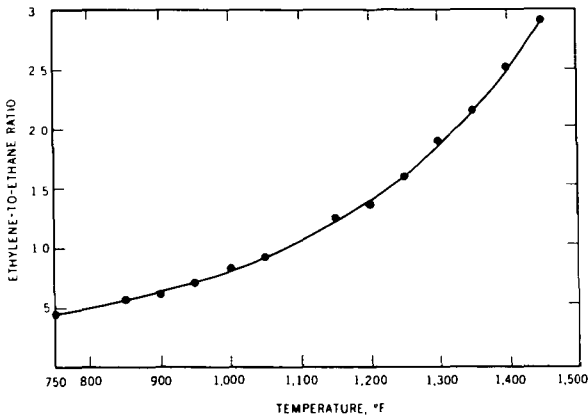


FIGURE 6. - Ethylene-to-Ethane Ratio Versus Temperature.

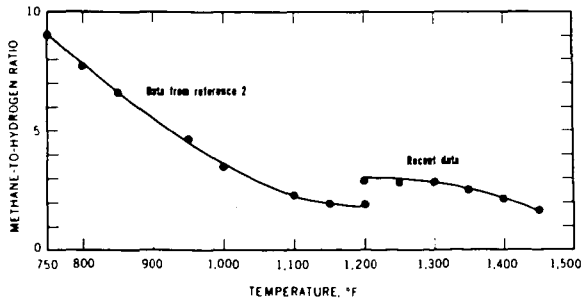


FIGURE 7. - Methane-to-Hydrogen Ratio Versus Temperature.

GAS TRANSPORT THROUGH SECTIONS OF SOLID COAL

F. S. Karn, A. G. Sharkey, Jr., B. M. Thames,
and R. A. Friedel

U.S. Department of the Interior, Bureau of Mines,
Pittsburgh Coal Research Center, Pittsburgh, Pa. 15213

ABSTRACT

Measurements were made for helium and methane flowing through thin disks of coal. Flow increased with pressure differential and temperature. At room temperature and a pressure differential of one atmosphere the flows along the bedding plane were: helium, $873 \times 10^{-10} \text{ cm}^2 \text{ sec}^{-1}$, and methane $1.2 \times 10^{-10} \text{ cm}^2 \text{ sec}^{-1}$. Flow rates were 50 percent lower across the bedding plane of the coal than along the coal seam. Activation energies were $3.9 \text{ kcal mole}^{-1}$ for helium and $13.6 \text{ kcal mole}^{-1}$ for methane for flow measured either along or across the bedding plane.

Knowing the rate at which gases will diffuse through coal will help not only in understanding reactions that can alter the properties of coal, such as oxidation, but also in studying the drainage of methane and other combustible gases from coal mines. Of all the methods of measuring diffusion, varying from the determination of massive emission from a coal-mine face to the measuring of desorption from micron-size particles, gas transport through solid coal sections appears the most promising. For the present experiments, thin disks were prepared from sections of coal cut parallel and perpendicular to the bedding planes of the coal seam. Tests with a series of disks from various locations in the same mine have shown reproducible results. Previous investigators have encountered difficulty in measuring low flow rates through solid coal. With a high sensitivity (500,000 divisions per torr) mass spectrometer we have measured the flow of methane and of helium, a reference gas, through solid sections of coal. Methane, the chief component of fire damp in a coal mine, has a very low rate of diffusion at the temperatures usually found in mines. Cervik^{1/} has discussed the flow of gas in coal mines; flow mechanisms include diffusion through the micropore structure and permeation through the fracture system.

Laboratory-diffusion experiments reported by other investigators have been of two types. One type of experiment is the measurement of sorption or desorption on ground coal where gas penetration into the ultrafine pore structure is diffusion controlled. A second technique is the direct measurement of gas flow across a thin section--the method used in this investigation. Zwietering^{2/} and Schilling^{3/} based diffusion coefficients on methane sorption on powdered coal. Graham^{4/} and Sevenster^{5/} reported diffusion coefficients for methane flow through a thin section of coal.

Investigator	Coal form	Pressure differential, torr	Gas flow rate, $\text{cm}^2 \text{ sec}^{-1}$
Swietering ^{2/}	Powder	27	2×10^{-12}
Schilling ^{3/}	Powder	736	3×10^{-10}
Graham ^{4/}	Disk	760	15×10^{-8}
Sevenster ^{5/}	Disk	400	3×10^{-11}

Sorption methods require an estimate of surface area, path length, and frequently a temperature extrapolation. Hofer^{6/} using adsorption and Walker using desorption^{7/} reported data in terms of $\text{cm}^3\text{g}^{-1}\text{sec}^{-1}$. These data are useful for comparing gas flow at various temperatures and pressures. The data presented in this paper may be more properly defined as flow rates than diffusion coefficients. The rates are expressed as $\text{cm}^2\text{sec}^{-1}$ based on the volume of gas transported, the geometric area of the face, and the thickness of the coal disk.

EXPERIMENTAL

Our experimental procedure is a modification of the method reported by Sevenster.^{5/} Coal disks were prepared from sound coal samples selected from the Bruceston Mine in the Pittsburgh seam (hvab coal). A sample was considered sound if it had no visible cracks and if the helium flow met standards established by testing a large number of coal disks. The disks were cut and ground to 13 to 19 mm diameter and 1 to 6 mm thickness. Disks about 1 mm thick were good for pressure differentials of 20 to 120 torr, but 6 mm thickness was necessary for pressure differentials of about 1 atmosphere. The disks were prepared so that gas flow could be measured either along or across the bedding plane of the coal. Each coal disk was sealed with epoxy cement to the flared end of a glass tube which had been fused inside another glass tube (Figure 1). This established two bulbs separated by the coal disk. The bulbs were evacuated to less than 1 micron pressure over a period of 18 hours at 100° C. After evacuation bulb A was filled with helium or methane at 20 to 760 torr. Bulb B was opened at appropriate intervals and the gas analyzed by mass spectrometry. Gas flows were measured at approximately 10° C intervals between room temperature and 100° C with the temperature controlled with an electric heating jacket and thermostat. Gas flow rates were expressed as cubic centimeters (at standard conditions) of helium or methane which would pass per second through a disk 1 square centimeter in cross section and 1 centimeter in thickness ($\text{cm}^2\text{sec}^{-1}$). The pressures in the two bulbs remained essentially constant during each experiment.

The pretreatment of the coal disk strongly influenced the initial rate of gas flow. The standard pretreatment (evacuation at 100° C for 18 hours) was designed to evacuate gases from the coal-pore system without altering the coal. Gas flow through a freshly evacuated disk was rapid at first but decreased with time, and reproducible data could only be obtained after an induction period of several days. After 3 days a constant flow rate was observed. Initial flow rates varied with the extent of evacuation, but in all cases the data were reproducible after a steady flow rate was established.

RESULTS

Data were obtained for 10 disks of varying thickness and cut either along or across the bedding plane of the coal seam. Helium flows were measured both along and across the bedding planes at several temperatures between 24° and 100° C. Arrhenius plots gave activation energies of 3.9 kcal mole⁻¹ for flow in either direction. The flow rate along the bedding plane was approximately three times the rate across the bedding plane. Helium flows were measured also at a series of pressures between 4 torr and 760 torr and at room temperature. These data were extrapolated to zero flow at zero pressure drop.

Since the flow varied directly with pressure, helium flow rates could be calculated at room temperature and a pressure differential of 1 atmosphere.

Gas flows at room temperature and a pressure differential of 1 atmosphere, observed directly, have been verified by extrapolation of a series of observations at several pressures and temperatures.

	Helium flow, $\text{cm}^2\text{sec}^{-1}\text{atm}^{-1} \times 10^{10}$		
	from temperature data	from pressure data	direct
Flow along	1114	786	780
Flow across	361	325	300

In like manner methane flows were measured both along and across the bedding plane at several temperatures. Arrhenius plots (Figure 2) gave activation energies of $13.6 \text{ kcal mole}^{-1}$ for flow in either direction. Methane flow also varied with pressure (Figure 3).

Methane flow rates were obtained from three sources.

	Methane flow, $\text{cm}^2\text{sec}^{-1}\text{atm}^{-1} \times 10^{10}$		
	from temperature data	from pressure data	direct
Flow along	1.2	1.2	1.2
Flow across	0.3	1.2	0.5

DISCUSSION

The mechanism for gas flow through coal could be molecular diffusion through the small pores, bulk diffusion through the larger pores, or permeation through the fracture system of the coal bed. Zwietering and van Krevelen,^{8/} using mercury penetration, measured the pore-size distribution for a low-volatile bituminous coal and found pores varying from a few angstroms to 50,000 Å. Cervik^{1/} described the various flow mechanisms encountered in mine workings. The reproducibility between coal disks makes it unlikely that fracture porosity was encountered in the laboratory tests described in this paper. Diffusion of gases through porous solids has been described^{9/} as proportional to the concentration gradient (Fick's law) and inversely proportional to the square root of the molecular weights of the gases. This paper has confirmed the applicability of Fick's law but not the molecular weight dependence. For molecular flow helium should diffuse at twice the rate of methane; the ratios observed were 800:1 at room temperature and 40:1 at 100°C . This might be explained as diffusion modified by gas adsorption on the pore walls or by activated diffusion as suggested in references 5 and 8.

Flow along the bedding plane was faster than flow across the bedding plane. The assumption that the rate of gas transport would vary inversely with the disk thickness was supported where a disk 2.2 mm thick was compared with a disk 6.0 mm thick.

Methane flow data obtained in this study ($1.2 \times 10^{-10} \text{ cm}^2\text{sec}^{-1}\text{atm}^{-1}$ along the bedding plane, 0.7×10^{-10} across) can be compared with the value $0.28 \times 10^{-10} \text{ cm}^2\text{sec}^{-1}\text{atm}^{-1}$ reported by Senenster.^{5/} The two experiments were carried out on different coals and possibly different orientations of the bedding plane. The activation energies reported here for methane ($13.6 \text{ kcal mole}^{-1}$) and helium ($3.9 \text{ kcal mole}^{-1}$) are consistent with data in the recent literature. Kayser^{10/} measured gas sorption on a 30-percent volatile-matter coal and reported 10.9 and 2.4 kcal mole^{-1} respectively.

REFERENCES

1. Cervik, J., Mining Congress Journal, 1967, 52.
2. Zwietering, P., Overeem, J., and van Krevelen, D. W., Fuel, Lond., 1956, 35, 66.
3. Schilling, H., Juntgen, H., and Peters, W., Sixth Inter'l Conf. on Coal Science, Munster, W. Germany, 1965.
4. Graham, I., Trans. Instn. Min. Engrs., Lond., 1918, 58, 32.
5. Sevenster, P. G., Fuel, Lond., 1959, 38, 403.
6. Hofer, L. J. E., Bayer, J., and Anderson, R. B., Bureau of Mines Rept. of Investigations 6750, 1966, 13 pp.
7. Walker, P. L., and Nandi, S. P., Special Report of Research SR-42, Feb. 15, 1964, The Pennsylvania State University, University Park, Pa.
8. Zwietering, P., and van Krevelen, D. W., Fuel, Lond., 1954, 33, 331.
9. Peters, W., and Juntgen, H., Brennstoff-Chemie, 1965, 46, No. 2, 38-44.
10. Kayser, H., and Peters, U., Seventh Inter'l Conf. on Coal Science, Prague, Czechoslovakia, 1968.

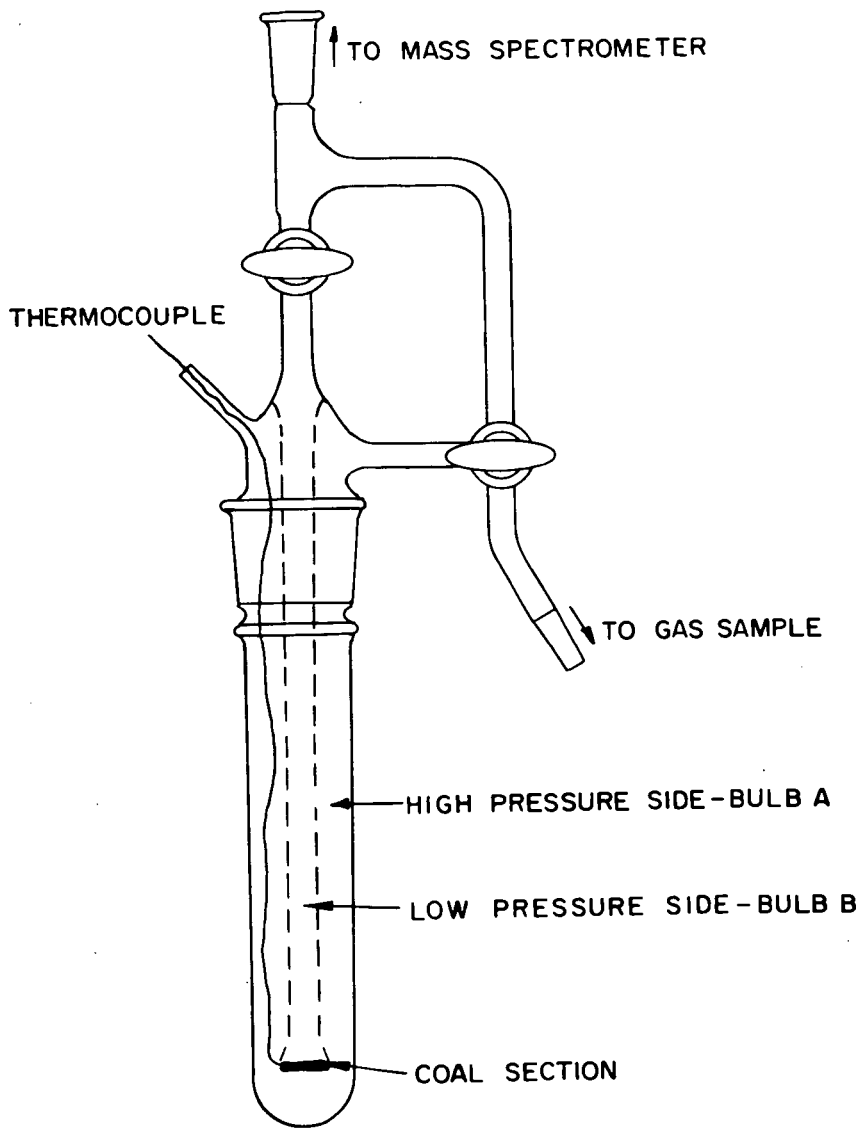


Figure 1.- Diffusion apparatus.

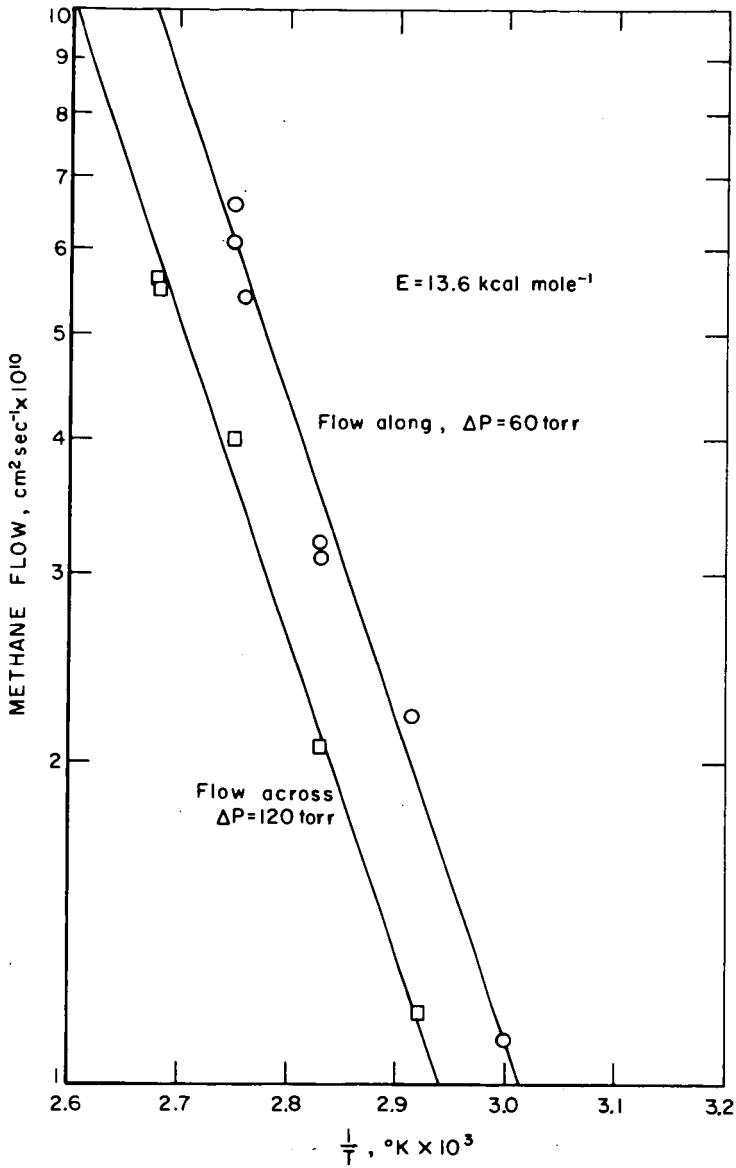


Figure 2.- Gas flow as a function of temperature. Methane flow along and across the bedding plane of Pittsburgh seam coal.

L-10760

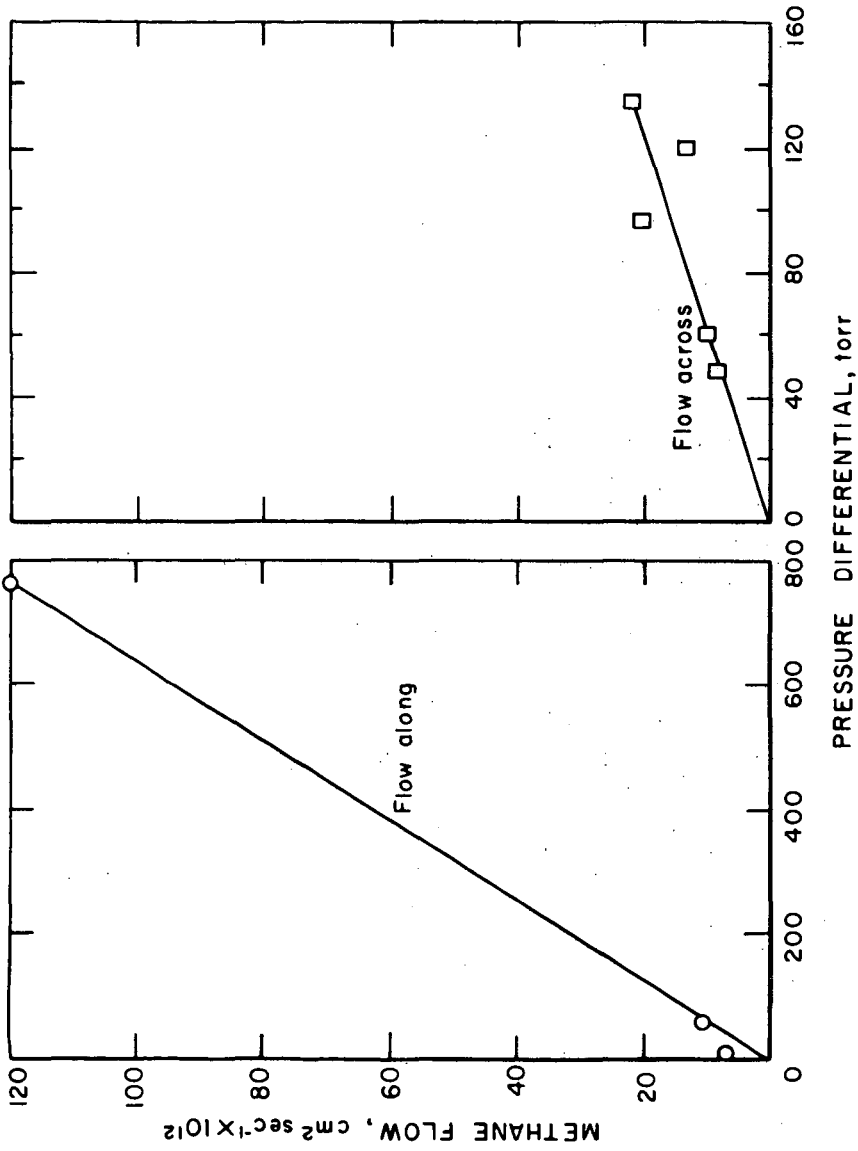


Figure 3.- Gas flow as a function of pressure differential. Methane flow along and across the bedding plane of Pittsburgh seam coal. Temperature 24° C.

The Different Effects of Flame Chemistry on the Formation
of Ethylene and the Oxides of Nitrogen in Flames

R. B. Rosenberg, S. A. Weil and I. H. Larson

Institute of Gas Technology, IIT Center,
Chicago, Illinois 60616

I. Introduction

The presence of atoms and free radicals in a methane-air flame produces not only carbon dioxide and water but also a large number of trace constituents in part-per-million and part-per-billion concentration levels. These include the oxides of nitrogen, unsaturated hydrocarbons, and partially oxygenated species. This paper will discuss the effects of flame chemistry on ethylene and the oxides of nitrogen. It will be shown that similarities do exist in the formation of these species in flames at atmospheric pressure, but the dissimilarities are of even greater interest than the similarities. In particular, ethylene is found in much higher concentrations in the flame than NO and NO₂ despite the fact that it is thermodynamically unstable whereas the nitrogen oxides are not.

Studies of the reactions of nitrogen, nitric oxide, and oxygen at high temperature indicate that the formation and disappearance of nitric oxide, the primary oxide of nitrogen found in flames and flue products, occur at very low rates.¹ With the additional fact that, in

¹ Kaufman, F. and Decker, L. J., "Seventh Symposium (International) on Combustion," Butterworths, London, 57 (1958).

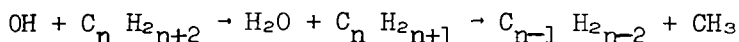
the methane-air flame and its hot reaction products, where there is usually little, if any, oxygen as such, it is apparent that the occurrence of the oxides of nitrogen are due to processes involving the reaction intermediates of the fuel-oxygen reaction. Details of such elementary processes are not known. The evidence obtained from studies on hydrogen-nitric oxide and hydrocarbon-nitric oxide flames indicates that if any nitric oxide exists in the reaction products, it is in equilibrium amounts² (that is, with nitrogen and oxygen).

² Wolfhard, H. G. and Parker, W. G., "Fifth Symposium (International) on Combustion," Reinhold, 71^a (1955).

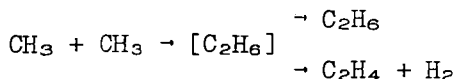
The general pattern of hydrocarbon oxidation in flames has been extensively studied although many of the detailed reactions remain to be identified and measured. It has been indicated³ that in oxygen-rich

³ Fristrom, R. M. and Westenberg, A. A., "Flame Structure," McGraw-Hill, New York, 750 (1955).

saturated hydrocarbon flames, hydrocarbons lower than the initial fuel are formed through the reaction sequence



This is the case when the initial radical formed is higher than ethyl, the CH_3 radical being split off to form the next lower olefin. In the methane-air flame, however, ethylene and other C_2 species are expected to arise as a result of the recombination of methyl radicals



From this point of view, ethylene formation in flames might be expected to follow the pattern of the cracking reaction of methane.⁴ However,

⁴ Palmer, H. B., Lahaye, J., and Hou, K. C., J. Phys. Chem., 72, 348 (1968).

it must be noted, as will be emphasized in this paper, that the rate of formation and decay of ethylene (as well as the oxides of nitrogen) cannot be considered as merely a pure pyrolysis or direct thermal reaction, the chemistry of combustion grossly interfering and competing with these mechanisms.

II. Experimental

This work was carried out with a large, single-port atmospheric pressure burner. The burner, schematically depicted in Figure 1, consists of a long vertical tube, approximately 3/4 inch in diameter, through which various methane-air mixtures are fed, surrounded by a larger annular region providing a secondary feed to the flame. By means of batch-sampling with a quartz microprobe⁵ and analysis with a

⁵ See Reference 3, Chapter 9.

Varian Aerograph series 1200 Chromatographic unit (employing a flame-ionization detector), concentration profiles for the various flat methane-air flames were obtained. A batch sampling time of about 15 seconds was used in most cases. The adjustable quartz probe was connected to the sampling and detection loop by means of Teflon-tubing. The diameter of the porous plate burner was 5.2 cm. Aeration of the primary mixture was varied from 84% to 100% to 120% of the stoichiometric air required for combustion. Primary mixture flow rates were varied from 15 to 30 SCF per hour, and secondary air flow rates were varied from 10 to 20 SCF per hour. NO and NO_2 were separated by means of molecular sieve/silica gel column. Ethylene concentration profiles were separated from other flame products by means of a column of Poropak-5 (50-80 mesh). The columns were operated at a temperature of 52°C to ensure good peak readout. Matheson Ultra-High Purity grade methane was employed in the study with no further purification.

III. Results and Discussion

A. Oxides of Nitrogen

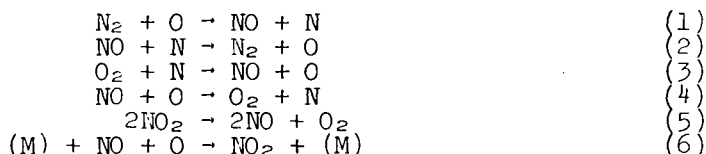
The formation of the oxides of nitrogen in methane-air flames is frequently considered as a side reaction of the combustion process; the oxides forming because air is heated to a high temperature. The data presented here indicates that this is not the case.

Figures 2 and 3 and Table 1 indicate that NO_2 is found in the "preheat" or transport region between the surface of the flat flame burner and the flame. The concentration of NO_2 increases from zero to as much as 10 ppm over this 1 mm distance. (In most cases, all reported concentrations are reproducible to within ± 1 ppm.)

The measured concentrations of the oxides of nitrogen before and after the flame show both an increase in the total, $\text{NO} + \text{NO}_2$, and a change in the ratio between these two species. For a stoichiometric methane-air flame with a secondary stream of air the concentrations are 7.5 ppm of NO_2 and 0 ppm of NO at a height of 0.1 cm. At a height of 1.1 cm (about 1.0 cm above the flame), the concentrations along the centerline of the burner have become 2.0 ppm of NO_2 and 11.0 ppm of NO . The decrease in the concentration of NO_2 is 5.5 ppm while the increase in NO is 11.0 ppm. Both Figures 1 and 2 indicate that the bulk species (nitrogen oxides) concentrations are essentially constant in the region above the flat flame.

Beyond this "flame zone" the final ratio of NO to NO_2 is strongly affected by the conditions in the "cooling" region above the flame. For example, in a stoichiometric flame the NO_2 is observed in increase from about 2 ppm at a height of 1.1 cm to almost 5 ppm at 3.6 cm above the burner. The NO concentration decreases from about 10 ppm to 7 ppm over this same distance. The total concentration remains constant at 12 ppm.

A model of the detailed chemistry of NO and NO_2 was developed to explain the rates of formation observed for the oxides of nitrogen. The reaction set includes the following reactions:



The importance of these reactions for NO_x formation in flames can be determined by comparing the calculated time required for each of these reactions to form the observed amount of NO and NO_2 with the actual time available for reaction in the flame. In this way, the relative importance of the reactions can be determined. The results are expressed for three specific regions. The regions, of course, are not independent but are closely linked to each other (Table II). The process can be visualized as follows: The fuel-air mixture leaves the burner and flows through the preheat region. Here, the gases rapidly increase in temperature because of the heat flowing back to the burner. The preheated mixture then ignites, causing a rapid change

in composition and a further increase in temperature. These rapid changes in composition from a fuel-air mixture to combustion products together with the steep temperature gradients make the flame analysis complex - hence, the segregation of the flame into regions which are easier to handle by conventional calculations.

In the preheat region, NO_2 is formed by rapid formation of NO and subsequent complete oxidation of the NO to NO_2 . The calculated residence times of reactions 1, 2, 3, and 4 are in good agreement with the actual residence time in the system. Figure 4 shows that the total concentration of the oxides of nitrogen (NO_x) increases while NO_2 decreases. The kinetics of reaction 5 adequately describe the decomposition step, while reactions 1 and 3 accounted for the increase in ($\text{NO} + \text{NO}_2$). Beyond the combustion region, the concentration of NO_x remains constant. The reaction of NO with atomic oxygen roughly predicts (within ± 10 ppm) the observed oxidation.

In an attempt to refine the calculations for the system, reactions 1 through 6 were combined with a mathematical model of a flat flame^{6,7} so that a complete time-temperature composition history of

⁶ Weil, S. A., Staats, W. R. and Rosenberg, R. B., Amer. Chem. Soc. (Div. Fuel Chem.) Preprints 10, No. 3, 84 (1966).

⁷ Weil, S. A., Institute of Gas Technology Res. Bull. No. 35, Chicago (1964).

the feed mixture could be determined. This calculation, performed on an electronic computer, did not serve to improve the disparity between observed and calculated values. The computation used the data for rate constants presently available in the literature.⁸ The combustion

⁸ Schofield, K., Planet Space Sci. 15, 643 (1967).

reactions were described by an overall kinetic expression of the form

$$\frac{d[\text{CH}_4]}{dt} = k_0 e^{-E_a/RT} [\text{CH}_4]^a [\text{O}_2]^b \quad (7)$$

The sources of the atomic species were assumed to be the equilibrium set of reactions:



The numerical predictions from this model show that this mechanism can produce only about 1 ppm of NO and almost no NO_2 . The most obvious source of error in the model is the assumption of equilibrium of O and N . It is well known that these species exist in concentrations greater than equilibrium (for N_2 and O_2 in a "non-reacting" system) but the exact concentrations at various points in an atmospheric pressure flame are not known.

B. Ethylene

The concentration of ethylene in various regions of a flame is strongly dependent upon the fuel/air ratio in the primary mixture. For a fuel-rich mixture (84% of stoichiometric air in the primary mixture with a secondary air stream), the peak ethylene concentration is almost 800 ppm. This occurs at a radial position of about 0.7 cm from the burner centerline (the burner diameter is 2.6 cm). The ethylene concentration at the centerline is about 650 ppm. For a stoichiometric primary fuel-air mixture, the maximum ethylene concentration occurs at the same point but its concentration is only 400 ppm. The concentration at the centerline of this flame is almost zero. For a fuel-lean flame (120% of stoichiometric) the maximum concentration of about 300 ppm occurs at the burner centerline. This concentration decreases slowly with distance from the center out to 2 cm. At this point, dilution by the secondary air becomes large, and the concentration decreases from about 240 ppm to about 50 ppm between 2.0 and 2.5 cm. (See Figures 5 and 6.)

One striking difference between NO_x and C_2H_4 is in the radial concentration profiles. As noted, both the fuel-rich and the stoichiometric flames show peak ethylene concentrations at 0.7 cm from the burner centerline. By contrast, the peak NO_x concentration occurs at the centerline in both of these flames, the concentration decreasing with increasing distance. The shape of the NO_x vs. distance curve changes as a function of the fuel/air ratio but the position of the maximum concentration is always at the burner centerline.

A second difference between NO_x and C_2H_4 involves the postcombustion reactions. Ethylene forms in the visible flame region in concentrations as high as 800 ppm. Most of this ethylene reacts in the post-combustion region with 3 ppm or less persisting to a height of 3.5 cm above the burner. Consequently, the conditions in the post-combustion region are of primary importance in determining the final emissions of C_2H_4 . By contrast, the total concentration of NO_x is determined by the flame and not by the post-combustion reactions. The total NO_x concentration remains constant in this region with only the ratio of NO to NO_2 changing. For example, the concentration of NO_x produced by a stoichiometric flame is about 12 ppm. Leaving the flame front, the combustion products will contain about 2 ppm of NO_2 and 10 ppm of NO. At a height of 3.5 cm, the concentrations are 5 ppm of NO_2 and 7 ppm of NO with the total concentration remaining constant.

C. Ethylene Formation in Methane-Air Flames

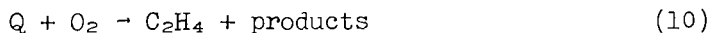
We have experimentally characterized the formation of ethylene (C_2H_4) in a flat methane-air flame. Analysis of the data has yielded these important conclusions:

- Oxygen has two important effects on C_2H_4 formation. 1) Oxygen or air in the primary methane-air mixture decreases the production of C_2H_4 . 2) Oxygen from the secondary air has the opposite effect. The diffusion of secondary air into the flame increases the C_2H_4 formation, with the increase being greatest for fuel-rich primary mixtures. We have developed a hypothesis for the effect of O_2 to explain this anomaly which is consistent with studies of ethylene formation in other systems.

- A methane-air flame does produce significant amounts of C_2H_4 in the combustion products. As much as 5 ppm have been observed. However, almost 800 ppm of C_2H_4 is present in the visible reaction zone of the flame.
- All of the C_2H_4 forms in the visible reaction zone. Most of this C_2H_4 reacts (to form CO_2 and H_2O) downstream of the flame. Quenching the flame by impinging it on a cold surface could greatly increase the amount of C_2H_4 in the combustion products by preventing the downstream reactions of C_2H_4 .

Hypothesis for Ethylene Formation

We are postulating that ethylene forms via a reaction of some species, as yet undetermined with oxygen. This can be illustrated as follows:



The oxygen has an alternate reaction path available to it:



Thus, there is a competition for the available oxygen between species Q (which forms ethylene) and CH_4 (which does not form ethylene). It is probable that this is not the only path by which ethylene forms, another being -



The effect of oxygen in the primary methane-air mixture is to consume CH_4 . By so doing, it decreases the formation of ethylene via Reaction 12. The effect of oxygen from the secondary air is to enhance Reaction 1 and thereby increase ethylene formation.

For the fuel-rich and stoichiometric flames (Figures 5 and 6), there is a considerable difference in the C_2H_4 concentrations between the burner center line and 0.7 cm from the center line; there is more ethylene at 0.7 cm than at the center line. This must be the result of some physical or chemical difference between the two points that is caused by some outside influence on the system because temperatures and species concentrations across a flat flame burner would otherwise be uniform.

The possibility of temperature differences causing C_2H_4 concentration differences was ruled out; previously obtained profiles show that the temperature difference between these two points is only a few degrees Kelvin - not enough to account for a 150-350 ppm concentration difference.

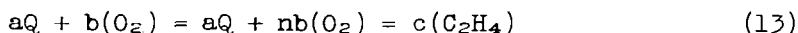
It appears that O_2 enhances the formation of C_2H_4 and that the difference in C_2H_4 concentrations between the two sampling points is the result of differing O_2 concentrations. Essentially, O_2 diffuses into the primary reaction zone from the secondary air stream. A concentration gradient results where there is approximately 0.5-3% more O_2 at a radial position of 0.7 cm than at the center line of the burner (Figures 7 and 8). The additional O_2 at 0.7 cm then causes C_2H_4 to form in excess of what is formed at the center line.

The O_2 profiles show that no oxygen from the secondary is present at the burner center line. Therefore, the value of the C_2H_4 concentration at this point is the value that would appear uniformly across the burner should no secondary air exist.

Beyond a radial position of 0.7 cm (Figures 5 and 6), the lower concentrations of ethylene are probably caused by lower temperatures overshadowing O_2 enhancement. More extensive dilution by secondary air will also account for part of the concentration decrease. In this region the formation reaction or reactions would have the potential of being speeded up by the additional O_2 found nearer the secondary. However, the lower temperatures would have the opposite effect of slowing the formation reaction. Apparently, temperature is the stronger of the two effects. This results in less C_2H_4 being produced at the edges of the burner.

The data indicate that there is also some upper limit of O_2 concentration in the primary, above which C_2H_4 formation is no longer detectably enhanced by secondary O_2 . For a 120% of stoichiometric flame composition, where considerable excess O_2 already exists in the primary reaction zone, the highest C_2H_4 concentration is at the center line and steadily decreases away from the center line (Figure 9).

We believe the excess O_2 from the primary stream overshadows any effect of O_2 from the secondary stream. For example, if some species Q reacts with O_2 to form C_2H_4 and the reaction is fast enough so that all of Q reacted prior to sampling, then the addition of even more O_2 (from the secondary) would not result in detecting more C_2H_4 :



where $n > 1$.

Literature lends support to the postulate of O_2 enhancing ethylene formation. Some related experiments by Robertson and Matson (reported by Minkoff and Tipper⁹) indicate that the addition of small quantities

⁹ Minkoff, G. J. and Tipper, C.F.H., "Chemistry of Combustion Reactions," London, Butterworths (1962).

of O_2 - up to 2% - to a fuel-rich acetylene mixture can increase ethylene production. More recently, Fenimore and Jones,² investigating ethylene flames, found the same indications of O_2 enhancement. The work of Haskell¹⁰ on the pyrolysis of propane between 350° and 700°C

¹⁰ Haskell, W. W., Dissert. Abst. 18, 80 (1958).

shows that an increase in ethylene formation is caused by the addition of small amounts of O_2 . The applicability of Haskell's work to the combustion of CH_4 is, however, in doubt.

Ethylene in Combustion Products

Our subsequent studies of ethylene formation will center around the primary reaction region because little or no formation occurs in other regions of this specific flame. The C_2H_4 concentration drops drastically just beyond the reaction zone and then remains essentially constant. The drop in concentration is approximately 500 ppm (Figure 1) and is probably due to the reaction of CH_4 with O_2 to form CO_2 and H_2O . The result is a final concentration of 0.5 to 3 ppm just beyond the reaction zone. The flue gas exiting from the experimental chamber also contains about 3.0 ppm of C_2H_4 . This concentration can presumably be enhanced if the C_2H_4 reactions are prevented from occurring, such as by quenching.

IV. Conclusion

The data of this work have confirmed that the formation of the oxides of nitrogen in atmospheric methane-air flames is primarily determined by the combustion chemistry with the chemistry of heated air playing a secondary role. Two different processes describe the NO_x -methane flame system: a) the decomposition of NO_2 to NO , and b) formation of additional NO from N_2 and O_2 -derived flame species. The disparity between calculated and observed values is attributed to the lack of a quantitative inclusion of the effects of "superequilibrium" concentrations of N and O atoms.

Ethylene is shown to form to a very large extent within the combustion zone of the flame (visible region). Although the final flue products contain little ethylene, concentrations approaching one part per thousand or observed in this flame region. Ethylene formation in flames is seen to be dependent upon post-combustion reactions whereas NO and NO_2 formation depend only upon flame zone reactions.

V. Acknowledgement

The authors wish to express their grateful appreciation to the American Gas Association whose support made this work possible.

Table I. CONCENTRATION CHANGES OF NO AND NO₂ WITH INCREASING HEIGHT OF THE BURNER FOR A STOICHIOMETRIC METHANE-AIR FLAME WITH AN AIR SECONDARY

	<u>0.0</u>	<u>-0.7</u>	<u>1.4</u>
	<u>ppm</u>		
0.1 cm Above Burner			
NO	0.0	0.0	0.0
NO ₂	7.5	7.1	5.7
NO + NO ₂	7.5	7.1	5.7
1.1 cm Above Burner			
NO	11.0	2.0	0.0
NO ₂	2.0	5.6	3.5
NO + NO ₂	13.0	7.6	3.5
Conc. Increases			
NO	+11.0	+2.0	0.0
NO ₂	-5.5	-1.5	-2.2
NO + NO ₂	+5.5	+0.5	-2.2

Table II. CALCULATED AND ACTUAL RESIDENCE TIMES*

	<u>Calculated</u>	<u>Actual</u>	<u>Difference</u> [†]
	Seconds		
<u>In the Preheat Region</u>			
$N_2 + O \rightarrow NO + N$	0.587×10^{-2}	1.22×10^{-2}	-0.634×10^{-2}
$O_2 + N \rightarrow NO + O$			
$N_2 + O_2 \rightarrow 2NO$	2.0×10^1	1.22×10^{-2}	$\approx 2.0 \times 10^1$
$NO + O \rightarrow NO_2$	2.12×10^{-2}	1.22×10^{-2}	$+0.90 \times 10^{-2}$
$2NO + O_2 \rightarrow 2NO_2$	4.25×10^{15}	1.22×10^{-2}	$\approx 4.25 \times 10^{15}$
<u>In the Combustion Region</u>			
$N_2 + O \rightarrow NO + N$	0.35×10^{-2}	1.04×10^{-1}	-0.965×10^{-1}
$O_2 + N \rightarrow NO + O$			
$2NO_2 \rightarrow 2NO + O_2$	0.78×10^{-2}	1.04×10^{-1}	-0.922×10^{-1}
$N_2 + O_2 \rightarrow 2NO$	1.1×10^1	1.04×10^{-1}	$\approx 1.1 \times 10^1$
<u>In the Cooling Region</u>			
$NO + O \rightarrow NO_2$	5.0×10^{-2}	6.25×10^{-2}	-1.25×10^{-2}
$2NO + O_2 \rightarrow 2NO_2$	4.8×10^{15}	6.25×10^{-2}	$\approx 4.8 \times 10^{15}$

* The comparison of these reactions has been made on the basis of the residence time of reaction necessary to form the experimental observed quantity of NO_x .

† Seconds calculated minus seconds actual.

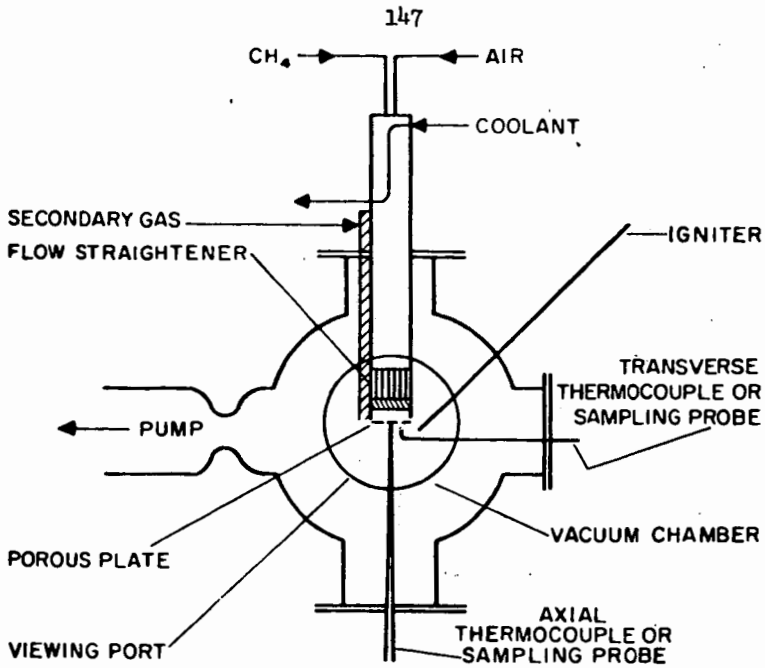


Fig. 1. - BURNER DESIGNED TO DETERMINE CHEMISTRY OF NITROGEN OXIDES PRODUCED IN METHANE-AIR FLAMES

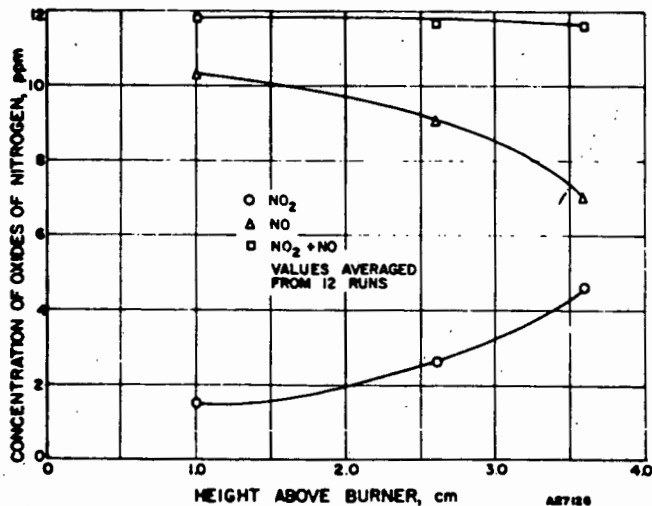


Figure 2. TOTAL CONCENTRATION OF OXIDES OF NITROGEN IN A METHANE-AIR STOICHIOMETRIC FLAME AT THE BURNER CENTER LINE

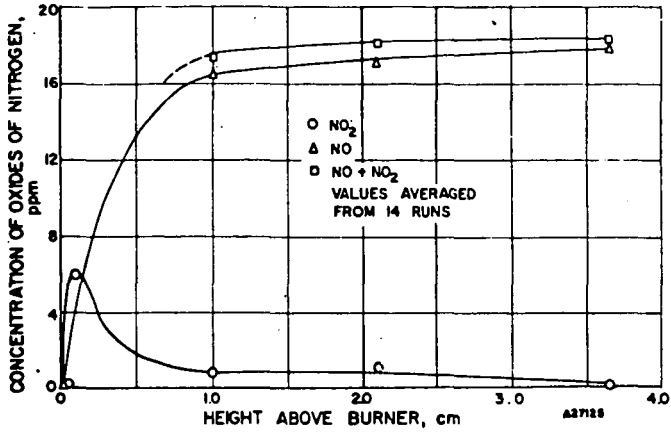


Figure 3. TOTAL CONCENTRATION OF OXIDES OF NITROGEN IN A FUEL-RICH (84% of Stoichiometric) FLAME AT BURNER CENTER LINE

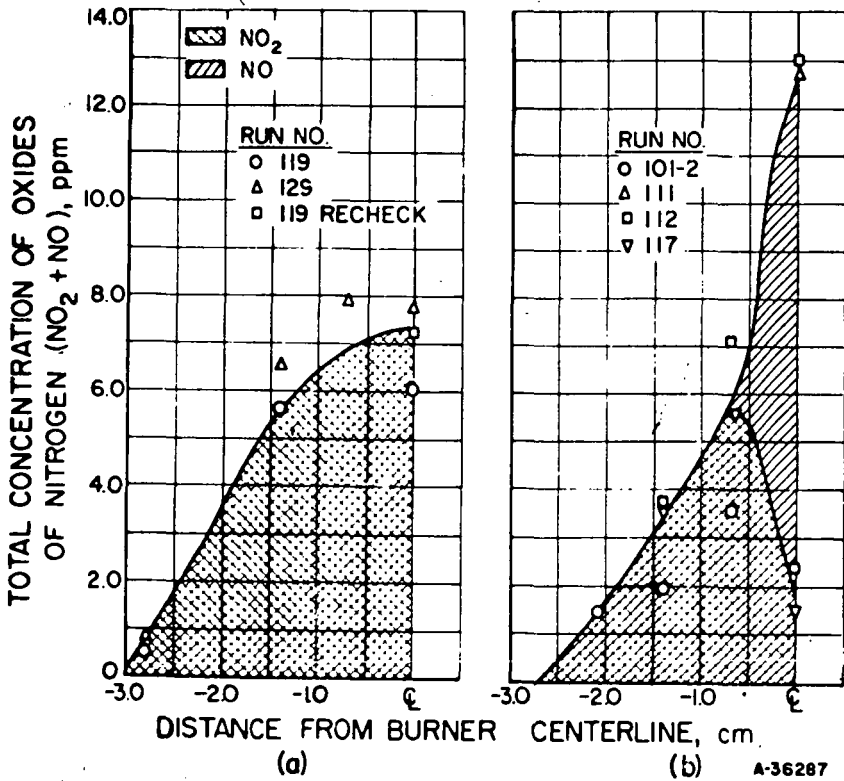
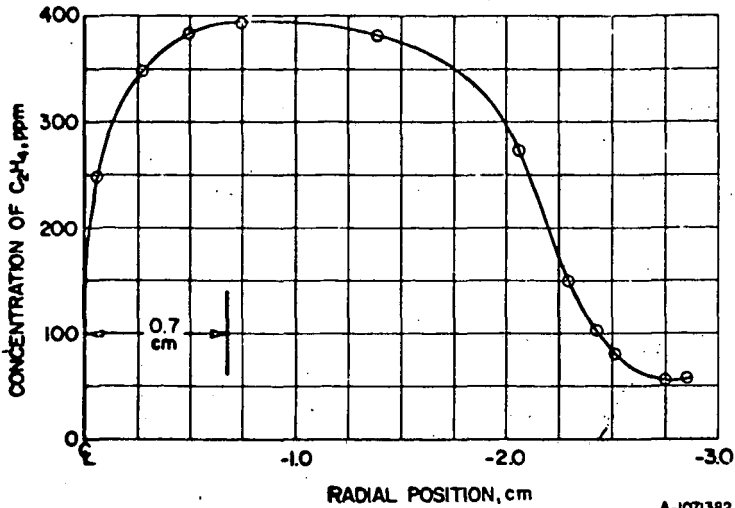
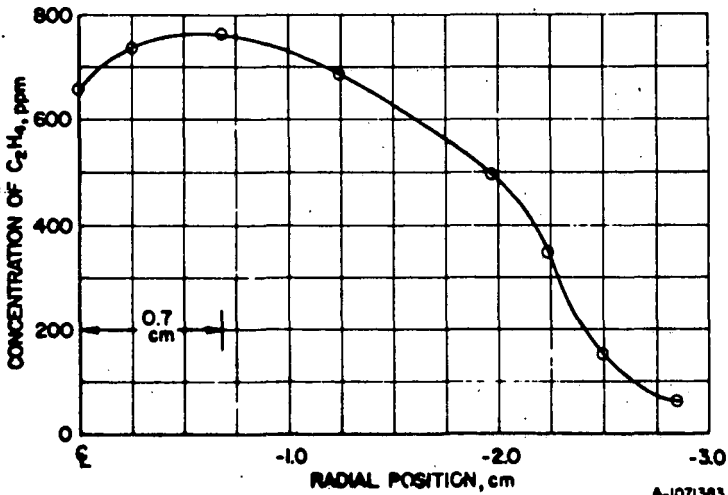


Figure 4. TOTAL CONCENTRATION OF NITROGEN FOR A METHANE-AIR STOICHIOMETRIC FLAME AT a) 0.1 cm AND b) 1.1 cm ABOVE BURNER



A-1071382

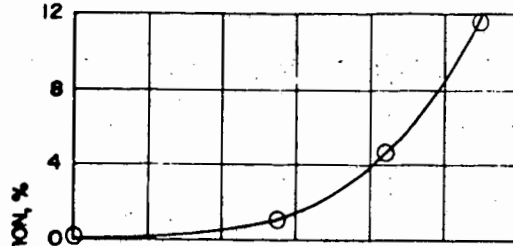
Figure 5 ETHYLENE CONCENTRATION AS A FUNCTION OF RADIAL POSITION AT 0.1 cm ABOVE THE BURNER FOR STOICHIOMETRIC CH_4 -AIR FLAME



A-1071383

Figure 6. ETHYLENE CONCENTRATION AS A FUNCTION OF RADIAL POSITION AT 0.1 cm ABOVE THE BURNER FOR 84% OF STOICHIOMETRIC CH_4 -AIR FLAME

(a)



(b)

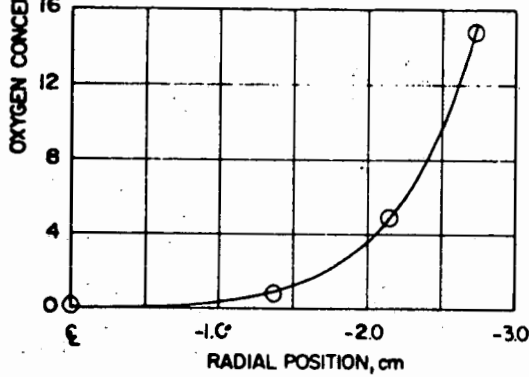
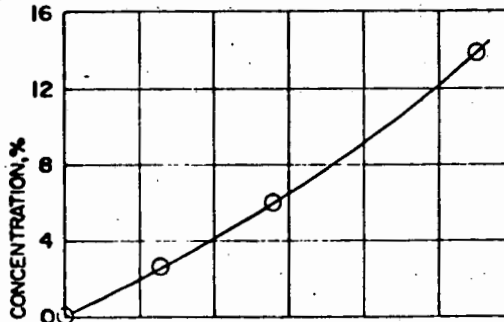


Figure 7. OXYGEN CONCENTRATION IN 84% OF STOICHIOMETRIC CH₄-AIR FLAME (From Secondary Air Only) AT a) 1.1 cm AND b) 0.5 cm ABOVE BURNER

(a)



(b)

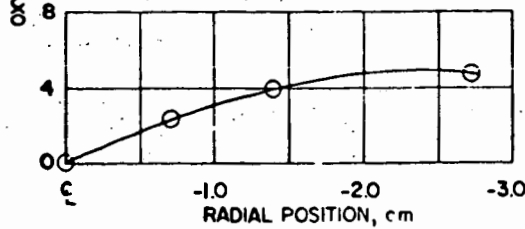


Figure 8. OXYGEN CONCENTRATION IN 100% OF STOICHIOMETRIC CH₄-AIR FLAME (From Secondary Air Only) AT a) 1.1 cm AND b) 0.5 cm ABOVE BURNER

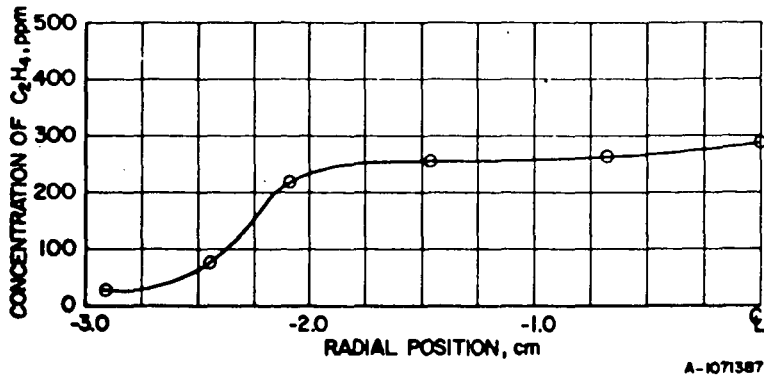


Figure 9. ETHYLENE CONCENTRATION AS A FUNCTION OF RADIAL POSITION AT 0.1 cm ABOVE BURNER FOR 120% OF STOICHIOMETRIC CH₄-AIR FLAME

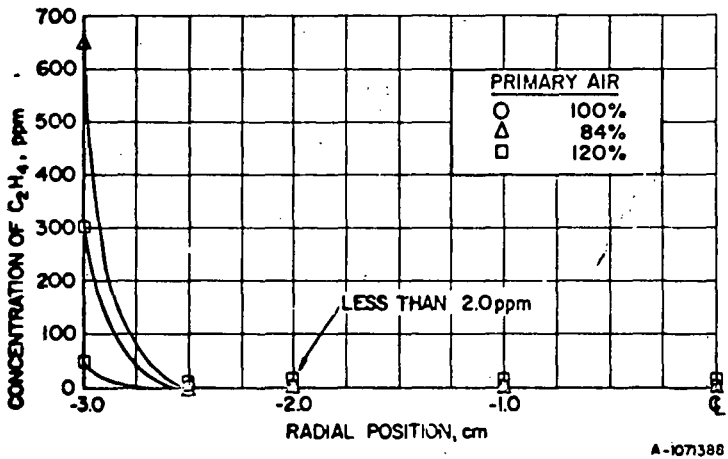


Figure 10. CONCENTRATION OF ETHYLENE AT CENTER LINE OF CH₄-AIR FLAMES

Fast-Flow Kinetic Studies of Methane Reactions with Atomic Oxygen at Room Temperature

R. V. Serauskas and R. A. Keller

Institute of Gas Technology, IIT Center
Chicago, Illinois

I. Introduction

Many contributions to kinetic rate knowledge have resulted from premixed flame studies.^{1,2,3} A flame, consisting of a multi-reaction complex medium, lends

1. R. M. Fristrom, and A. A. Westenberg, "Flame Structure," McGraw-Hill, New York (1965).
 2. S. W. Benson, "The Foundations of Chemical Kinetics," McGraw-Hill, New York, 276 (1960).
 3. N. Basco and R.G.W. Norrish, *Can. J. Chem.* **38**, 1769 (1960).
- itself to unambiguous kinetic analysis only with difficulty. Specifically, the more recent flame studies of combustible methane mixtures⁴ have directed much inter-
4. R. M. Fristrom, C. Grunfelder, and S. Favin, *J. Phys. Chem.* **64**, 1386 and 1393 (1960).

est of late toward the elementary reactions in the methane oxidation scheme. New and improved techniques for the study of atom and radical reactions have led to renewed kinetic studies which have confirmed some earlier results and have been at odds with others. The addition of various chemically perturbing agents to the O-atom/CH₄ system, for example, allow for the study of some elementary oxidation reactions at room temperature by the more convenient and unambiguous flow-discharge techniques. However the results in all cases have not been uniform, especially in systems containing oxygen.⁵

5. F. Kaufman, in "Progress in Reaction Kinetics," Vol. 1 (ed. G. Porter), Pergamon Press, New York, 1 (1961).

In this work, a number of methane-oxygen reactions have been studied employing a fast-flow reaction system, coupled directly with a Bendix model 3015 time-of-flight mass spectrometer. N and H-atom titrations as well as Woods-Bonhoeffer discharges are employed in generating the active species.

II. Experimental

The reaction system employed is depicted schematically in Figure 1. A Woods-Bonhoeffer discharge-flow system is in train with a Bendix model 3015 time-of-flight mass spectrometer. Atoms or radicals enter in the central annular space in the reaction train. Reactants enter through the central tube fitted with a Teflon "Swage" gland to permit movement along the reaction train axis. In this way, the distance of the mixing region from the molecular leak (aluminum foil disk with an 0.005 inch pinhole) can be varied. A 40 liter/sec Stokes' pump throttled through a linear flow velocity of about 10 meters/sec and a reaction region pressure in the 10 to 1000 millitorr range. Knowing the volumetric flow rate, v , and the diameter, d , of the reactor, the distance, z , of the tube mouth from the TÖF sampling leak can be related to the time variable, t , in an absolute fashion by the relation:

$$t = \left(\frac{\pi d^2}{4v}\right) z^{-1}$$

This reaction holds strictly for the case of a cylindrical reactor and laminar flow.⁵ The methane, used without further purification, was Matheson Ultra-High Purity grade. Matheson Research grade HCl was employed in the catalytic study. Matheson High Purity grade NO₂ was redistilled in vacuo for use in the generation of OH radicals. The oxygen used was Ultra-High Purity grade Matheson, employed without further purification.

Oxygen atoms were generated by two methods: (1) the discharge of a 1 to 9 O₂/Ar mixture (2) the very rapid gas-phase titration of NO by N atoms (N + NO →

N_2+O), the N atoms being generated by discharging N_2 . The hydroxyl radicals were generated by the rapid gas phase titration of NO_2 with H atoms ($H+NO_2 \rightarrow NO+OH$), the H atoms being generated by discharge of a 5% $H_2/95\%$ Ar mixture containing a trace of water in order to aid dissociation (The walls of the reaction train were coated with phosphoric acid to give low, reproducible wall-recombination effects.) In all cases the temperature remained within 1° of $298^\circ K$.

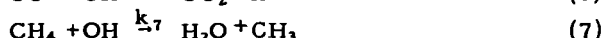
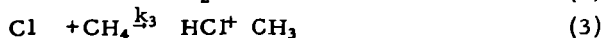
III. Results and Discussion

A. Methane-O-atom Reaction with HCl Catalyst

At room temperature the reaction between methane and atomic oxygen is extremely slow because the reaction has a heat of activation between 8-9 kcal/g-mole.¹ Consequently, if one wished to study the reaction, the investigation must be conducted at elevated temperatures or a suitable catalyst must be added for room temperature studies.

We selected hydrogen chloride gas as a catalyst for this study because it is known to accelerate the reaction between methane and atomic nitrogen.

The following reactions may be considered in this system:



This reaction scheme yields a series of 12 simultaneous differential equations that are extremely difficult to solve analytically.

As a first approximation, we might eliminate all of the reactions with an energy of activation of 8 kcal/g-mole or more. At $300^\circ K$, the difference in rate between a reaction with $E_a = 4$ kcal/g-mole and one with 8 kcal/g-mole is a factor of about 10^3 . Thus, two reactions with approximately equal reactant concentrations and frequency factors will differ in rate by 1000 if they have such an activation energy difference.

Using this criterion, Table I^{1,6} shows that Reaction 7 through 11 can be eliminated from the reaction scheme. K. Schofield, *Planet. Space Sci.* 15, 643 (1967).

We will show later that an error has apparently been introduced by eliminating Reaction 9. The concentration of H atoms apparently is sufficiently high to offset the activation energy difference.

A second approximation involves the "steady-state assumption." This assumption specifies that the rate expressions for all of the active species be set equal to zero. For example, the rate of formation of chlorine atoms is as follows:

$$\frac{d(Cl)}{dt} = k_1(HCl)(O) - k_3(Cl)(CH_4) \quad (13)$$

Using the steady-state assumption yields the following equation:

$$k_1(HCl)(O) - k_3(Cl)(CH_4) = 0 \quad (14)$$

The following equations are obtained by using the steady-state assumption for CH_2 , CH_3 , and OH :

$$k_4(\text{CH}_3)(\text{O}) - k_5(\text{CH}_2)(\text{O}) = 0 \quad (15)$$

$$k_3(\text{Cl})(\text{CH}_4) - k_4(\text{CH}_3)(\text{O}) = 0 \quad (16)$$

$$k_1(\text{HCl})(\text{O}) - k_2(\text{OH})(\text{O}) + k_4(\text{CH}_3)(\text{O}) - k_6(\text{CO})(\text{OH}) = 0 \quad (17)$$

This series of four algebraic equations can now be solved for the concentrations of the active species:

$$(\text{Cl}) = \frac{k_1(\text{HCl})(\text{O})}{k_3(\text{CH}_4)} \quad (18)$$

$$(\text{CH}_2) = \frac{k_1(\text{HCl})}{k_5} \quad (19)$$

$$(\text{CH}_3) = \frac{k_1(\text{HCl})}{k_4} \quad (20)$$

$$(\text{OH}) = \frac{2k_1(\text{HCl})(\text{O})}{k_2(\text{O}) + k_6(\text{CO})} \quad (21)$$

The rates of the reactions of O, CO, and CO₂ can now be written and simplified using the above expressions for the concentrations of the active species.

$$\frac{d(\text{O})}{dt} = -3k_1(\text{HCl})(\text{O}) - \frac{2k_1k_2(\text{HCl})(\text{O})^2}{k_2(\text{O}) + k_6(\text{CO})} \quad (22)$$

$$\frac{d(\text{CO})}{dt} = k_1(\text{O})(\text{HCl}) - \frac{2k_1k_6(\text{HCl})(\text{O})(\text{CO})}{k_2(\text{O}) + k_6(\text{CO})} \quad (23)$$

$$\frac{d(\text{CO}_2)}{dt} = \frac{2k_1k_6(\text{HCl})(\text{O})(\text{CO})}{k_2(\text{O}) + k_6(\text{CO})} \quad (24)$$

For the conditions of this study, $(\text{CO}) < 1/5 (\text{O})$ so that $k_2(\text{O}) \gg k_6(\text{CO})$. The rate expression for the disappearance of atomic oxygen is, therefore:

$$+ \frac{d(\text{O})}{dt} = -5k_1(\text{HCl})(\text{O}) \quad (25)$$

Integrating this expression yields -

$$\ln(\text{O}) = -5k_1(\text{HCl})t + \ln(\text{O})_0 \quad (26)$$

With $t = \text{time} = \frac{z}{u}$, $z = \text{reactor distance}$, and $u = \text{linear flow velocity}$,

$$\ln(\text{O}) = -5k_1(\text{HCl})\frac{z}{u} + \ln(\text{O})_0 \quad (27)$$

Therefore, a plot of $\ln(\text{O})$ vs. z should yield a straight line. Figure 2 shows the experimental data plotted in this manner. The reaction exhibits first-order behavior between 100 and 300 mm, but deviates from this behavior beyond this point. It almost appears that the reaction stops shortly beyond the 300-mm point. Our analysis will concentrate on the first 300 mm of the reactor. In this region the slope of the curve yields a rate constant of 2.65×10^{-15} cu cm/particle-sec. If this reaction has a steric factor of 0.1, the activation energy is about 5 kcal/g-mole.

This value for the rate constant is consistent with the postulated mechanism. The rate expression for O atom disappearance (Equation 25) shows that Reaction 1 is the slowest or rate-controlling step of the mechanism. Comparison of the value of $k_1(2.65 \times 10^{-15})$ with the values in Table II shows that this is indeed the case.

Equation 23 for the formation of CO can be simplified by applying the values of the rate constants and the various concentrations:

$$\frac{d(\text{CO})}{dt} = k_1(\text{O})(\text{HCl}) \quad (28)$$

Substituting the expression for the O atom concentration yields -

$$\frac{d(\text{CO})}{dt} = k_1(\text{HCl})(\text{O})_0 e^{-5k_1(\text{HCl})t} \quad (29)$$

Integrating Equation (29) yields -

$$(\text{CO}) = \frac{(\text{O})_0}{5} [1 - e^{-5k_1(\text{HCl})\frac{z}{u}}] \quad (30)$$

The rate expression for CO₂ can now also be integrated:

$$(\text{CO}_2) = \frac{0.4k_1k_6}{k_2} (\text{HCl})(\text{O})_0 \left[t + \frac{e^{-5k_1(\text{HCl})t} - 1}{5k_1(\text{HCl})} \right] \quad (31)$$

The integrated expressions show the correct qualitative details for the reaction, but the quantitative predictions are not accurate. For example, the equations

predict that CO should be present in greater concentrations than CO₂. Figure 3 shows that this effect is indeed observed. However, the quantitative predictions are not in agreement; the predicted rates of formation are too low.

Another qualitative feature of the reaction is shown in Figure 4. The amount of CO formed increases by a factor of 5 (in the early stages of the reaction) as the initial HCl concentration is increased. This is predicted by Equation (30).

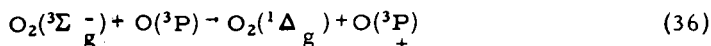
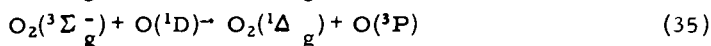
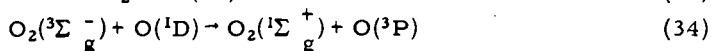
The equations predict the qualitative but not the quantitative features of the experimental data. The data quality has been determined from a mass balance on the reactants and products. About 80% of the O atoms that react are recovered as either CO or CO₂. The reaction also forms water and molecular oxygen. The amount of water is quite small and the amount of O₂ formed is also small and cannot be accurately determined because of the large background O₂ concentration. Within these limitations, the mass balance is good and indicates that the data are internally consistent. From this, it appears that the reaction scheme is incomplete.

The most probable discrepancy in the proposed scheme is the elimination of Reaction (9). This reaction can be rapid if the concentration of H atoms is sufficiently high. H atoms are formed by Reactions (2) (a very fast reaction), (5), and (6). Therefore, they may be present in a sufficiently high concentration to make Reaction (9) significant. Reaction (9) produces both CH₃ and OH radicals. CH₃ reacts, via CH₂, to form CO, and the CO is oxidized to CO₂ by OH. Hence, inclusion of Reaction (9) should provide for faster rates of CO and CO₂ formation.

B. Possible Influence of Excited O₂

The above data shows that about 25% of the original methane will be converted to products (CO + CO₂) over a reaction zone length of 350 mm. Figure 5 presents some data for this system, comparing the reaction of discharged O₂ with CH₄ to that of O atoms generated in the titration of NO with N atoms. Curve A indicates the formation of CO₂ from a CH₄/HCl mixture using O atoms generated in the gas-phase titration: N + NO → N₂ + O. Curve B gives the data for the same system after adding about 15 X 10⁻³ mm Hg of ground-state O₂ to the atom stream, which also contains about 15 X 10⁻³ mm Hg of O atoms as determined by the gas-phase titration. Discharged O₂ (with about 15 X 10⁻³ mm Hg of O atoms and 15 X 10⁻³ mm Hg of O₂) used in place of the O atom stream obtained by titration yields Curve C, which shows considerable enhancement of the combustion process over Curves A and B. The data of Curves A and B lend support to the possibility of a specific effect of molecular oxygen on O atom reactions; excited-state molecular O₂ may be the chemically perturbing agent for these systems.

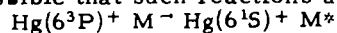
The only difference between Curves C and B is that the former presents data for the CH₄/HCl/O system in the presence of excited molecular O₂, while the latter involves only added ground-state O₂. In an electrical discharge, the following processes can take place:



The radiative loss rate constant for O₂(¹Σ⁺) may be as large as 10⁻¹³cc/particle-sec. and 10⁻²²cc/particle-sec. for O₂(¹Δ_g),⁸ thus allowing O₂(¹Δ_g) to interfere in chemical reaction systems at moderate ⁸ to rapid flow rates.⁷ ⁸ (Although quite

7. A. M. Falick and B. H. Mahan, *J. Chem. Phys.* 47, 4778 (1967).
 inert toward saturated hydrocarbons, O₂(¹Δ_g) is known to react readily with atoms, free-radicals, and unsaturated compounds.)⁸

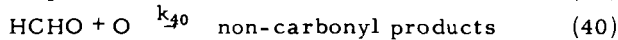
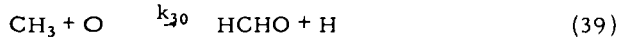
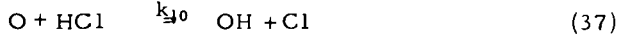
It is also possible that such reactions as



may occur in systems manometered with mercury, this effect should be observable regardless of the type of discharge used. Preliminary indications show that (37) is not significant in our system.

C. Detection of Carbonyls in CH₄-O atom Reactions

Our flow system provides for a "residence time-to-reaction length" ratio of $t/z = u^{-1} \approx 1$ msec/cm. (The linear flow rate is about 10 meters/sec.) The kinetic data points are usually spaced 10 cm apart. Therefore, any formaldehyde originally formed in the reaction of methyl radicals with O atoms must be reduced to a concentration lower than the detectable limit (about 1.60×10^{13} molecules/cu cm in this case) within 0.01 sec. The problem of HCHO formation can then be demonstrated by a crude estimate employing the following simplified steady-state scheme:



$$\frac{d[\text{Cl}]}{dt} = \frac{d[\text{CH}_3]}{dt} = \frac{d[\text{HCHO}]}{dt} = 0 \quad (41)$$

Then,

$$[\text{Cl}] = \frac{k'_{10}[\text{O}][\text{HCl}]}{k_{20}[\text{CH}_4]} \quad (42)$$

$$[\text{CH}_3] = \frac{k_{20}[\text{CH}_4][\text{Cl}]}{k_{30}[\text{O}]} \quad (43)$$

$$[\text{HCHO}] = \frac{k_{30}[\text{O}][\text{CH}_3]}{k_{40}[\text{O}]} = \frac{k_{30}}{k_{40}}[\text{CH}_3] \quad (44)$$

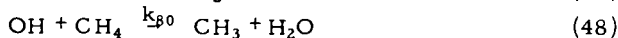
Thus,

$$[\text{HCHO}] = \frac{k'_{10}}{k_{40}}[\text{HCl}] \quad (45)$$

With $[\text{HCHO}] = 0.5$ millitorr and $[\text{HCl}] = 20$ millitorr, and with an estimated $k'_{10} \approx 10^{-12}$ cu cm/mole-sec, the most reliable data for Reaction 40 yields a value $k_{40} \approx 8 \times 10^{-13}$ cu cm/mole-sec, which would make the steady-state value of $[\text{HCHO}] \approx 25$ millitorr, an amount readily detectable by the 3015 TOF. In short, if carbonyls are intermediates in the reaction of CH₄ with O atoms at room temperature, our results demand that they be present as reactive species (such as formyl radicals, HCO) rather than stable molecules.

D. Reaction of OH with CH₄

The primary scheme associated of OH radicals in the flow reactor is as follows:



(The initial reaction to produce OH has $k_5 \gg k_6, k_7,$ and $k_8,$ and hence the conversion of H into OH is considered to be instantaneous.) In the absence of methane, the k_8 step is noncontributing and -

$$\text{Rate}(\text{OH}) = + \frac{d[\text{OH}]}{dt} = -k_{60}[\text{OH}]^2 - k_{70}[\text{O}][\text{OH}] - \gamma_{\text{OH}}[\text{OH}] \quad (50)$$

Since k_{60} and k_{70} are comparable at room temperature, we may assume a steady-state condition for O atoms such that $d[\text{O}]/dt = 0$. This yields $k_{70}[\text{O}] = k_{60}[\text{OH}]$ and hence,

$$\text{Rate}(\text{OH}) = \frac{d[\text{OH}]}{dt} = -2k_{60}[\text{OH}]^2 - \gamma_{\text{OH}}[\text{OH}] \quad (51)$$

In the presence of CH_4 , k_{80} contributes and, assuming that CH_4 does not alter the kinetic wall behavior of OH ,

$$\text{Rate}_{(\text{CH}_4, \text{OH})} = \frac{d[\text{OH}]}{dt(\text{with CH}_4)} = -2k_{60}[\text{OH}]^2 - (k_{80}[\text{CH}_4] + \gamma_{\text{OH}})[\text{OH}] \quad (52)$$

Both Equations 17 and 18 are of the form -

$$\frac{dy}{dt} = -y(ay + b) \quad (53)$$

(with $y = [\text{OH}]$) which may be solved by the substitution -

$$\mu = \frac{y}{ay + b} \quad (54)$$

which yields

$$\frac{\mu}{\mu_0} = e^{-bt} \quad (55)$$

$[\text{CH}_4]$ is assumed essentially constant since its concentration is 59 times greater than $[\text{OH}]$ in this system.

Figure 6 presents some recent data on the fast-flow reaction between CH_4 and OH . (\square indicates the reaction without CH_4 ; \circ indicates the reaction in the presence of CH_4 .)

In this system, $k_{80} \ll 2k_{60}$ and $(k_{80}[\text{CH}_4] + \gamma) \ll 2k_{60}[\text{OH}]$. These numerical values make it difficult to use the method of initial rates to analyze the data. However, it is possible to use the integrated rate equation (55). This equation can be simplified by expanding the exponential term, e^{-bt} , as a power series, neglecting the higher powers of bt since they are much less than unity:

$$\frac{y_0/(y_0 + b)}{y/(ay + b)} \approx 1 + \left(\frac{b}{vz}\right) z = 1 + bt \quad (56)$$

or rearranging Equation (56) yields -

$$y^{-1} \approx \left[\frac{1}{v} (a + by_0^{-1})\right] z + y_0^{-1} \quad (57)$$

Thus, a plot of y^{-1} against z (reciprocal of $[\text{OH}]$ versus distance, z , from inlet) should be linear. From the difference in slopes of two such straight lines (one for a run with CH_4 , one for a run without it) one can obtain k_4 , the rate constant in question. The data plotted in Figure 7 show the predicted linear relation.

From Equation 57, the definitions of a , b , and y , and setting $\text{SLOPE}_{\text{CH}_4}$ and SLOPE_0 equal to the slopes of the y^{-1} versus z curves for the run with CH_4 and the run without, respectively, yields -

$$k_{80}[\text{CH}_4] = [\text{OH}]_0(\text{CH}_4) [v_{\text{CH}_4} (\text{SLOPE}_{\text{CH}_4}) - 2k_{60}] - [\text{OH}]_0(\text{O}) [v_0(\text{SLOPE}_0) - 2k_{60}] \quad (58)$$

From Figure 10 and the 3015 sensitivity value for OH (1.60×10^{13} particles/cu cm = 10 units), and using the reported value⁶ for k_{60} (2.5×10^{-12} cu cm/part-sec) we have -

$$2k_{60} = 80 \text{ unit}^{-1} \text{ sec}^{-1}$$

$$[\text{OH}]_b(\text{CH}_4) = 10 \text{ units}$$

$$[\text{OH}]_b(\text{O}) = 7.0 \text{ units}$$

$$\text{SLOPE}_{\text{CH}_4} = 0.0326 \text{ unit}^{-1} \text{ cm}^{-1}$$

$$\text{SLOPE}_0 = 0.0474 \text{ unit}^{-1} \text{ cm}^{-1}$$

In the run with CH_4 , the flow rate $v_{\text{CH}_4} = 2.635 \times 10^3 \text{ cm-sec}^{-1}$. Thus, $k_{80}[\text{CH}_4] = 58.94 \text{ sec}^{-1}$. Since $[\text{CH}_4] = 2.43 \times 10^{16} \text{ molecules/cu cm}$, we have $k_{80} = 2.42 \times 10^{-15} \text{ cu cm/particle-sec}$. This is roughly an order of magnitude lower than that recently reported by Greiner,⁸ and about 3 times lower than that reported by Wilson

8. N. R. Greiner, J. Chem. Phys. 46, 490 (1967).

and Westenberg.⁹ In the absence of data at other temperatures we may use the
 9. W. E. Wilson and A. A. Westenberg, "11th Symposium (International) on Com-
 bustion," Combustion Institute (1967).

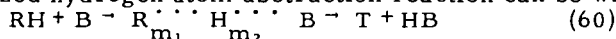
approximate collision theory argument² that the rate constant is given by -

$$k_{30} = 10^{-10} \cdot 5 e^{-E_a/RT} \quad (59)$$

which gives an activation energy of 5.65 kcal/mole for the $\text{CH}_4 + \text{OH}$ reaction.

Whether at high or low temperatures, a chain propagation step in the combustion process for a hydrocarbon is the abstraction of a hydrogen atom from the hydrocarbon by atomic oxygen or hydroxyl.

The generalized hydrogen atom abstraction reaction can be written¹⁰



10. H. S. Johnston, "Gas Phase Reaction Rate Theory," Ronald Press, New York (1966).

where m_1 and m_2 are the bond orders, in the transition state, of the "breaking bond" $\text{R} \cdot \cdot \cdot \text{H}$ and the "forming bond" $\text{H} \cdot \cdot \cdot \text{B}$. This bond-order concept has its intuitive appeal to the chemist and structural chemist on the bases of bond length, bond strength, and coordinating valence. Thus, in a single covalent bond involving one pair of shared electrons as in H_2 or HCl , the bond order is 1. In nitrogen, however, since one may see that there are three pairs contributing to bonding (a so-called " $\sigma_2 \pi_4$ " orbital configuration) the bond order there is 3. The important result here is to remember that, in the bimolecular reaction above, the underlying assumption is that the sum of bond orders remains constant throughout such abstraction reactions. That is, $m_1 + m_2 = 2$.

One may then treat such reactions by assuming a valence bond potential for the transition state given by

$$V = D_{\text{RH}} - C_{\text{RH}}(m_1^p) - D_{\text{HB}}(m_2^q) + V_r \quad (61)$$

where the D 's are the bond dissociation energies, V_r is the energy of repulsion arising from the parallel electron spins on R and B , and q are empirical parameters indicating the strength of the intermolecular valence forces. For oxygen species where triplet states are involved (two parallel electron spins on the same species), twice the repulsion energy has to be included for a more reasonable estimate.

Recently, our results indicated a room temperature rate constant of about 10^9 cu cm-mole⁻¹-s⁻¹ for the $\text{OH} + \text{CH}_4 \rightarrow \text{CH}_3 + \text{H}_2\text{O}$ reaction. This implies that the activation energy for such a reaction is about 5 to 6 kcal-mole⁻¹. The bond energy-bond order method yields about 5 kcal-mole⁻¹ as an activation energy.

We have also indicated that the combustion of methane is significantly enhanced in the presence of discharged rather than titrated oxygen. Our first interpretations associated this extra activity with excited O_2 , namely (Δ g) O_2 . Table III is a brief compendium of rate constants and activation energies as calculated by the bond energy-bond order method.

From the above table, it is obvious that the $\text{CH}_4 + \text{O}_2(\Delta\text{g})$ reaction should be about 10,000 times more rapid than the ground-state O_2 reaction at flame temperatures. Although the Σg^+ state of O_2 indicates an even greater reaction, the lifetimes (collisional and radiative) for this species are much too short to compete with that for the Δg state (46 minutes). Thus, no significant concentration of this Σg^+ species is expected. Each of the rate constants¹¹ in Table III is computed by the prescription

11. S. W. Mayer and L. Schieler, *J. Phys. Chem.* **72**, 2628 (1968).
 of activated complex theory. Successive variation of the parameters of Equation 8 leads to a "saddle point curve," or curve of steepest ascent. The maximum of this path may be taken as the activation energy, E_a . Assuming a linear complex, one can readily calculate the rate constant from

$$k_{\text{rate}} = K \frac{kT}{h} \cdot \frac{Q^\ddagger}{Q_A Q_B} e^{-E_a/RT} \quad (62)$$

where the Q_A and Q_B are reactant partition functions, Q^\ddagger is the partition function of the complex, R is the gas constant (in cal-mole⁻¹-deg⁻¹ if E_a is in cal-mole⁻¹), k is Boltzmann's constant, h is Planck's constant, and K is the transmission coefficient

for the potential barrier. Quantum mechanically, even though the energy of a system is less than the potential at that point, there is a finite probability of finding the system in the configuration beyond that point. This probability is the transmission coefficient, and the "process" is referred to as quantum-mechanical "tunnelling." In any event, Equation 62 can be readily calculated for most simple reactions and has been shown to give very reliable estimates of the rate constants for a great number of elementary reactions.

It should be observed that the reactions in Table III for $\text{CH}_4 + \text{O}_2$ are not as fast as the corresponding reactions with O atoms. However, one would expect that the reactions of $\text{O}_2(^1\Delta_g)$ with $\text{CH}_3\cdot$ radicals or with unsaturated hydrocarbon intermediates might be quite competitive with attack by oxygen atoms. For example, the best values for O atom attack on CH_4 give an activation energy of $10.5 \text{ kcal-mole}^{-1}$. However, the rate constants for reaction of O atoms with $\text{CH}_3\cdot$ may be comparable to $\text{CH}_3\cdot$ reaction with excited O_2 , since each reaction involves encounter between species having free valences. The actual concentration of excited O_2 made by an electrical discharge (concentration in the downstream effluent) may be as high as 10% of the total pressure.⁷ This would mean that in the experiments with CH_4 and HCl it would be reasonable to expect that concentrations of the order of 20 microns Hg (about 6×10^{14} molecules/cu cm) of $^1\Delta_g \text{O}_2$ were available in the reaction zone. Assuming that the reaction rates of $\text{O}_2(^1\Delta_g)$ and $\text{O}(^3P)$ atoms with CH_3 are similar, one would expect about a three-fold increase in oxidation rate in the electrical discharge experiment.

IV. Conclusions

Although both HCl (and Cl_2) catalyze the reaction of CH_4 with O and O_2 , the extent of the reaction at room temperature is small. We could detect no quantitative evidence for the formation of any carbonyls or carbonyl fragments during the course of the oxidations (this, however, does not preclude their presence as very short-lived intermediates in such systems). The presence or absence of ground-state O_2 produced no effect on the reaction of O atoms with CH_4 . Addition of O_2 to the N + NO stream gave no evidence of any rate changes. Discharged O_2 , however, significantly enhances the formation of combustion products. This result has been tentatively attributed to the presence of excited ($^1\Delta_g$) O_2 in the system. The reaction of CH_4 with OH radicals has been studied at room temperature, yielding a rate constant of $2.42 \times 10^{-15} \text{ cc/particle-sec}$.

V. Acknowledgements

The authors of this paper are deeply indebted to the American Gas Association for their support in this work.

Table I. ACTIVATION ENERGIES

<u>Reaction Number</u>	<u>Heat of Activation, kcal/g-mole</u>
(2)	4
(7)	11
(8)	8-9
(9)	8
(10)	≈ 53
(11)	≈ 58
(12)	≈ 60

Table II. RATE CONSTANTS FOR REACTIONS AT 300° K,
cu cm/particle-sec

$k_1 = \text{Unknown}$

$k_2 = 2.06 \times 10^{-11}$

$k_3 = 1.53 \times 10^{-14}$

k_4 , assumed to be between 10^{-10} - 10^{-11}

k_5 , assumed to be between 10^{-10} - 10^{-11}

$k_6 \sim 2 \times 10^{-13}$

Table III. ACTIVATION ENERGIES AND RATE CONSTANTS FOR HYDROCARBON-OXYGEN AND METHANE-OXYGEN REACTIONS (cc-mole⁻¹-sec⁻¹)

Species	<u>O₂(³Σ_g⁻)</u> (Ground State)	<u>O₂(¹Δ_{g)}</u> (Excited State)	<u>O₂(¹Σ_g⁺)</u> (Excited State)
		<u>With H₂</u>	
E _a	58 kcal-mole ⁻¹	35 kcal-mole ⁻¹	20 kcal-mole ⁻¹
k (300°K)	4 X 10 ⁻³⁰	1 X 10 ⁻¹⁴	1 X 10 ⁻⁶
k (1000°K)	3	3 X 10 ⁴	1 X 10 ⁵
		<u>With CH₄</u>	
E _a	57	34	19
k (300°K)	6 X 10 ⁻³⁰	4 X 10 ⁻¹⁴	2 X 10 ⁻⁶
k (1000°K)	6	6 X 10 ⁴	5 X 10 ⁶

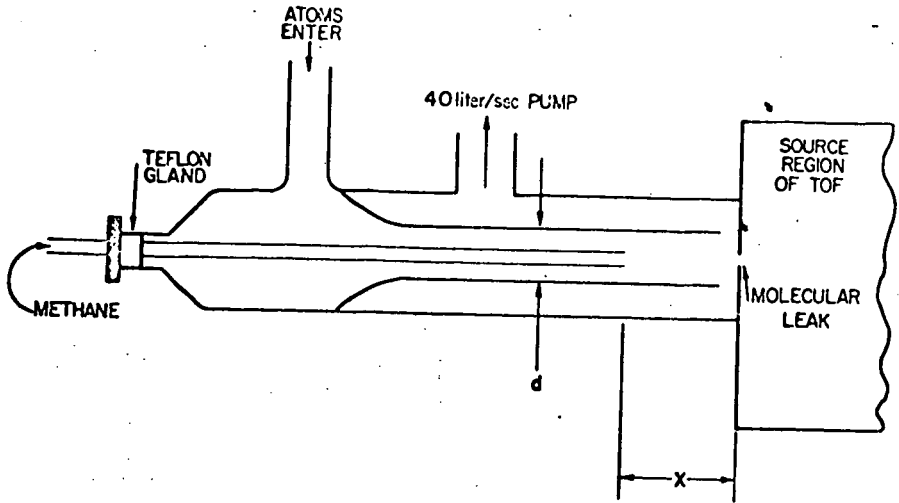


Figure 1 . FLOW REACTOR

A-1071396

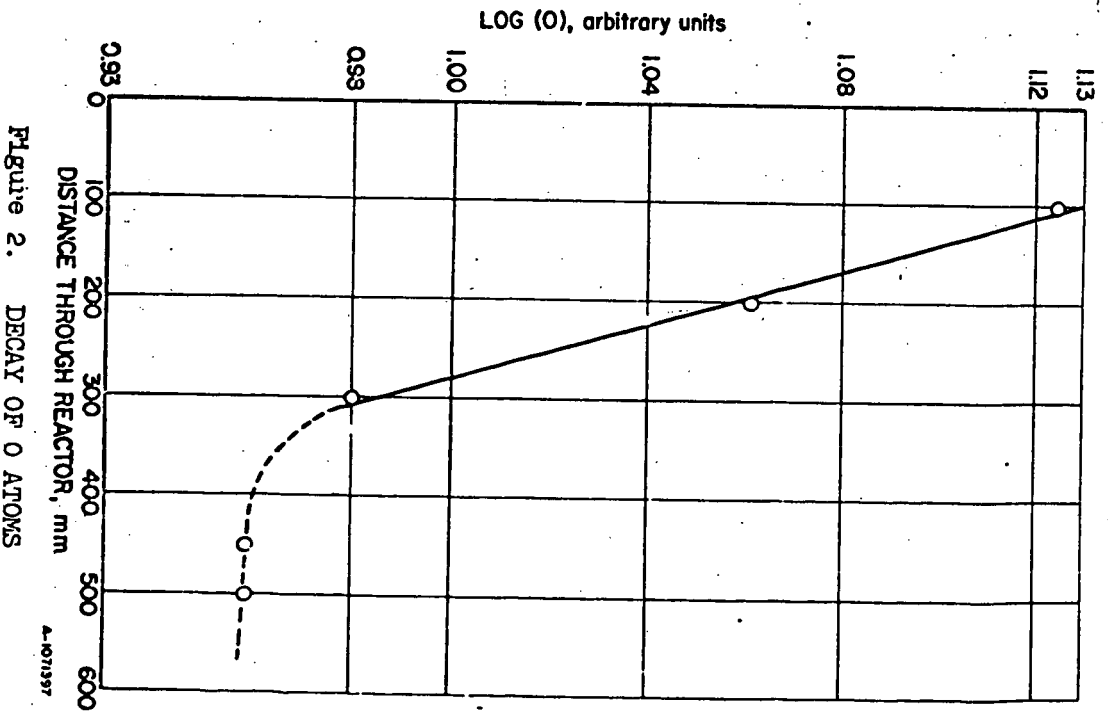


Figure 2. DECAY OF O ATOMS

A-1071397

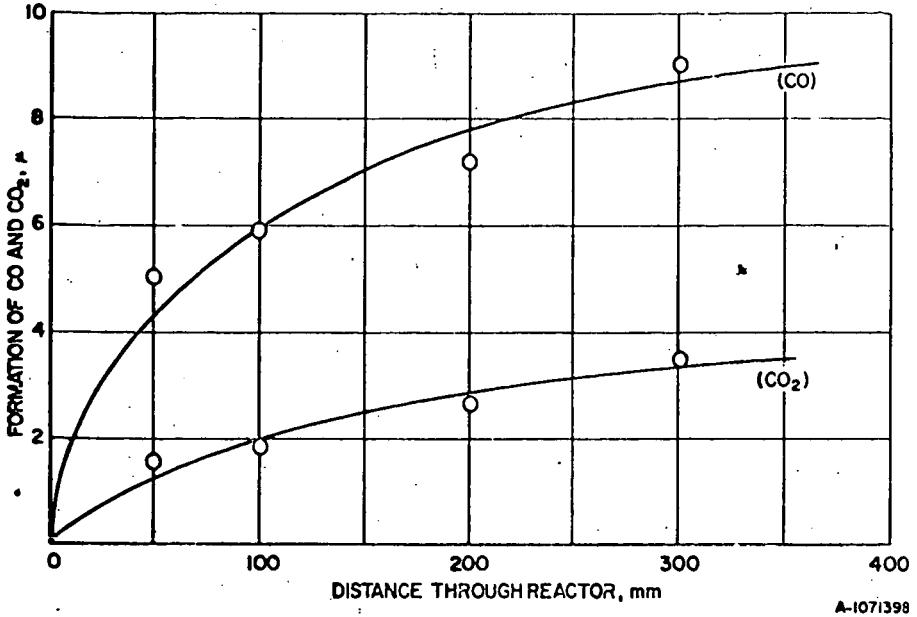


Figure 3. RELATIVE FORMATION OF CO AND CO₂
WHEN 37 μ OF HCl IS ADDED

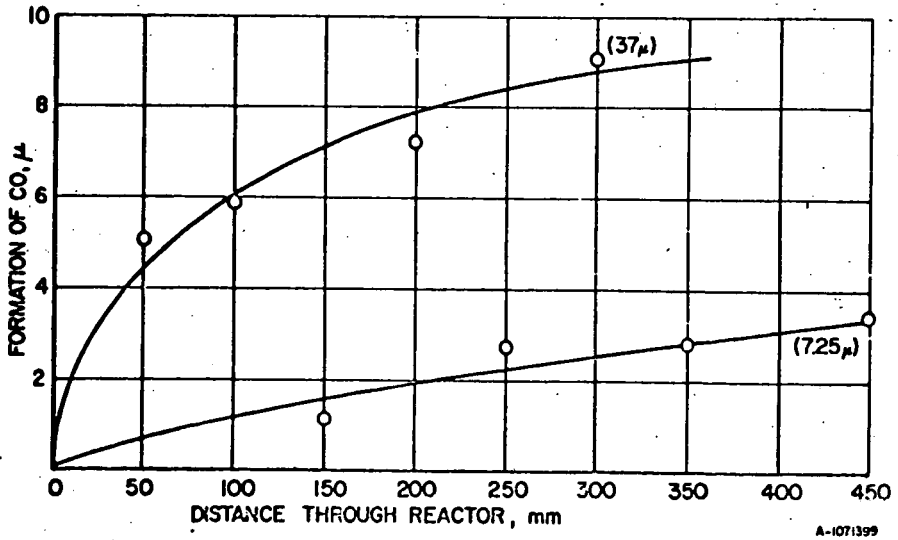


Figure 4. RELATIVE FORMATION OF CO FOR
DIFFERENT ADDITIONS OF HCl

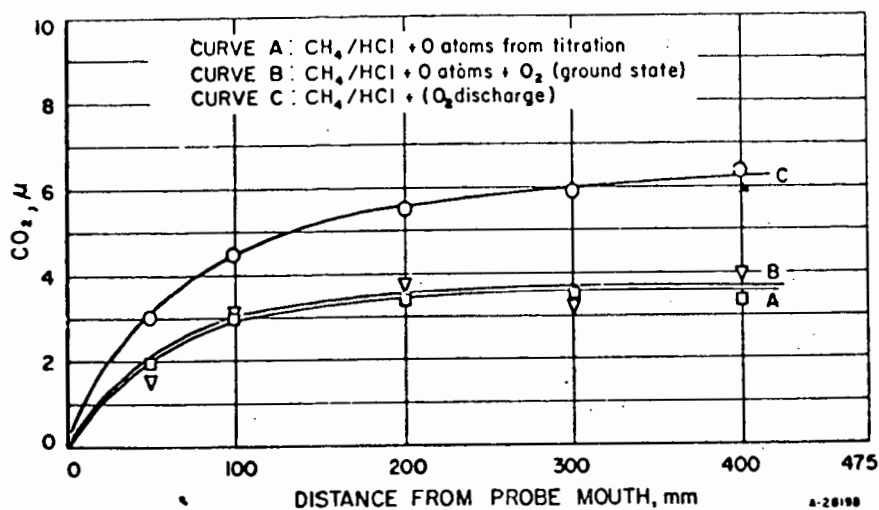


Figure 5. FORMATION OF CO_2 FOR VARIOUS $\text{CH}_4/\text{HCl}/\text{O}$ SYSTEMS

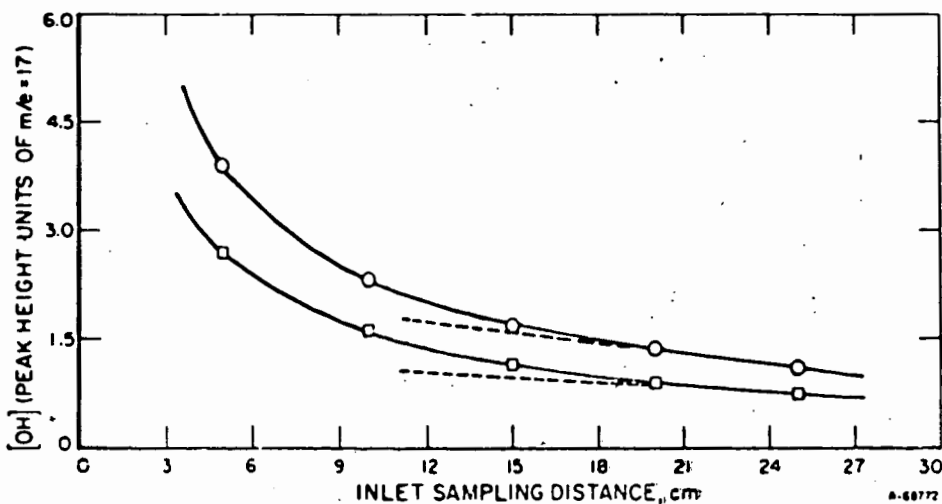


Figure 5. REACTION OF CH_4 WITH OH (at Different Initial Concentrations of OH)

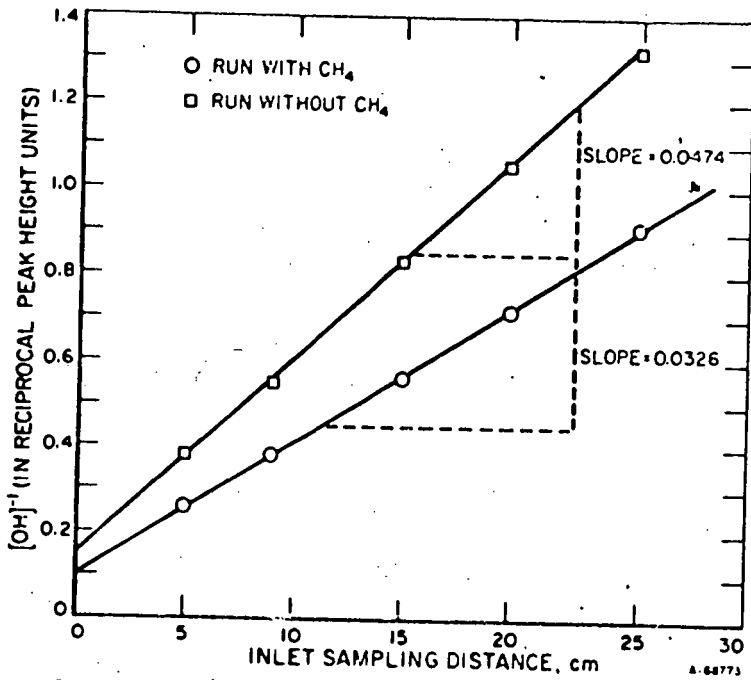


Figure 7. RECIPROCAL CONCENTRATION OF OH AS A FUNCTION OF DISTANCE FROM THE INLET DURING CH_4 -OH REACTION

CHEMISTRY OF HIGH TEMPERATURE SPECIES AT LOW TEMPERATURE

W. F. Libby

University of California at Los Angeles
Los Angeles, California 90024Part A Positive Ion Chemistry

Hydrocarbon positive ions in low temperature media, such as liquid argon and liquid xenon, are particularly fascinating species. We have found that in concentrations of a percent or less, methane readily polymerizes when a solution in liquid argon is irradiated with cobalt 60 gamma radiation. It forms a polymer with general formula of $C_{20}H_{40}$ which is very similar to that found earlier in solid methane at liquid nitrogen temperatures. (1)

It is our present suggestion (2) that the mechanism of polymerization may involve the Auger transition in the argon atom, i.e. the polymer is formed only when an inner electron in argon is ionized. The resulting explosion caused by successive Auger transitions would produce a congregation of positive argon ions in the immediate vicinity of the original point of internal level excitation and each of the ions would then be neutralized by electron transfer from methane solute since the argon ionization potential is higher. Thus about 20 methane ions would be produced within a radius of a few 10's of Angstroms of the original site. The subsequent neutralization of these ions by electrons being a fast or vertical process (in the sense of the Franck-Condon Principle) would cause dissociation of the methane to form radicals and fragments such as CH, CH_2 and CH_3 . These then would subsequently recombine for there would be little else for them to do. This theory is still under experimental test. We are studying the effects on the isotopic composition of the polymer versus

that or the other principal product ethane, and we are further studying the small effect of diluting the methane on the molecular weight of the polymer.

The ability of hydrocarbon ions to react at low temperatures in the presence of ionizing gamma radiation has been well known for a long time in that the hardening of the plastic polymer polyethylene by gamma rays has been well studied. It is our present belief that this too is an ionic process in most part.⁽³⁾ Though once again, to say that the proof is complete would be an exaggeration. It would seem on balance that at low temperatures ionic processes may be dominant and that at ordinary temperatures they are very, very important in radiation chemistry in general.

Part B Carbon Vapor at Low Temperature

Our studies of the chemical reactions of carbon vapor with cold benzene and with diamond surfaces will be discussed. It is clear that carbon atoms are able to react with benzene even at 77°K. It is not certain that trace amounts of oxygen may not be involved in a critical way also.

Our attempts to prepare to grow diamonds by evaporating carbon vapor on to seed diamonds under high vacuum conditions will be described and any progress towards this goal discussed. It seems clear that the quality of the vacuum may be all important in this process. We indeed are using this as an example of the possible chemical value of the extremely high vacua that are attainable in the space chambers in the aerospace industry and in the laboratories such as Jet Propulsion Laboratory and, of course, in orbiting satellites. It seems to

us that we should be able to develop a chemistry of surfaces, which has been highly inhibited because of air, if we take the pains to eliminate air and this may be a chemical benefit of the space environment.

- (1) Chemistry of Positive Ions. VI. Positive-Ion Chemistry in Solid Methane. Donald R. Davis, W. F. Libby and W. G. Meinschein. *J. Chem. Phys.* 45, 4481-(1966).
- (2) Polymer Production in the Gamma Radiolysis of Methane in Liquid Argon. W. F. Libby, Peter Hamlet, Jai Mittal and Jeffrey Moss. To be published in *The Journal of The American Chemical Society*.
- (3) The Chemistry of Ionic States in Solid Saturated Hydrocarbons. Larry Kevan and W. F. Libby. *Advances in Photochemistry*, Vol. 2, Interscience Publishers, New York, 183-(1964).

THE CHEMISTRY OF ATOMIC CARBON

Richard Wolfgang
 Department of Chemistry
 University of Colorado
 Boulder, Colorado

A decade ago it was still said that the chemistry of atomic carbon was the first page of the book of organic chemistry, and that that page was blank. But even in the late forties and early fifties there were already some markings on the page.¹ The present rapid development of the field started about 1961 when it was proposed that the basic reaction mechanisms of atomic carbon with hydrocarbons was by insertion into C-H and C-C bonds.^{2,3} That blank first page is now quite well filled in as far as the basic outlines are concerned.⁴

The reason that the study of atomic carbon came so late is that this species is so reactive that it is difficult to produce in controlled conditions. Now, however, at least four techniques have been used: nuclear recoil⁴, photochemistry⁵, evaporation from graphite^{6,7,8}, and laser flash.⁹ Other methods have also been demonstrated but will not be reviewed here.

Nuclear Recoil Techniques

Nuclear recoil was the first technique used and it has supplied the bulk and the backbone of what we know at present of atomic carbon.⁴ Radioactive carbon is produced by a nuclear reaction. For instance on simply irradiating C^{12} with high energy gamma rays (> 20 Mev) the following process occurs



The C^{11} as initially produced may possess a very large amount of kinetic energy (~ 100 kev). This is lost in successive collisions. When the energy of the atom falls into the chemical energy range below 100 eV it may react to combine. Labelled molecules are formed by this means and may be assayed by radiogase chromatography.

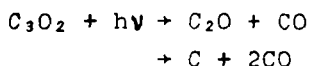
Considerations of atomic physics require, and experiment confirms, that as the carbon atoms reach the chemical energy range they are in a low-lying electronic state, either in 3P , 1D or 1S .^{10a,b} They may however react while they are still "hot",

i. e. have excess kinetic energy. This is rather an advantage, however, since one may control the energy of reaction by the use of moderators. In a system containing a large excess of a rare gas, essentially all reactions occur after the carbon atoms have been thermalized.

The nuclear method may be used with either C^{11} or C^{14} . However the half-life of C^{14} is so great that prolonged irradiation is required before enough is produced. This has led to serious difficulties with radiation damage effects. Most currently accepted data was obtained using C^{11} .

Photochemical Techniques

U.V. photolysis can be used to produce atomic carbon, e.g. with carbon suboxide.⁵



Atomic carbon is produced only if very short wave lengths ($\sim 1500 \text{ \AA}$) are used. This type of method has been employed both in the gas and solid phase. It is however severely restricted by the transparency of the medium to the needed radiation. For this reason methane is the only alkane whose reactions with atomic carbon have been studied by these means.

Evaporation Techniques

Several techniques have been developed in which carbon is evaporated from a heated graphite rod⁶, a carbon arc⁷, or an exploding filament⁸. The carbon vapor may be deposited on a surface on which it is allowed to react.

This technique tends to be restricted to the study of reactions of atomic carbon on solid surfaces. The interpretation of gas-phase reactions would present difficulties because of extensive pyrolysis and photolysis on the evaporating body.

Laser Flash Techniques

We have recently developed⁹ a variant of the evaporation technique in which a laser is used. A pulse is focused onto a carbon surface forming a small hot spot from which carbon evaporates. Reactions with a low-pressure gas can be studied because the hot spot is so small and short lived that extensive pyrolysis does not occur.

While the use of a laser flash represents an advantage in that reactions in the gas phase can be treated it still shares

with other evaporation techniques, the disadvantage that a range of carbon species C_1 , C_2 , C_3 etc. are formed.

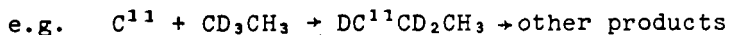
Comparison of Techniques

All techniques, though generally used under different conditions, tend to give very similar results in so far as a comparison can be made. However Skell has reported apparently significant differences in his evaporation techniques, which would tend to indicate that species of lower energy are involved⁷. In particular acetylene, a high energy product normally found when atomic carbon reacts with hydrocarbons is conspicuously absent when the particular method in question is used. This apparent discrepancy has not yet been resolved. One possible explanation¹⁰ stems from the fact that in this technique alone there is an appreciable delay between production and reaction of the carbon atoms. Conceivably this might allow complexing of the carbon atoms, reducing their reactivity, something that commonly happens to active species on aging in ordinary vacuums. Such complexed species could act as carbon atom donors, with reactions similar to but less energetic than those of free carbon atoms. Indeed a time dependence of reactivity is found in these experiments⁷, though this has been attributed to decay of spin states.

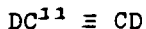
Summary of Findings

So much is now known of the reactions of atomic carbon that it is impossible to give a brief yet comprehensive review. Reactions with inorganic oxides¹¹, with nitrogen¹¹ and with hydrogen¹² are reviewed elsewhere. With hydrocarbons there are three principal modes of primary reactions.

1) Insertion into a C-H bond

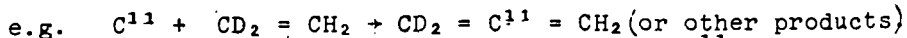


+



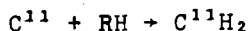
As expected the acetylene formed in such reaction with CD_3CH_3 is either $C^{11}D \equiv CD$ or $C^{11}H \equiv CH$ with little $C^{11}D \equiv CH$ being formed^{4a}.

2) Insertion into a C = C bond



As expected the allene formed by this reaction is C^{11} center labeled and has the hydrogen isotope distribution shown.^{4a}

3) Abstraction to form CH_2



Primary modes 1) and 2) yield an intermediate adduct which is highly excited due to the energy released in forming

the new bonds. The further fate of such complexes depends on their spin states and on how rapidly energy is moved by collisional deactivation. This topic is well understood and is fully discussed elsewhere.^{13,14}

Insertion in C-C and C-F bonds has not been observed. Instead in perfluorocarbons the dominant reaction appears to be abstraction to form C-F, fluoromethyne.⁹ The probable explanation for this pattern of primary insertion will be discussed.

Acknowledgement

This work was supported by the U. S. Atomic Energy Commission.

- References -

1. See for instance A.P. Wolf, Ann. Rev. Nuc. Sci. 10, 259 (1960).
2. C. MacKay and R. Wolfgang, J. Am. Chem. Soc. 83, 2399 (1961).
3. C. MacKay et al, J. Am. Chem. Soc., 84, 308 (1962).
4. a) C. MacKay and R. Wolfgang, Science, 148, 899 (1965).
b) R. Wolfgang, Progr. Reaction Kinetics, 3, 99 (1965).
c) A.P. Wolf, Adv. in Phys. Org. Chem., 2 (1964).
d) D.E. Clark and A.F. Voig , J. Chem Soc. 87, 5558 (1965).
5. L.J. Stief and V. J. De Carlo, J. Chem. Phys., 43, 2552 (1965).
6. J.L. Sprung, S. Winstein and W.F. Libby, J. Am. Chem. Soc. 87, 1812 (1965).
7. P.R. Skell and R.R. Engel, J. Am. Chem. Soc. 87, 1135 (1965).
8. C.W. Spangler, S.K. Lott and M.J. Joncich, Chemm. Comm., 842 (1966).
9. D. Bla~~x~~ell, C. MacKay and R. Wolfgang, unpublished (1968).
10. J.E. Nicholas, C. MacKay and R. Wolfgang, J. Am. Chem. Soc., 87, 3008 (1965).
11. J. Dubrin et al, J. Inorg. and Nuc. Chem., 26, 2113 (1964).
12. C. MacKay, J. Nicholas and R. Wolfgang, J. Am. Chem. Soc., 89, 5758 (1967).
13. J. Dubrin, C. MacKay and R. Wolfgang, J. Am. Chem. Soc., 86, 4747 (1964).
14. J. Nicholas, C. MacKay and R. Wolfgang, J. Am. Chem. Soc., 88, 1610 (1966).

REACTIONS OF C₁, C₂, C₃, C₄

Philip S. Skell

The Pennsylvania State University
University Park, Pennsylvania 16802ABSTRACT

Evaporation of graphite has been carried out producing the following species in proportions which vary with the method of vaporization and ageing.

C ₁	3 _p , 1 _p , 1 _s
C ₂	Triplet, Singlet
C ₃	Singlet, Triplet
C ₄	

The reactions of these species, with a range of substrates in condensed phase (low temperature) will be reported: alkanes, cycloalkanes, alkenes, alkynes, alcohols, aldehydes, ketones, epoxides, alkyl halides.

D. G. Skell and J. H. Flynn
The Pennsylvania State University, University Park, Pa. 16802

Numerous examples of the carbene character of atomic carbon produced in a low intensity arc under high vacuum have recently been reported from this laboratory.

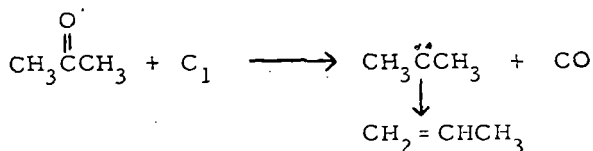
In an effort to find reactions of atomic carbon which might not be classified as normal carbene processes, the reactions of atomic carbon with carbonyl compounds were studied. The reaction of carbon atoms with acetone cocondensed on a liquid nitrogen cooled surface produced carbon monoxide and propylene in good yield (see Table I).

Table I

<u>Compound</u>	<u>Yield^a</u>
CO	59.6%
CH ₂ = CHCH ₃	54.2%

^a calculated as Mm product/MmC₁ vaporized

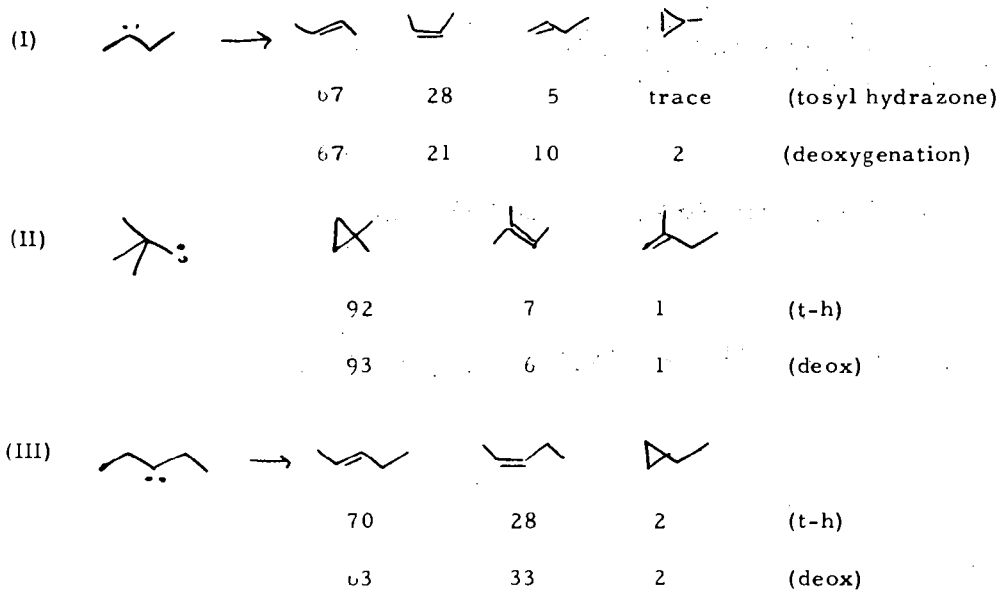
The production of Carbon monoxide and propylene in nearly equal amounts suggested the following reaction sequence:



If this scheme were operative, the reaction was novel deoxygenation process to produce the subvalent carbene species and would thus provide an opportunity to generate a wide variety of carbenes at low temperatures. To test the proposed scheme, the reaction of acetone with C¹⁴ enriched electrodes was examined. As

This method was found to be a general preparation of alkyl carbenes and the data gathered on product distribution from the deoxygenation method closely resemble those from tosyl hydrazone decompositions.

Three such comparisons are given below:



Thus, it appears that deoxygenation produces an intermediate very similar to the process generally assumed to be a carbene preparation. It is quite striking that the similarities between reaction at a liquid nitrogen cooled surface and a decomposition performed at $\sim 160^\circ$ are so great. We feel this indicates a low activation energy for the intramolecular, carbene reactions.

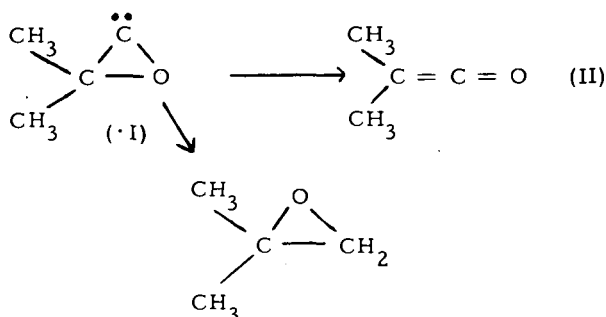
Deoxygenation was extended to other materials. It was observed that propylene oxide deoxygenated to propylene and carbon monoxide:

From the above data, we feel that oxygen abstraction is a convenient method for the generation of carbenes and radicals, free of complexing at low temperatures.

would be expected from the scheme, the propylene gave a molar activity 0.039 while the Carbon monoxide was found have a molar activity 0.91. This established that Carbon monoxide did indeed arise from a deoxygenation process involving C_1 and that the propylene was formed in a process not involving carbon from the electrodes.

As a second check, the reaction forming propylene should also be intramolecular if a carbene were involved since simple hydrogen transfer is all that is required for product formation. A mixture of acetone $d_6/d_o = 1.25$ was subjected to the reaction conditions and the resultant propylene analyzed by mass spectroscopy. The ratio propylene $d_6/d_o = 1.32$, confirming the intramolecular character of the process.

The dimer of the carbene, 2,3-dimethyl-2-butene, was not observed. This may be attributed to the relative rapidity of hydrogen transfer as opposed to the rate of diffusion of dimethyl carbene through the acetone matrix. It also appears that the process of Carbon atom insertion into carbon-carbon double bonds does not take place into carbonyl functions since such an adduct (I) would be expected to give either dimethyl ketene (II) or isobutylene oxide (III).



Neither of these products were formed.

RECENT SPECTROSCOPIC STUDIES OF HIGH-TEMPERATURE
MOLECULES

G. Herzberg

National Research Council of Canada,
Ottawa, Ontario

ABSTRACT

Molecules that are important in high temperature studies of gases may be studied spectroscopically not only in absorption at high temperature but also in emission or absorption in electric discharges or their afterglows, or in absorption in flash photolysis of various parent compounds. Recent spectroscopic work on high-temperature molecules by all of these methods will be described. This work includes studies of diatomic hydrides (BH, AlH, CH, SiH,) of several homonuclear diatomic molecules and ions (H_2 , C_2 , C_2^- , N_2^+ , O_2 , Mg_2 , Si_2) and a few heteronuclear non-hydride molecules (BF, CF, NF, NCl, SO). A good deal of work on spectra of triatomic free radicals has been done and will be briefly described.

SPECTROSCOPY OF HIGH TEMPERATURE MOLECULES

Leo Brewer

Inorganic Materials Research Division of
Lawrence Radiation Laboratory and Department of Chemistry
University of California, Berkeley, California 94720

High temperature furnaces, flames, arcs, and similar sources of high excitation are the conventional sources of spectra of high temperature molecules. However, spectra from such sources are often difficult to resolve because of the high electronic, vibrational, and rotational excitation resulting in extensive overlapping of spectral bands. Excitation of impurity molecules increases the complications due to overlapping.

It is important to obtain complete analyses of the band systems of high temperature molecules to establish the spectroscopic constants needed for calculation of the high temperature thermodynamic properties. In particular the establishment of the degeneracies and energies of all low lying electronic states is very important.

The failure of conventional methods to produce the needed information has stimulated a variety of new approaches. This paper will discuss the potential advantages and handicaps of the new methods and will suggest other approaches.

A rather widely applied method in the last few years involves the entrapment of high temperature molecules in a rare gas or other inert matrices at liquid hydrogen or helium temperatures. This method offers a simplification of the analysis of the spectrum in that one would expect the entrapped molecules to be in their lowest electronic and vibrational states. The absorption spectrum of S_2 in a matrix is found to consist of a simple progression arising from the $v''=0$ level of the ground electronic state. When there are almost degenerate electronic states around the ground state energy, it is possible that interactions with the matrix might invert their order and thus indicate the incorrect gas ground state. A more severe disadvantage of matrix absorption spectra is the lack of sharpness and detail such that electronic spectra can not be unambiguously

identified without knowledge of the gas spectra. A most serious disadvantage of matrix absorption spectra is that information is not obtained for low lying electronic states.

Another fruitful approach to simpler high temperature spectra is through use of molecular beams from a Knudsen cell or some other high temperature source of vapor. During the typical transit times of 10^{-4} to 10^{-5} seconds, one would expect the excited electronic states to decay to the lowest state of each multiplicity for light molecules and to the ground state for heavier molecules for which the spin change prohibition is not rigid. Thus the molecular beam should provide simpler spectra. A variety of spectral measurements can be made on a beam. For example, electric-resonance and magnetic deflection experiments by Klumperman and his coworkers have been used to establish an O^+ ground electronic state for SrO and BaO. Also for triatomic and more complicated molecules, they have shown that electric-deflection experiments can be used to determine the symmetry of the molecules. The combination of a Stern-Jerlach experiment with a mass spectrometer detector offers to be a useful way of distinguishing singlet from triplet ground states or of determining the splitting of triplet ground states of heavier molecules. For example, Scarcy and Maschl have used this method to confirm that the 1 sublevel of the $^3\Sigma$ ground state of Te_2 lies so far above the O^+ sublevel that the beam of Te_2 shows no deflection. Optical absorption or fluorescent experiments may also be carried out on molecular beams. In this manner Brewer and Welch have established the ground state of LaO and Brewer and Green have shown that the lowest singlet and triplet states of ScF are virtually degenerate since both states persist in a molecular beam for longer than 10^{-4} sec. Although these various applications of molecular beams have been useful in establishing the very lowest electronic states, they do not provide information about the low-lying excited states which are important with respect to their contribution to the high temperature partition function since these states will have usually decayed in the

transit time of the beam.

There is a possibility of eliminating the limitation of absorption spectra of molecular beams and matrices through use of fluorescent spectra. By exciting to very high electronic states, one can observe cascading through the lower electronic states. The matrix spectra offer the advantage of relatively rapid vibrational deactivation and the fluorescent spectra often consist of simple progressions arising from the $v' = 0$ level of the upper electronic state. The matrix method offers the other advantage of enhancement of forbidden transitions which could allow the fixing of the energies of singlet and triplet states relative to one another. Meyer, Phillips, and Smith have applied this method recently to SO_2 .

A new method has been suggested that might be able to provide direct information about the energies of all of the low-lying electronic states of a molecule. For example, the first excited $^1\Sigma^+$ state of CaO is perturbed by six different low-lying states or sublevels. From the perturbations observed for Ca^{16}O , the vibrational and rotational constants of these states can be established, but their energies are not known. A similar analysis of the perturbations for Ca^{18}O may allow fixing of the energies of each of the states from the isotope shift.

The application and potential future applications of the above methods will be discussed. This work has been supported by the Research Division of the Atomic Energy Commission.

MATRIX ISOLATION INFRARED SPECTROSCOPY
OF HIGH TEMPERATURE SPECIES

J. L. Margrave, J. W. Hastie and R. H. Hauge
Department of Chemistry, Rice University

Matrix isolation in rare gases has been widely used for infrared studies of reactive species. An advantage of matrix isolation for infrared studies of high temperature species is apparent if one compares the usual band widths of gas phase absorption spectra to those obtained in matrix isolation spectra. In fact the narrow band widths often make possible accurate isotope shift measurements of vibrational bands which in turn can be used to calculate accurate force constants. For XY_2 triatomic molecules isotope shifts of the antisymmetric stretch (ν_3) can often set close limits on the bond angle. Alternatively, isotope shifts of the ν_1 and ν_2 can be used in combination to determine the bond angle but the measurements are sometimes made difficult because of their relatively low absorption intensities.

A simple use may be made of the isotope shifts of some diatomic molecules to determine their anharmonicity. A comparison of the measured anharmonicity of a molecule trapped in a rare gas matrix to its gas phase value serves as an indication of the effect of the matrix on the shape of the potential energy curve. The following table lists $\omega_e x_e$ for matrix isolated, using Ne or Ar, and gas phase molecules.

	$\omega_e x_e$ (cm^{-1})	
	matrix isolated	gas phase
LiF	9.4 ± 1	8.0
LiCl	3.1 ± 1	4.2
SiO	7.8 ± 3	6.0

It is clear from the above table that anharmonicities are affected only a very small amount, if at all, by a rare gas matrix. This is true for LiF even though the ν_e value shifts about 50 cm^{-1} from the gas phase to an argon matrix.

Isotope shift measurements of the ν_3 for symmetric triatomic XY_2 molecules may be exactly related to the bond angle by the following equation:

$$\sin \alpha = \frac{\left[\frac{M_x (M_y w_3^2 - M_y^i w_3^{i2})}{2M_y M_y^i (w_3^{i2} - w_3^2)} \right]^{1/2}}$$

where 2α equals the bond angle and w_3 is the zero-order antisymmetric stretch frequency. In practice one uses measured ν_3 values and estimates the anharmonic effect which in most cases has little influence on the measured bond angle.

It also follows from the above equation that a $\pm 0.1 \text{ cm}^{-1}$ error in the isotope shift measurement of ν_3 will cause a bond angle close to 180° to be less well determined than one close to 90° . The effect is such that with present instruments it becomes difficult to distinguish between bond angles of 160° and 180° . Although for these cases an isotope shift measurement can clearly establish a lower limit. The triatomic molecules listed in the following table have been studied in our laboratory and for the few cases (eg. NiF_2 , CuF_2 and ZnF_2) where these molecules have also been studied by other investigators the agreement with our work is very good.

	Bond Angles (degrees)		
	<u>This work</u>	<u>Microwave</u>	<u>This work</u>
SO_2	117 ± 2	119.3	ZnF_2 160 - 170
SeO_2	110 ± 3	113.5	CuF_2 163 - 170
TeO_2	110 ± 2	-	NiF_2 154 - 167
SiF_2	100.5 ± 2	100.9	FeF_2 155 - 170
GeF_2	94 ± 2	-	CrF_2 160 - 180

	Bond Angles (degrees)		
	<u>This work</u>	<u>Microwave</u>	<u>This work</u>
SnF ₂	92 [±] 3	-	MnCl ₂ 180
TiF ₂	120 [±] 4	-	VCl ₂ 180

It is apparent from the above data that the bond angle decreases slightly as the central atom size is increased down a column of the periodic table. One also notes that all of the isoelectronic 18 valence-electron molecules listed above are bent as predicted by Walsh rules. The bent configuration of TiF₂ indicates that its d-electrons are involved in the bonding to a considerable extent.

Infrared absorption data obtained for Group IV difluorides, SiF₂, GeF₂, SnF₂, and PbF₂ are given in the following table along with other molecular parameters. The force constants for GeF₂, SnF₂ and PbF₂ were calculated with the assumption of a zero stretch-bend interaction. The force constant values for CF₂ are taken from Milligan and Jacox J.C.P. 48, 2265, (1968) and for SiF₂ from V. M. Khanna et al J.C.P. 47, 5031 (1967).

mdyn/Å	CF ₂	SiF ₂	GeF ₂	SnF ₂	PbF ₂
k ₁	6.0	5.02	4.07	3.52	3.02
k ₁ /l ²	1.40	0.44	0.32	0.16	0.11
k ₁₂	1.45	0.31	0.22	0.17	0.10
r _{X-MX} (Å)	1.30	1.595	(1.73)	(1.92)	(2.01)
bond angle	104.9	100.9	94 [±] 4	92 [±] 3	(90)
D _{X-MX} (kcal/mole)	108	153	115	114	104
k ₁ r _{X-MX} / D _{X-MX} (x 100)	7.2	5.2	6.1	5.9	5.8

It is apparent from the above table that k₁ varies rather smoothly through the Group IV series this is not the case however for the D_{X-MX} energies. The ratio of k₁r_{X-MX} / D_{X-MX} might be expected to remain constant through the Group IV

series and in fact does for Ge, Sn, and Pb difluorides. The deviation of the ratio from an average value of 6 for SiF₂ and CF₂ seems to indicate a strengthening of the F-SiF bond by approximately 20 kcal and a weakening of the F-CF bond by approximately 20 kcal. A strengthening of the F-SiF bond might be attributed to some type of d-orbital involvement in the bonding. The weakening of the F-CF bond might well be due to strong fluorine-fluorine or fluorine-lone pair repulsion. It has been pointed out by others that the quite high value of the bond-bond interaction force constant for CF₂ is good evidence for strong fluorine-fluorine interaction.

Infrared data obtained for the first row transition metal dihalides are given in the following table. The gas phase frequencies have been estimated by arbitrarily adding $0.7\Delta(\text{Ne-Ar})$ to the measured frequency in a Neon-matrix. The force constants have been calculated using a three constant valence force field.

	Transition Metal Difluorides		$\Delta(\text{Ne-Ar})$ cm ⁻¹	$\nu_3(\text{Ne})+0.7(\Delta)$ cm ⁻¹	k_1-k_{12} md/A
	$\nu_3(\text{Most Abundant})$ Isotope cm ⁻¹	Isotope cm ⁻¹			
	Neon	Argon			
Ca ⁴⁰	581 ^a	561 ^a	20	595	2.17
Sc ⁴⁵	700.2	685.5	14.7	710.6	3.34
Ti ⁴⁸	753.3	740.6	12.6	762.1	4.03
V ⁵¹	743.3	733.7	9.6	750.0	3.80
Cr ⁵²	680.5	654.8	25.7	698.5	3.18
Mn ⁵⁵	722.6	700.6	22.0	740.0	3.67
Fe ⁵⁶	753.3	731.8	21.5	768.3	4.00
Co ⁵⁹	746.3	723.6	22.7	762.2	4.02
Ni ⁵⁸	801.2	780.6	20.6	815.6	4.57
Cu ⁶³	767.0	744.4	22.6	782.8	4.33
Zn ⁶⁴	782.0	764.0	18.0	794.6	4.48
Ge	655 ^b	648 ^b	7	660	3.82

a. A. Snelson, J. Phys. Chem., 70, 3208 (1966).

b. J. W. Hastie, R. H. Hauge, and J. L. Margrave, J. Phys. Chem. (in press) (1968).

The stretch force constants for the difluorides, dichlorides and their ratio are listed in the following table. The dichlorides of Mn, Fe, Co, Ni, Cu and Zn have been taken from Leroi et al J.C.P. 36, 2879 (1962).

	MF_2 $k_1(\text{mdyn./\AA})$	MCl_2 $k_1(\text{mdyn./\AA})$	$\frac{k_1(\text{MF}_2)}{k_1(\text{MCl}_2)}$
Ca	2.17	-	-
Sc	3.34	(1.88)	-
Ti	4.03	(2.27)	-
V	3.80	2.19	1.74
Cr	3.18	(1.79)	-
Mn	3.67	1.99	1.84
Fe	4.00	2.23	1.79
Co	4.02	2.30	1.75
Ni	4.57	2.51	1.82
Cu	4.33	2.43	1.78
Zn	4.48	2.67	1.68
Ge	3.82	2.17	1.76

The ratio of stretch force constants is almost invariant and provides a convenient means of estimating the unmeasured dichloride force constants. The estimated values are bracketed in the above table.

Infrared spectra obtained for SeO_2 , TeO_2 and TeO are listed in the following table.

	$\frac{\nu_3-1}{\text{cm}}$	$\frac{\nu_1-1}{\text{cm}}$	$\frac{k_1-k_1^2}{\text{mdyn./\AA}}$
SeO_2	974	924	7.00
TeO_2	845	827	5.75
TeO	791		5.25

Polymeric forms of these species have also been identified in the matrices.

Mass spectrometric studies have indicated that the polymeric species **also**

exist in the high temperature vapors. However for the SiO system where the vapor species is almost completely monomeric SiO, matrix isolation leads to extensive polymerization even at relative SiO to rare gas concentrations of 1/1000. Similarly the electronically similar high temperature species, BF is difficult to isolate in these matrices.

Reactions of NaF and SiF₂ and Na + SiF₂ have been studied by co-condensation of both species. New absorption bands were observed and are tentatively assigned to NaSiF₃ and NaSiF₂. These products decomposed when the condensate was warmed to room temperature to form elemental Si and Na₂SiF₆.

DICHLOROCARBENE FROM CHLOROFORM PYROLYSIS

P. S. Skell and M. S. Cholod
The Pennsylvania State University, University Park, Pa. 16802

Although cyclopropane formation from photolysis of suitable diazo compounds in the presence of an olefin is generally regarded to proceed through a free divalent carbon intermediate, there is much question as to the nature of the intermediate when alpha-elimination reactions are carried out in the presence of olefins to form cyclopropanes. Some species as ICH_2ZnI and LiCHCl_2 have been postulated as directly transferring the CXY moiety to olefin forming cyclopropanes without the intermediacy of a free carbene, but rather a carbene complex or carbenoid. On the other hand, indications are that the action of base on CHF_2X (X = Cl, Br) yield a free carbenic species, CF_2 .

In the instance of dichlorocarbene produced through alpha-elimination, there is much controversy as to whether the intermediate carbene is a free or a complexed species. The aim of this work was to resolve this conflict by comparing the reactivity of an unambiguously free dichlorocarbene with that of the species from alpha-elimination.

Unambiguously free dichlorocarbene was produced via chloroform pyrolysis: chloroform was passed through a pyrolysis zone ($\sim 1400^\circ$) which led into a high vacuum system, allowing molecular flow to a cooled solution of substrate. The substances leaving the pyrolysis chamber experienced a 10^{-5} second free flight before encountering the stirred liquid solution of olefin and hydrocarbon solvent. The dichlorocyclopropanes formed under these conditions are the products derived from the reaction of free dichlorocarbene with the olefin substrate. This variety of dichlorocarbene was found to add stereospecifically to the 2-butenes as does the dichlorocarbene from base and chloroform.

Reactions were run in which olefin pairs were allowed to compete for the free dichlorocarbene. Results of these competitions were compared with those for dichlorocarbene systematically generated by a number of alpha-elimination reactions in a variety of solvents, and over an extensive temperature range.

The reactivity of trichloromethylithium, a dichlorocarbene precursor stable at low temperatures ($\sim -80^\circ$) was also studied. The mode of reaction of this compound with olefins is of great interest, since it can conceivably react by both a carbene and an organometallic route.

Arrhenius plots were made for the relative reactivities of pairs of olefins. A common line was obtained independent of the mode of generation of the dichlorocarbene, with alpha-elimination or pyrolysis of chloroform.

Since all methods of generating dichlorocarbene gave an intermediate showing the same selectivity it follows that all generate the same intermediate, free dichlorocarbene.

PREPARATIVE PROSPECTS OF "HIGH TEMPERATURE" SPECIES

Thomas D. Coyle, F. E. Brinckman, J. J. Ritter
National Bureau of Standards
Washington, D. C. 20234

and

Gerald F. Kokoszka
State University of New York
Plattsburgh, New York 12901

Much of the emphasis of traditional high temperature chemistry in the past two decades has been placed on the elaboration of thermodynamic, kinetic, and structural features of chemical systems. Less attention, perhaps, has been given until quite recently to the implications of the results of high-temperature investigations for the synthetically oriented chemist. It has become increasingly evident, however, that the variety of unconventional and intrinsically interesting species accessible in significant concentrations under energetic regimes are potentially valuable reagents, and that these reactive intermediates can provide the means for syntheses of novel systems not yet achieved by more usual routes.

From the synthetic viewpoint, the availability of potential intermediates under energetic conditions is of primary importance, and the nature of the excitation employed is perhaps secondary. Accordingly, "high temperature" techniques in the literal sense are but one facet of a more general synthetic rationale, which also embraces alternate modes of excitation such as electric or microwave discharge procedures and photochemical syntheses. Even more generally, one may extend this synthetic viewpoint to the rational utilization of stable compounds, themselves formed by energetic routes, which provide sources of preformed

submolecular entities not otherwise available for synthetic exploitation. Thus, the energetic synthesis may provide the starting point for a derivative chemistry that might not be accessible by exclusively high energy procedures.

In this paper, we describe some recent activities in the authors' laboratories utilizing this somewhat permissive view of "high temperature" processes as a synthetic tool.

The preparation of catenated systems involving elements other than carbon is an area in which synthesis has traditionally relied heavily on the "energetic chemistry" approach. While conventional condensation reactions are applicable under some conditions, much of the synthetic progress in the area of catenated hydrides and halides of the representative elements, for example, has relied either on hydrolytic procedures using derivatives in which the catenation is "preformed" by high temperature preparative routes, or on thermal or discharge excitation. Thus, synthesis of catenated halides has been frequently achieved by discharge routes involving chlorides or compounds of the heavier halogens. Procedures involving fluorides have been generally unsuccessful, and it is frequently assumed that the reactive species in fluoride discharges are incompatible with retention of homoelemental bonding. In the course of investigations of the discharge reactions of covalent fluorides of elements such as boron, silicon, germanium, and phosphorus, we have demonstrated, mass spectrometrically and in bulk, the occurrence of catenation in fluoride-based systems. In more complex systems involving silicon, halogen redistribution and catenation to mixed halopolysilanes has been observed.

Some of these compounds have subsequently been prepared by alternate routes and investigated in detail by NMR double resonance techniques.

Of more general occurrence in microwave-excited fluoride plasmas is reaction with oxides or oxygen itself to produce oxyhalide species such as OBF and OSiF_2 which appear to undergo a series of secondary reactions to produce an array of simple and polymeric oxyfluorides. Progress made to date toward the elucidation of products and of principal reaction pathways suggests that relatively straightforward four-center addition reactions of the principal oxyfluoride intermediates are involved.

The well-known discharge synthesis of the boron subhalides provides a ready source of these compounds, which exemplify a class of reagents, accessible by energetic routes, for which an extensive derivative chemistry can be developed. A number of hitherto unreported organo derivatives have now been prepared. Reactions with a number of organic and organo-metallic reagents have been observed in which these compounds function as a formal source of BX groups. A comparison is suggested with the high-temperature boron-halogen chemistry investigated by others, including the possibility that the nominally stable subhalides may function under some conditions as low temperature sources of high temperature species.

Photochemical excitation is a particularly attractive source of a more selective energy input in systems, such as organometallics, that are potentially degradable by more rigorous high-temperature procedures. New synthetic results in organoboron photochemistry include the synthesis of an ethynyl derivative of three-coordinate boron. The relationship of photochemical and other energetic processes has been probed in studies of free radical chemistry of phosphorus. The radicals PCl_2 and PCl_4 have been characterized and their chemical consequences investigated.

THE USE OF SPECIES FORMED BY HIGH TEMPERATURE
EVAPORATION IN CHEMICAL SYNTHESIS

P. L. Timms

Over the last thirty years, there has been growing interest in the high temperature, vacuum evaporation of many solid elements and compounds to form thin films, special alloys and new solid phases. As a result, methods and apparatus now exist for the evaporation of at least a gram an hour of most materials at any temperature up to 3500°C at pressures of 10^{-6} torr or lower.

There has also been increasing study of vapor species formed when materials vaporize at above 1000°C. The species have mostly been identified by their mass spectra or ultra-violet spectra, and vapor equilibrium measurements have been made.

Atoms of the metals and metalloids, vapors of low valent compounds, and vapors of some normal valent compounds, formed at high temperatures, are all "high energy" species. They may be capable of chemical reactions not shown by the original material in the condensed phase at lower temperatures. Yet despite their physical characterization and commonplace generation for other purposes, the possible use of high temperature vapors as reagents in chemical synthesis has been overlooked until the last few years.

The purpose of this paper is to discuss the conditions necessary to use high temperature species in synthesis, to indicate the synthetic potentialities of such species, and to summarise the results of relevant research underway in the author's laboratory.

Conditions for using high temperature vapors in synthesis

Whenever a vapor is formed by heating a material in the condensed phase, the energy supplied overcomes the forces which hold the

molecules or atoms together. Relative to the condensed phase of the material at room temperature, the vapor is a species of higher energy. For a material with a normal boiling point of above 1500°C , the difference in free energy between the solid at room temperature and its vapor at room temperature will usually be above 30 Kcals per mole. The vapors of metals, with a few exceptions, will be atomic species with free energies of formation of +30 to +180 Kcals relative to the solid metal. Such atomic species may have a chemical reactivity far greater than that of the original metals.

Of course, the vapors formed by evaporation at high temperatures are not stable at ordinary temperatures and will immediately condense to reform the starting material. They can thus be made to undergo gas-phase reactions only with the relatively few other molecules which are stable at high temperatures. However, the potential reactivity of the high temperature vapors towards a wide range of compounds can be exploited by cocondensing the high temperature vapor and the vapor of another compound on a surface at -196° . This requires that the high temperature vapor is generated under high vacuum and passes by a collision free path to a cold surface, on to which another molecule is also being condensed. The high temperature species will either react with itself on the cold surface or with the other molecule. Which reaction is favored depends on both thermodynamic and kinetic factors. Only reactions with an activation energy less than about 5 Kcals can occur to a measureable extent at -196° , but fortunately the reactions of many high temperature species do have very low activation energies.

Synthetic possibilities of high temperature species

Two types of uses are seen for cocondensation reactions of high temperature species with ordinary molecules at low temperatures. In the first, the high temperature atom or molecule will become incorporated in another molecule with which it reacts. This use has been well illustrated by published work on carbon and silicon vapor, and by reactions of other high temperature species such as boron monofluoride, silicon difluoride, and silicon dichloride¹. It is to be expected that atoms and homonuclear molecules of almost all metals and metalloids, and molecules like BC_2 , SiC , SiO , etc., will all react with other molecules to form new compounds which contain the species.

In the second use, the high temperature species may be used as powerful and selective reagents for removal of halogens and other active atoms from molecules. Although nearly all metals might serve in this role, it is to be expected that the greatest selectivity will be shown by the later transition metals, for which intermediates may be governed by particular complexing ability.

Present work in the author's laboratory

A. Methods of Evaporation

Two main methods are being used to evaporated metals and other materials inside a chamber with liquid nitrogen cooled walls, at a pressure less than 10^{-6} torr.

The first is electron bombardment heating using a Varian "e-Gun", which permits downward evaporation from a rod of material. For those materials which melt before evaporation, a molten drop is held on the end of

the rod by surface tension. The rod can be advanced as material vaporises from the tip. The method gives a rate of evaporation of about one gram an hour for most metals boiling below 3000°C , and for carbon, silicon, and boron. The method has the disadvantage that it does not allow evaporation of very large quantities of metals. There is also some uncertainty about the temperature at which evaporation is occurring, and the electronic state of the vapor species formed. Occasionally there have been problems due to stray electrons inside the vacuum chamber exciting the vapor which is being cocondensed with the high temperature species.

The second method is simple evaporation from resistively heated molybdenum boats or baskets, with or without alumina linings. It is easy to evaporate 1 to 3 g. an hour of metals like copper or silver, and it will probably prove the best method for most metals boiling below 3000°C . It can be scaled up to permit evaporation of many grams of a metal.

B. Reactions of atoms being studied

Boron Atoms

The reactions of boron with hydrogen halides, boron trichloride, phosphorus trichloride, and some organic compounds have already been reported by the author². Further reactions being carried out all tend to confirm the idea that boron atoms react destructively with most compounds. Free radical polymerisation occurs, and the yields of products in which boron has undergone simple insertion into a bond or any similar process, are always low.

Silicon Atoms

One reaction of silicon atoms, their insertion into the Si-H bond

of trimethylsilane, has already been reported by Skell³. In this work, silicon has been reacted with B_2F_4 in an effort to make compounds in the series $SiF_{4-n}(BF_2)_n$ (the first two members of this series, SiF_3BF_2 , and $SiF_2(BF_2)_2$, have resulted from the action of SiF_4 on boron at $2000^\circ C$). The only new volatile material obtained from the cocondensation of B_2F_4 and Si atoms, has been characterised as $SiF(BF_2)_3$. This structure was assigned from its mass spectrum, ^{11}B and ^{19}F nmr spectrum, and infrared spectrum. The compound $Si(BF_2)_4$ was not formed.

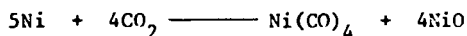
Iron Atoms

Iron has been cocondensed with a large excess of benzene in an effort to make the as yet unknown compound dibenzeneiron, $Fe(C_6H_6)_2$. On warming the cocondensate to about -50° under vacuum, most of the benzene could be pumped off. On warming further to 0° , the cocondensate exploded liberating benzene, and a little diphenyl and hydrogen. The residue was metallic iron. If the cocondensate was allowed to warm from -50° to room temperature in the presence of one atmosphere of hydrogen, there was no explosion. The volatile material which could be pumped off was then mostly cyclohexane. The results suggest that a very unstable iron benzene compound was being formed. The reactivity of benzene in the compound was far higher than usual as it would be reduced to cyclohexane under very mild conditions. The formation of dibenzeneiron would be consistent with the data so far obtained, but more work is necessary to prove its existence.

This work with iron atoms does demonstrate that cocondensation reactions may be a useful route to unstable zero-valent transition metal complexes.

Nickel Atoms

Nickel was cocondensed with carbon dioxide. On warming the cocondensate a little above -196° some carbon monoxide was evolved. About 15% of the nickel deposited was recovered as nickel carbonyl, the rest remained as a black nickel oxide, approximating to NiO in composition. The yield of $\text{Ni}(\text{CO})_4$ was about 75% of that required by the equation



Nickel was also condensed with boron trifluoride to try to obtain $\text{Ni}(\text{BF})_4$. Reaction occurred but the product seemed to be a mixture of a nickel boride and the known complex $\text{NiF}_2 \cdot \text{BF}_3$. No evidence of stepwise reduction of the boron trifluoride was obtained.

Copper and Silver Atoms

Copper has been found to be a very effective reagent for removing chlorine from B-Cl bond and coupling the boron atoms. When copper atoms and BCl_3 were cocondensed in a 1:6 mole ratio, B_2Cl_4 was formed in 40% of the yield required by the equation



Using copper atoms and CH_3BCl_2 , a similar yield of the new compound 1,2-dimethyl-1,2-dichlorodiboron was obtained. This was characterised by its mass spectrum and its ^{11}B and proton nmr spectrum, and by its quantitative reversion to CH_3BCl_2 on treatment with chlorine at -80° . The cocondensation reaction of copper with $(\text{CH}_3)_2\text{BCl}$ was very complex, although an unstable compound $(\text{CH}_3)_4\text{B}_2$ may have been among the products.

Cocondensation of copper atoms generated by electron bombardment heating with a mixture of BCl_3 and SiCl_4 , gave B_2Cl_4 and $\text{SiCl}_3\text{BCl}_2$. Cocondensation of copper evaporated from a molybdenum boat at 1400° with the same mixture, gave B_2Cl_4 but no $\text{SiCl}_3\text{BCl}_2$. This is an example of electronic excitation either of the copper vapor or of the SiCl_4 which can occur with electron bombardment heating.

Silver atoms, formed by evaporation from molybdenum boats, react with B-Cl compounds in a similar way to copper atoms, but the yields are much poorer. The bulk of the silver is recovered as metal from the surface where cocondensation takes place.

References

1. For a general review see P.L. Timms, *Endeavour*, 27, 133 (1968)
2. P.L. Timms, *Chem. Commun.*, 258 (1968)
3. P.S. Skell and P.W. Owen, *J. Am. Chem. Soc.*, 89, 3933 (1967)

THE OXIDATION OF HYDROGEN CHLORIDE IN ELECTRODELESS
RADIOFREQUENCY DISCHARGES

Raymond F. Baddour and D. F. Flamm

Department of Chemical Engineering
Massachusetts Institute of Technology, Cambridge, Massachusetts 02139

A study of the oxidation of Hydrogen Chloride in electrodeless glow discharges between 3.75 and 150 torr is described. A cylindrical quartz reactor was used at 2450 MHz in a tapered waveguide section. Other work done at 7 and 20 MHz used cylindrical vessels with external sleeve electrodes and pillbox-shaped reactors with external electrodes painted onto the flat top and bottom surfaces. Power at 20 MHz was coupled from a self-excited oscillator through a coupling coil in the tank and at 7 MHz a helical resonator was used.

For sufficiently high driving frequencies there is not sufficient time during a cycle for electrons to be swept to the walls of a discharge reactor. Electron loss is then controlled, in a non-attaching gas, by diffusion. For a constant electron momentum collision frequency ν_m , the average power input per unit

$$P = \frac{n_e e^2 E_o^2}{2m\nu_m} \frac{\nu_m^2}{\omega^2 + \nu_m^2}$$

and likewise the electron energy is given by

$$E = E_{dc} - \frac{k\nu_m}{2\omega} E_{dc} \sin 2\omega t$$

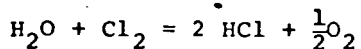
where

$$E_{dc} = \frac{e\mu E_o^2}{2k\nu_m}$$

is that energy obtained in a d.c. electric field of magnitude equal to the a.c. R.M.S. value and where ω is the frequency of the applied field, k is the average fraction of energy lost per collision and is assumed constant, m is the electron mass, and E_o is the peak applied field, and μ is the mobility.

The behavior is explained by the balance between electron attachment and detachment processes in the different regions of the discharge.

Limited data were also obtained on the reverse reaction



which gave some evidence that at moderate pressures the reaction approached an asymptotic composition at long residence time.

Finally it is shown that a major method of energy loss for electrons is vibrational excitation of HCl and subsequent infrared radiation.

FREE ENERGY CHARTS FOR HIGH TEMPERATURE CHEMICAL CALCULATIONS

T. B. Reed

Lincoln Laboratory, * Massachusetts Institute of Technology
Lexington, Massachusetts 02173

To calculate the degree of chemical reaction for



at any temperature, it is necessary to know the Gibbs free energy change

$$\Delta G(T) = \Delta H(T) - T\Delta S(T) \quad (2)$$

One can then find the concentrations of the reactants and products from the equilibrium constant K

$$\Delta G = -RT \ln K \equiv -RT \ln \frac{p_M^m p_N^n}{p_A^a p_B^b} \quad (3)$$

where p is the activity of each reactant. For reactants whose standard state is gaseous at the reaction temperature, p is approximately equal to the partial pressure.

The heat capacities, and other thermodynamic properties of elements and compounds, are not simple functions of temperature and are usually presented in extensive tabulations such as JANAF Tables. However, in forming ΔG from these properties, the non-linear terms largely cancel so that to a very good approximation

$$\Delta G(T) = \Delta \bar{H} - T\Delta \bar{S} \quad (4)$$

where now $\Delta \bar{H}$ and $\Delta \bar{S}$ are respectively the asymptote and slope of a plot of ΔG vs T , and may differ by 5-10% from $\Delta H(T)$ and $\Delta S(T)$. For instance, the free energy of formation of Al_2O_3 varies from the straight line $\Delta G = -402.3 + 77.2T$ by at most 0.08% between 1,000 and 2,300^oK, while $\Delta H(T)$ varies by 1.5% and $\Delta S(T)$ varies by 5% over this range.

It is possible to summarize a great deal of the data on chemical reactions in the form of families of straight lines on plots of ΔG vs T . Free energies of reactions for the formation of the chalcogenides, halides and hydrides, disassociation of polyatomic gases and ionization of elements are assembled here as a convenient summary of the thermodynamic data on these reactions. The straight line values of $\Delta \bar{H}$ and $\Delta \bar{S}$ are tabulated.

*Operated with support from the U. S. Air Force.

A plot of ΔG vs T has a number of advantages in the presentation of free energy data. It enables the relative reactivity of various materials to be easily visualized over a wide range of temperature. Phase changes are marked by changes in slope so that melting points and boiling points of reactants are recorded. The charts become simple nomograms in several ways. A fixed value of K lies on a line passing through the origin so that by adding one scale it is possible to read K or p for reactions involving only one gas. Other scales can be constructed to give the results of compound reactions such as hydrogen reduction of oxides. The free energy change is proportional to the emf of electrochemical reactions so that a separate scale gives this conversion.

At temperatures above $2,000^{\circ}\text{K}$ many of the diatomic gases begin to dissociate. Above $10,000^{\circ}\text{K}$ most molecules have dissociated to atoms and the atoms begin to ionize thermally to give electrons and ions. For dissociation and ionization at one atmosphere total pressure, it is possible to read on the free energy charts the degree of dissociation or ionization and the partial pressures of molecules, atoms, ions, and electrons. By moving the scale it is possible to read these quantities at any other total pressure. The use of the charts in measuring very high temperature is discussed.

The major source of entropy change in chemical reactions involving at least one gaseous species is the production or consumption of gas, since the entropy of a mole of gas is much higher than that of the corresponding solid or liquid. It becomes apparent on examining the charts that the entropy change is given approximately by $\pm \Delta \bar{S} = \pm k \Delta n$, where Δn is the increase in the number of moles of gas for the reaction. For the formation of the chalcogenides and halides, the constant k is approximately 40-50 e. u./mole, but is smaller for reactions involving dissociation or ionization. Provided that the reactions are all written for one mole of gas, the free energy charts then show a series of parallel lines of slope $\Delta \bar{S}$. From this it is seen that the relative magnitude of ΔG is determined primarily by $\Delta \bar{H}$ and the relative stability of oxides, sulfides, etc. stays constant over a wide range of temperatures.

The oxygen pressure at equilibrium between a metal and its oxide or between an oxide and a higher oxide provides a scale of stability toward oxidation similar to the EMF or electronegativity scale. We define "pO" as the negative log of oxygen pressure, $-\log p_{\text{O}_2}$ (analogous to the definition of pH as the negative log of hydrogen